
iAtlantic Deliverable 4.2

Baseline ecosystem functioning in selected deep-sea environments

Project acronym:	iAtlantic
Grant Agreement:	818123
Deliverable number:	4.2
Deliverable title:	Baseline ecosystem functioning in selected deep-sea environments.
Work Package:	4
Date of completion:	February 2024
Author:	Andrew K. Sweetman, Danielle de Jonge, Daniela Gaurisas, Angelo Bernadino, Loïc N. Michel, Corentin Le Goff, Christophe Brandily, Marjolaine Matabos, Eve-Julie Pernet, Julie Tourolle, Lénaïck Menot, Sebastian Hennige, Kelsey Barnhill, Marina Carreiro Silva, Laurence De Clippele, Covadonga Orejas.



This project has received funding from the European Union's Horizon 2020 research and innovation programme under grant agreement No 818123 (iAtlantic). This output reflects only the author's view and the European Union cannot be held responsible for any use that may be made of the information contained therein.

Contents

List Of Tables	3
List of Figures	6
List of Acronyms	9
Executive Summary	10
1. Introduction	12
2. Case study 1 – <i>In situ</i> and modelled benthic ecosystem functioning on the Cabo Verde Abyssal Basin and comparisons to other Atlantic sites.	17
2.1 Materials and Methods	17
2.2 Results	38
2.3 Discussion of the data from Case-Study 1	48
3. Case study 2 – Soft sediment ecosystem functioning at the Cabo Verde upper bathyal slope compared to other oceanic regions.	54
3.1 Methods & Materials.....	54
3.2 Results	58
3.3 Discussion of data from case study 2	62
Conclusion	66
4. Case study 3 – How do shifts in upper-ocean ecosystems directly impact abyssal scavenger communities? – insights from baited camera lander deployments in the Cabo Verde Abyssal Basin (tropical East Atlantic).	67
4.1 Materials & Methods.....	67
4.2 Results	71
4.3 Discussion of data from case study 3	83
5. Case study 4 - Trophic niches of the cold-water corals <i>Desmophyllum pertusum</i> (<i>Lophelia pertusa</i>) and <i>Madrepora oculata</i> in the Lampaul Canyon (Bay of Biscay)	91
5.1 Material & Methods	91
5.2 Results	95
5.3 Discussion of data from case study 4	98
6. Case Study 5 – Comparisons of the live and dead coral framework from multiple Atlantic sites	99
6.1 Materials and methods.....	99
6.2 Results	110
6.3 Discussion of data from case study 5	120
7. Key conclusions from the different case studies	127
8. References.....	129
9. Document Information	145

List of Tables

Table 1. Benthic Respirometer Lander deployment stations: latitude (Lat) and longitude (Lon) in decimal degrees (DD), depth in meters, and date.....	19
Table 2. C stocks of food-web model compartments (mmol C m ⁻²) at the Porcupine Abyssal Plain (PAP) and Cape Verde Abyssal Plain (CVAB).....	27
Table 3. Food-web fluxes (mmol C m ⁻² d ⁻¹) used in the LIM models [min, max]. References: (1) Van Oevelen et al. (2012), (2) Durden et al. (2017); (3) Dadou et al. (2001); (4) Lahajnar et al. (2005); (5) Eardly et al. (2001); (6) Fukuda et al. (1998); (7) Relexans et al. (1996); (8) Auffret et al. (1992); (9) Danovaro et al. (2008); (10) Brunnegård et al. (2004), (11) Rabouille et al. (1993); (12) Lebrato et al. (2011); (13) Lebrato et al. (2013), (14) Lebrato et al. (2019); (15) Lucas et al. (2014); (16) Pierre (2001); (17) Pfannkuche and Lochte (2001); (18) Sweetman et al. (2019).	27
Table 4. Characteristics of the studied sites Porcupine Abyssal Plain (PAP) and the Cape Verde Abyssal Basin (CVAB). References: (1) Rabouille et al. (2001); (2) Witbaard et al. (2000); (3) Relexans et al. (1996); (4) Galéron et al. (2000); (5) Hall et al. (2007); (6) Buchanan, 1984.....	29
Table 5. Taxon-specific relative abundance of feeding types and individual biomass (mmol C ind ⁻¹) for metazoan meiofauna. B = bacterivore, EF = epistrate feeder, SDF = selective deposit feeder, DF = deposit feeder, OP = Omnivores and Predators. References for feeding type (FT) and biomass (BM): (1) Sebastian et al. (2007); (2) Wieser (1953); (3) Jumars et al. (2015); (4) Gowing and Wishner (1986); (5) Paterson et al. (1998); (6) Bianchelli et al. (2010); (7) Zeng et al. (2018); (8) Galéron et al. (2000); (9) Rowe (1983); (10) Jensen (1984); (11) Ikeda et al. (2006); (12) Salonen and Sarvala (1980).	32
Table 6. Taxon-specific biomass conversion factors and feeding types for the metazoan macrofauna. Conversion factors are taken from Rowe (1983) and adjusted for an estimated 25% C loss due to formaldehyde preservation of macrofauna as reported in Salonen and Sarvala (1980). C = carbon, DM = dry mass, WM = wet mass. FSF = filter and suspension feeders, SDF = surface deposit feeders, DF = deposit feeders, O = omnivores, PS = predators and scavengers. References (FT = feeding types, CN = C:N ratios): (1) Jumars et al. (2015); (2) Blazewicz-Paszkowycz and Ligowski (2002); (3) Iken et al. (2001); (4) Trott (1998); (5) Scheltema (1997); (6) Fox et al. (2003); (7) Thiel and Kruse (2001); (8) Murina (1984); (9) McClain et al. (2004); (10) Menzies (1962).	32
Table 7. Taxon-specific biomass conversion factors and feeding types for the metazoan megafauna. Conversion factors are the macrofaunal and epifaunal conversion factors from Rowe (1983) and adjusted for an estimated 25% C loss due to formaldehyde preservation of macrofauna as reported in Salonen and Sarvala (1980). C = carbon, WM = wet mass. FSF = filter and suspension feeders, SDF = surface deposit feeders, DF = deposit feeders, O = omnivores, PS = predators and scavengers. References feeding types (FT): (1) Aberle and Witte (2003); (2) Jumars et al., (2015); (3) Fox et al. (2003); (4) Iken et al. (2001); (5) McClain et al. (2004); (6) Smith and Stockley (2005); (7) Marine Species Traits database.	33
Table 8. Physiological constraints [min, max] and feeding selectivity. NGE = Net growth efficiency, AE = Assimilation efficiency, SP = Secondary Production, MR = Maintenance respiration, GR = growth respiration. References: (1) van Oevelen et al. (2012); (2) de Jonge et al. (2020).	36
Table 9. Sediment Community Oxygen Consumption (SCOC, mmol O ₂ m ⁻² d ⁻¹) and DIC production rates (mmol C m ⁻² d ⁻¹). SCOC was estimated with both Micro-Winkler titrations and in situ oxygen concentration data as measured with Aanderaa oxygen optodes (model 4330F). n.d. = no data were collected due to a malfunction in the sampling device.	38
Table 10. Nutrient fluxes measured for each lander deployment. A positive flux means efflux (i.e., flux out of the sediment) and a negative flux means influx (i.e., flux into the sediments). Reported p-values are for the 1-sample Wilcoxon signed rank test to assess if the tracer experiment mean was significantly different from the background value.	39
Table 11. Bacterial biomass and bacterial C uptake (μmol C m ⁻² d ⁻¹) in the tracer experiments for different sediment horizons (0–2, 2–5, 5–10 cm) based on the C15:0i PLFA biomarker.	39
Table 12. Meiobenthic (excluding Foraminifera) density (individuals 10cm ⁻²), biomass (mg dry mass m ⁻² , and mg C m ⁻²), and C uptake (mg C m ⁻² d ⁻¹) for the 0–5 cm sediment horizon.....	40
Table 13. Macrofaunal (excluding Foraminifera) density (ind. m ⁻²), biomass (mg dry mass m ⁻² , and mg C m ⁻²), and C uptake (mg C m ⁻² d ⁻¹) for various sediment horizons. Reported mean ± SD. Note: data for macrofauna C-uptake are not available (NA) for macrofauna at this time, though the samples have been sent for analysis.....	43
Table 14. Comparison of ecosystem characteristics over all iterations (mean ± stdev) between the PAP and CVAB C-based food webs. Certain C cycling pathways (mmol C m ⁻² d ⁻¹) are reported, including Total System	

Throughflow (TST), secondary production, and C uptake. For size-based groups their relative contribution to these pathways is reported. System organisation indices include Finn's Cycling Index (FCI), Relative Ascendancy (RA), and Average Mutual Information (AMI). Trophic indices related to trophic interactions and energy transfer include PB-ratios (community and size-based), burial efficiency i.e. deep C burial flux relative to total C influx, synergism (S), average system trophic level (TL), and the Omnivory Index (OI). Significance: ** highly significant, * significant, or – no difference between sites.

.....	45
Table 15. SCOC rates (mean \pm se, n = 4, mmol O ₂ mm ⁻² d ⁻¹) measured at various points in time after seafloor retrieval (Incubation time) at 6.5°C (current seafloor conditions) and 8.5°C (future temperature increase at the seafloor) during the equilibration period. Values in brackets are mean SCOC rates converted to mg C m ⁻² d ⁻¹ . Significant differences (p < 0.05) in bold. The differences in rate between the two temperatures (and how much greater SCOC is for the warm temperature between brackets) is also given. The Q ₁₀ value was only calculated for the significant differences.	59
Table 16. Comparison of SCOC rates at various slopes in the Atlantic at similar depth (700–1,000 m) extracted from the global SCOC database (Stratmann et al., 2019). References: (1) this study; (2) Duineveld et al. (1997); (3) Main et al. (2015); (4) Makela et al. (2018); (5) Jahnke and Jahnke (2000); (6) Glud et al. (1994).	62
Figure 15. Relative abundance (individuals m ⁻²) and biomass (mg DM m ⁻²) for Cabo Verde bathyal soft sediments for a) major macrofaunal taxa; b) polychaete families; c) crustaceans orders. Data are from 7 MUC corers.	64
Table 17. Deployments of the Baited Camera Lander and the Baited Trap Lander. Latitude and longitude (Lat, Lon) are given in decimal degrees (DD), Depth in meters. Pictures (n) show the number of pictures taken at the seafloor.	68
Table 18. A summary of the Baited Camera Lander experiment at the Cabo Verde Abyssal Basin at 4,200 m. Per bait type the mean \pm SE 1) time of first arrival (hours), 2) maximum number of individuals in one image (maxN), and 3) time of maxN (hours) for each morphospecies (Biigle ID in brackets). If the morphospecies is not observed at all for a certain bait type, it's noted as NA. Significant differences, i.e. p<0.05, are in bold.	73
Table 19. Results of SIMPER analysis on both the full diversity matrix ('Original analysis') and a matrix treating the <i>Coryphaenoides</i> morphospecies as a single complex (' <i>Coryphaenoides</i> complex'), limited to the morphospecies cumulatively contributing the first 70% of differences between bait types and/or with a significant permutation test (significant values in bold).	77
Table 20. <i>Coryphaenoides</i> spp. and <i>Barathrites iris</i> density estimates N (ind km ⁻²) based on the 'Time of first arrival' model from Priede and Merrett (1996), using the bottom water current speed in the first hour of lander deployment (V _w , in m s ⁻¹) as measured with the in-situ lander ADCP. To estimate <i>Coryphaenoides</i> spp. density N ₁ a fish swimming velocity based on observed in situ departure speed was used (V _{fa} = 0.077 m s ⁻¹ , C. Wylie in Henriques et al. (2002)). A fish swimming velocity based on Code-Activated Transponders employed at the Cape Verde Abyssal Basin was used to estimate <i>Coryphaenoides</i> spp. density N ₂ (V _{fb} = 0.15347 m s ⁻¹) and <i>B. iris</i> density N (V _f = 0.2135 m s ⁻¹) (Henriques, 2004).	78
Table 21. Tissue composition, size and trophic level of reference specimens: dry mass to wet mass ratio, C content (wt% of DM), N content (wt% of DM), $\delta^{13}\text{C}$ (‰) corrected following Post et al. (2007), $\delta^{15}\text{N}$ (‰), size (mm; pre-anal fin length for fish, dorsal line from tip rostrum to tip telson for amphipods), and the trophic level (TL) based on their mean $\delta^{15}\text{N}$ referenced against the local zooplankton with an assumed TL = 2. The 'pelagic jelly' sample is a mix of a salp, siphonophore, and medusa jelly.	85
Table 22. Results from comparing living layer: whole colony ratio using van der Kaaden and De Clippele's (2021) method on the images from Vad et al. (2017).	101
Figure 33. Histogram of differences between LL: WC for the method used in Vad et al. (2017) and the whole colony approach in De Clippele et al. (2021) applied to the same images. Difference values relate to the difference in ratio values, with most images having a higher ratio of live: whole colony values between 0.2 to 0.3 using methods by De Clippele et al. (2021). Of note is the range of differences.	102
Table 23. Collection sites and depths of the cold-water coral species used in the study.	105
Table 24. Physical-chemical parameters at the study sites. Data on Norwegian reefs from Büsher et al. (2019).	106
Table 25. Coral growth simulation parameters for Smooth Particle Hydrodynamic models to simulate coral growth and death (Georgoulas et al., 2023).	110
Table 26. Locations of the three study sites for surface area of live and dead coral framework in the Atlantic .	110
Table 27. The average carbon turnover rates (\pm SE) per g of coral (live, dead and total) per m ² per year. Values are	

highlighted of framework forming corals *Desmophyllum pertusum* (*Lophelia pertusa*) (LP) and *Madrepora oculata* (MO) in Angola, Mingulay, Pisces and Canada. Mingulay values (*) were already published in De Clippele et al. (2021) but converted here from T of Carbon into g of Carbon for comparative purposes. Values are also combined to give a total comparative value. Image sample sizes across sites were uneven and ranged from 4–28 available images. 111

Table 28. Average carbon turnover rates per g of live coral per m² per year for *M. oculata* in Angola. Values are compared using *M. oculata* specific polyp numbers, polyp weight and respiration values from two different studies, with equations from *D. pertusum* (*L. pertusa*) (De Clippele et al., 2021). 112

Table 29. Results from the Canadian *Lophelia* Coral Conservation Area of living layer: whole colony ratio, and the percentage of live coral overall compared to the whole image area with average, standard error, and median metrics. 113

Table 30. Site comparisons of Living Layer: Whole Colony ratio of framework forming corals including *D. pertusum* (*L. pertusa*) (LP) off Angola, Canada, the Mingulay Reef Complex (MRC) and Pisces, with standard error, median, and min/max values. Published values for the live and dead ratio are included in the table for comparative purposes, although absolute values may differ due to the Vad et al. methodology used (compared in full in earlier section). Angola *M. oculata* values are from Orejas et al. (2021) (*) and show LL:WC values using published average coral live and dead sizes. 114

Table 31. Skeletal density parameters (micro-density, bulk density and porosity) for the different species studied and for the different study sites within three geographic regions (NE Atlantic, Central NE Atlantic, NW Mediterranean). Values are mean ± SD, n=3–12. 115

Table 32. Dynamic energetic reserves in 2D SPH simulations. The presented properties of the coral colonies are taken from the 100th growth-steps of the simulations. 118

Table 33. Ratio of live to total coral particles in the domain at the 50th and 100th growth steps based on the simulated ability of the colonies to replenish their energetic reserves. 122

List of Figures

Figure 1. Cape Verde Archipelago and Benthic Chamber Lander deployment stations at ~4,200 m near the island of Brava of Cabo Verde. The red square indicates the lander region.	18
Figure 2. Benthic Chamber Lander onboard the RV <i>Sarmiento de Gamboa</i> being processed after a deployment. Photo by Murray Roberts, iMirabilis2.	19
Figure 3. Locations of the three sites discussed in case study 1 mapped onto the Net Primary Productivity (NPP) estimated from satellite-based chlorophyll measurements (Oregon State University, 2019). The Porcupine Abyssal Plain (PAP) in the North Atlantic, and two sites in the Cabo Verde Abyssal Basin (CVAB): the site studied during the EUMELI project used in the food-web model, and the site studied using the Benthic Chamber Lander (BCL).	25
Figure 4. Species accumulation curve showing the macrofaunal number of taxa per number of collected samples.	41
Figure 5. Relative abundance (individuals m ⁻²) and biomass (mg dry mass m ⁻²) in the 0–10 cm sediment layer at the Cabo Verde Abyssal Basin of a) major macrofaunal taxa; b) polychaete family; c) crustacean order. Data are from 14 benthic chambers.	42
Figure 6. Vertical distribution of a) total macrofaunal abundance (individuals m ⁻²) and b) total macrofaunal biomass (mg DM m ⁻²) within the sediment.	43
Figure 7. Resolved food-web of the Porcupine Abyssal Plain (PAP, above) and the Cabo Verde Abyssal Basin (CVAB, below). Flow size is the Bayesian (mean) solution of 50,000 iterations. Food web compartments: (1) Labile detritus, (2) Semi-labile detritus, (3) Refractory detritus, (4) Dissolved Organic C, (5) Prokaryotes, (6) Foraminifera, (7) Meiofauna, bacterivores, (8) Meiofauna, epistrate feeders, (9) Meiofauna, selective deposit feeders, (10) Meiofauna, deposit feeders, (11) Meiofauna, omnivores and predators, (12) Macrofauna, filter and suspension feeders, (13) Macrofauna, surface deposit feeders, (14) Macrofauna, deposit feeders, (15) Macrofauna, omnivores, (16) Macrofauna, predators and scavengers, (17) Megafauna, filter and suspension feeders, (18) Megafauna, surface deposit feeders, (19) Megafauna, deposit feeders, (20) Megafauna, omnivores, (21) Megafauna predators and scavengers.	45
Figure 8. Comparison between ecosystem functioning at the Cabo Verde Abyssal Basin and the Porcupine Abyssal Plain based on in situ experimental data. These two datasets are the only studies of its kind in the Atlantic Ocean to compare, but it should be acknowledged they occurred over 20 years apart.	50
Figure 9. Sampling station where multicores (MUC) were obtained for the ex-situ multistressor experiment. ...	54
Figure 10. CTD data for the MUC sampling station (credit: Angela Mosquera-Gimenez, iMirabilis2).	55
Figure 11. Set-up of the multi-stressor incubation experiment during a SCOC measurement interval. Sediment in cores, sealed at the bottom, are placed in buckets of water, and located in cooled incubators. The sealing lid carries the stirrer bar (white) and FireSting oxygen optodes (blue label). After the SCOC interval, the lid including stirrer and optode were removed, and an air stone was replaced to oxygenate the open core. Note that this image was taken shortly after sampling i.e. before the 1-week equilibration period, and the overlying water in some cores were somewhat cloudy.	57
Figure 12. SCOC rates (mmol O ₂ m ⁻² d ⁻¹) at 60, 85, 95, and 125 hours into the equilibration period (i.e., before the algae injection) for the 6.5°C and 8.5°C temperature treatments (n=4 per treatment).	60
Figure 13. Bacterial standing stock (mg C m ⁻²) in the unincubated cores (Treatment = None, n=3) and in the incubated cores at either 6.5°C or 8.5°C after a 48-hour stable isotope tracer experiment with injected algae (n=4). Error bars represent 1 standard error.	61
Figure 14. Mean bacterial phytodetritus-derived C uptake (mg C m ⁻² d ⁻¹) at 6.5°C and 8.5°C after a 48-hour stable isotope tracer experiment with injected algae (n=4). Error bars represent 1 standard error.	61
Figure 15. Relative abundance (individuals m ⁻²) and biomass (mg DM m ⁻²) for Cabo Verde bathyal soft sediments for a) major macrofaunal taxa; b) polychaete families; c) crustaceans orders. Data are from 7 MUC corers.	64
Figure 16. Baited Camera Lander recovery after a deployment to the Cabo Verde Abyssal Basin at ~4,200 m (picture by Beatriz Vinha, iMirabilis2).	67
Figure 17. Baited Trap Lander used to collect reference specimens.	69
Figure 18. Scavenging rates on squid (<i>Doryteuthis gahi</i>) and fish (<i>Scomber scombrus</i>) bait, reported as a) removal time (h), b) wet consumption rate (kg WM d ⁻¹), and c) energy consumption rate (kJ d ⁻¹). ** highly significant (p<0.01), * significant (p<0.05).	72
Figure 19. Species accumulation curve for all eight deployments.	75
Figure 20. Rarefaction curves for the different camera lander deployments.	76

- Figure 21.** nMDS plot of the community diversity matrix based on maxN data. Solid lines delineate the convex hull per bait type, where fish bait (*Scomber scombrus*) was used at site 1, 3, 5, and 8, and squid bait (*Doryteuthis gahi*) was used at site 2, 4, 6, and 7. 76
- Table 20.** *Coryphaenoides* spp. and *Barathrites iris* density estimates N (ind km^{-2}) based on the 'Time of first arrival' model from Priede and Merrett (1996), using the bottom water current speed in the first hour of lander deployment (V_w , in m s^{-1}) as measured with the in-situ lander ADCP. To estimate *Coryphaenoides* spp. density N_1 a fish swimming velocity based on observed in situ departure speed was used ($V_{fa} = 0.077 \text{ m s}^{-1}$, C. Wylie in Henriques et al. (2002)). A fish swimming velocity based on Code-Activated Transponders employed at the Cape Verde Abyssal Basin was used to estimate *Coryphaenoides* spp. density N_2 ($V_{fb} = 0.15347 \text{ m s}^{-1}$) and *B. iris* density N ($V_f = 0.2135 \text{ m s}^{-1}$) (Henriques, 2004). 78
- Figure 22.** Mean total number of scavengers over time for fish (*Scomber scombrus*, top) and squid (*Doryteuthis gahi*, bottom) bait with 95% CI. 79
- Figure 23.** Mean number of *Coryphaenoides* spp. complex (black), *Barathrites iris* (blue), *Hymenopenaeus laevis* (red), all Mysidae morphospecies (yellow), and amphipods msp. 2 (green) over time with 95% CI. ... 80
- Figure 24.** Fitted Zero-Inflated Negative Binomial regression model for total Crustacea versus total Actinopteri counts over all eight deployments, indicating the slope is highly significantly different from 0 ($p < 0.001$). 81
- Figure 25.** Total fish (blue) and total crustacean (red) abundances during deployment AKS299 using fish *S. scombrus* bait. Lines are smoothed with a Local Polynomial Regression Fitting using an α of 0.3 to show how peaks and troughs of Crustacea and Actinopteri appear opposite. The black line indicates the current direction in degrees, the grey horizontal line is at 180° i.e. below the grey line are eastward currents, the grey line itself is a southward current, and above the grey line are westward currents. 82
- Figure 26.** Isospace biplot based on $\delta^{13}\text{C}$ (‰) and $\delta^{15}\text{N}$ (‰) of pelagic and demersal reference specimens. The convex hulls delineate the pelagic and demersal communities. For comparison, the used bait species *S. scombrus* and *D. gahi* are also included. Error bars show standard errors. 84
- Figure 27.** Map of the Lampaul canyon (A) in the northern Bay of Biscay (B). 91
- Figure 28.** Map of the sampling dives during the ChEReef 2021 cruise. 94
- Figure 29.** Isotopic compositions of CWCs and associated fauna in the Lampaul Canyon. Top: carbon and nitrogen isotopic ratios. Bottom: carbon and sulphur stable isotope ratios. Points are means; error bars are standard deviations. Grey points indicate suspended particulate organic matter, other colours pertain to larger taxonomic groups (blue: CWCs, red: other cnidaria, green: Mollusca, Purple: Polychaeta, black: Crustacea, orange: Echinodermata, brown: Urochordata). 96
- Figure 30.** Isotopic niches of CWCs and associated fauna in the Lampaul Canyon. Top: carbon and nitrogen ellipses. Bottom: carbon and sulphur ellipses. Points are individual measurements. Colours pertain to different taxa. 97
- Figure 31.** $\delta^{13}\text{C}$ - $\delta^{15}\text{N}$ scatterplot with standard ellipses corrected for small sample size population (SEA_C) overlaid for the three CWC species from the central oligotrophic Mediterranean Sea. Image from Da Ros et al. (2022). 98
- Figure 32.** The difference in methods shown for Colony 1. (A). Image adapted from Vad et al. (2017) who calculated the living layer: whole colony ratio as 0.14.; (B). Image segmentation output from Photoshop using the method by van der Kaaden and De Clippele's (2021) which calculated the living layer: whole colony ratio as 0.44. 100
- Figure 33.** Histogram of differences between LL: WC for the method used in Vad et al. (2017) and the whole colony approach in De Clippele et al. (2021) applied to the same images. Difference values relate to the difference in ratio values, with most images having a higher ratio of live: whole colony values between 0.2 to 0.3 using methods by De Clippele et al. (2021). Of note is the range of differences. 102
- Figure 34.** The difference in methods shown for Colony 17. A. Image adapted from Vad et al. (2017) who calculated the living layer: whole colony ratio as 0.17. B. Image segmentation output from Photoshop using the method by van der Kaaden and De Clippele (2021) which calculated the living layer: whole colony ratio as 0.15. 102
- Figure 35.** Scleractinian cold-water corals examined in the study: (a) *Desmophyllum pertusum* (*Lophelia pertusa*); (b) *Madrepora oculata*; (c) *Dendrophyllia cornigera*; (d) *Desmophyllum dianthus*; (e) *Caryophyllia* sp. Photo credit: a, c, d © Eduardo Obis, b © Andrea Gori, CSIC aquaria facilities; e c © Rodrigo Sá da Bandeira, DeepSeaLab facilities, IMAR-UAZ. 104
- Figure 36.** Map showing the collection sites of corals used the study. 105
- Figure 37.** Graphical comparison of average carbon turnover rates (\pm SE) per g of coral (live, dead and total) per

	m ² per year. Values are highlighted of framework forming corals <i>D. pertusum</i> (<i>L. pertusa</i>) (LP) and <i>Madrepora oculata</i> (MO) in Angola, Mingulay, Pisces and Canada. Mingulay values (*) were already published in De Clippele et al. (2021) but converted here from T of Carbon into g of Carbon for comparative purposes.	112
Figure 38.	Skeletal density parameters (micro-density, bulk density and porosity) for the different species studies in three geographic regions (NE Atlantic, Central NE Atlantic, NW Mediterranean).	116
Figure 39.	Coral Growth using the Goldilocks Principle (that coral will grow where conditions are ‘just right’) in simulations with A) infinite initial energetic reserves, B) low initial energetic reserves and C) high initial energetic reserves. Growth is shown between the 20 th , 60 th and 120 th growth steps. Flow is in one direction and is from left to right at 0.5 m/s.	117
Figure 40.	Including the effects of gravity in coral growth. Initially a coral colony grew from a single point for 60 growth steps (A). At this point a break-down mechanism was initiated and the resultant colony is shown to include gravitational effects (B). Finally, growth in the domain has been re-initiated and coral growth at 120 growth steps is shown (C).	119
Figure 41.	Velocity profile with streamlines around the coral colony at the 70 th growth step. Red particles show live coral particles while yellow particles denote dead coral framework. For interpretation of the references to colour in this figure legend, please refer to Georgoulas et al. (2023).	119
Figure 42.	Adapted from Barnhill et al. (2022). Examples illustration how the ratio of live:dead coral reef framework by be impacted by environmental conditions.	123
Figure 43.	Scaling up from branch to habitat. Schematic of how the structural integrity model of a theoretical coral is reproducible and can be expanded through mathematical and computational modelling to create much larger, complex framework. The structural integrity of the framework can then be assessed by integrating information of the exposure to, and severity of the stressor to quantify timescales of habitat crumbling. The shaded area with coral fragments below the coral framework represents coral rubble infilled with sediment, and (...(n)) indicates how the framework can be extended to much larger sizes in a reproducible way. The starting ratio of live:dead coral would dictate whether this framework is susceptible to ocean acidification/ the proportion that is. Image adapted from Hennige et al. (2020).	125
Figure 44.	Present-day environmental conditions at the deep seafloor. Temperature (°C), dissolved oxygen (mL L ⁻¹), pH, and seafloor POC flux (mg C m ⁻² d ⁻¹) conditions at the deep (> 200 m) seafloor. Figure from Sweetman et al. (2017).	126

List of Acronyms

Acronym	Full name
AE	Assimilation Efficiency
AMI	Average Mutual Information
BCL	Benthic Chamber Lander
CTD	Conductivity Temperature Depth
CVAB	Cabo Verde Abyssal Basin
CVFZ	Cabo Verde Frontal Zone
CWC	Cold-Water Coral
DBD	Dry Bulk Density
DIC	Dissolved Inorganic Carbon
DOC	Dissolved Organic Carbon
EA-IRMS	Elemental Analyser-Isotope Ratio Mass Spectrometer
FCI	Finn's Cycling Index
GR	Growth Respiration
LD	Linkage Density
HROV	Hybrid Remotely Operated Vehicle
LIM	Linear Inverse Model
MR	Maintenance Respiration
NGE	Net Growth Efficiency
OI	Omnivory Index
PAP	Porcupine Abyssal Plain
PB-ratio	Production Biomass Ratio
PLFA	Phospho-Lipid Derived Fatty Acids
POC	Particulate Organic Carbon
POM	Particulate Organic Matter
RA	Relative Ascendancy
RV	Research Vessel
SCOC	Sediment Community Oxygen Consumption
SD	Standard Deviation
SE	Standard Error
SP	Secondary Production
TOC	Total Organic Carbon
TST	Total System Throughput
VME	Vulnerable Marine Ecosystem
VPDB	Vienna Pee Dee Belemnite

Executive Summary

The initial objective of Deliverable 4.2 was to compare deep-ocean ecosystem dynamics from a number of habitats within the Atlantic Ocean Basin which are characterised by different environmental conditions (e.g., trophic regime) to be able to try and assess the response of deep Atlantic ecosystems to anthropogenic climate change using a space-for-time approach. The Covid-19 pandemic, as well as alterations to ship schedules (caused by Covid-19 and sudden ship repairs), prevented us from visiting many of the study sites (e.g. Argentinian Basin, Santos Basin) that we initially planned to visit. Nevertheless, several studies in the Atlantic Basin were undertaken and the data gathered has allowed us to compare our results to similar studies conducted in other regions of the Atlantic enabling a number of conclusions to be made about how climate change will possibly impact the deep Atlantic Ocean.

Comparing two datasets (*in situ* and modelled data) derived from samples collected from soft-sediment abyssal experiments conducted around Cabo Verde during the iMirabilis2 expedition (4,200 m), and the Porcupine Abyssal Plain (in 2,000 at 4,800 m) showed that short-term bacterial and meiofaunal processing efficiency (i.e., per unit biomass) is greater on the more mesotrophic Cabo Verde Abyssal Plain (CVAB) compared to the more eutrophic PAP. This suggests that declining productivity caused by climate change could lead to a reduction in benthic biomass as noted in earlier studies, but an increase in bacterial and meiofaunal C-processing efficiency and greater C-recycling at the seafloor. The greater importance of microbes under more oligotrophic conditions was also suggested when isotope data from cold-water coral (CWC) reefs from Lampaul Canyon in the eutrophic NE Atlantic were compared to the same species of CWCs from more oligotrophic environments (e.g., Mediterranean Sea).

In addition to facilitating experiments to quantify abyssal soft-sediment ecosystem function, the iMirabilis2 expedition allowed us to study how shifts from fish-dominated, upper ocean ecosystems to squid-dominated environments may impact demersal and benthic scavengers in the Atlantic. Using a baited camera system, we found a clear difference in the community composition of scavengers and feeding activity at squid and fish baits. Our results suggest that changes to more squid-dominated ecosystems will likely benefit faster swimming fauna at the seafloor, and clearly highlighted how changes to upper ocean ecosystems may cause effects thousands of meters below the ocean surface.

Finally, we compared the carbon turnover and framework composition of CWC reefs from 4 sites in the Atlantic, which included areas beneath eutrophic waters that were characterised by high O₂ and pH conditions, as well as areas in more oligotrophic settings (Angola) naturally exposed to lower O₂ concentrations and pH levels. Our findings showed a dominance of dead coral material at the majority of sites, and the total carbon turnover m⁻² was highest in the Angola site compared to NE and NW Atlantic sites. Changing O₂, pH conditions and a reduction in food availability could therefore lead to a loss of live and dead coral framework, which may have significant impacts on Atlantic Vulnerable Marine Ecosystems (VMEs). These results are complemented by analysis of skeletal densities of several coral species and theoretical growth models that simulate how reductions in food availability leads to a relative increase in dead coral framework.

Peer-reviewed publications, submitted from Deliverable 4.2 so far:

- de Jonge, D., Smith, A., & Sweetman, A.K. Changes to upper-ocean ecosystems may directly impact abyssal scavenger communities. In review to *Limnology and Oceanography*.
- de Jonge D.S.W., Gaurisas, D.Y., Smith, A.J., Holmes, E., Orejas, C., Mosquera-Giménez, A.

Roberts, J.M., Bernardino, A.F., Sweetman, A.K. Dominance of small organisms in the Cabo Verde Abyssal Basin (tropical NE Atlantic) results in high phytodetritus processing efficiency by the sediment ecosystem. In review at *Progress in Oceanography*.

- Gaurisas, D.Y., de Jonge, D.S.W., Sweetman, A.K. Bernardino, A.F. Effects of increased temperature and altered POC composition on a bathyal macrofaunal community in Cape Verde (North-East Atlantic). In review at *Progress in Oceanography*.

1. Introduction

Global climate change is caused by high concentrations of anthropogenically emitted greenhouse gases such as carbon dioxide and methane, which trap solar heat in the atmosphere and cause many subsequent impacts on global biogeochemical cycling. As the ocean acts as a heat sink and as a buffer for the large human emissions of atmospheric CO₂, climate change will affect environmental conditions at the deep abyssal and bathyal seafloor, which will most likely experience an increase in temperature and a decrease in pH (Smith et al., 2008a; Sweetman et al., 2017). Additionally, warmer deep-sea water masses will likely hold less oxygen causing an increase in the number and vertical extent of oxygen minimum zones (Breitburg et al., 2018).

Some more complex knock-on effects include alterations to Particulate Organic Carbon (POC) flux quantity and quality. Increased temperatures cause greater stratification in the upper ocean, which inhibits nutrient upwelling and stimulates nanophytoplankton growth (Bopp et al., 2005). These smaller phytoplankton sink slower, especially if carbonate ballasted Particulate Organic Matter (POM) is reduced due to ocean acidification, which increases the residence time of POM in shallow water where it undergoes significantly more degradation thus reducing overall POC export (quality and quantity) to deeper ocean layers. This reduced overall POC export is predicted mostly for the abyssal and bathyal regions of the Pacific, Atlantic, and Indian oceans with reductions up to 55% by the year 2100 (Sweetman et al., 2017). In contrast, in upwelling regions the increase in overall wind speeds due to climate change will boost nutrient upwelling, causing local increases in primary productivity and growth of larger, faster-sinking, phytoplankton, hence an increase in POC flux to the underlying benthos (Jones et al., 2014; Wang et al., 2015). At the poles, contrasting mechanics will influence the change in POC flux. The melting of sea ice on the one hand will allow extended phytoplankton blooms hence increase the POC export flux (Arrigo et al., 2008), but the freshening of the water, due to both ice melting and an increase of fresh terrestrial run-off, stimulates slow-sinking nanophytoplankton growth which will reduce the POC export flux (Li et al., 2009).

Ecosystem functioning can be defined as interactions between biotic and abiotic components of a system resulting in transfer of energy and/ or matter, which are sustaining the system's state or trajectory (Jax, 2005). This is in contrast to ecosystem characteristics, such as species diversity and biomass, which provide information about what an ecosystem is like at a specific moment in time and space. Examples of deep-sea benthic ecosystem functions include Sediment Community Oxygen Consumption (SCOC), nutrient recycling, carbon (C) sequestration, and interactions between organisms and their environment. These local functions of sedimentary ecosystems can be upscaled to global biogeochemical cycles, as SCOC provides a proxy for various organic matter degradation pathways in the sediment, nutrient recycling releases nutrients back into the water column boosting primary production when upwelled, and C sequestration removes C from global cycling on geological timescales (Snelgrove et al., 2018; Thurber et al., 2014).

Benthic ecosystem functioning at both bathyal and abyssal depths will likely be affected under changing seafloor environments. As POM influx is a major driver of food-limited abyssal ecosystems (Smith et al., 2008b), a reduction in the quality and quantity of food reaching the seafloor is predicted to change seafloor characteristics reducing benthic biomass, SCOC, and bioturbation rates and intensity (Jones et al., 2014; Smith et al., 2008b). However, it is difficult to study these effects directly in deep ocean settings. As a result, there is a large gap in the current understanding of these changes in most ocean basins. An obvious method to study the effects of changing environmental variables on ecosystems and

the organisms living in them, is to expose them to controlled experiments where climate change is simulated. However, performing such controlled experiments at abyssal depths requires specialised equipment, and retrieving abyssal sediments for shipboard *ex situ* incubations is not recommended, as it can introduce large temperature and pressure related artefacts in the measured rates and fluxes and don't represent realistic functioning (Amano et al., 2022; Glud et al., 1994). An alternative method is conducting space-for-time substitution experiments. In such an experiment, changes in ecosystem functioning over natural spatial gradients can be used to extrapolate how changes in environmental conditions over time may impact benthic processes.

Food-falls are large parcels of food and include animal carcasses or macroalgae, sinking to the seafloor where they are consumed by benthic and demersal scavengers (Drazen and Sutton, 2017; Havermans and Smetacek, 2018). The contribution of food-falls to benthic carbon influx has long been neglected, as they were often missed by sediment traps due to their relatively fast sinking rates and sporadic distribution (Burd et al., 2010) as well as their fast removal at the seafloor (Sweetman and Chapman, 2015). Food-falls are increasingly recognised as an important food source for deep benthic communities, with studies showing that food-falls can potentially explain part of the observed discrepancy between particulate organic carbon input and carbon demand at several deep-sea sites (e.g., Henschke et al., 2013; Sweetman and Chapman, 2015; Hoving et al., 2017). Also, variation in food-fall types has been suggested as a bottom-up driver of deep-sea scavenger evolution, as they differ in nutritional value, chemical composition, distribution, and frequency of deposition (Havermans and Smetacek, 2018). Scavenging activity can be considered an important ecosystem function, because benthic and demersal scavengers control benthic biomass, alter the behaviour and habitat choices of benthic fauna (Sweetman et al., 2014; Leitner et al., 2017), and consume and redistribute organic material thereby contributing to nutrient cycling and energy transfer (Priede et al., 1991; Trueman et al., 2014).

In addition to climate change altering the environmental conditions at the deep-seafloor, human activities are likely to alter the composition of food-fall types reaching the seafloor as well by causing changes to upper ocean pelagic ecosystems e.g. through fisheries (Edwards and Richardson, 2004; Purcell, 2011). A clear example of a shift in the pelagic community composition over the past decades is increasing squid stocks due to changing ocean conditions, whereas fish stocks have been falling due to overfishing (Doubleday et al., 2016). This shift from fish to squid-dominated pelagic communities is predicted to continue with future climate change due to squid's capability to cope with lower oxygen levels and accelerated life cycles at higher temperatures (Doubleday et al., 2016). However, it is unclear how seafloor scavenging activity might be impacted by changing food fall compositions.

Scavenging activity can be studied using baited vehicles, which attract scarcely distributed scavengers from distal locales and allow researchers to observe their feeding behaviour and interactions. Previous baited camera experiments using a variety of bait types – fish, jellyfish, squid, macroalgae - have shown the scavenging response can be bait-specific, but it depends on the measure of scavenging activity (e.g. scavenging rates, maximum abundance, time of maximum abundance, community composition) and study location (Fleury and Drazen, 2013; Sweetman et al., 2014; Rohlfer et al., 2022; Scheer et al., 2022). For example, Sweetman et al. (2014) found that benthic scavengers rapidly consumed jellyfish carrion at 1,250 m depth and attracted the same suite of scavengers as oily fish baits, but changes in the type of jellyfish bait used led to different aggregation of scavengers. However, Scheer et al. (2022) documented different scavenger assemblages gathering at, and consuming fish and squid carcasses at 1,400 m depth relative to when jellyfish baits were used.

Under the iAtlantic Task 4.2 (*Compare natural spatial gradients in deep pelagic and benthic ecosystem functioning*), soft-sediment experimental and modelling studies were undertaken to assess how benthic processes differ between two abyssal regions of the Atlantic with naturally varying POC influx regimes (**Case study 1**). Abyssal *in situ* incubations were undertaken during the iMirabilis2 expedition to the Cabo Verde abyssal basin (CVAB) using benthic chambers and the response of the benthos here to labelled phytodetritus was assessed. The CVAB is considered a generally oligotrophic region with seafloor POC fluxes of $<0.5 \text{ g POC m}^{-2} \text{ y}^{-1}$ at depths below 4,000 m (Khripounoff et al., 1998). We therefore visited this ocean basin and conducted *in situ* stable isotope tracer experiments using an autonomous benthic respirometer lander, measuring SCOC, CO_2 production, nutrient fluxes, and C processing by bacteria, foraminifera, meiobenthos, and macrobenthos. This data was compared to similar data collected by Witte et al. (2003) on the Porcupine Abyssal Plain. The Porcupine Abyssal Plain (PAP) receives seasonal high influx of POM, with visible phytodetrital mats (Witbaard et al., 2000), with a seafloor POC flux of approximately $1 \text{ g POC m}^{-2} \text{ y}^{-1}$. Witte et al. (2003) visited PAP in 2000 and is currently the only study conducted *in situ* in the Atlantic Ocean to report SCOC alongside C cycling through multiple abyssal food-web compartments (bacteria, foraminifera, meiobenthos, macrobenthos) using a stable isotope tracer experiment. As our study and the study by Witte et al. (2003) used consistent methodologies and are currently the only studies of their kind in the Atlantic Ocean, they are suitable to compare ecosystem functioning under varying POC influx regimes. Observed differences may help extrapolate expected changes in seafloor functioning under future climate scenarios.

Although *in situ* investigations provide useful insights into how benthic ecosystems operate in different ecosystem settings, it is nearly impossible to measure all hypothesised C food-web flows in the field due to the logistic limitations of *in situ* measurements (e.g., small sized benthic chambers, low biomass of different organisms). Linear Inverse Models provide a useful toolkit for data-sparse systems, as they allow unknown flows, which can be algorithmically resolved resulting in a fully quantified system (van Oevelen et al., 2010). Such quantified systems can then be analysed for specific C pathways and environmental network indices. Network indices provide a robust method to summarise certain network characteristics into a single value, which can be compared between different systems to make inferences about network structure, organisation, and functioning (Kones et al., 2009; Heymans et al., 2014). Therefore, in addition to studying benthic ecosystem functioning *in situ*, we ran LIM models to model C-flows through the benthic ecosystem at the eutrophic PAP and oligotrophic CVAB to study food-web interactions and C cycling at the two sites. A C-based steady-state linear inverse model (LIM) was created for both sites, delineating food-web compartments, and C flows between them and quantified with published data (Soetaert and Van Oevelen, 2010). Because reduced POC flux has been linked to a reduction in ecosystem functions like SCOC, nutrient remineralisation rates, and secondary production rates as previously discussed (Smith et al., 2008), we expected to see reduced Total System Throughflow (*TST*) (i.e., the sum of C in the system, reduced overall respiration, and reduced overall secondary production) at the CVAB compared to the PAP. Additionally, reduced POC flux is correlated to a relative dominance of smaller organisms, potentially causing a reduced system's efficiency of biomass production and energy transfer to higher trophic levels (Smith et al., 2008). Therefore, at CVAB we expected to see reduced PB-ratios, an increased relative importance of microbes and meiofauna in C-cycling and reduced trophic levels. Trophic interactions were summarised in the indices Synergism (*S*, comparing the proportion positive to negative interactions) and the Omnivory Index (*OI*, quantifying diet variety). To assess the maturity and stress level of both systems, we additionally looked at the

network indices Average Mutual Information (*AMI*, level of ecosystem development and specialisation), Relative Ascendancy (*RA*, measure of how 'tight' the system is organised), and Finn's Cycling Index (*FCI*, summarising the efficiency of energy distribution).

As well as studying how the deep-sea benthos responds to phytodetrital inputs in different areas of the Atlantic, the iMirabilis2 expedition also allowed us to examine ecosystem functioning (e.g., sediment community oxygen consumption, bacterial C-cycling activity) and ecosystem characteristics (e.g., bacterial biomass, macrofauna community composition) of the upper bathyal slope in the Cabo Verde archipelago (**Case study 2**). Comparing our results with other bathyal slope systems exposed to different environmental conditions in the Atlantic provided insights into how bathyal ecosystem functioning varies over environmental gradients allowing us to infer how they may respond to future climate change. Furthermore, the cruise allowed us to test the response of the scavenging community in the Cabo Verde Abyssal Basin to fish (Atlantic Mackerel, *Scomber scombrus*) and squid (Patagonian squid, *Doryteuthis gahi*) bait (**Case study 3**). We selected this site for this experiment for two reasons. The high productivity and upwelling off the coast of West-Africa supports high abundances of deep demersal fish scavengers east of the Cabo Verde islands (Henriques et al., 2002), and other carnivorous megafauna, like amphipods, also have high abundances (Thurston, 1990; Sibuet et al., 1993). Additionally, Cabo Verde is a hotspot for cephalopod diversity (Merten et al., 2021). We hypothesised that the smaller size of individual squid compared to the large body size of mackerel would lead to faster squid bait removal times and a different scavenger assemblage developing at squid versus fish baits. To test this hypothesis, we deployed a baited camera lander eight times to depths of 4,200 m using mackerel or squid bait. A baited trap lander was also used to capture scavengers for formal identification and to sample organisms for natural stable isotope signatures to assess natural trophic ecology of scavengers in the area.

In addition to studying how soft-sediment bathyal and abyssal ecosystems function in different regions of the Atlantic, as well as their response to the effects of climate change, iAtlantic Work Package (WP) 4 also undertook studies to document the ecological functioning of cold-water corals (CWCs) in different habitats (**Case studies 4 and 5**). Cold-water corals (CWCs) are reef-building foundation species, and harbour abundant and diverse communities (Henry and Roberts 2017), and the dead coral framework is crucial for this biodiversity support (Mortensen et al., 1995; Roberts et al., 2008). There have been a small number of pioneering studies to date to investigate live and dead coral framework, including by Vad et al. (2017) in the North-East Atlantic, and Orejas et al. (2021) in the South-East Atlantic. The overall ratios of live to dead coral biomass never exceeded ca. 30% (Vad et al., 2017). A recent method by De Clippele et al. (2021) adapted these methods and used Photoshop to annotate the entire portion of live and dead coral colonies in an image, allowing for the calculation of total surface area and percentage of live and dead portions in an image. This was then used to estimate biomass. Despite recent advances, how the live to dead coral framework varies geographically and how this contributes to carbon turnover is poorly known. As such, in Deliverable 4.2, in Case Study 5 we used the methods by De Clippele et al. (2021) to evaluate the live: dead coral framework from the NE Atlantic using the image data from Vad et al. (2017) for comparative purposes using methodology of De Clippele et al. (2021), and then quantified the variability of live and dead coral ratios across multiple sites of the Atlantic to assess carbon turnover. To assess the drivers and constraints on live: dead coral framework, we also assessed the skeletal density of several key CWC species throughout the Atlantic to determine the variability in density between species, which will impact structural stability, and modelled coral growth and how the proportion of live and dead framework depends upon environmental variables

using novel methodology.

In the absence of endogenous production, CWCs mostly depend on photosynthetic organic matter produced in the euphotic zone and exported through benthic-pelagic coupling for their nutrition. Food is therefore limited for CWCs, and usually available through infrequent but massive resource pulses ('feast & famine' environment) (Maier et al., 2019b). As a result, energy acquisition is a major challenge for CWCs. Several ecological traits allow CWCs to cope with low and/ or irregular food availability. They are notably able to feed on multiple items, including bacteria, phytoplankton, detritus, dissolved free amino acids, and zooplankton in variable proportions (Carrier et al., 2009; Gori et al., 2014; Maier et al., 2019a, 2019b; Mueller et al., 2014; Orejas et al., 2016; van Oevelen et al., 2016, 2018a, 2018b). Moreover, besides classical feeding, some species are able to rely on multiple energetic pathways and derive part of their nutrients from bacterial symbionts associated to their mucus, therefore functioning as a holobiont with their microbiome (Middelburg et al., 2015).

Reliance upon these multiple, non-mutually exclusive ecological mechanisms has been shown to vary spatially and temporally in CWCs, presumably in order to match environmental availability of food items (Maier et al., 2019a). CWCs are therefore considered capable of a considerable amount of ecological plasticity, that could be a key factor to facilitate their future survival under changing environmental conditions (Larsson et al., 2013; Mueller et al., 2014). Climate-change associated stressors, chiefly ocean acidification, could perturb coral energy budgets by increasing the energy cost associated with carbonate skeleton building and maintenance. This is likely to cause energy acquisition to become an even bigger challenge for CWCs over the next decades than it already is under current conditions.

At least two species of CWCs (*Desmophyllum pertusum* (*Lophelia pertusa*) and *Madrepora oculata*) co-occur and form reefs at a depth range of 650 m to 1,200 m in the Lampaul Canyon (Bay of Biscay), with most of the larger formations occurring around 800 to 900 m (van den Beld et al., 2017). The co-occurrence of these two species raises important questions regarding niche segregation and potential competition for resources under changing environmental conditions. In this deliverable, we therefore investigated the trophic ecology and feeding habits of these two species in the Lampaul Canyon to tackle the following questions: (1) What is the realised trophic niche of CWCs in the Lampaul Canyon?; (2) Do the two co-occurring species share some major dietary resources?; and (3) Are the trophic niches of CWCs overlapping with those of associated fauna, particularly suspension feeders that live associated to CWC reefs? To achieve these goals, stable isotope ratios of carbon, nitrogen and sulphur were measured. These time-tested integrative trophic markers have proven very efficient ways to tackle animal feeding ecology. They yield complementary results pertaining to multiple aspects of consumer ecological niches and allow the identification of food items consumed by animals in natural ecosystems, as well as delineation of ecological strategies or computations of trophic position estimates (Boecklen et al., 2011; Layman et al., 2012; Middelburg, 2014).

2. Case study 1 – *In situ* and modelled benthic ecosystem functioning on the Cabo Verde Abyssal Basin and comparisons to other Atlantic sites.

2.1 Materials & Methods

In situ methods

Algal culturing

Axenic *Phaeodactylum tricornutum* (Bigelow National Centre for Marine Algae & Microbiota) was cultured in F/2 algal medium in artificial seawater with 25% NaH¹³CO₃ and 25% Na¹⁵NO₃. After approximately 1.5 months the culture was filtered over a 0.45-µm cellulose acetate filter using a Büchner funnel and flask. Harvested cells were rinsed from the filter with sterile artificial seawater into a 50-ml centrifuge tube and concentrated by centrifuging at 400 g for 15 min. The supernatant was carefully decanted, and any remaining labelled nutrients (NaH¹³CO₃ and Na¹⁵NO₃) were washed from the cells three times by resuspending the pellet in sterile artificial seawater, centrifuging at 400 g for 15 min, and decanting the supernatant. The washed pellet was directly transferred to a -80°C freezer. Frozen algal pellets were freeze-dried for at least 48 hours and homogenised with a pestle and mortar. Freeze-dried algae were stored at -80°C until usage. Carbon and nitrogen content, C:N ratio, and ¹³C/¹⁵N labelling of the algae cultures were determined using an Elemental Analyser-Isotope Ratio Mass Spectrometer (EA-IRMS) at the Stable Isotope Facility of UC Davis (California, USA). To do this, freeze-dried algae subsamples were mixed with freeze-dried unlabelled and acidified terrestrial soil to reduce the enriched stable isotope signal to below the threshold value required by the EA-IRMS. Enrichment of the pure algae cultures were back calculated from soil controls. PLFA analysis of the freeze-dried algae cultures was conducted at the James Hutton Institute in Aberdeen to determine potential bacterial contamination (for analytical details see Cecchetto et al., (2023)). The *P. tricornutum* algae culture had 26.9±6.7 wt% C, 3.0±0.6 wt% N, C: N of 9.1±2.2, with 11.8 at% ¹³C enrichment. No contamination for the bacterial PLFA biomarker C15:0i was detected.

Study site

The CVAB was visited in August of 2021 during the iMirabilis2 research expedition on the RV *Sarmiento de Gamboa*. The specific region where we deployed the seafloor lander was situated about 50 km south-west of the island Brava and will from here on forward be referred to as the benthic chamber lander (BCL) region. A CTD deployment (Sea-Bird SBE 9) in the lander region (14.6754°N, 25.1533°W) measured a bottom water temperature of 2.3°C, salinity of 34.88 PSU, and oxygen concentration of 223 mmol L⁻¹. There are various currents influencing the Cabo Verde basin, with the Cabo Verde Frontal Zone (CVFZ) being a specifically important divide separating the tropical southern water from subtropical northern water masses (Peña-Izquierdo et al., 2012). The oceanic region off Western Africa regularly receives deposition of Saharan dust carried by trade winds (Dadou et al., 2001). Using the polygon outline of the iAtlantic Cabo Verde region¹ and the global seafloor POC dataset from Sweetman et al. (2017), the average seafloor POC flux at 4,000 m in the Cabo Verde Basin was estimated to be 2.36 mg C m⁻² d⁻¹ or 0.9 g C m⁻² y⁻¹.

¹ iAtlantic Geonode: <https://www.geonode.iatlantic.eu/maps/495>

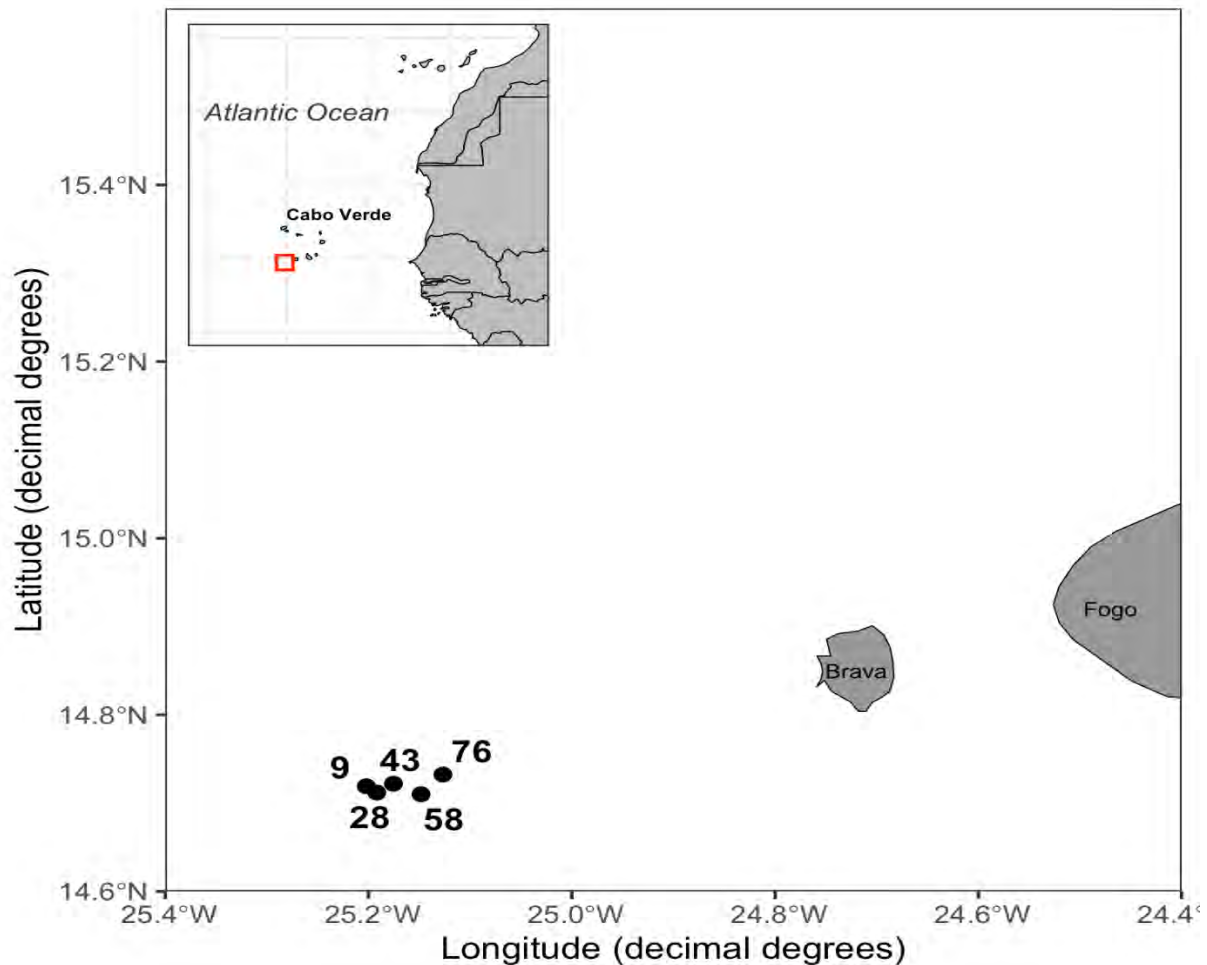


Figure 1. Cape Verde Archipelago and Benthic Chamber Lander deployment stations at ~4,200 m near the island of Brava of Cabo Verde. The red square indicates the lander region.

Benthic chamber lander (BCL) deployments

The BCL was deployed five times at ~4,200 m depth ([Figure 1](#), [Table 1](#)). Overall, four successful stable isotope tracer experiments with the enriched *P. tricornutum* were conducted, and eleven incubations were available to measure background respiration, and natural stable isotope values. A detailed description of the BCL (KUM, Kiel, Germany, [Figure 2](#)) can be found in the iMirabilis2 cruise report by Orejas et al. (2022). In short, four incubation chambers (22x22 cm), separated about 0.5 m from each other were mounted on a lander frame with Nautilus Vitrovex glass flotation. Each chamber had a lid-mounted stirrer, a syringe sampler for 7 water samples, a substrate injector, a chamber closing mechanism, and an Aanderaa 4330F optode. These components were operated by two pre-programmed lander-mounted computers powered by a Deep-Sea Power & Light® battery.

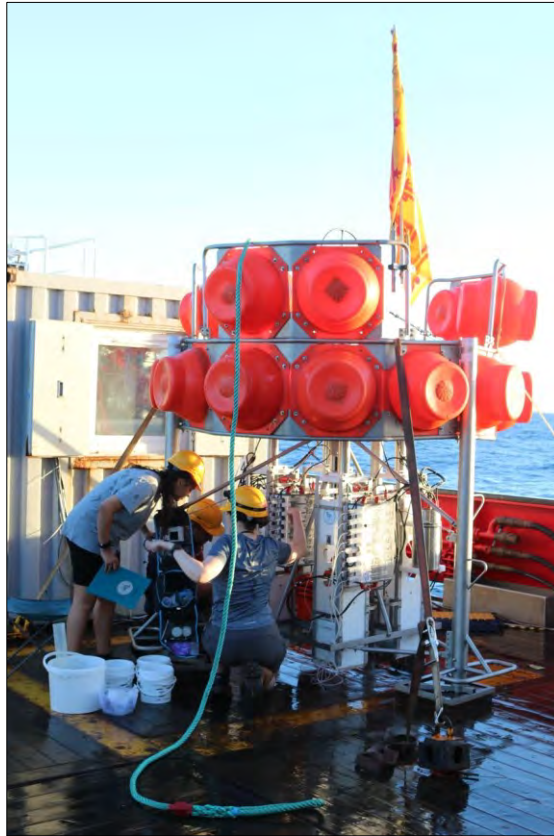


Figure 2. Benthic Chamber Lander onboard the RV *Sarmiento de Gamboa* being processed after a deployment. Photo by Murray Roberts, iMirabilis2.

Table 1. Benthic Respirometer Lander deployment stations: latitude (Lat) and longitude (Lon) in decimal degrees (DD), depth in meters, and date.

Station (iMirabilis2)	Station (AKS)	Lat, Lon (DD)	Depth (m)	Date
9	AKS295	14.7190, -25.2021	4,168	6 Aug 2021
28	AKS300	14.7119, -25.1919	4,178	11 Aug 2021
43	AKS302	14.7219, -25.1755	4,197	15 Aug 2021
58	AKS306	14.7100, -25.1483	4,215	19 Aug 2021
76	AKS309	14.7323, -25.1268	4,208	22 Aug 2021

On the vessel, the freeze-dried *P. tricornutum* was soaked in cold, filtered (0.2 mm) seawater, and then transferred to the injectors of the BCL. Each injector received 30.4 mg of freeze-dried algae with a C content of 8.37 mg C, corresponding to an addition of 0.17 g C m⁻² that was equivalent to about 20% of the estimated annual seafloor C influx. The BCL was then deployed and sank to the seafloor autonomously (approx. 80 m min⁻¹), reaching the seafloor in approx. one hour. The BCL was programmed to have the chambers fully pushed down into the sediment at a certain moment in time, which is referred to as T_{0-hr} of the incubation. This exact time was dependent on the time of setting the lander overboard, considering the sinking rate and a conservative couple of hours to avoid the experiment starting too early if there were delays during deployment. After the chambers were pushed into the sediment, stirrers gently started to mix the overlying chamber water and a control water sample was collected by the syringe sampler 5 minutes later ($T_{0.33-hr}$). Injection of the labelled algae occurred 20 minutes after the control water sample was collected, and the stirrers were stopped for

an hour after the injection to allow the algal material to sink to the sediment surface within the benthic chamber. Then, the stirrers were restarted to gently mix the overlying water to maintain a sufficiently thin diffusive boundary layer during the incubation. Six more water samples were taken at T_2 , T_{10} , T_{19} , T_{28} , T_{37} , and T_{46-hr} . After the last water sample was collected, the stirrers were stopped, the chamber door was closed so that the incubated sediment was sampled inside the benthic chamber, and the chamber was pulled back up from the sediment into the lander frame. The full programme was finished at T_{48-hr} . A signal to the acoustic releases dropped the lander weights, allowing the lander to ascent back to the surface (approx. 60 m min^{-1}). The lander was recovered back onto the vessel's deck to download the optode data and process the water and sediments samples.

Onboard sample processing

Syringe water samples

As soon as the lander was secured on deck, the syringe water samples were collected from the lander, stored at 4°C , and processed as soon as possible. Per syringe, water was collected to analyse dissolved inorganic carbon (DIC), oxygen, and nutrient concentrations. Water samples for later DIC analysis were collected in a 12 ml glass exetainer through a 0.45 mm cellulose acetate syringe filter and Vygon tubing and preserved with 10 ml 6% mercury chloride solution. DIC samples were stored and shipped upside down at 4°C until further processing. Oxygen water samples were collected without a filter into a 12 ml glass exetainer containing a glass bead. To precipitate all oxygen in the water sample, 150 ml of Winkler I and 150 ml of Winkler II solution was added to the exetainer, the cap screwed back on, and shaken to mix the solutions. The Winkler solutions were made up at the start of the expedition: Winkler I was made by dissolving 600 g of manganese (II) chloride tetrahydrate ($\text{MnCl}_2 \times 4\text{H}_2\text{O}$) in 1L of Milli-Q water while gently stirring on a hotplate, and Winkler II was made by dissolving 320 g of sodium hydroxide (NaOH) and 600 g of sodium iodide (NaI) in 1L of milliQ water while gently stirring. The exetainers were stored dark, and shaken again after 30 minutes, before undertaking a Micro-Winkler titration procedure after all samples had been collected and preserved/ frozen. Mean O_2 -values were determined from titrating two samples. Water samples for nutrients analysis (see below) were collected into plastic scintillation vials (previously cleaned with 10% hydrochloric acid [HCl]) through a 0.45 mm cellulose-acetate syringe filter and stored and shipped at -80°C .

Sediment samples

The overlying water in each chamber was siphoned off through a $32\text{-}\mu\text{m}$ sieve, while minimising disturbance of the sediment surface. The sieve contents were transferred to the storage container for meiobenthos, and the water volume was determined with a volumetric cylinder. The distance from the sediment surface to the bottom of the chamber lid was measured at the four sides of the chamber to be able to also calculate the volume of overlying water. Comparison of the directly measured volume to calculated volume showed an overestimation of $19.3 \pm 1.3\%$ ($n=7$) of the calculated volume, so when only calculated volumes were available, they were adjusted accordingly.

One push-core for Total Organic Carbon (TOC), and three push-cores for meiobenthos were inserted into the sediment at the edge of the chamber. The push-cores were sawed off 50 ml plastic Luer syringes with an inner diameter of 2.8 cm, which were cleaned between deployments. A clean ruler was pushed at the side of the chamber, to aid removing the 0-2 cm, 2-5 cm, and the 5-10 cm sediment layers around the push-cores into clean buckets. The sediment push-cores and buckets were stored cold (4°C) until further processing. The TOC push-cores were sliced into sediment horizons (0-0.5 cm, 0.5-1 cm, 1-1.5 cm, 1.5-2 cm, 2-3 cm, 3-5 cm, 5-7 cm and 7-10 cm) and stored and shipped in sterile

sample bags at -20°C. The three meiobenthos push-cores were sliced into sediment horizons (0-2 cm and 2-5 cm), the three slices per sediment horizon of the cores combined and stored and shipped in a 250 ml HDPE bottle in 4% buffered formaldehyde seawater solution. The sediment in the buckets were gently homogenised with a clean spackle knife, and 40 ml of sediment collected in a 50 ml Falcon tube stored and shipped at -80 °C for later PLFA analysis. The remaining sediment in the buckets was sliced into sediment horizons (0-2 cm, and 2-5 cm), but four buckets were additionally sampled at 5 to 10 cm. Each horizon was sieved over a 300 µm mesh with cold, filtered (0.2 µm) seawater, and stored and shipped in 500 ml HDPE bottles in 4% buffered formaldehyde seawater solution for later macro-benthic analysis.

Sediment Community Oxygen Consumption

The collected optode data was refitted using information on the hydrostatic pressure during the deployment, and from lab-based optode calibrations. Optode calibrations were performed within three months after their usage and soaked in fresh water for at least 24 hours before the calibrations to ensure a wet optode sensor foil. Optode readings were collected at three different temperatures (1°C, 18 °C, and 30 °C) for 100% oxygen saturation by bubbling air through fresh water, and for 0 % oxygen saturation by bubbling nitrogen gas through fresh water. Air pressure readings from a desk weather station and the water temperature from an independent thermometer were noted for each calibration set. The calibration data was then used to get new foil calibration coefficients using the model from Bittig et al. (2018). The raw optode data (phase degrees) was adjusted for the effect of hydrostatic pressure on foil luminescence lifetime by implementing eq. 28 from Bittig et al. (2018), converted to oxygen partial pressure using the updated calibration coefficients, corrected for the effect of hydrostatic pressure on quenching and on the membrane O₂ equilibrium level by implementing eq. 32 from Bittig et al. (2018), and finally converted to oxygen concentrations using the salinity as measured with the CTD (see 'Study site') and pressure based on deployment depth.

A linear regression through the mean oxygen concentration points from the Micro Winkler titrations and through the adjusted optode readings (from T₂ to T₄₆) was used to calculate SCOC flux in mmol O₂ m⁻² d⁻¹ using the (adjusted) overlying chamber water volumes and chamber sediment surface. The SCOC flux in the tracer experiments was corrected for background SCOC and converted to mg C m⁻² d⁻¹ using a respiratory quotient of 1 (Glud, 2008) to obtain the overall C degradation flux. The C degradation flux was corrected for the amount of algae added to the incubation chamber to obtain overall phytodetrital turnover rates (d⁻¹).

Dissolved Inorganic Carbon

Water samples for DIC analysis were sent to the Royal Netherlands Institute for Sea Research in Yerseke (the Netherlands). Total DIC concentration was measured on the Apollo Sci Tech AS-C5 DIC Analyser and DIC-d¹³C on an elemental analyser coupled to an isotope ratio mass spectrometer (EA-IRMS, Flash 1112, DELTA-V, THERMO, see Maier et al. (2020)).

DIC production over time resulting from respiration of the enriched algal substrate was determined from excess ¹³C (*E*). This excess was calculated from reported DIC-d¹³C values: $E = F_{sample} - F_{background}$, where $F = \frac{R}{R+1}$ and $R = (1 + \delta^{13}C/1000) * R_{VPDB}$ ($R_{VPDB} = 0.0112372$). Background DIC-d¹³C values were the values measured in the control water sample at T_{0.33-hr}. Excess ¹³C was then converted to DIC production at each incubation time point (mg C m⁻²) using the labelling of the injected algae (11.8 at %), seawater density of 1035 g/L, and the chamber surface area of 484 cm². For each

chamber experiment, a linear regression through the DIC production points over time was used to calculate an average DIC production rate over the incubation.

Nutrient fluxes

Water samples for nutrient analysis were sent to the Royal Netherlands Institute for Sea Research in Yerseke (the Netherlands). Nutrient concentrations (NH_4 , NO_2 , NO_3 , PO_4 , Si in $\mu\text{mol L}^{-1}$) were measured on a SEAL QuAAtro segmented continuous flow analyser. Linear regression, the (adjusted) overlying water volumes, and chamber sediment surface were used to calculate fluxes ($\text{mmol m}^{-2} \text{d}^{-1}$) from the reported concentrations (mmol l^{-1}).

As only one background water sample could be collected, a 1-sample Wilcoxon signed rank test was performed to test if the mean tracer experiment flux was significantly different from the background incubation i.e. assuming the single value represents a valid representation of background fluxes.

Phospholipid derived Fatty Acids

Sediment samples for Phospho-Lipid derived Fatty Acids (PLFA) were freeze-dried, homogenised with pestle and mortar, and sent to James Hutton Institute in Aberdeen for PLFA analysis (for analytical methods see Cecchetto et al. (2023) and references therein). The biomarker C15:0i is an indicator for bacterial biomass and was used to calculate overall bacterial biomass and C uptake as described below. PLFA biomarkers degrade quickly when an organism dies, and thus indicates biomass of alive bacteria only. Labelling of PLFA only occurs in metabolically active cells, and thus the labelling of biomarker C15:0i indicates active C uptake by bacteria in the sediment. The C15:0i biomarker was not present in the injected algae culture, indicating the algae remained axenic, i.e. no bacterial contamination had taken place during the culturing process. Bacterial biomass in each sediment horizon (0-2, 2-5, 5-10 cm) was calculated as $B = C_{C15:0i} / (F \times C_{PLFA})$, where B is the bacterial biomass in nmol C g^{-1} dry sediment, $C_{C15:0i}$ is the concentration of the C15:0i marker in the sample in nmol g^{-1} dry sediment, F is the average specific fraction of the C15:0i marker in the background samples of this study (2.4%), and C_{PLFA} is the average concentration of PLFA in bacterial biomass ($0.056 \text{ g C PLFA g}^{-1} \text{ C bacterial biomass}$, (Brinch-Iversen and King, 1990)). Biomass was then converted to mg C m^{-2} using a Dry Bulk Density (DBD) of 2.65 g cm^{-3} (Buchanan, 1984), a sediment porosity of 0.72 (average for 0-5 cm at the Cabo Verde Abyssal Basin, as per Relexans et al. (1996)), and the depth of the sediment horizon in cm. For bacterial C uptake, the $\delta^{13}\text{C}$ values for PLFA biomarker C15:0i in the different sediment horizons (0-2, 2-5, 5-10 cm) were used to calculate the excess ^{13}C (E) in the experimental sediment samples, as $E = F_{\text{sample}} - F_{\text{background}}$, where $F = \frac{R}{R+1}$ and $R = (1 + \delta^{13}\text{C}/1000) * R_{VPDB}$, where $R_{VPDB} = 0.0112372$). The excess ^{13}C in total PLFA concentration of biomarker C15:0i reported in nmol ester g^{-1} (dry sediment) was converted to overall C uptake by the benthic bacterial community ($\text{mmol C m}^{-2} \text{d}^{-1}$), using the same F, C_{PLFA} , DBD and sediment porosity as for the bacterial biomass calculation, combined with the ^{13}C labelling of the injected algae culture (11.8 at-%), and the total incubation time of 2 days.

Meiobenthos

The meiobenthos sediment samples preserved in 4% formaldehyde were washed over a 32- μm sieve with tap water. The sieve contents were transferred to 50 ml centrifugation tubes with colloidal silica fluid, so that there was less than 10 ml of sediment and more than 40 ml of undiluted Ludox HS-40 (1.3 g/ml, as used in Rohal et al. (2018)). A small amount of kaolin was added, enough to cover the sample. The tubes were centrifuged three times at 1,800 g for 6 minutes, with the supernatant decanted through a 32- μm sieve between runs. The sieve contents were washed and transferred to a petri-dish

with tap water.

Meiobenthos were identified to 'Nematode' or 'Other meiobenthos' under a dissection microscope (meiobenthic Foraminifera were omitted as they cannot be extracted consistently through density separation and would require heavy manual labour) and transferred with an eyelash mounted on a glass pipette to pre-weighed tin capsules containing some milliQ. The capsules were dried at 45°C in a drying cabinet for at least 72 hours, and then weighed to obtain dry mass. To reach the biomass threshold for the subsequent stable isotope analysis, the 0-2 and 2-5 sediment horizons were pooled. The samples were analysed at the James Hutton Institute in Aberdeen using continuous flow EA-IRMS on low carbon mode.

The meiobenthic $\delta^{13}\text{C}$ values were used to calculate the excess ^{13}C (E) in the experimental samples, as $E = F_{\text{sample}} - F_{\text{background}}$, where $F = \frac{R}{R+1}$ and $R = (1 + \delta^{13}\text{C}/1000) * R_{\text{VPDB}}$ ($R_{\text{VPDB}} = 0.0112372$). Meiobenthic C uptake rates ($\text{mg C m}^{-2} \text{d}^{-1}$) were then calculated using the C biomass of each sample, labelling of the injected algae (11.8 at%), total surface area of the push-core (18.5 cm^2), and the incubation time of 2 days. Meiobenthic density and biomass are reported but should be considered semi-quantitative as only a small sediment volume was analysed.

Macrobenthos

For macro-benthic analysis, sediment samples from benthic chambers were washed with filtered tap water over a 300-mm mesh sieve to remove the formaldehyde and transferred to 70% alcohol until sorting. All microbenthic specimens were identified to family (Annelids) or order (crustaceans and other taxa). Abyssal macrofauna community from Cabo Verde were analysed by their taxonomic composition, abundance, and biomass, and compared with other studies in the Atlantic Ocean. An accumulation curve was made to compare the macrofaunal diversity between samples based on taxa richness using the *vegan* package (Oksanen et al., 2019) in R version 4.1.0 (R Development Core Team, 2021).

Once the identifications were completed, the organisms were prepared for isotopic analyses. Single organisms were placed in pre-weighed tin caps, dried at 45°C for a period of five days, and reweighed for biomass determinations (mg dry mass). Calcareous shelled organisms were placed into pre-weighed silver caps, decalcified with 0.5 M HCl, and dried as above. To obtain sufficient biomass for isotope measurements, some individual organisms from different sediment layers but from the same taxa and chamber were combined into feeding guilds according to Fauchald and Jumars (1979).

Large foraminifera were placed in pre-weighed glass petri dishes, dried, and re-weighed as mentioned above to obtain total biomass (including tests) for each chamber horizon. Subsequently, subsamples from each chamber were placed in pre-weighed double-boated silver caps, acidified, and dried following the protocol for calcareous organisms. As acidified dry mass includes the weight of CaCl crystals formed by the reaction between the hydrochloric acid and calcium carbonate, it does not represent organic dry mass. Instead, organic dry mass was estimated as 5% of the unacidified dry mass (conservative value from Kamenskaya et al. (2013)). All dried caps were closed and pressed ensuring all air was removed before they were sent to the UC Davis Stable Isotope Facility to carry out the isotopic analyses. The isotopic analysis has not been completed at UC Davis at the time of this deliverable's submission, so no data on the contribution of macrofauna to C-uptake is available at present. Macrofaunal dry mass was converted to C using the average conversion factor for macrofauna (0.33 unit C unit DM^{-1}) in Rowe (1983). Foraminifera organic dry mass was converted to C using a conversion factor of 0.010 unit C unit DM^{-1} . This conversion factor was established from Foraminifera collected at

700 m retained on a 250 µm sieve that were picked unstained, acidified, dried and weighed, and analysed with a PDZ Europa ANCA-GSL elemental analyser (Sercon Ltd., Cheshire, UK) at the Stable Isotope Facility of UC Davis (A. Sweetman, unpublished data). Total C content of each sample was corrected for the average C content of blanks and divided by the dry total biomass count.

Total Organic Carbon

Total Organic Carbon was analysed at IsoAnalytical (Crewe, UK) with an Elemental Analyser connected to Isotope Ratio Mass Spectrometry (EA-IRMS, Europa Scientific). TOC content per m² wet sediment was calculated assuming the same DBD and porosity as for the PLFA analysis (see 'Phospholipid derived Fatty Acids').

Comparison to *in situ* benthic ecosystem function data from the PAP

In situ benthic ecosystem function data was also extracted from the text and figures in Witte et al. (2003) using PlotDigitizer (*PlotDigitizer Online App*, n.d.): SCOC was extracted from their Figure 1; biomasses, C cycling, and DIC respiration rates were taken from their Figure 2. Nematoda C cycling values could not be extracted from their Figure 2, therefore the Nematoda excess ¹³C was extracted from their Figure 3 and used to calculate C cycling using their reported algae labelling of 98 at % ¹³C. Only values for the 0-5 cm sediment horizon were compared. Bacterial biomass at PAP was estimated by Witte et al. (2003) using bacterial cell counts for 0-10 cm (2.5 g C m⁻²), and raw data was not reported to allow calculation for the 0-5 cm horizon. Therefore, an alternative bacterial biomass at PAP was calculated using bacterial cell counts from Eardly et al. (2001), which were converted to bacterial C standing stock using a conversion factor of 1.25×10⁻¹⁴ g cell⁻¹ (Fukuda et al., 1998), resulting in an estimate of 92.6 mg C m⁻².

Modelling benthic ecosystem function on the CVAB versus PAP

To further elucidate benthic ecosystem function on the eutrophic PAP and more oligotrophic CVAB, two C-based linear inverse models (LIMs) of the seafloor food web were constructed and compared for C cycling and network indices. These models were constructed before the iMirabilis2 expedition as an alternative for cancelled fieldwork due to COVID19, and thus do not focus on the lander region in the CVAB but rather a site further north studied during the EUMELI project (Sibuet et al., 1993). As the sites are far apart within the CVAB (**Figure 3**), it was decided to keep using the older but site-specific published data rather than adding in new iMirabilis2 and mixing values from two study sites.

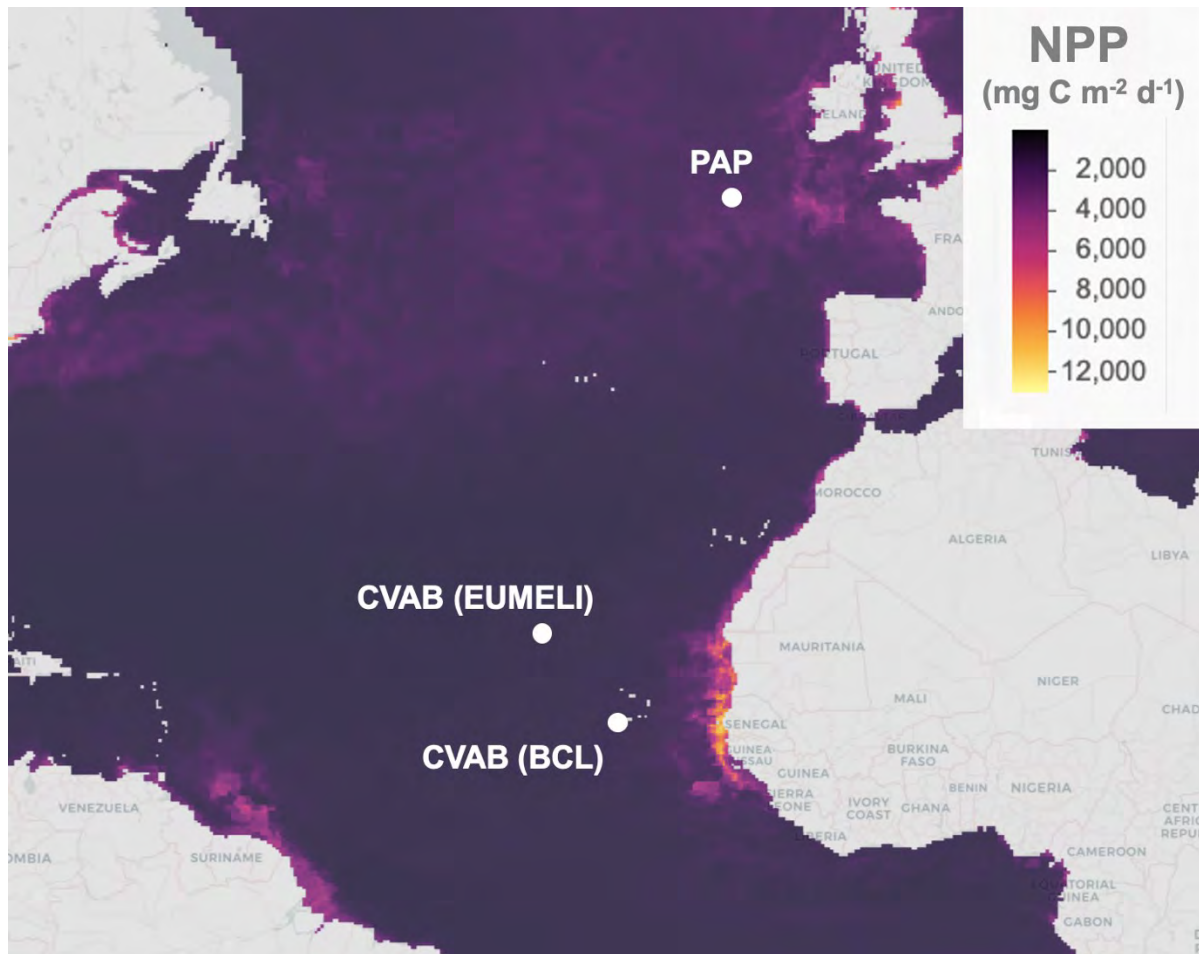


Figure 3. Locations of the three sites discussed in case study 1 mapped onto the Net Primary Productivity (NPP) estimated from satellite-based chlorophyll measurements (Oregon State University, 2019). The Porcupine Abyssal Plain (PAP) in the North Atlantic, and two sites in the Cabo Verde Abyssal Basin (CVAB): the site studied during the EUMELI project used in the food-web model, and the site studied using the Benthic Chamber Lander (BCL).

Food-web components for the linear inverse models

Food-web components for the two study areas for the LIMs were first defined. The labile detritus pool (lDet) was characterised by relatively fresh phytodetritus and defined as having a C:N ratio up to 4.0 (for comparison, 2.7 is pure protein and 6.0 is fresh oceanic plankton). The semi-labile detritus pool (sDet) was characterised by partially degraded particulate organic material and animal carcasses with a C:N ratio between 4.0 and 10.04. The refractory detritus pool (rDet) was defined as the remaining pool of particulate organic matter in the surface sediments with a C:N ratio greater than 10.0. Dissolution of organic materials into the sediment formed the dissolved organic matter (DOM) pool.

Unicellular organisms included in the models were benthic prokaryotes (Prok, i.e., bacteria and archaea) and Foraminifera (Foram). Fauna was grouped into food-web compartments based on size and feeding strategy. We distinguished between metazoan meiofaunal bacterivores (MeiB), epistrate feeders (MeiEF), selective deposit feeders (MeiSDF), deposit feeders (MeiDF), and omnivores and predators combined (MeiOP). Metazoan macrofaunal and megafaunal functional groups were filter and suspension feeders (MacFSF, MegFSF), surface deposit feeders (MacSDF, MegSDF), deposit feeders (MacDF, MegDF), omnivores (MacO, MegO), and predators and scavengers (MacPS, MegPS).

External compartments for import and export of material were the suspended particulate organic matter pools (LDET_BW, SDET_BW, RDET_BW), the DOM pool in bottom water (DOM_BW), deep burial (BURIAL), mineralised matter (MINERAL), and a general pool of organisms outside the system (EXPORT) connected through processes like food falls (into system) and migration or external predation (out of system).

In the models, organic matter was programmed to enter the system through the POM flux, food-falls, and chemoautotrophy. POM (external pools LDET_BW, SDET_BW, RDET_BW) was modelled to deposit into the benthic system in labile (lDet), semi-labile (sDet), and refractory fractions (rDet). Filter and suspension feeders (MacFSF, MegFSF) and Foraminifera (Foram) (Gooday et al., 1992) fed directly on the LDET_BW and SDET_BW. Larger pieces of partially degraded OM entered the sDet pools as food falls from the external EXPORT pool. Prokaryotes (Prok) performed chemoautotrophy, where they fixed DIC from the external MINERAL pool into cellular organic matter (Sweetman et al., 2019).

Prokaryotes were programmed to be able to dissolve the detritus pools of all lability fractions into sedimentary DOM through extracellular enzymatic activity, which other prokaryotes then ingested for prokaryotic production and respired to the external MINERAL pool. Prokaryotic mortality caused by viral lysis (Danovaro et al., 2008) resulted in a flux of DOM back into the sediment. There was efflux of DOM out of the sediment into bottom water (external DOM_BW pool). Sedimentary rDet was permanently buried in deep sediment layers (external BURIAL pool).

Foraminifera were modelled to feed on sedimentary labile and semi-labile detritus, prokaryotes, and they utilised sedimentary DOM (Gooday et al., 1992) in addition to uptake of suspended detritus described earlier. All fauna and foraminifera respired C to the external MINERAL pool. Ingestion of labile detritus by fauna and foraminifera resulted in defecation into the semi-labile detritus pool. Ingestion of all other material by fauna and foraminifera was defecated into the refractory detritus pool. Mortality of fauna and foraminifera resulted in a flux into the labile and semi-labile detritus pool.

Bacterivores (MeiB) were modelled to only feed on prokaryotes, epistrate feeders (MeiEF) fed on labile detritus, prokaryotes, and Foraminifera. Labile detritus, semi-labile detritus, prokaryotes, and foraminifera were grazed upon by selective deposit feeders (MeiSDF), surface deposit feeders (MacSDF, MegSDF), other deposit feeders (MeiDF, MacDF, MegDF), and omnivores (MeiOP, MacO, MegO). Additionally, deposit feeding macrofauna (MacSDF, MacDF, MacO) and megafauna (MegSDF, MegDF, MegO) ingested all metazoan meiofaunal groups. Omnivorous and predatory meiofauna (MeiOP) predated on all meiofaunal compartments, including itself. Omnivorous, predatory, and scavenging macrofauna (MacO, MacPS) predated on all meiofaunal and macrofaunal compartments, including itself. Omnivorous, predatory, and scavenging megafauna (MegO, MegPS) predated on all macrofaunal and megafaunal compartments, but no cannibalism occurred. The model included an export flow of unconsumed macro- and megafaunal secondary production through processes like external predation and mobility of fauna.

Data sources for the models

The food-web model of CVAB was a novel construction as described below. The food-web model of PAP originally published by van Oevelen et al. (2012) and updated in Durden et al. (2017) was set up as described below to use consistent methodology across the two sites. The C-stocks for the various food-web components can be found within [Table 2](#) and the food-web fluxes can be found in [Table 3](#).

Table 2. C stocks of food-web model compartments (mmol C m⁻²) at the Porcupine Abyssal Plain (PAP) and Cape Verde Abyssal Plain (CVAB).

Food-web compartment	PAP	CVAB
<i>Detritus</i>		
Labile detritus (lDet)	1.33	0.48
Semi-labile detritus (sDet)	658	963
Refractory detritus (rDet)	6158	5858
Sedimentary Dissolved Organic Matter (DOM)	18.6	2.96
<i>Unicellular organisms</i>		
Prokaryotes (Prok)	7.71	5.87
Foraminifera (Foram)	1.89	2.41
<i>Metazoan meiofauna</i>	5.60	1.17
Bacterivores (MeiB)	9.09×10 ⁻⁴	1.44×10 ⁻⁴
Epistrate feeders (MeiEF)	0.269	3.72×10 ⁻²
Selective deposit feeders (MeiSDF)	0.266	0.433
Deposit feeders (MeiDF)	4.41	0.509
Omnivores and Predators (MeiOP)	0.656	0.190
<i>Metazoan macrofauna</i>	10.7	0.272
Filter and suspension feeders (MacFSF)	5.71×10 ⁻³	3.15×10 ⁻²
Surface deposit feeders (MacSDF)	2.55	0.139
Deposit feeders (MacDF)	2.52	0.083
Omnivores (MacO)	0.102	1.66×10 ⁻²
Predators & Scavengers (MacPS)	5.54	1.10×10 ⁻³
<i>Metazoan megafauna</i>	0.20	0.024
Filter and suspension feeders (MegFSF)	1.15×10 ⁻²	4.04×10 ⁻⁴
Surface deposit feeders (MegSDF)	9.27×10 ⁻²	1.10×10 ⁻⁴
Deposit feeders (MegDF)	6.52×10 ⁻²	3.13×10 ⁻⁴
Omnivores (MegO)	1.45×10 ⁻²	2.28×10 ⁻²
Predators & Scavengers (MegPS)	2.57×10 ⁻²	3.60×10 ⁻⁴

Table 3. Food-web fluxes (mmol C m⁻² d⁻¹) used in the LIM models [min, max]. References: (1) Van Oevelen et al. (2012), (2) Durden et al. (2017); (3) Dadou et al. (2001); (4) Lahajnar et al. (2005); (5) Eardly et al. (2001); (6) Fukuda et al. (1998); (7) Relexans et al. (1996); (8) Auffret et al. (1992); (9) Danovaro et al. (2008); (10) Brunnegård et al. (2004), (11) Rabouille et al. (1993); (12) Lebrato et al. (2011); (13) Lebrato et al. (2013), (14) Lebrato et al. (2019); (15) Lucas et al. (2014); (16) Pierre (2001); (17) Pfannkuche and Lochte (2001); (18) Sweetman et al. (2019).

Food-web flux	PAP	Ref.	CVAB	Ref.
lDet deposition	[0.0010, 0.0227]	1	< sDet	-
sDet deposition	[0.03, 0.26]	1	< rDet	-
rDet deposition	[0.063, 0.647]	2	-	-
Particulate organic matter deposition	[9.4×10 ⁻² , 0.93]	1,2	[1.04×10 ⁻² , 0.151]	3
Food falls	[9.61×10 ⁻⁶ , 0.101]	12, 13, 14, 15, 17	[1.31×10 ⁻⁴ , 0.206]	12, 13, 14, 15, 16
Total mineralisation	[0.40,0.54]	1	[0.001, 0.69]	7

Food-web flux	PAP	Ref.	CVAB	Ref.
DOM efflux from sediment	$[5 \times 10^{-2}, 8 \times 10^{-2}]$	1	$[6.29 \times 10^{-3}, 3.63 \times 10^{-2}]$	3, 4
Prokaryotic production	$[8.87 \times 10^{-4}, 2.50 \times 10^{-2}]$	5, 6	$[1.40 \times 10^{-3}, 1.72 \times 10^{-3}]$	5, 6
Virally induced prokaryotic mortality	$[0.87, 0.91] \times$ prokaryotic production	9	$[0.87, 0.91] \times$ prokaryotic production	9
Prokaryotic DCF	$[3.07 \times 10^{-3}, 5.60 \times 10^{-3}] \times$ Prok stock	18	$[3.07 \times 10^{-3}, 5.60 \times 10^{-3}] \times$ Prok stock ^a	18
Burial	0.03	7, 8	0.003	1

^a Minimum constraint for Prokaryotic DCF is dropped to solve model incompatibilities.

Detritus

The IDet C stock at PAP and CVAB was determined using the average total Chl-a concentration for the upper 5 cm sediment from Witbaard et al. (2000) and Lochte and Soltwedel (1999) respectively. A C: Chl-a ratio was calculated with the model based on Jakobsen and Markager (2016):

$$C: Chl_a = win + amp \left(\frac{\cos \left(\frac{month - 0.5 - peak\ time}{12} \cdot 2\pi - \pi \right) + 1}{2} \right)$$

where *win* is the mean winter C: Chl-a ratio for open waters (19 ± 2.0 , $n=7$, Jakobsen and Markager, 2016), *month* is 1 (Jan) to 12 (Dec), *peak time* is the peak time relative to July 1st (assumed 0), and *amp* is the summer amplitude of C: Chl-a. This amplitude is significantly correlated to total mean nitrogen concentration (TN) in surface waters ($R^2 = 0.532$, Jakobsen and Markager (2016)), and could therefore be calculated as:

$$amp = Z + \frac{C}{[TN]}$$

where *Z* and *C* are fitted parameters ($Z = 15.07 \pm 5.6$, $C = 793.1 \pm 159$, (Jakobsen and Markager, 2016), and *[TN]* represents the open ocean value of $33.3 \pm 1.4 \mu\text{mol L}^{-1}$ ($n=9$, continental slope, North-West Atlantic, $40^\circ 20' \text{N}$, $64^\circ 35' \text{W}$) as measured by Guildford and Hecky (2000). The calculated annual mean C: Chl-a ratio of 38.4 is close to the C: Chl-a ratio of 40 (De Jonge, 1980), and was used to convert Chl-a to C equivalents.

At CVAB the sediment profile of carbohydrate, protein, and lipid sediment content and porosity for the upper 5 cm was reported by Relexans et al. (1996), and this was converted to biopolymeric C stock using the conversion factors 0.40, 0.49, 0.70 for carbohydrates, proteins, and lipids respectively (Fabiano et al., 1995), site specific porosity (Table 4), and a sediment dry bulk density of 2.65 g cm^{-3} (Buchanan, 1984). At PAP, the biopolymeric C stock from the upper 0-5 cm was taken from (Danovaro et al., 2001) and converted to mmol C m^{-2} using site specific DBD and porosity (Table 4). The semi-labile C stock for both sites was calculated by subtracting the labile C stock from the biopolymeric C stock.

The calculated labile and semi-labile detritus C stock for CVAB were subtracted from the sum of POC for the upper 5 cm reported by Relexans et al. (1996) to obtain the refractory C stock. The refractory C stock for PAP was used as in Durden et al. (2017). At PAP the POC flux was taken from Durden et al. (2017). At CVAB the near bottom POC flux (4,400 m, 200 mab) measured from sediment traps ranged

from 0.125 to 1.813 mg C m⁻² d⁻¹ (Dadou et al., 2001). The average POC flux (1.05 mg C m⁻² d⁻¹ from Dadou et al., 2001) corresponds well to the POC flux of 1.10 mg C m⁻² d⁻¹ reported by (Galéron et al., 2000).

Table 4. Characteristics of the studied sites Porcupine Abyssal Plain (PAP) and the Cape Verde Abyssal Basin (CVAB). References: (1) Rabouille et al. (2001); (2) Witbaard et al. (2000); (3) Relexans et al. (1996); (4) Galéron et al. (2000); (5) Hall et al. (2007); (6) Buchanan, 1984.

	CVAB	PAP
Location (Lat, Lon in DD)	21.05, -31.17	48.83, -16.58
Depth (m)	4,480 – 4,640	4,800
Trophic regime	Oligotrophic	Eutrophic
Dry Bulk Density (DBD, g cm ⁻³)	2.65 ⁶	0.74 ¹
Porosity (%)	0.75 ³	0.81 ²
Bottom water temperature (T_{BW})	2.4 ⁴	2.6 ⁵

At PAP the deposition of labile C was estimated from the minimum and maximum Chl-a values in sediment trap deployments from Witbaard et al. (2000) using the calculated C: Chl-a ratio of 38.4 (see above). The deposition of semi-labile C at PAP was taken from van Oevelen et al. (2012), while the deposition of refractory C at PAP was taken from Durden et al. (2017). There was no data to quantify the deposition of labile, semi-labile, and refractory C at CVAB. Therefore, POC deposition of the different lability fractions was constrained so that lDet < sDet < rDet C deposition.

Deposition of food falls was constrained by modelling the temperature-dependent decay of sinking gelatinous zooplankton biomass in the respective regions *sensu* Lebrato et al. (2011) and adjusting it for the number of expected annual blooms. The reduction of sinking biomass per day is:

$$\frac{dM}{dt} = -Mk_{(T)}$$

with M being gelatinous biomass at time t (days), and $k_{(T)}$ is the temperature (T) dependent decay rate (d⁻¹). The decay constant $k_{(T)}$ was experimentally found to be $k = 0.140e^{0.145T(z)}$, where $T_{(z)}$ is the temperature at depth z in meters (Lebrato et al., 2011). The biomass of gelatinous zooplankton, which were reported separately for the phyla Chordata, Cnidaria and Ctenophora, for the North Atlantic Drift Longhurst province (NADR) was used for the PAP model, and for the North Atlantic Tropical Gyre Longhurst province (NATR) was used for the CVAB model (Lucas et al., 2014). The water column temperature gradient at the CVAB oligotrophic site was taken from Pierre (2001), and for PAP from Pfannkuche and Lochte (2001). The biomass for each phylum was divided over depth bins equalling the temperature depth bins, based on the relative density distribution of each phylum (conservatively using the upper depth of the depth range, or the lower depth if upper depth was not available) in the respective Longhurst regions as reported in the JeDI database (Lucas et al., 2014). These depth bins were taken as the death depth (z_D) at which the zooplankton die, and decay begins. Sinking rates were 1,195 m d⁻¹ for Chordata, 2015 m d⁻¹ for Cnidaria, and 1,000 m d⁻¹ for Ctenophora Lebrato et al. (2013). The biomass reaching the seafloor was modelled for each phylum, each depth bin, and for the maximum and mean estimated biomass. Assuming there are 1 to 6 annual blooms (Lebrato et al., 2019), the minimum and maximum estimated food fall flux (mmol C m⁻² d⁻¹) was estimated.

Sediment DOC efflux constraints for CVAB were calculated using the correlation ($r^2 = 0.98$) between seafloor POC flux and DOC efflux rates (in mmol C m⁻² y⁻¹) found for remote deep-ocean regions by

Lahajnar et al. (2005):

$$DOC_{efflux} = 0.2136 \times POC_{influx} + 1.483$$

Ficks' First Law was then used to estimate the DOC concentration ($\mu\text{mol L}^{-1}$) in the sediment ($[DOC_{sed}]$) at 2 cm depth from the estimated minimum and maximum estimated DOC efflux rates:

$$DOC_{efflux} = -\varphi^m \times D_{sw} \times \frac{[DOC_{sed}] - [DOC_{bw}]}{dz_0}$$

Where DOC efflux rates are given in $\mu\text{mol cm}^{-2} \text{ s}^{-1}$, φ^m is the porosity of the CVAB surface sediment (0.745 between 0-2 cm, (Relexans et al., 1996)), D_{sw} is the molecular diffusion coefficient of DOC ($2.96 \times 10^{-7} \text{ cm}^2 \text{ s}^{-1}$, (Lahajnar et al., 2005)), $[DOC_{bw}]$ is the DOC concentration in CVAB bottom water at 4,568 m ($59.4 \mu\text{mol L}^{-1}$, Avril 2013), and dz_0 is the distance of the concentration gradient, in this case 2 cm (Lahajnar et al., 2005). By assuming the DOC concentration at 2 cm was a representative average for the upper 5 cm, sedimentary DOC concentration was converted to sedimentary DOC stock in mmol C m^{-2} . DOC efflux for PAP was taken as reported in van Oevelen et al. (2012).

The burial rate of refractory C at PAP was used as reported in van Oevelen et al. (2012). Burial of refractory C at CVAB (B_{rdet} , $\text{mmol C m}^{-2} \text{ d}^{-1}$) was calculated following Ståhl et al. (2004) as:

$$B_{rdet} = \omega \times DBD \times \text{wt}\%$$

where ω is the sediment accumulation rate (0.5 cm ky^{-1} ; Auffret et al., 1992), DBD is the dry bulk density (2.65 g cm^{-3} ; Buchanan 1984), and $\text{wt}\%$ is the average TOC content of the 10–27 cm sediment layer ($0.11 \pm 7.69 \times 10^{-3} \text{ wt}\%$, $n = 2$, Relexans et al. (1996)) well below the mixed sediment layer of 2.5 cm (Legeleux et al., 1994).

Total benthic C mineralisation at PAP was included as an inequality by using the minimum and maximum average SCOC value reported in Witbaard et al. (2000). For CVAB, benthic C mineralisation was estimated using the minimum and maximum DOU reported in Relexans et al. (1996) converted to C equivalents using a respiration quotient of 1 (Glud, 2008). However, these constraints might be overestimations (Relexans et al., 1996), and reported oxygen fluxes are larger than expected from sediment profiles (Rabouille et al., 1993), POM influx (Dadou et al., 2001), and compared to SCOC values at PAP. The minimum constraint is therefore set as the respiration rate estimated with a ^{14}C tracer experiment from Relexans et al. (1996). Total benthic C mineralisation excludes respiration by megafauna.

Prokaryotes and Foraminifera

Prokaryotic biomass for both PAP and CVAB was calculated using the average cell counts for the upper 5 cm sediment (PAP: $7.41 \times 10^8 \pm 1.48 \times 10^8 \text{ cell cm}^{-2}$, CVAB: $5.64 \times 10^8 \pm 7.04 \times 10^7 \text{ cell cm}^{-2}$, $n=8$) from Eardly et al. (2001) and a conversion factor of $1.25 \times 10^{-14} \text{ g C per cell}$ as measured in Fukuda et al. (1998), because the conversion factor used by Eardly et al. (2001) likely results in an overestimation of bacterial biomass.

The minimum and maximum prokaryotic biomass production rates for both PAP and CVAB were calculated from the reported Thymidine and Leucine incorporation rates and incorporation to cell production conversion factors by Eardly et al. (2001) combined with a prokaryotic carbon content per cell also used for the biomass calculations (Fukuda et al., 1998).

To our knowledge, there is only one study that quantified prokaryotic Dark Carbon Fixation (DCF) *in situ* at abyssal depths (Sweetman et al., 2019). They measured DCF rates ($n=2$) at two locations in the CCFZ

at 4,040-4,200 m, which were meso- to oligotrophic sites, using labelled bicarbonate in a pulse chase experiment with benthic chambers. The minimum and maximum DCF rate was divided by the mean bacterial biomass to obtain biomass specific DCF rates to constrain prokaryotic C fixation from DIC for both PAP and CVAB.

The minimum and maximum value for virus-induced prokaryotic lysis, i.e., the fraction of prokaryotic production reduced to DOC due to cell mortality was taken from Danovaro et al. (2008), by subtracting the standard deviation from the reported mean for sediments deeper than 1,000 m ($89 \pm 2\%$, $n=67$). The same constraints were used for PAP and CVAB.

Foraminiferal biomass at PAP and CVAB was based on the site-specific average unfragmented and stained foraminifera density for the upper 1 cm sediment reported by Gooday (1996). To obtain individual biomass data, Foraminifera collected at 700 m from the 0-2 cm sediment horizon retained on a 250 μm sieve were picked unstained, acidified, dried, and weighed, and analysed with a PDZ Europa ANCA-GSL elemental analyser (Sercon Ltd., Cheshire, UK) at the Stable Isotope Facility of UC Davis. Total C content of each sample was corrected for the average C content of blanks and divided by the specimen count to get individual biomass values. Foraminifera (>250 μm , 0–2 cm) C content was $0.31 \pm 0.10 \mu\text{g C ind}^{-1}$ ($n=20$). For comparison, this is a conservative value, as a previously used biomass conversion factor for this foraminifera size class was $5 \mu\text{g C ind}^{-1}$ (Ahrens et al., 1997). The density of the >250 μm size fraction at PAP and CVAB was converted to foraminifera C stock using the calculated individual C content. The densities of other size fractions were not converted to C stock due to a lack of data.

Metazoan fauna

Metazoan meiofauna (retained on 40 μm mesh sieve) density at CVAB were obtained by Galéron et al. (2000). They collected sediment with an USNEL boxcorer and SMBA multicorers from which a 5.31 cm^2 sub-core was taken of the upper 5 cm and preserved in 3% buffered formaldehyde. At PAP, metazoan meiofauna (retained on 32- μm mesh sieve) density data was collected by Galéron et al. (2001). Sediment collected with a multicorer was sliced into horizons from 0 to 5 cm sediment depth and fixed in 4% buffered formaldehyde. In both studies organisms were extracted using a centrifugation protocol before identification and counting. Taxon-specific densities were converted to biomass using taxon-specific individual C content conversion factors, and biomass was assigned to feeding types as presented in 5. For comparison, our nematode biomass at PAP derived from density and individual C content ($0.94 \text{ mmol C m}^{-2}$) was similar to the nematode biomass used in van Oevelen et al. (2012) ($0.90 \text{ mmol C m}^{-2}$) which was the derived average from two other field studies (Heip et al., 2001; Witte et al., 2003). For both sites, the relative abundance of feeding types of nematodes was based on the reported community composition in Sebastian et al. (2007). Meiofauna taxonomy was done to family level at PAP but not at CVAB. Therefore, the relative abundance of feeding types of meiofaunal polychaetes at CVAB was based on the macrofauna polychaete trophic groups reported in Paterson et al. (1998). The group with other meiofauna counts at PAP ('Others') were omitted in this study as no functional group could be assigned and they had a negligible density.

Metazoan macrofauna (>250 μm) biomass data was used from Aberle and Witte (2003) at PAP (reported in dry mass) and from Galéron et al. (2000) at CVAB (reported in wet mass). At PAP, sediment was collected using benthic chambers and a multi-corer, individual sediment horizons sieved over a 250 μm mesh and frozen at -20°C . At CVAB, sediment was collected with an USNEL boxcorer (sample area of 0.25 m^2), and the upper bioturbated 2.5 cm sediment layer was preserved in 3% borax-buffered

formaldehyde and used for macrofauna identification *sensu stricto* (i.e. excluding meiobenthic taxa). Reported macrofauna dry mass and wet mass data were converted to mmol C m⁻² using the taxon-specific conversion factors adjusted for preservation effects, and subsequently assigned to feeding types based on peer-reviewed literature (Table 6).

Table 5. Taxon-specific relative abundance of feeding types and individual biomass (mmol C ind⁻¹) for metazoan meiofauna. B = bacterivore, EF = epistrate feeder, SDF = selective deposit feeder, DF = deposit feeder, OP = Omnivores and Predators. References for feeding type (FT) and biomass (BM): (1) Sebastian et al. (2007); (2) Wieser (1953); (3) Jumars et al. (2015); (4) Gowing and Wishner (1986); (5) Paterson et al. (1998); (6) Bianchelli et al. (2010); (7) Zeng et al. (2018); (8) Galéron et al. (2000); (9) Rowe (1983); (10) Jensen (1984); (11) Ikeda et al. (2006); (12) Salonen and Sarvala (1980).

Taxon	Feeding types	Specific biomass	Reference	
			FT	BM
Nematoda	PAP: 41.2% DF, 28.7% EF, 28.4% SDF, 1.7% OP. CVAB: 51.1% DF, 26.7% EF, 22.2% SDF.	1.18×10 ⁻⁶ ^a	1-3	8-10
Copepoda	100% DF	8.08×10 ⁻⁵ ^b	4	8, 11, 12
Polychaeta	PAP: 100% DF. CVAB: 78.6% SDF, 14.3% OP, 7.1% DF.	1.48×10 ⁻⁴	3 5	7
Kinorhyncha	50% B, 50% DF	4.22×10 ⁻⁶	6	6
Ostracoda	100% OP	4.98×10 ⁻⁴	7	7
Tanaidacea	100% OP	1.18×10 ⁻⁵	6	6
Tardigrada	100% B	1.05×10 ⁻⁷	6	6

^a Site-specific nematode formaldehyde preserved wet mass m⁻² is given by (Galéron et al., 2000) based on the biovolume method. This wet mass was converted to nematode biomass in C m⁻² using the conversion factor from formaldehyde WM to C for deep-sea nematodes from (Rowe, 1983), adjusted for an average 23% loss of C due to formaldehyde preservation of meiofauna as given in (Jensen, 1984). Total nematode C biomass was divided by the reported density to obtain an average individual nematode C content.

^b Site-specific copepod formaldehyde preserved wet mass m⁻² is given by (Galéron et al., 2000) based on the biovolume method. This wet mass was converted to copepod biomass in C m⁻² using the conversion factor from frozen WM to C for copepods living at 3,000-5,000 m from (Ikeda et al., 2006), adjusted for an average 14% loss of C due to freezing as given in (Salonen and Sarvala, 1980). Total copepod C biomass was divided by the reported density to obtain an average individual copepod C content.

^c The minimum and maximum for other groups are used.

A metazoan megafauna biomass time-series (1989–1999) at PAP is reported by Billett et al. (2001). As total biomass did not differ significantly over the years (Billett et al., 2001), the decadal biomass average was used. Biomass values which included fresh wet mass and the general group ‘Vermes’ with a negligible biomass were excluded from the analysis. At CVAB metazoan megafauna were sampled by beam trawl and preserved in 3% borax-buffered formaldehyde by Galéron et al. (2000). In the lab they identified the specimens to phylum, class, or order, and weighed the specimens after washing to obtain preserved wet mass. At CVAB decapods were reported as either ‘Natantia’ or ‘Reptantia’. For both sites, preserved wet mass was converted to C stocks using taxon-specific conversion factors adjusted for preservation effects as reported, and partitioned to feeding groups based on peer-reviewed literature (Table 7).

Table 6. Taxon-specific biomass conversion factors and feeding types for the metazoan macrofauna. Conversion factors are taken from Rowe (1983) and adjusted for an estimated 25% C loss due to formaldehyde preservation of macrofauna as reported in Salonen and Sarvala (1980). C = carbon, DM

= dry mass, WM = wet mass. FSF = filter and suspension feeders, SDF = surface deposit feeders, DF = deposit feeders, O = omnivores, PS = predators and scavengers. References (FT = feeding types, CN = C:N ratios): (1) Jumars et al. (2015); (2) Blazewicz-Paszkowycz and Ligowski (2002); (3) Iken et al. (2001); (4) Trott (1998); (5) Scheltema (1997); (6) Fox et al. (2003); (7) Thiel and Kruse (2001); (8) Murina (1984); (9) McClain et al. (2004); (10) Menzies (1962).

Taxon	Feeding types	Conversion factor		Ref.
		C/DM	C/WM	
Polychaeta	PAP: 42.4% SDF, 40.6% DF, 16.6% PS, 0.5% O. CVAB: 61.1% SDF, 28.7% DF, 6.5% FSF, 3.7% O.	0.54	0.068	1
Tanaidacea	100% DF	0.58	0.038	2
Isopoda	100% SDF	0.63 ^a	0.060 ^a	3
Amphipoda	100% PS	0.63	-	3
Cumacea	100% DF	0.45	0.036	2
Bivalvia	100% PS	0.33	0.045	3
Priapulida	100% O	0.53 ^b	-	4
Aplacophora	100% O	0.50	0.076	5
Cnidaria	100% FSF	0.31 ^c	-	3
Porifera	100% FSF	-	0.011	6
Nemertea	100% PS	-	0.042 ^d	7
Sipuncula	100% DF	-	0.069	8
Gastropoda	90% DF, 10% PS	-	0.045	9
Holothuroidea	100% DF	-	0.025	3
Asteroidea	50% DF, 50% PS	-	0.053	3
Echinoidea	85% O, 15% DF	-	0.017	10
Tunicata	100% FSF	-	0.011	6

^a Conversion factor for Amphipoda used.

^b Conversion factor for Sipunculids used.

^c Conversion factor for Hydrozoa used.

^d Conversion factor for Nematoda used.

Table 7. Taxon-specific biomass conversion factors and feeding types for the metazoan megafauna. Conversion factors are the macrofaunal and epifaunal conversion factors from Rowe (1983) and adjusted for an estimated 25% C loss due to formaldehyde preservation of macrofauna as reported in Salonen and Sarvala (1980). C = carbon, WM = wet mass. FSF = filter and suspension feeders, SDF = surface deposit feeders, DF = deposit feeders, O = omnivores, PS = predators and scavengers. References feeding types (FT): (1) Aberle and Witte (2003); (2) Jumars et al., (2015); (3) Fox et al. (2003); (4) Iken et al. (2001); (5) McClain et al. (2004); (6) Smith and Stockley (2005); (7) Marine Species Traits database.

Taxon	Feeding types	Conversion factor (C/WM)	Reference
			FT
Porifera	100% FSF	0.011	3,4
<i>Anthozoa</i>			
Ceriantipatharia	100% FSF	0.029 ^a	3,4
Actiniaria	100% FSF	0.029 ^a	3,4
Other Zoantharia	100% FSF	0.029 ^a	3,4
Annelida	PAP: 42.4% SDF, 40.6% DF, 16.6%	0.068 ^c	1,2

Taxon	Feeding types	Conversion factor (C/WM)	Reference
	PS, 0.5% O. ^h CVAB: NA		
Decapoda	PAP: 83.3% PS, 16.7% SDF. ⁱ CVAB: 100% O	0.065	4 7
Other Crustacea	PAP: 50% FSF, 50% SDF. ⁱ	0.045 ^d	4
Pycnogonida	100% SDF	0.065 ^e	4
Gastropoda	90% DF, 10% PS	0.045	5
Scaphopoda	100% PS	0.053	3
Bivalvia	100% PS	0.045	4
Cephalopoda	100% PS	0.121	4
Asteroidea	60% PS, 40% DF. ⁱ	0.032 ^f	4
Ophiuroidea	100% SDF	0.034 ^f	4
Echinoidea	85% O, 15% DF	0.029	6
Holothuroidea	60% SDF, 40% DF. ⁱ	0.009 ^f	4
Crinoidea	100% FSF	0.034 ^f	4
Tunicata	50% FSF, 50% SDF. ⁱ	0.011 ^g	4

^a Conversion factor for Anthozoa used.

^b Conversion factor for Nematoda used.

^c Conversion factor for Polychaeta used.

^d Average conversion factor for Amphipoda, Tanaidacea, Cumacea used.

^e Conversion factor for Decapoda used.

^f Average conversion factor for epifaunal species in this taxonomic group was used.

^g Conversion factor for Porifera used.

^h As no information specifically for megafaunal annelids was available, the feeding groups of macrofaunal polychaetes was used.

ⁱ Based on relative abundance of feeding types, as no information was available on the relative abundance of different taxa.

Physiology

Physiological parameters such as assimilation efficiency (AE), net growth efficiency (NGE), secondary production rates (SP), maintenance respiration rates (MR), growth respiration rates (GR), and feeding selectivity, for meiofauna, macrofauna, and megafauna are presented in (Table 8).

Assimilation of material (A) is the physiological process where ingested food is divided in a fraction to be used for energy and building biomolecules, and a fraction that is defecated, so that $A = I - F$, where I is the ingestion and F is the defecation flux. Therefore, the assimilation efficiency (AE) can be defined as: $AE = (I - F)/I$, and consequently, $A = I \times AE$.

It was assumed labile detritus was assimilated more efficiently than semi-labile detritus. Therefore, the descriptive statistics applied to a water depth-dependent dataset with AE values for invertebrate metazoan meiofauna, macrofauna, and megafauna as presented in de Jonge et al. (2020) was used to set AE constraints. The median and maximum AE values were used as constraints for assimilation of labile material, whereas the Q1 and Q3 AE values were used as constraints for assimilation of semi-labile material. The AE constraints for assimilation of labile material by meiofauna was included as in van Oevelen et al. (2012) due to a lack of data in the descriptive statistics dataset. The corresponding AE constraints for semi-labile assimilation was assumed with a maximum between the constraints for labile material: $AE_{sDet,max} = (AE_{lDet,min} + AE_{lDet,max})/2$, and a minimum constraint based on the constraint range for labile material so that: $AE_{sDet,min} = AE_{sDet,max} - (AE_{lDet,max} - AE_{lDet,min})$. The lower constraints for Foraminifera AE were equal to the lower constraints of meiofauna sensu (van

Oevelen et al., 2012), but the upper constraints were set to 1, as unicellular organisms don't defecate and can use all of the OM absorbed in the cell.

Part of the assimilated material is respired to drive secondary production: growth respiration (GR) is:

$$GR = gr \times C \text{ stock}$$

where gr is the specific growth respiration rate (d^{-1}). Additionally, faunal maintenance respiration (MR) maintains the existing biomass:

$$MR = mr \times C \text{ stock}$$

where mr is specific maintenance respiration (d^{-1}). Maintenance respiration burns stored organic material, i.e., it comes out of the secondary production. In other words, the maintenance (or basal) respiration rate is dependent on the biomass and results in a biomass decrease if no secondary production takes place. Therefore, secondary production (SP) is defined as:

$$SP = A - GR.$$

It was assumed all metabolic processes respond to water temperature, which is included in the model using a Q_{10} factor of 2, meaning rates will double with every 10°C temperature increase. Consequently, rates were corrected using a T_{lim} factor obtained as:

$$T_{lim} = 2^{(new \text{ } ^\circ C - old \text{ } ^\circ C)/10}$$

Maintenance respiration is included as in van Oevelen et al. (2012), adjusted for current water temperatures at PAP and CVAB with T_{lim} . Specific respiration rates constraints were the first and third quartile values from the water-depth dependent dataset used as in de Jonge et al. (2020), but adjusted to abyssal bottom water temperatures if necessary, assuming an average water temperature of 4°C on continental slopes (200–2,000 m) and of 20°C at near-shore areas (0–50 m). Similarly, secondary production was included as:

$$SP = sp \times C \text{ stock}$$

where sp is the biomass specific secondary production rate constraints as reported in de Jonge et al. (2020), and adjusted to abyssal bottom water temperatures if necessary. Mortality rates always ranged between zero and the upper limit of SP .

Net growth efficiency (NGE) is the efficiency at which assimilated material is transformed into biomass:

$$NGE = SP/A \text{ or } NGE = SP/(SP + GR)$$

NGE values for macrofauna and megafauna were used as presented in de Jonge et al. (2020) and complemented with NGE values for prokaryotes and meiofauna from van Oevelen et al. (2012). The NGE range for Foraminifera was calculated using the specific secondary production and growth respiration rates.

Selective uptake of labile detritus by deposit feeders was included in the model *sensu* van Oevelen et al. (2012). Selective uptake was defined as the ratio between the fraction ingested labile detritus (compared to total detritus ingestion) and the fraction labile detritus in the total detritus stock, where a value of 1 represents uptake proportional to the relative abundance of labile material, and larger values represent increasing preference for feeding on labile material.

Table 8. Physiological constraints [min, max] and feeding selectivity. NGE = Net growth efficiency, AE = Assimilation efficiency, SP = Secondary Production, MR = Maintenance respiration, GR = growth respiration. References: (1) van Oevelen et al. (2012); (2) de Jonge et al. (2020).

Parameter	Constraint	Ref.
NGE		
Prokaryotes	[0.05, 0.45]	1
Foraminifera	[0.14, 0.84] ^e	2
Meiofauna	[0.60, 0.90]	1
Macrofauna	[0.57, 0.68]	2
Megafauna	[0.23, 0.95] ^d	2
AE		
Foraminifera, labile sources	[0.57, 1.0] ^f	1
Foraminifera, semi-labile sources	[0.47, 1.0] ^f	-
Meiofauna, labile sources	[0.57, 0.77]	1
Meiofauna, semi-labile sources	[0.47, 0.67] ^g	-
Macrofauna, labile sources	[0.75, 0.97]	2
Macrofauna, semi-labile sources	[0.68, 0.88]	2
Megafauna, labile sources	[0.54, 1.0] ^h	2
Megafauna, semi-labile sources	[0.40, 0.75]	2
SP		
Foraminifera	$[8.98 \times 10^{-3}, 2.69 \times 10^{-2}] \times C \text{ stock}^a$	1
Meiofauna	$[5.99 \times 10^{-3}, 3.43 \times 10^{-2}] \times C \text{ stock}^a$	2
Macrofauna	$[1.15 \times 10^{-2}, 1.91 \times 10^{-2}] \times C \text{ stock}^b$	2
Megafauna	$[1.14 \times 10^{-4}, 1.72 \times 10^{-2}] \times C \text{ stock}^{b,c}$	2
MR	$[0.003] \times C \text{ stock}^a$	1
GR		
Foraminifera	$[4.98 \times 10^{-3}, 5.44 \times 10^{-2}]^b$	2
Meiofauna	$[6.35 \times 10^{-3}, 6.81 \times 10^{-2}] \times C \text{ stock}^{b,c}$	2
Macrofauna	$[3.57 \times 10^{-5}, 4.21 \times 10^{-2}] \times C \text{ stock}$	2
Megafauna	$[9.32 \times 10^{-8}, 1.26 \times 10^{-3}] \times C \text{ stock}^d$	2
Selectivity		
MeiSDF, MacSDF, MegSDF	[50, 1,000]	1
MeiDF, MacDF, MegDF	[1, 50]	1

^a The original rate valid at ~20°C water temperature was adjusted to a water temperature of 2.4-2.6°C using $T_{lim} = 0.3$ based on a Q_{10} factor of 2.

^b The original rate valid at ~4°C water temperature was adjusted to a water temperature of 2.4-2.6°C using $T_{lim} = 0.9$ based on a Q_{10} factor of 2.

^c For the lower limit not Q1 but the minimum value in the dataset was used due to model incompatibilities.

^d For the upper limit not Q3 but the maximum value in the dataset was used due to model incompatibilities.

^e Calculated as $NGE = SP / (SP + GR)$.

^f Lower constraints equal to meiofauna as some Foraminifera utilize waste products in their stercomata. The upper constraint is set to 1 to indicate potential full utilization of the absorbed organic matter by the cell.

^g Calculated as $AE_{sDet,max} = (AE_{IDet,min} + AE_{IDet,max}) / 2$, and $AE_{sDet,min} = AE_{sDet,max} - (AE_{IDet,max} - AE_{IDet,min})$.

^h Minimum labile AE constraint for MegDF at CVAB was omitted to solve model incompatibility.

Linear Inverse Modelling

The topological network, and data for stocks and fluxes were used to create a LIM of the steady-state C-based food web. A LIM is a set of linear functions formed by an equality and inequality matrix equation following van Oevelen et al. (2010):

$$\begin{aligned} \mathbf{E} \cdot \mathbf{x} &= \\ \mathbf{G} \cdot \mathbf{x} &\geq \mathbf{h} \end{aligned}$$

where vector \mathbf{x} contains the unknown fluxes, vectors \mathbf{f} and \mathbf{h} contain the empirical equality and inequality data respectively, whereas the coefficients in matrices \mathbf{E} and \mathbf{G} specify the combination of unknown fluxes that should meet the requirements defined in vectors \mathbf{f} and \mathbf{h} .

The constructed LIM comprised 21 mass-balances i.e., food-web components, which were treated as equalities, 1 specified equality, and 226 specified inequalities, meaning the model was mathematically under-determined (there were less equalities than unknowns). Mathematically under-determined models have multiple valid solutions for unknown fluxes. Therefore, the unknown fluxes were quantified using the likelihood approach van Oevelen et al. (2010), using a Markov-chain sampling algorithm in the R-package *LIM* (Soetaert and Van Oevelen, 2010), randomly sampling 50,000 solutions from the multi-dimensional solution space. To reduce calculation time, each site model was sampled 10,000 times in five parallel jobs on a High-Performance Computing cluster. Expected convergence of standard deviations to $\pm 2\%$ error margin, histograms of flows, and coverage of the expected sample range was reviewed to confirm the number of iterations of the Markov-chain was sufficient to sample the majority of the multi-dimensional solution space and obtain reliable probability density distributions.

Network and statistical analysis

The R-package *NetIndices* (Soetaert, 2009) was used to summarise the topological network (number of internal compartments [N], number of internal linkages [L], Linkage Density [LD], and Connectance [C]) and calculate network indices to capture the system size and organisation for each iterative model solution. The latter indices comprise of the Total System Throughflow (*TST*), Finn's Cycling Index (*FCI*), Relative Ascendancy (*RA*), Average Mutual Information (*AMI*), and Synergism (*S*). The *NetIndices* package (Soetaert, 2009) was also used to calculate the Trophic Level (*TL*) and Omnivory Index (*OI*) of each compartment for each iteration.

Carbon pathways that were compared between sites were 1) total C influx, and the relative roles of labile POC, semi-labile POC, refractory POC, food-falls and Dark Carbon Fixation, 2) total C respiration, 3) total secondary C production, 4) total C uptake, 5) the relative roles of prokaryotes, foraminifera, meiofauna, macrofauna, and megafauna in total respiration, secondary production, and uptake, 6) PB-ratios, i.e. secondary production relative to site-specific biomass, for prokaryotes, foraminifera, meiofauna, macrofauna, and megafauna, and 7) deep C burial efficiency (burial flux relative to total C influx).

The Bayesian solution (mean \pm SD over all 50,000 iterations) was calculated for each flow, flow pathway, and network index (with the exception of the topological indices which do not change with each iteration).

Due to the mathematical nature of LIM solutions, the standard deviation does not reflect statistically significant differences. Rather, a difference between flows, flow pathways, and network indices was

defined as ‘significant’ or ‘highly significant’ if in a randomised comparison of values more than 90% or 95%, respectively, of values in one food-web model are always greater than in the other.

2.2 Results

In situ benthic ecosystem functioning at CVAB

Study site

The sediments retained in the chamber were light brown in colour, contained many calcite foraminifera tests, often displayed bioturbation activity in the form of small burrowing holes, and occasionally polychaete tubes and ophiuroids were retrieved. In one deployment (AKS309, Ch1) a small jelly and crustacean were retrieved from the overlying and surface sediment respectively. No other fauna visible by the naked eye were found on the 300 μm sieve. In various chambers small leaf-shaped fragments of macroalgae was found. The bottom water oxygen concentration measured with the optodes was $230.5 \pm 1.4 \mu\text{mol L}^{-1}$, which corresponds with the $223 \mu\text{mol L}^{-1}$ measured by the CTD. The upper 5 cm of sediment had a mean TOC content of $0.77 \pm 0.03 \text{ wt } \%$, equivalent to $5.07 \pm 0.19 \text{ mg C g}^{-1}$ wet sediment and $244.38 \pm 7.56 \text{ g C m}^{-2}$.

Table 9. Sediment Community Oxygen Consumption (SCOC, $\text{mmol O}_2 \text{ m}^{-2} \text{ d}^{-1}$) and DIC production rates ($\text{mmol C m}^{-2} \text{ d}^{-1}$). SCOC was estimated with both Micro-Winkler titrations and in situ oxygen concentration data as measured with Aanderaa oxygen optodes (model 4330F). n.d. = no data were collected due to a malfunction in the sampling device.

Station— Incubation	SCOC $\text{mmol O}_2 \text{ m}^{-2} \text{ d}^{-1}$		DIC $\text{mg C m}^{-2} \text{ d}^{-1}$
	<i>Micro-Winkler</i>	<i>Optode</i>	
Background			
9 – AKS295 Ch2	n.d.	0.70 ($R^2 = 0.99$)	NA
28 – AKS300 Ch2	n.d.	0.64 ($R^2 = 0.99$)	NA
43 – AKS302 Ch2	n.d.	0.56 ($R^2 = 0.99$)	NA
58 – AKS306 Ch1	1.49 ($R^2 = 0.52$)	0.53 ($R^2 = 0.67$)	NA
Ch2	n.d.	0.41 ($R^2 = 0.98$)	
76 – AKS309 Ch2	n.d.	0.60 ($R^2 = 0.98$)	NA
Average \pm s.e.	1.49 (n=1)	0.57\pm0.04 (n=6)	NA
Tracer experiment			
9 – AKS295 Ch1	0.85 ($R^2 = 0.73$)	0.78 ($R^2 = 0.98$)	0.84 ($R^2 = 0.99$)
28 – AKS300 Ch1	1.16 ($R^2 = 0.78$)	n.d.	0.61 ($R^2 = 0.98$)
43 – AKS302 Ch1	0.45 ($R^2 = 0.62$)	0.67 ($R^2 = 0.95$)	0.62 ($R^2 = 0.96$)
76 – AKS309 Ch1	0.75 ($R^2 = 0.84$)	0.66 ($R^2 = 0.89$)	1.02 ($R^2 = 0.99$)
Average \pm s.e.	0.80\pm0.15 (n = 4)	0.70\pm0.04 (n = 3)	0.77\pm0.10 (n = 4)

SCOC, DIC, nutrient fluxes, and TOC

The background SCOC rate based on optode measurements was $0.57 \pm 0.04 \text{ mmol O}_2 \text{ m}^{-2} \text{ d}^{-1}$ (Table 9). The SCOC rate during the tracer experiments based on optode data was $0.70 \pm 0.04 \text{ mmol O}_2 \text{ m}^{-2} \text{ d}^{-1}$, which corresponded well to the SCOC rate as obtained with Micro-Winkler titration $0.80 \pm 0.14 \text{ mmol O}_2 \text{ m}^{-2} \text{ d}^{-1}$ (Table 99).

The overall C degradation rate of injected phytodetrital material was estimated to be $1.56 \text{ mg C m}^{-2} \text{ d}^{-1}$, based on background-corrected SCOC measured with the optodes. As 170 mg C m^{-2} of algae was added to the incubations, we estimate a phytodetritus turnover rate of 0.0092 d^{-1} . The mean DIC

production rate derived from respiration of the injected labelled substrate was $0.77 \pm 0.10 \text{ mg C m}^{-2} \text{ d}^{-1}$ (Table 9).

Nutrient concentrations in the water samples taken during the incubations were variable, resulting in often low R^2 values in the linear regressions to obtain fluxes. Nutrient fluxes in the tracer experiments were not significantly different from the single background flux (one-sample Wilcoxon signed rank test, Table 10). However, nitrite, nitrate, and phosphate efflux were consistently larger in all tracer experiments compared to the background incubation. Additionally, ammonium efflux during the background incubation was reduced in one tracer experiment and reversed to ammonium influx in the three other tracer experiments. There was a negative linear correlation between DIC production rates and nitrite ($R^2 = 0.58$, p-value = 0.24), nitrate ($R^2 = 0.68$, p-value = 0.18), phosphate ($R^2 = 0.80$, p-value = 0.11) and silicate ($R^2 = 0.67$, p-value = 0.18) flux.

Table 10. Nutrient fluxes measured for each lander deployment. A positive flux means efflux (i.e., flux out of the sediment) and a negative flux means influx (i.e., flux into the sediments). Reported p-values are for the 1-sample Wilcoxon signed rank test to assess if the tracer experiment mean was significantly different from the background value.

Station– Incubation	Flux ($\text{mmol m}^{-2} \text{ d}^{-1}$)				
	Ammonium (NH_4^+)	Nitrite (NO_2^-)	Nitrate (NO_3^-)	Phosphate (PO_4^{3-})	Silicate (SiO_3^{2-})
Background					
58– AKS306 Ch1	4.46×10^{-2} ($R^2 = 0.27$)	2.65×10^{-5} ($R^2 = 0.002$)	2.88×10^{-2} ($R^2 = 0.04$)	4.25×10^{-3} ($R^2 = 0.59$)	9.33×10^{-2} ($R^2 = 0.19$)
Tracer experiment					
9– AKS295 Ch1	2.07×10^{-2} ($R^2 = 0.07$)	1.75×10^{-3} ($R^2 = 0.66$)	4.78×10^{-2} ($R^2 = 0.02$)	1.30×10^{-2} ($R^2 = 0.23$)	-5.10×10^{-2} ($R^2 = 0.003$)
28– AKS300 Ch1	-2.36×10^{-2} ($R^2 = 0.23$)	1.75×10^{-3} ($R^2 = 0.60$)	5.11×10^{-1} ($R^2 = 0.54$)	2.92×10^{-2} ($R^2 = 0.58$)	1.03 ($R^2 = 0.49$)
43– AKS302 Ch1	-2.86×10^{-2} ($R^2 = 0.04$)	1.46×10^{-3} ($R^2 = 0.33$)	1.11×10^{-1} ($R^2 = 0.05$)	1.96×10^{-2} ($R^2 = 0.48$)	3.52×10^{-1} ($R^2 = 0.22$)
76– AKS309 Ch1	-2.91×10^{-2} ($R^2 = 0.20$)	4.85×10^{-4} ($R^2 = 0.06$)	-1.57×10^{-1} ($R^2 = 0.11$)	8.74×10^{-3} ($R^2 = 0.16$)	-1.21×10^{-1} ($R^2 = 0.02$)
Mean	-1.52×10^{-2}	1.36×10^{-3}	1.28×10^{-1}	1.76×10^{-2}	3.02×10^{-1}
± se	$\pm 6.01 \times 10^{-3}$	$\pm 1.50 \times 10^{-4}$	$\pm 6.99 \times 10^{-2}$	$\pm 2.23 \times 10^{-3}$	$\pm 1.32 \times 10^{-1}$
p-value	0.40	0.40	0.80	0.80	0.80

Bacteria

Bacterial biomass at the lander site was estimated to be $27.5 \pm 2.1 \text{ mg C m}^{-2}$ for 0–5 cm, with biomass decreasing with sediment depth, Table 11). Bacterial incorporation of algal derived C was $0.139 \pm 0.009 \text{ mg C m}^{-2} \text{ d}^{-1}$ for 0–2 cm sediment depth, and $0.016 \pm 0.2 \text{ mg C m}^{-2} \text{ d}^{-1}$ for 2–5 cm sediment depth (Table 11), so an overall microbial C incorporation rate of $0.155 \text{ mg C m}^{-2} \text{ d}^{-1}$ was calculated for the upper 5 cm of sediment.

Table 11. Bacterial biomass and bacterial C uptake ($\mu\text{mol C m}^{-2} \text{ d}^{-1}$) in the tracer experiments for different sediment horizons (0–2, 2–5, 5–10 cm) based on the C15:0i PLFA biomarker.

Station– Incubation	Bacterial biomass (mg C m^{-2})		
	0–2 cm	2–5 cm	5–10 cm
9– AKS295 Ch1	19.5	8.3	6.8

Station– Incubation	Bacterial biomass (mg C m ⁻²)		
28-- AKS300 Ch1	12.9	9.6	5.4
43-- AKS302 Ch1	19.0	13.7	NA
76-- AKS309 Ch1	15.7	11.3	NA
Means±s.e.	<i>16.8±1.5</i>	<i>10.7±1.2</i>	<i>6.1±0.7</i>
	Bacterial C uptake (mg C m ⁻² d ⁻¹)		
	0-2 cm	2-5 cm	5-10 cm
9-- AKS295 Ch1	0.161	0.018	0.005
28-- AKS300 Ch1	0.118	0.017	0.001
43-- AKS302 Ch1	0.145	0.010	NA
76-- AKS309 Ch1	0.130	0.019	NA
Means±s.e.	0.139±0.009 (n=4)	0.016±0.2 (n=4)	0.003±0.002 (n=2)

Meiobenthos

The average meiobenthic density at our study site was 164±15 individuals 10 cm⁻² for 0-5 cm sediment depth (Table 12). Nematoda were the major taxonomic group, comprising of 82.7±3.2% of the meiobenthic community. The second largest group were the Copepoda, comprising 5.2±0.8% of meiobenthic density. The remaining meiobenthos included individuals from various taxa, such as Polychaeta, Crustacea, Tardigrada, Priapulida, Kinoryncha, and Gromiidea. The average meiobenthic biomass was estimated at 99.1±45.6 mg DM m⁻² and 38.1±15.1 mg C m⁻² for 0-5 cm sediment depth (Table 12). Meiobenthic C uptake from the injected algal tracer ranged from 0.7 to 34.9 mg C m⁻² d⁻¹, with an average of 13.0±7.6 mg C m⁻² d⁻¹ (Table 12).

Table 12. Meiobenthic (excluding Foraminifera) density (individuals 10cm⁻²), biomass (mg dry mass m⁻², and mg C m⁻²), and C uptake (mg C m⁻² d⁻¹) for the 0–5 cm sediment horizon.

Station	Density Ind. 10 cm ⁻²			Biomass		C uptake
	Nematoda	Other	Total	mg DM m ⁻²	mg C m ⁻²	mg C m ⁻² d ⁻¹
Background						
AKS295 Ch3	115	7	122	58.5	17.5	NA
Tracer experiment						
AKS295 Ch1	106	32	138	31.9	21.1	0.7
AKS300 Ch1	155	47	202	276.6	96.4	5.0
AKS302 Ch1	156	31	188	92.0	37.7	34.9
AKS309 Ch1	140	30	170	36.3	17.6	11.4
Average ± s.e.						
Tracer (n=4)	139±12	35±4	174±14	109.2±57.5	43.2±18.3	13.0±7.6
All (n=5)	135±10	29±6	164±15	99.1±45.6	38.1±15.1	

Macrofauna

The macrofaunal species accumulation curve was asymptotic, meaning that the sample size adequately represented the macrofaunal assemblages (Figure 4). Overall, the Cabo Verde abyssal basin was represented by six macrofaunal *sensu stricto* phyla, and macrofaunal size nematodes were considered in our analysis given their large size. Polychaeta was the most diverse phylum (23 families), followed by Crustacea (5 orders), and Mollusca (4 orders).

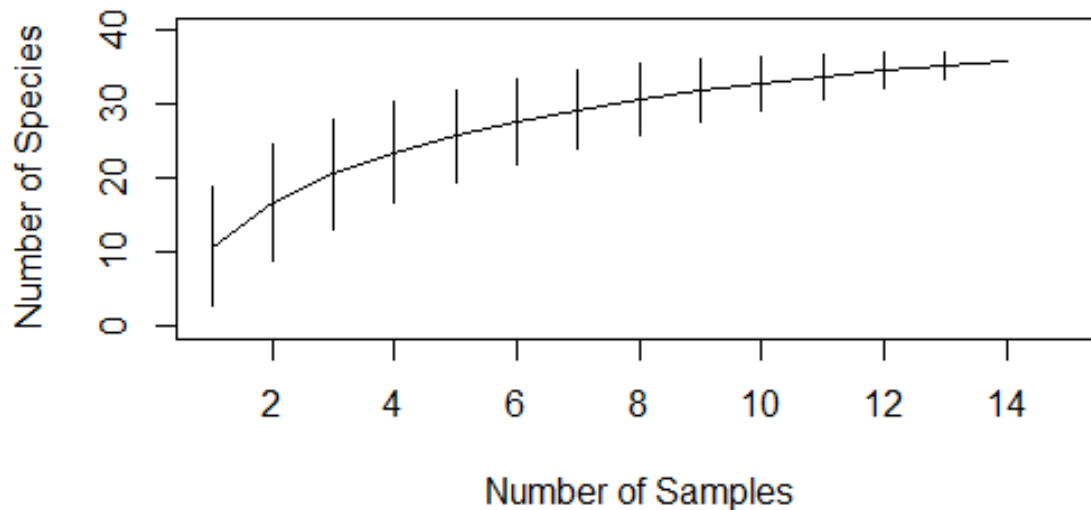


Figure 4. Species accumulation curve showing the macrofaunal number of taxa per number of collected samples.

The average macrofaunal density (i.e., omitting Foraminifera) at our study site was 506 ± 266 (SD, $n=14$) ind. m^{-2} (Error! Reference source not found.13). Overall macrofaunal density (0-10 cm layer) was dominated by polychaetes (37.7%) and crustaceans (33.0%), comprising 70.7% of all macrofauna taxa (Figure 5a). A total of 23 families of Polychaeta were identified, where the Spionidae showed the highest relative abundance (18%), followed by Acrocirridae (14%), Maldanidae (13%), and Paraonidae (10%). Families like Lumbrineridae, Sigalionidae, Opheliidae, and Chaetopteridae were represented by only one individual (Figure 5b). Crustaceans comprised five different orders: Harpacticoida (19%), Tanaidacea (19%), Isopoda (16%), and the less abundant Amphipoda (8%), and Cumacea (3%) (Figure 5c). Macrofaunal-sized nematodes were the third major taxa with the highest abundance (17%), followed by nemertean worms (7%). Other phyla present were Acanthocephala, Echinodermata and Mollusca, which all showed the same abundance with only 2% of the total organisms. Even though Mollusca had a low relative abundance, they were represented by four classes (Bivalvia, Caudofoveta, Scaphopoda, and Solenogastres) (Figure 5a).

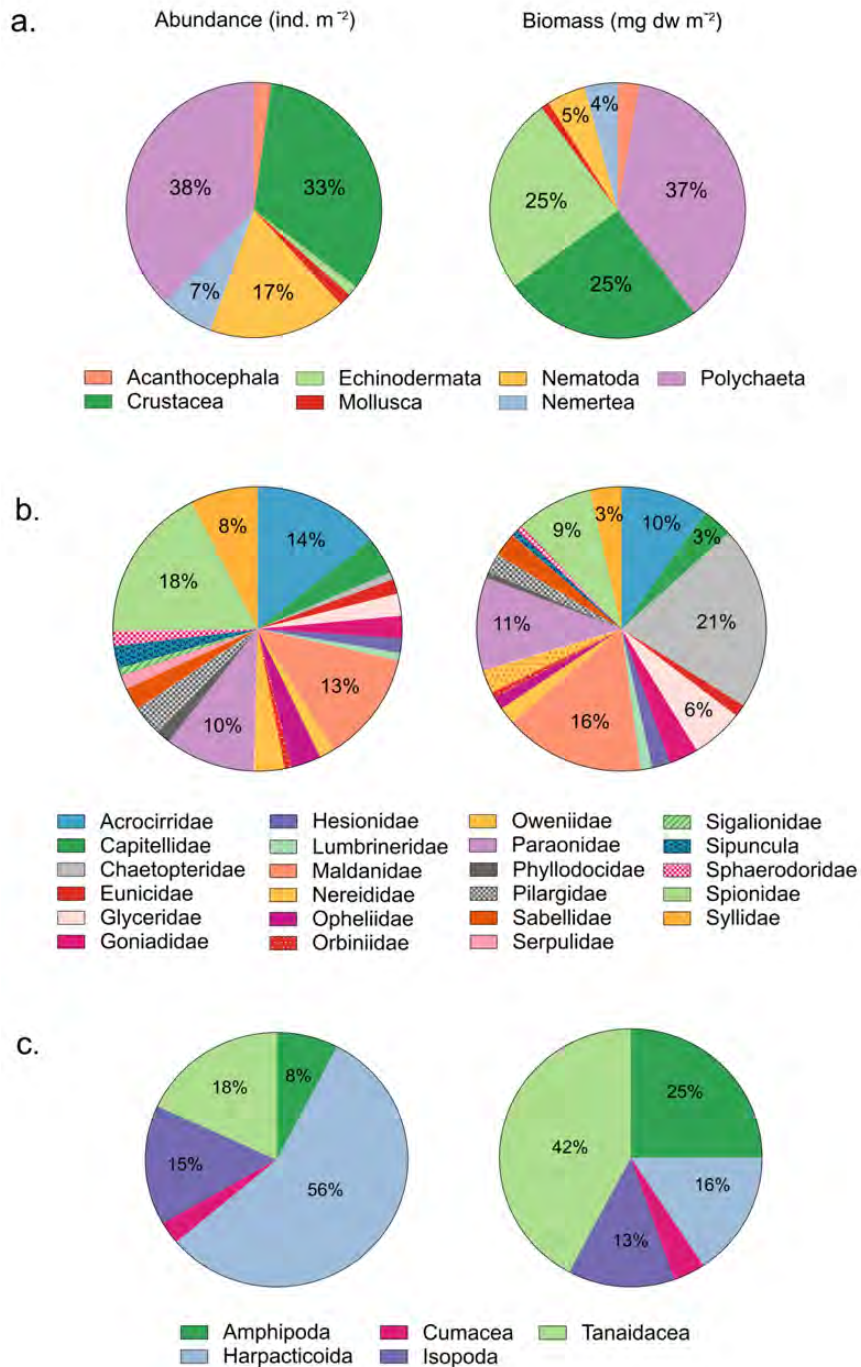


Figure 5. Relative abundance (individuals m⁻²) and biomass (mg dry mass m⁻²) in the 0–10 cm sediment layer at the Cabo Verde Abyssal Basin of a) major macrofaunal taxa; b) polychaete family; c) crustacean order. Data are from 14 benthic chambers.

The vertical distribution of the Cape Verde abyssal macrofaunal abundance showed that most of the organisms (86%) lived within the top 5 cm of the sediment (Figure 6a). The top 2 cm of sediment comprised the greatest concentration (55%) of the macrofauna with 308±52 ind. m⁻² (n = 14) compared to deeper sediment layers, where the number of organisms decreased to 31% (176±37 ind. m⁻², n = 14), and 14% (78±57 ind. m⁻², n = 4) of the community within the 2 to 5 cm and 5 to 10 cm horizons, respectively (Figure 66a). The vertical distribution of the most dominant taxa, Polychaeta, and Crustacea showed a similar pattern. A total of 62% of all crustaceans and polychaetes (112±88 ind. m⁻²

polychaetes and 112 ± 74 ind. m^{-2} crustaceans, $n = 14$) were found in the upper 2 cm of the sediment. Their abundance in the 2–5 sediment layer was lower (72 ± 16 ind. m^{-2} polychaetes and 54 ± 17 ind. m^{-2} crustaceans, $n=14$).

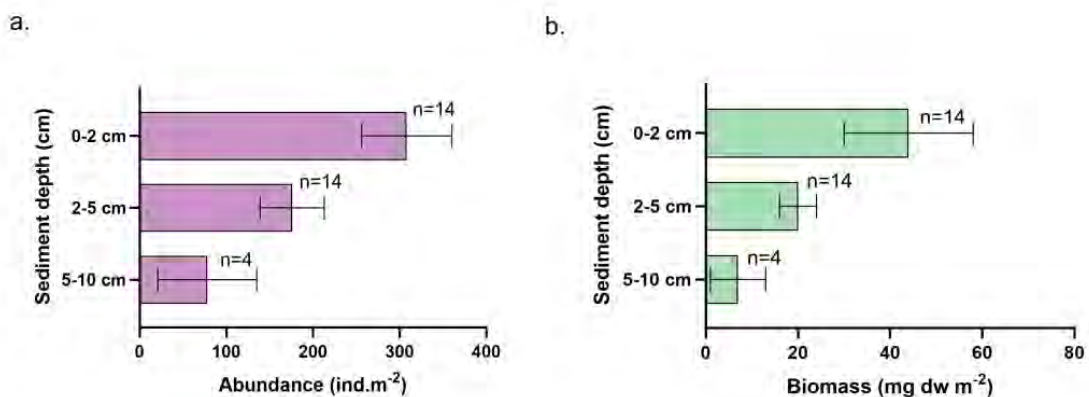


Figure 6. Vertical distribution of a) total macrofaunal abundance (individuals m^{-2}) and b) total macrofaunal biomass (mg DM m^{-2}) within the sediment.

Mean macrofaunal biomass for 0-10 cm sediment depth was 66 ± 62 mg DM m^{-2} (SD, $n=14$) or 21.8 mg C m^{-2} (Table 13). Thirty seven percent of the total dry mass biomass was represented by the polychaetes, followed by the crustaceans and ophiuroids (both 25%), which differs from their relative abundances. Biomass was quite evenly distributed throughout the polychaete families with relative biomass generally following the trends of the relative abundances (Figure 5b). The exception was the Chaetopteridae, which had a much larger share of biomass than abundance. The Chaetopteridae, Maldanidae, and Paraonidae together contributed 48% of the total polychaete biomass (21%, 16%, and 11% respectively, Figure 5b). Within the crustaceans, Tanaidacea (42%) represented the highest biomass value followed by Amphipoda (25%), while Harpacticoida consisted of 16% (Figure 5c). The upper 5 cm of the sediment contained 90% of the total macrofaunal biomass (44 ± 14 mg DM m^{-2} or 14.5 mg C m^{-2} , $n=14$, in the 0-2 cm horizons, and 20 ± 4 mg DM m^{-2} or 6.6 mg C m^{-2} , $n=14$ within 2 to 5 cm horizons, Figure 5b). The presence of one ophiuroid in the 5-10 cm sediment horizon (6.8 mg DM m^{-2}) drastically altered biomass estimates, therefore, this organism was omitted from the analysis of the macrofaunal vertical distribution.

The phylum Foraminifera were represented by large agglutinated foraminifera mainly from the suborder Komokioidea, totalling a mean unacidified biomass of $3,003 \pm 1,540$ mg DM m^{-2} , corresponding to an estimated organic biomass of 150.2 mg DM m^{-2} or 1.5 mg C m^{-2} . The highest unacidified biomass was observed in the upper layer (0–2 cm) with $2,524 \pm 429$ mg DM m^{-2} (estimated organic biomass 126.2 mg DM m^{-2} or 1.3 mg C m^{-2}), which decreased five-fold in the 2–5 cm sediment horizon at 479 ± 84 mg DM m^{-2} (estimated organic biomass 24.0 mg DM m^{-2} or 0.2 mg C m^{-2}). However, given that abundance data is not available as most of them were fragmented and therefore made it difficult to count the organisms. Biomass shares were reported and compared to macrofauna biomass, but not detailed in the total biomass macrofauna analyses as organic biomass was estimated.

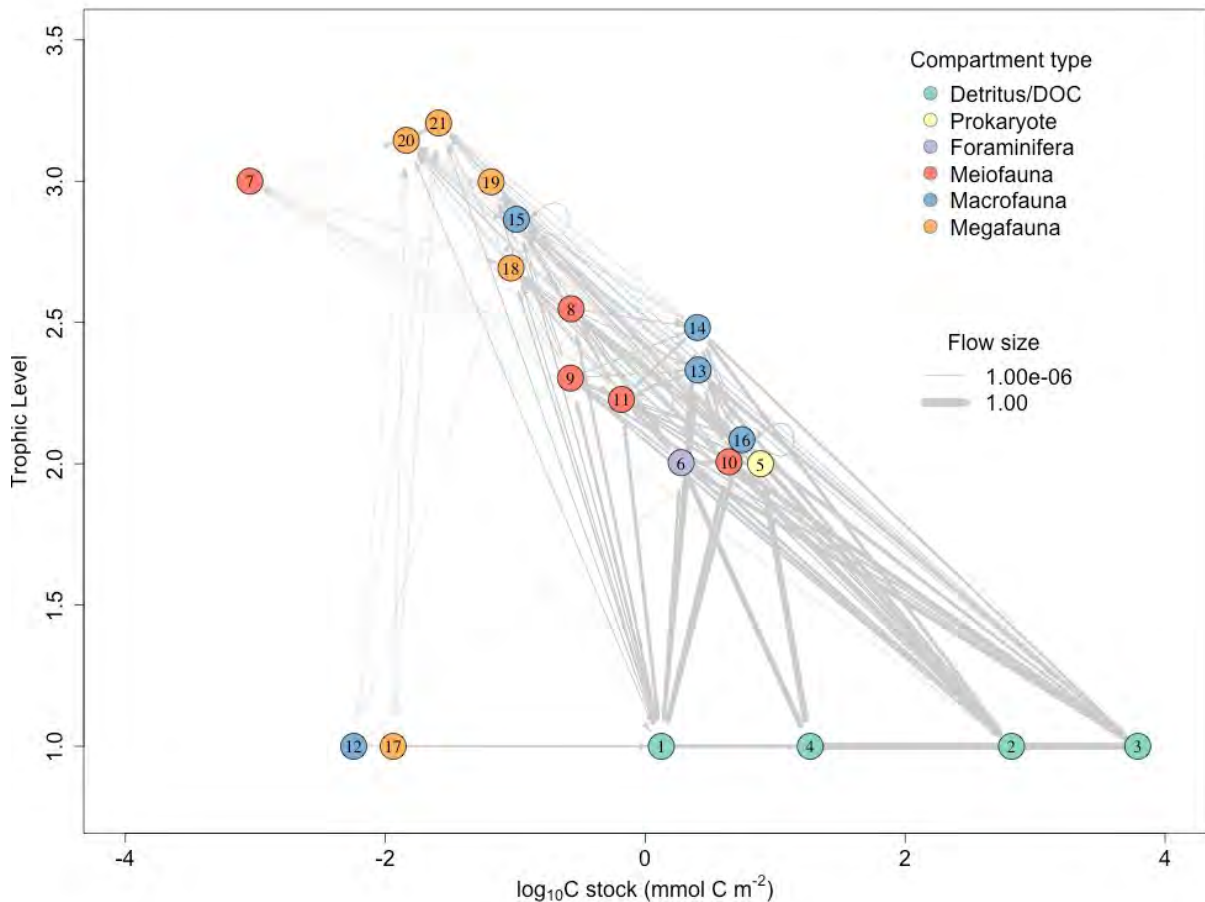
Table 13. Macrofaunal (excluding Foraminifera) density (ind. m^{-2}), biomass (mg dry mass m^{-2} , and mg C m^{-2}), and C uptake (mg C $m^{-2} d^{-1}$) for various sediment horizons. Reported mean \pm SD. Note: data for macrofauna C-uptake are not available (NA) for macrofauna at this time, though the samples have been sent for analysis.

Treatment	Density	Biomass		C uptake
	Ind. m ⁻²	mg DM m ⁻²	mg C m ⁻²	mg C m ⁻² d ⁻¹
Background				
0–2 cm (n = 9)	221±139	28±30	9.24	NA
2–5 cm (n = 9)	166±172	18±17	5.94	NA
5–10 cm (n = 2)	22±32	1±2	0.33	NA
Tracer experiment				
0–2 cm (n = 5)	465±209	73±75	24.09	NA
2–5 cm (n = 5)	192±51	23±18	7.59	NA
5–10 cm (n = 2)	134±158	14±16	4.62	NA
Overall	506±266	66±62	21.8	

Linear inverse model results comparing the PAP and CVAB

Model resolution

The topological network was the same for both sites, with 23 internal compartments, 198 internal linkages, a linkage density of 9.09 and a connectedness of 0.39. The 50,000 iterations in the Markov-chain showed a convergence of flow standard deviations to ±2 % error margin, no unusual patterns in flow histograms, and a coverage of 65% and 67% of the solution space for PAP and CVAB, respectively. A comparison of network characteristics is given in Table 14 and reported below. The resolved food-web is plotted as biomass (log¹⁰-transformed) against computed trophic level (over the 50,000 iterations) with link weights scaled according to the estimated mean flux size (Figure 7).



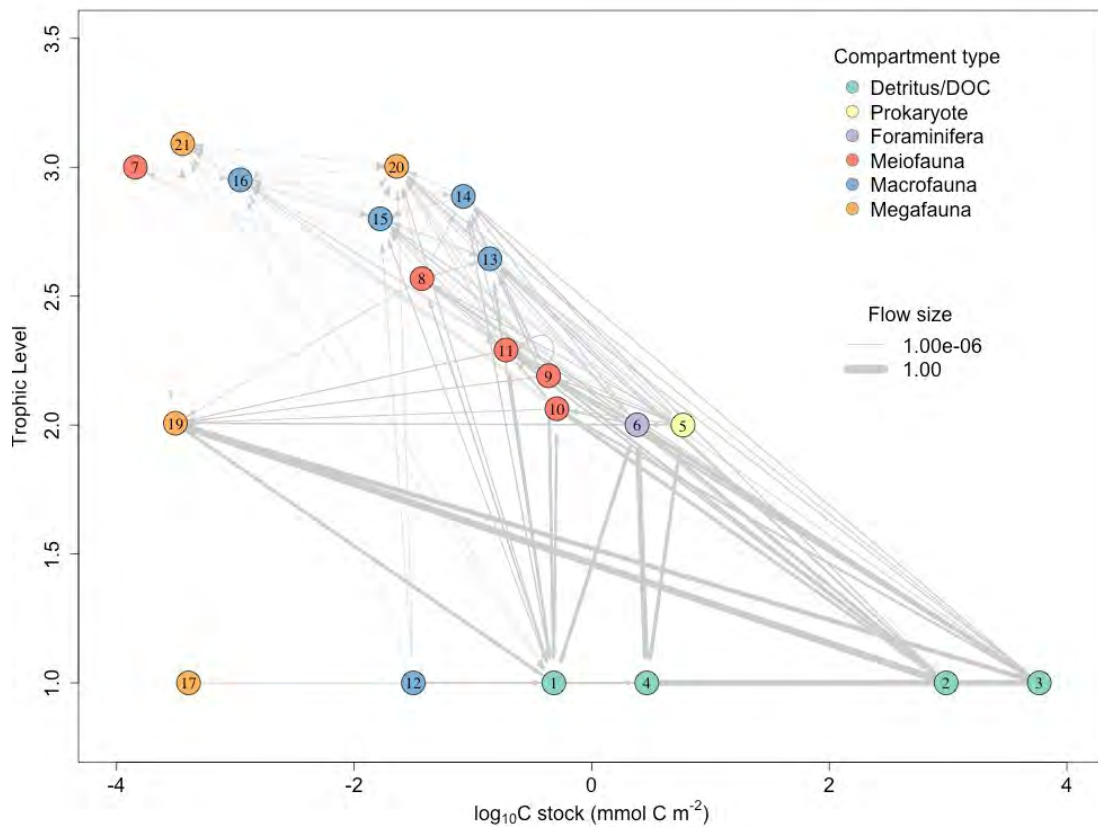


Figure 7. Resolved food-web of the Porcupine Abyssal Plain (PAP, above) and the Cabo Verde Abyssal Basin (CVAB, below). Flow size is the Bayesian (mean) solution of 50,000 iterations. Food web compartments: (1) Labile detritus, (2) Semi-labile detritus, (3) Refractory detritus, (4) Dissolved Organic C, (5) Prokaryotes, (6) Foraminifera, (7) Meiofauna, bacterivores, (8) Meiofauna, epistrate feeders, (9) Meiofauna, selective deposit feeders, (10) Meiofauna, deposit feeders, (11) Meiofauna, omnivores and predators, (12) Macrofauna, filter and suspension feeders, (13) Macrofauna, surface deposit feeders, (14) Macrofauna, deposit feeders, (15) Macrofauna, omnivores, (16) Macrofauna, predators and scavengers, (17) Megafauna, filter and suspension feeders, (18) Megafauna, surface deposit feeders, (19) Megafauna, deposit feeders, (20) Megafauna, omnivores, (21) Megafauna predators and scavengers.

Table 14. Comparison of ecosystem characteristics over all iterations (mean ± stdev) between the PAP and CVAB C-based food webs. Certain C cycling pathways (mmol C m⁻² d⁻¹) are reported, including Total System Throughflow (TST), secondary production, and C uptake. For size-based groups their relative contribution to these pathways is reported. System organisation indices include Finn’s Cycling Index (FCI), Relative Ascendancy (RA), and Average Mutual Information (AMI). Trophic indices related to trophic interactions and energy transfer include PB-ratios (community and size-based), burial efficiency i.e. deep C burial flux relative to total C influx, synergism (S), average system trophic level (TL), and the Omnivory Index (OI). Significance: ** highly significant, * significant, or – no difference between sites.

System parameter	PAP	CVAB	Sig.
C-cycling (mmol C m ⁻² d ⁻¹)			
TST	3.37±0.25	2.34±0.04	**
Total C influx	0.60±0.043 (100%)	0.18±0.017 (100%)	**
Labile POC	0.015±0.005 (3%)	0.011±0.007 (6%)	**
Semi-labile POC	0.24±0.017 (40%)	0.014±0.007 (8%)	**

System parameter	PAP	CVAB	Sig.
Refractory POC	0.23±0.065 (38%)	0.016±0.008 (9%)	**
Food falls	0.073±0.029 (12%)	0.12±0.007 (63%)	-
Dark Carbon Fixation	0.041±0.002 (7%)	0.027±0.006 (15%)	*
Total respiration	0.48±0.040 (100%)	0.15±0.014 (100%)	**
Prokaryotes	0.27±0.038 (56%)	0.03±0.002 (17%)	**
Foraminifera	0.089±0.011 (18%)	0.11±0.014 (73%)	**
Meiofauna	0.043±0.003 (9%)	0.013±0.002 (8%)	**
Macrofauna	0.083±0.008 (17%)	0.003±0.0002 (2%)	**
Megafauna	2.2×10 ⁻⁴ ±1.8×10 ⁻⁵ (<0.1%)	2.5×10 ⁻⁵ ±3.0×10 ⁻⁶ (<0.1%)	**
Total secondary production	0.49±0.023 (100%)	0.13±0.007 (100%)	**
Prokaryotes	0.064±0.003 (13%)	0.028±0.006 (22%)	**
Foraminifera	0.045±0.005 (9%)	0.062±0.002 (48%)	**
Meiofauna	0.19±0.012 (38%)	0.033±0.002 (25%)	**
Macrofauna	0.19±0.015 (39%)	0.005±0.0003 (4%)	**
Megafauna	0.004±0.0002 (0.8%)	0.0005±2.7×10 ⁻⁵ (0.4%)	**
Total C uptake	1.00±0.076 (100%)	0.89±0.015 (100%)	**
Prokaryotes	0.29±0.038 (29%)	0.028±0.001 (3%)	**
Foraminifera	0.22±0.046 (22%)	0.26±0.014 (30%)	-
Meiofauna	0.33±0.019 (33%)	0.065±0.006 (7%)	**
Macrofauna	0.15±0.017 (15%)	0.009±0.0006 (1%)	**
Megafauna	0.006±0.0006 (0.6%)	0.53±0.003 (59%)	**
System organisation indices			
Finn's Cycling Index	0.20±0.02	0.56±0.02	**
Relative Ascendancy	0.44±0.02	0.53±0.01	**
AMI	2.18±0.06	2.06±0.03	-
Trophic indices			
PB-ratio, overall	0.019±0.0009	0.013±0.0007	**
Prokaryotes	0.008±0.0008	0.005±0.0007	**
Foraminifera	0.024±0.003	0.026±0.002	-
Meiofauna	0.034±0.002	0.027±0.002	**
Macrofauna	0.018±0.001	0.020±0.001	-
Megafauna	0.018±0.001	0.019±0.001	-
Burial efficiency	0.050±0.004	0.017±0.002	**
Synergism	3.16±0.13	4.41±0.09	**
Trophic Level	2.07±0.027	2.14±0.036	*
Omnivory Index	0.14±0.014	0.20±0.017	**

C-pathways

Total C influx at the oligotrophic CVAB (0.18±0.017 mmol C m⁻² d⁻¹) was about a third the influx at the more eutrophic PAP (0.60±0.043 mmol C m⁻² d⁻¹) (Table 14). Even though at PAP food-falls had a non-negligible role by providing 12% of the total C influx, at CVAB they provided the majority (63%) of C influx. The role of overall DCF rate was higher at PAP (0.041±0.002 mmol C m⁻² d⁻¹) comprising 7 % of organic C influx into the system but playing a relatively more important role at CVAB providing 15% of organic C influx into the system (0.027±0.006 mmol C m⁻² d⁻¹) (Table 14).

The *TST*, reflecting the ecosystem size, was significantly greater at the eutrophic PAP site (3.37±0.25 mmol C m⁻² d⁻¹) compared to the oligotrophic CVAB site (2.34±0.04) (Table 14). Similarly, overall respiration rate and overall secondary production was significantly greater at PAP (respiration:

0.48 ± 0.040 mmol C m⁻² d⁻¹, 14% of *TST*; secondary production: 0.49 ± 0.023 mmol C m⁻² d⁻¹, 15% of *TST*) compared to CVAB (respiration: 0.15 ± 0.014 mmol C m⁻² d⁻¹, 6% of *TST*; secondary production: 0.13 ± 0.007 mmol C m⁻² d⁻¹, 6% of *TST*), both in absolute terms and relative to *TST*. In contrast, overall C ingestion was similar between sites (1.00 ± 0.076 mmol C m⁻² d⁻¹ and 0.89 ± 0.015 mmol C m⁻² d⁻¹ for PAP and CVAB respectively), but relatively greater at CVAB comprising 38% of *TST* compared to 30% of *TST* at PAP (Table 13).

Unicellular organisms dominated overall respiration at both sites (74% and 90% of overall respiration at PAP and CVAB respectively) (Table 14). Even though the absolute C remineralisation flux by Foraminifera was similar between sites (0.089 ± 0.011 and 0.11 ± 0.014 mmol C m⁻² d⁻¹ at PAP and CVAB respectively), Foraminifera were dominant at CVAB (73% of overall respiration), whereas prokaryotes were dominant at PAP (56% of overall respiration). The relative contribution of meiofauna to overall respiration was similar between sites (9% and 8% at PAP and CVAB respectively). However, meiofauna dominated faunal respiration at CVAB (80%), whereas macrofauna dominated faunal respiration at PAP (65%). At both sites, megafauna contributed <0.01% to total C remineralisation rates (Table 14).

Meiofauna and macrofauna dominated secondary production at PAP (38% and 39% respectively) with Foraminifera playing a more minor role (9%), whereas Foraminifera and Meiofauna dominated secondary production at CVAB (48% and 25% respectively) with macrofauna playing a more minor role (4%) (Table 14). Prokaryotes (13% and 22% at PAP and CVAB respectively) and megafauna (0.8% and 0.4% at PAP and CVAB respectively) had somewhat similar relative contributions to secondary production between sites.

Interestingly, megafauna dominated C ingestion heavily at CVAB (0.53 ± 0.003 mmol C m⁻² d⁻¹ which is 59% of total C ingestion) compared to having only a minor role at PAP, both in absolute (0.006 ± 0.0006 mmol C m⁻² d⁻¹) and relative (0.6%) terms (Table 14). As megafauna only played a minor role in overall respiration and secondary production, this indicates a lot of organic carbon is potentially being defecated instead of being assimilated across the gut wall. Figure 7 shows megafaunal deposit feeders at CVAB ingested a large amount of labile and semi-labile detritus, causing their trophic level to be much lower compared to PAP where megafauna deposit feeders had a greater relative ingestion to other organisms (prokaryotes, foraminifera, meiofauna) and thus a higher trophic level. This indicates some benthic organisms play an important role in reworking the deposited organic carbon to allow availability to other food-web compartments. A closer inspection of flows shows that megafaunal deposit feeders took up 0.03 mmol C m⁻² d⁻¹ of labile detritus and 0.50 mmol C m⁻² d⁻¹ of semi-labile detritus and defecated 0.40 mmol C m⁻² d⁻¹ into the semi-labile detritus pool (75%) and 0.13 mmol C m⁻² d⁻¹ into the refractory detritus pool (25%). To put this into perspective, the total C influx at CVAB was only 0.18 mmol C m⁻² d⁻¹, meaning the majority of intake was recycled material i.e., defecated material and deceased other organisms. The redirection of organic C to the refractory pool allowed the high observed dissolution rate to dissolved organic matter (0.25 mmol C m⁻² d⁻¹), which, in turn, was needed to sustain the high respiration and secondary production rates of Foraminifera (Table 14).

Burial rates are included as equalities (i.e., a single value), and were a magnitude greater at PAP (0.03 mmol C m⁻² d⁻¹) compared to CVAB (0.003 mmol C m⁻² d⁻¹). The difference in burial efficiency, i.e., burial flux relative to total deposition was less extreme, with 1.7% of incoming C being buried at CVAB, and 5.1% of incoming C being buried at PAP (Table 14).

Trophic efficiency

The efficiency of energy distribution was found to be significantly greater at CVAB, where a single unit

of C travelled 36% further through the food web compared to PAP due to recycling processes (*FCI* in [Table 14](#)). This was also reflected in the significantly higher relative ascendancy at CVAB (0.53 ± 0.01), which indicated greater efficiency in energy processing and resistance against external disturbances, compared to PAP (0.44 ± 0.02). The *AMI* was not significantly different between the sites (2.18 ± 0.06 and 2.06 ± 0.03 for PAP and CVAB respectively), indicating they had similar levels of flow specialisation ([Table 14](#)).

The synergism index was significantly lower at PAP (3.16 ± 0.13), indicating more competition and predation pressure compared to the CVAB (4.41 ± 0.09). The higher system trophic level at CVAB (2.14 ± 0.036) compared to the PAP (2.07 ± 0.027) and mostly attributed to the higher trophic levels of macrofauna ([Figure 7](#)), also supported greater trophic efficiency at CVAB. The higher omnivory index at CVAB (0.20 ± 0.017) indicated a great variety in diet than the food-web compartments at PAP (0.14 ± 0.014) ([Table 14](#)).

The overall community PB-ratio at CVAB was significantly lower (0.013 ± 0.0007) compared to at the PAP (0.019 ± 0.0009) ([Table 14](#)). As there was no significant difference in PB-ratios of Foraminifera, macrofauna, and megafauna between the two sites, the overall difference in PB-ratio was caused by differences in the prokaryotic and meiofaunal compartment ([Table 14](#)).

2.3 Discussion

Case study 1 compares three different sites in the North Atlantic: the Porcupine Abyssal Plain (PAP), a northern site in the Cabo Verde Abyssal Basin (CVAB) studied during the EUMELI project which data is used in our model, and a more southern site in the CVAB visited during the iMirabilis2 expedition and examined using a Benthic Respirometer Lander (BCL) ([Figure 3](#)). The PAP is considered eutrophic, with a Net Primary Productivity (NPP) $1,998.2 \text{ mg C m}^{-2} \text{ d}^{-1}$ (Oregon State University, 2019²). The CVAB is generally considered oligotrophic, which corresponds to the lower estimated NPP of $317.9 \text{ mg C m}^{-2} \text{ d}^{-1}$ and $483.1 \text{ mg C m}^{-2} \text{ d}^{-1}$ for CVAB (north) and CVAB (south) respectively (Oregon State University, 2019). However, surface NPP does not translate directly to seafloor POC flux at the same location, due to lateral transport of materials, offsetting the origin of POC and the deposition site by many kilometres (Burd et al., 2010; Pelegrí et al., 2017). Therefore, modelled seafloor POC deposition is $1.9 \text{ mg C m}^{-2} \text{ d}^{-1}$ for PAP, $1.0 \text{ mg C m}^{-2} \text{ d}^{-1}$ for the northern CVAB site, and a much higher deposition of $2.6 \text{ mg C m}^{-2} \text{ d}^{-1}$ at the southern CVAB site (Sweetman et al., 2017), i.e., deviating from the pattern expected from NPP alone. This deviation may be caused by (seasonal) westward currents bringing material from Western Africa and the Cabo Verde islands (Pelegrí et al., 2017). Unfortunately, no direct seafloor POC deposition measurements are available for the lander region to ground truth modelled values. The *in-situ* results, as discussed below, do support the hypothesis that the CVAB lander region is not a strictly oligotrophic abyssal site, and form at least a transition zone between an oligotrophic to mesotrophic regime.

Abyssal macrofaunal assemblages in Cape Verde were dominated by annelids and peracarid crustaceans and mirrors the overall composition of the abyssal plain in other Atlantic regions (Ingels et al., 2021; Levin and Gooday, 2003). Together, annelids and crustaceans comprised over 60% of the Cape Verde abyssal macrofauna, with polychaetes representing the dominant taxa and contributing over 50% of the total macrofaunal abundance. The macrofaunal composition in Cape Verde was similar to the more eutrophic PAP in the NE Atlantic, where polychaetes and crustaceans showed the same

² <https://sites.science.oregonstate.edu/ocean.productivity/index.php>

composition pattern. In relation to crustaceans, they followed the distribution pattern previously described for the abyssal zones of the Gulf Stream including the oligotrophic Sargasso Sea, where Tanaidacea was the dominant group, that was in greater abundance than the Amphipoda, which dominates the upper slope (Sanders et al., 1965). Comparing macrofauna abundance between the more oligotrophic CVAB and eutrophic PAP, showed that macrofauna density at CVAB (506 ± 266 [SD] ind. m^{-2}) was higher than the macrofauna density at PAP (376 ± 198 [SD] ind. m^{-2}) (Aberle and Witte, 2003). However, macrofaunal biomass was six times higher at PAP ($120 \text{ mg C } m^{-2}$) compared to CVAB ($21 \text{ mg C } m^{-2}$). The lower biomass despite higher densities indicate macrofauna at CVAB are smaller in size. This contributes to the hypothesis that smaller organisms dominate in low POC flux environments (Smith et al., 2008) and could thus indicate one possible outcome if POC flux declines due to climate change.

Our *in situ* data from the lander region showed a higher (2-fold) abundance of macrofauna when compared to previous assessments at other localities of the oligotrophic CVAB (100–232 ind. m^{-2} ; (Cosson et al., 1997; Sibuet et al., 1989), and it was higher compared to other Atlantic abyssal plains such as the oligotrophic Sargasso Sea (30–130 ind. m^{-2} ; (Sanders et al., 1965), the abyss beneath the Gulf Stream (150–270 ind. m^{-2} ; (Sanders et al., 1965)), the New England abyssal plain (175 ind. m^{-2} ; (Rowe et al., 1974)), and the Porcupine Seabight (420 ind. m^{-2} ; (Sibuet et al., 1989)). These findings suggest a higher input of organic matter to the abyssal benthos in the region we studied than was predicted by pelagic ocean productivity datasets. Lateral and downslope transfer of organic matter to the abyss (as suggested by the presence of macroalgal material in the chambers and benthic camera data, see below) could be supporting a higher macrofaunal abundance in our study region of the CVAB. The dominance of surface and sub-surface deposit feeders in the upper 5 cm of the sediment on the CVAB was typical for other abyssal basin regions including the eutrophic NE Atlantic. For example, Paterson et al. (1998) also observed abundant deposit-feeding assemblages at the Tagus Abyssal Plain and the Cape Verde Abyssal Basin (4,800 m depth). The macrofaunal composition was similar to the findings from the PAP study conducted by Aberle and Witte (2003), albeit without representatives of the family Cirratulidae. The dominance of surface deposit-feeders additionally supports the fact that CVAB may not be as oligotrophic as was originally proposed (Hessler and Jumars, 1974), and it is possible that this zone is a transition area between the mesotrophic and oligotrophic zone.

Total macrofaunal biomass ($66 \pm 62 \text{ mg DM } m^{-2}$ [SD]) was 3-fold higher than previous estimates for the CVAB (10–20 $\text{mg DM } m^{-2}$; Sibuet et al., 1989) again consistent with a higher POC flux location, but lower compared with other Equatorial Atlantic abyssal zones such as Demerara abyssal plain (90 $\text{mg DM } m^{-2}$; Sibuet et al., 1984) and the Vema Fracture Zone (80 $\text{mg DM } m^{-2}$; Khripounoff et al., 1980), which also exhibited higher macrofaunal densities than CVAB (1,196–2,159 ind. m^{-2} and 860 ind. m^{-2} respectively (Khripounoff et al., 1980; Sibuet et al., 1984)). It is well known that while macrofaunal abundance decreases with depth, meiofaunal communities continue to be significant, however, in terms of biomass, macrofauna remain more important than meiofauna at abyssal depths (Levin and Gooday, 2003). In contrast to this general trend, meiofaunal biomass (99.1 ± 45.6 [SE] $\text{mg DM } m^{-2}$) at the CVAB lander sites were greater than macrofaunal biomass. The strong interdependence between both groups, which are closely linked by numerous types of interactions, is evident in the Cabo Verde and Demerara abyssal basins, where there is a strong correlation between meiofaunal and macrofaunal biomass (Sibuet et al., 1989). The vertical distribution of macrofaunal biomass was very similar to the vertical distribution of the abundance, with the highest values reported for the surficial sediments, decreasing below 5 cm depth (Aberle and Witte, 2003; Sweetman and Witte, 2008). On the CVAB, not

only was the total abundance in the 0–5 cm sedimentary horizon higher (86%) compared to the PAP (80%), but also the biomass was higher (90%) for the same horizon compared to the PAP (Aberle and Witte, 2003).

As the methodology employed in this study was largely consistent with the methodology used in Witte et al. (2003) (with the exception of the pulse amount), we compared the same measured ecosystem characteristics between both sites (Figure 8). Witte et al. (2003) reported a bacterial biomass at the PAP for the 0–10 cm sediment horizon of 2.5 g C m^{-2} , which was much greater than the estimated bacterial biomass at the CVAB for the 0-5 cm sediment horizon (27.5 mg C m^{-2}). The alternative bacterial biomass of 92.6 mg C m^{-2} estimated from cell counts by Eardly et al. (2001) for the 0-5 cm sediment horizon at PAP and conversion factor by Fukuda et al. (1998) was the same order of magnitude, but still more than three times the bacterial biomass estimate on the CVAB based on PLFA concentrations. Cell counts might not be appropriate to estimate bacterial biomass, as it has been theorised that many benthic bacterial cells are actually fall-out from the water column and dormant i.e., not metabolically active nor contributing to ecosystem functioning (Amano et al., 2022).

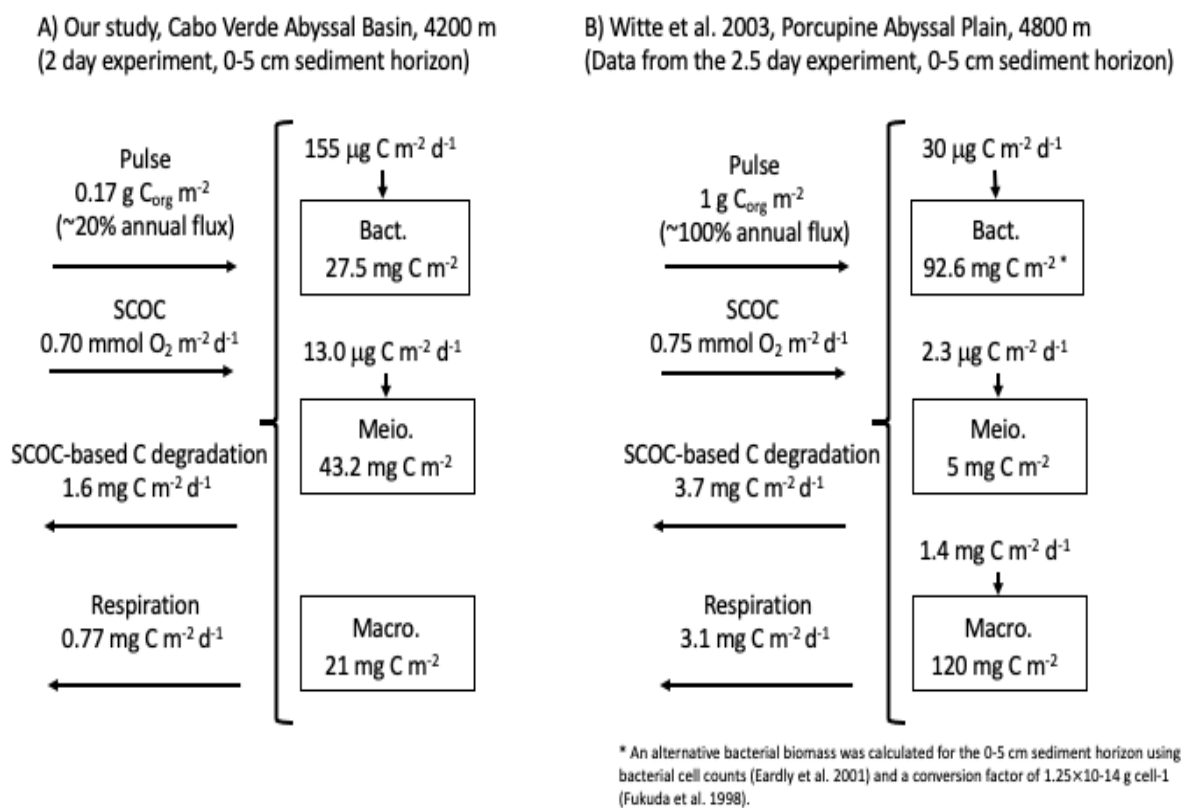


Figure 8. Comparison between ecosystem functioning at the Cabo Verde Abyssal Basin and the Porcupine Abyssal Plain based on in situ experimental data. These two datasets are the only studies of its kind in the Atlantic Ocean to compare, but it should be acknowledged they occurred over 20 years apart.

Abyssal bacterial biomass estimated from PLFA biomarkers across the oligotrophic Clarion-Clipperton Zone (CCZ, tropical Pacific) was lower (ranging from 1.35 to 3.25 mg C m^{-2} , Cecchetto et al., 2023) than the CVAB, which suggests that the CVAB region studied here was functioning as a mesotrophic, rather than oligotrophic area. However, while bacterial biomass at the CVAB was lower, bacterial processing of phytodetrital-derived C was five-fold greater at CVAB ($0.155 \text{ mg C m}^{-2} \text{ d}^{-1}$) compared to PAP (0.030

mg C m⁻² d⁻¹) despite much less organic C being supplied to the sediment (Figure 8). However, after 1-wk *in situ* experiment, the bacterial C processing rate at PAP became similar to our study (0.124 mg C m⁻² d⁻¹). Bacterial C processing rates were a magnitude greater compared to the abyssal oligotrophic CCZ, where they ranged from 0.01 to 0.02 mg C m⁻² d⁻¹ (Cecchetto et al., 2023). The combination of lower bacterial biomass but greater bacterial C processing rates at CVAB, indicated that initial bacterial processing efficiency (i.e., per unit biomass) was greater at the more oligotrophic CVAB (0.0056 d⁻¹) compared to at the PAP (0.0003 d⁻¹). Even when compared to delayed bacterial processing efficiency at PAP (0.0013 to 0.0019 d⁻¹ for 8 and 23 days respectively), the bacterial processing efficiency was greater at CVAB. This suggests that declining productivity caused by climate change could lead to a reduction in bacterial biomass, and an increase in bacterial C-processing efficiency.

At CVAB, both the meiobenthic biomass (43.2 mg C m⁻²) and C-cycling rate (13.0 µg C m⁻² d⁻¹) was greater compared to the PAP (5 mg C m⁻² biomass and 2.3 µg C m⁻² d⁻¹) (Figure 8). Per unit biomass C cycling efficiency was similar between the sites (0.0003 d⁻¹ and 0.0005 d⁻¹ for CVAB and PAP respectively). There was a delayed response by the Nematoda to C-cycling at PAP and it reached 16.8 µg C m⁻² d⁻¹ (similar to the CVAB value) only after 23 days. The Nematoda C-cycling efficiency also increased over time at the PAP (0.0011 d⁻¹ and 0.0034 d⁻¹ at 8 and 23 days, respectively). Witte et al. (2003) used the C-uptake into the Nematoda that were retained on a 63-µm sieve as a proxy for overall meiofaunal C cycling. In contrast, we used a 32-µm mesh sieve and included all meiobenthos but excluded the Foraminifera. At PAP, Nematoda comprised 93% of meiobenthic density retained on a 32-µm mesh sieve (Galéron et al., 2001), compared to 82.7% on the CVAB (this study). Therefore, using Nematoda as a proxy for overall meiobenthic biomass at PAP may not cause a major underestimation of meiofaunal biomass. However, the difference in mesh size might have caused an underestimation of Nematoda biomass in the Witte et al (2003) study. Converting the PAP meiobenthic densities in Galéron et al. (2001), which used the same mesh size as our study to meiobenthic C standing stock using the conversion factors from de Jonge et al. (2020) leads to a meiobenthic biomass at PAP of 67.4 mg C m⁻² – a far greater estimate compared to CVAB. Using this alternative biomass estimate for PAP reduces the meiobenthic C cycling efficiency to 3×10⁻⁵ d⁻¹, 8×10⁻⁵ d⁻¹, and 0.0003 d⁻¹ for 2.5, 8 and 23 days respectively, indicating greater meiofaunal C-cycling efficiency at the CVAB compared to the PAP.

Consistent with the *in situ* benthic ecosystem function results, LIM model analysis showed greater C-cycling efficiency at the CVAB compared to the PAP. The ecosystem size (expressed as the Total System Throughflow of C) at the CVAB ($TST = 2.34 \text{ mmol C m}^{-2} \text{ d}^{-1}$) was 69% of the ecosystem size at the PAP ($TST = 3.37 \text{ mmol C m}^{-2} \text{ d}^{-1}$). Thus, as food supply to the seafloor decreases due to climate change, differences in food-web organisation and flows will possibly force the system to use the available C more efficiently and have a relatively large *TST* compared to the total C influx. Bacteria and meiofauna have been shown to be twice as efficient in exploiting POC supply in the eastern Mediterranean Sea that receives tenfold less POM compared to the western side, potentially allowing the higher observed biomass than what would be expected from food availability alone (Danovaro et al., 1999). On the more oligotrophic CVAB, the community biomass production efficiency (PB-ratio) modelled by the LIM was lower compared to the PAP, which was caused by lower PB-ratios of the prokaryotic and bacterial components since the relative dominance of smaller organisms reduces the efficiency of biomass production (Smith et al., 2008).

The expected dominance of smaller organisms at the CVAB (Rex et al., 2006; Smith et al., 2008) was clearly observed in the model data, with unicellular organisms dominating total respiration (90% at CVAB vs. 74% at PAP) and total secondary production (70% at CVAB vs. 22% at PAP). Similarly, at CVAB

meiofauna played a large role in faunal respiration (80%) and faunal secondary production (85%), whereas macrofauna dominated faunal respiration (65%) and secondary production (51%) at PAP – results that show how climate change may impact abyssal Atlantic ecosystems.

A reduction in the efficiency of energy transfer to higher trophic levels was not evident in our results for the CVAB. Instead, the CVAB system was more efficient at recycling C (a unit of C was recycled 56% compared to only 20% at PAP as indicated by the *FCI* Finn (1976)). The increased C cycling efficiency was facilitated by a more tightly organised network, as indicated by the relative ascendancy, which means that there was less loss of energy through unorganised flows like respiration, import, export, and parallel pathways (Tobor-Kapłon et al., 2007). This is supported by the lower absolute and relative respiration rates modelled at CVAB compared to PAP. Overall, the community trophic level was greater at the CVAB, which is indicative of greater trophic transfer efficiency overall (Post, 2002). Also contrary to expectations (Campanyà-Llovet et al., 2017), competition for resources appeared lower at the CVAB as the synergism index indicated a greater proportion of positive interactions compared to at the PAP. The greater omnivory index, which indicated a wider variety in diet, and greater *TLs* indicative of vertical niche expansion (Iken et al., 2001) may explain the reduced competition at the CVAB. A study looking at megafauna in the Mediterranean Sea found no clear pattern of trophic niches from the oligotrophic east to the more eutrophic west side, nor evidence for niche specialisation that would reduce resource competition (Tecchio et al., 2013). Megafauna did however have a higher *TL* in the western Mediterranean compared to the oligotrophic eastern side (Tecchio et al., 2013), which was also observed in our model (Figure 7). The difference in overall community *TL* between our models was mostly caused by the macrofauna, which had higher *TLs* on the CVAB relative to the PAP (Figure 7).

In our models, bacteria dominated C cycling at PAP consistent with the results of the other PAP models (Durden et al., 2017; van Oevelen et al., 2012). Bacteria have been shown to play a dominant role in C cycling in the abyssal Peru Basin (de Jonge et al., 2020; Stratmann et al., 2018) and the eastern CCZ (Cecchetto et al., 2023; Stratmann, 2023; Sweetman et al., 2019), but these studies excluded Foraminifera. While the CVAB model showed that prokaryotes and metazoan meiofauna were important in the food-web at CVAB, the CVAB model also showed that Foraminifera played a more dominant role than prokaryotes in C-cycling. The C cycling by Foraminifera was so large in fact that the model could not be resolved without an additional C input as well as POC flux. The Foraminifera biomass in the model (28.9 mg C m⁻² for CVAB) was conservative as it only comprised the 0-1 cm sediment horizon, >250 µm size fraction, omitted the reported high abundance of xenophyophores (Sibuet et al., 1993), and we used a biomass conversion factor 10-fold lower than has been previously published (Ahrens et al., 1997). The conservative biomass estimates of the >300 µm size fraction Foraminifera in the CVAB lander region was an order of magnitude smaller at 1.5 mg C m⁻². Thus, interestingly, the estimated C stock of large Foraminifera was approximately 7% of macrofauna biomass at the more mesotrophic CVAB lander region, but almost 9 times greater than macrofauna biomass at the more oligotrophic CVAB region. It is clear that future studies need to start properly and consistently including this group in abyssal ecosystem studies as suggested by others (de Jonge et al., 2020; Gooday et al., 2020; Ingels et al., 2020; Stratmann, 2023).

Macrofaunal biomass was six times higher at PAP (120 mg C m⁻²) compared to the CVAB lander region (21 mg C m⁻²) (Table 14). The macrofauna biomass used in the CVAB model, i.e. in the more northern region, was an order of magnitude smaller at 3.3 mg C m⁻². Macrofauna from PAP were initially responsible for the highest C cycling rate (1.47 mg C m⁻² d⁻¹) and C-cycling efficiency (0.012 d⁻¹), though both decreased over time (PAP macrofaunal C cycling was 0.27 mg C m⁻² d⁻¹ at day 8 and 0.009 C m⁻² d⁻¹).

¹ at day 23 leading to a C cycling efficiency of 0.002 d⁻¹ at 8 days to 0.0008 d⁻¹ at 23 days). We still have yet to receive the stable isotope data for the CVAB macrofaunal analysis so cannot directly compare the PAP macrofaunal C-uptake rates with those from the CVAB.

Despite differences being observed in the *in situ* bacterial and meiofaunal C-cycling rates between sites and greater C-cycling efficiencies being observed in the *in-situ* and modelled data from the CVAB, overall metabolic activity measured as SCOC was similar between sites: 0.70 mmol O₂ m⁻² d⁻¹ and 0.75 mmol O₂ m⁻² d⁻¹ at the CVAB and PAP, respectively. However, overall degradation of phytodetrital derived C, based on background-corrected SCOC was greater on the PAP at 3.7 mg C m⁻² d⁻¹ compared to 1.6 mg C m⁻² d⁻¹ on the CVAB. The estimated total phytodetritus turnover rate of 0.0092 d⁻¹ on the CVAB was similar to the mesotrophic eastern Clarion-Clipperton Zone (CCZ) of the Pacific Ocean at 0.012 d⁻¹ (Sweetman et al., 2019), but greater than the estimated turnover rate at PAP (0.0048 d⁻¹) and the oligotrophic western CCZ (0.0042 d⁻¹) (Cecchetto et al., 2023). Respiration of phytodetritus derived-C (i.e., the amount of ¹³C that was transferred into the DIC pool) was four times greater at PAP (3.1 mg C m⁻² d⁻¹) compared to CVAB (0.77 mg C m⁻² d⁻¹). Respiration of C into the DIC pool on the CVAB was similar to the western CCZ, ranging from 0.51 to 0.75 mg C m⁻² d⁻¹ (Cecchetto et al., 2023). Comparison of overall respiration and degradation rates shows that the PAP is more of a respiration-dominated ecosystem, with 83%-85% of degradation being transferred into respiration flux, compared to the CVAB where active faunal uptake is present and only 49% of the degradation process is respiration (Woulds et al., 2009).

Nutrient fluxes were highly variable at the CVAB, but some general trends were observed. For example, ammonium efflux was observed in the background incubation. During the tracer experiment, ammonium efflux was reduced in one tracer experiment, and reversed to ammonium influx in all the remaining tracer experiments. Additionally, nitrate efflux out of the sediment was consistently larger in the tracer incubations compared to the background incubation. This pattern of increased ammonium influx and nitrate efflux may indicate chemoautotrophy (e.g., nitrification) occurring in abyssal sediments as previously observed in the mesotrophic eastern Pacific (Sweetman et al., 2019).

The model and *in situ* results from two sites in different trophic regimes indicate that a reduction in the quantity of POC quantity as predicted for most of the Atlantic abyssal systems under climate change (Sweetman et al., 2017), will lead to reduced C cycling, remineralisation, and secondary production rates, and there will be a shift to C-cycling processes being dominated by smaller multicellular and unicellular organisms. There was no significant difference in *AMI* between the two studied systems, indicating both the CVAB and PAP system have reached the same level of ecosystem development. In combination with the network indices showing efficient use of energy at CVAB, it appears that the CVAB system has successfully adapted to the reduced food availability i.e., the system does not appear permanently stressed or under pressure due to the more oligotrophic regime found here. However, as the energy efficiency found in the CVAB ecosystem is likely a result of a long period of adaptation, abyssal systems experiencing a relatively sudden drop in POC quantity and quality (i.e., over decades compared to evolutionary time scales) will possibly not respond similarly nor initially function in the same way as the CVAB. The ability of species and ecosystems to adapt at the rate of climate change is an ongoing point of discussion, see, e.g., Catullo et al. (2019). In fact, the relative ascendancy index, which is a proxy for resistance against external disturbances (Tobor-Kapton et al., 2007) is higher at CVAB. This means that eutrophic systems like PAP, which have not developed food-web structures to cope with low food availability, may be more vulnerable to climate change than already food-limited abyssal systems.

3. Case study 2 – Soft sediment ecosystem functioning at the Cabo Verde upper bathyal slope compared to other oceanic regions.

3.1 Materials & Methods

Study site

Continental slope sediments were collected during the iMirabilis2 research expedition on B/O *Sarmiento de Gamboa* to Cabo Verde (Tropical East Atlantic Ocean) in August 2021. A 'KC Denmark' multi-corer (MUC) sampled 6 cores (inner diameter 9.5 cm) of sediment per deployment from a depth of 874-876 m depth between the islands Santiago and Maio at 15.3165° N, 23.3691° W (Figure 9). A CTD profile at the site showed a bottom water (10 m.a.b.) temperature of 6.83°C and an oxygen concentration of 109 $\mu\text{mol L}^{-1}$ (Orejas et al., 2022). The CTD profile showed the sediments were sampled at the lower boundary of the oxygen minimum zone which occurred around 500 m (Figure 10).

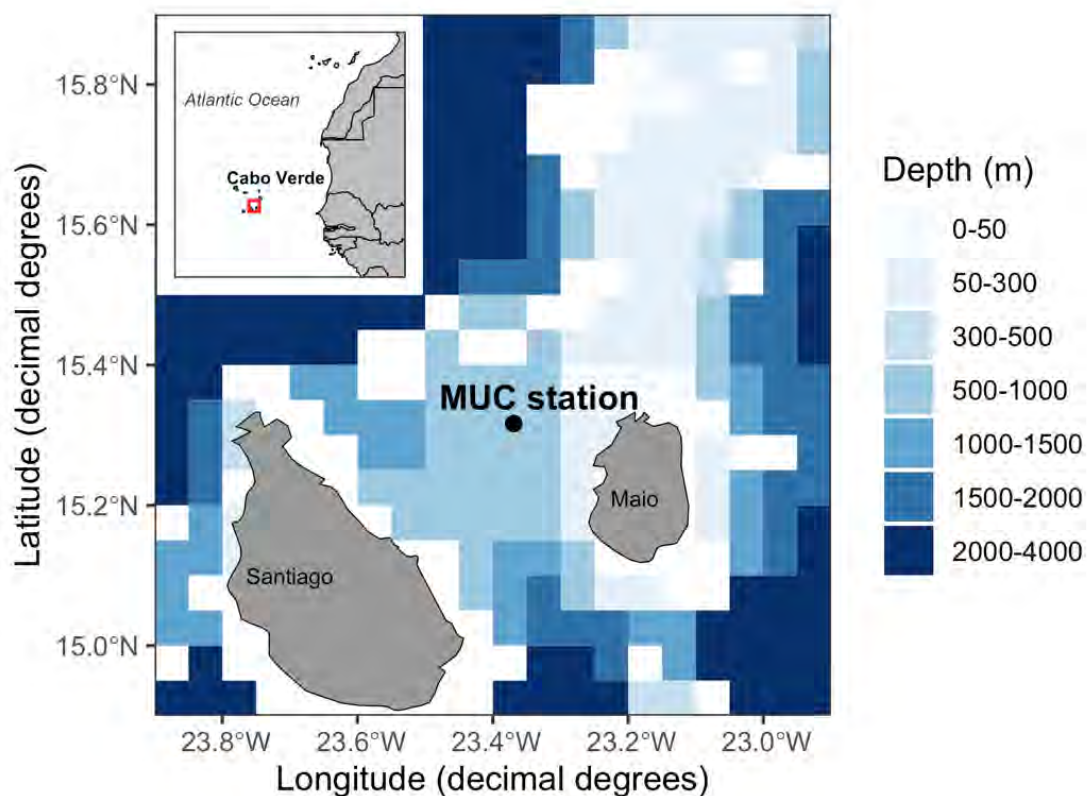


Figure 9. Sampling station where multicores (MUC) were obtained for the ex-situ multistressor experiment.

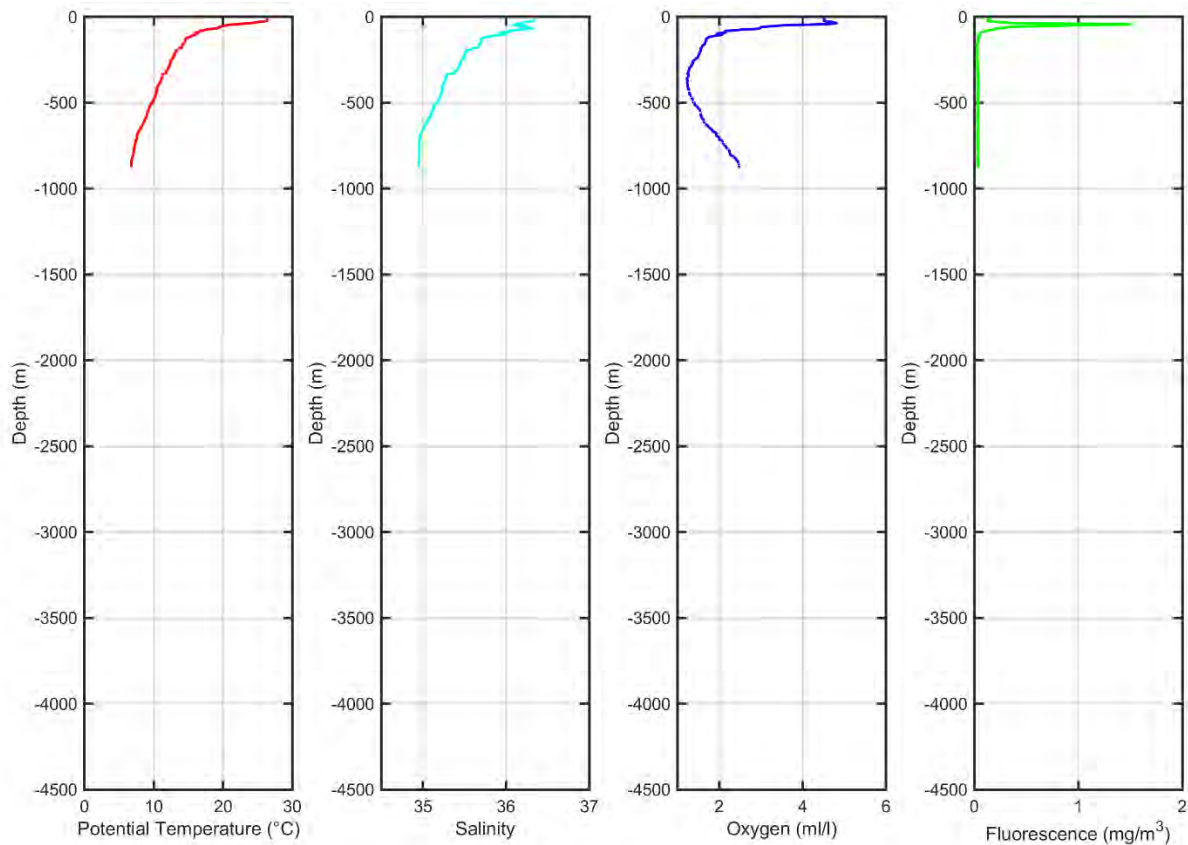


Figure 10. CTD data for the MUC sampling station (credit: Angela Mosquera-Gimenez, iMirabilis2).

Incubations

From the four MUC deployments, four cores with clear overlying water were randomly divided among two treatments, which included cores ($n=4$) held at the *in-situ* temperature of 6.5°C and cores ($n=4$) exposed to 8.5°C to assess the effect of a 2°C increase in temperature (Figure 11). The four cores assigned to each treatment came from 4 separate MUC deployments to maintain independence of replicates. The core topwater was siphoned off into a clean container, and 15–18 cm of sediment was extruded for transfer to an incubation core (inner diameter 10 cm). Once transferred, the top water was trickled back into the incubation core while minimising sediment disturbance. If necessary, the overlying water was topped off with filtered (5 μm) seawater collected by CTD and cooled to 6.5°C. Additionally, three additional cores were taken from three other MUC deployments and processed directly. These additional cores were extruded and sliced into 0–2 cm and 2–5 cm sediment horizons. A quarter of each slice was transferred to a 50 ml Falcon tube and stored at -80°C for PLFA analysis. Another half of the slice was transferred to a 500 ml HDPE bottle and fixed in 10% formalin for macrofauna analysis.

The incubation cores were placed in buckets with filtered seawater (already at the two experimental Temperatures) and placed into two LMS cooled incubators (series 3, model 300W, 290 L). The moment of placement in the incubator was considered $T_{0\text{-hr}}$ (0 hours). The cores were periodically incubated over a period of 1 week before a 24-hr stable isotope pulse chase experiment was started. During this 1-week equilibration period, a Sediment Community Oxygen Consumption (SCOC) measurement was conducted for each core at four points in time ($T_{60\text{-hr}}$, $T_{85\text{-hr}}$, $T_{95\text{-hr}}$, and $T_{125\text{-hr}}$). Every 24 hours throughout the study, the cores were topped off with fresh filtered seawater maintained at the experimental

temperature to partly flush built-up metabolites from the overlying water. Chamber waters were allowed to exchange and overflow each chamber into the surrounding water bath (that was periodically emptied), which maintained the independence of replicates. With the exception of when a core was being incubated for SCOC measurements, an air stone connected to an aquarium pump was always placed in the top 10 cm of water in each core to oxygenate the water.

For SCOC measurements, the cores were sealed and stirrers and FireSting oxygen optodes placed into the water overlying the core sediments (Figure 11). The stirrers created a gentle current in the chambers which maintained a sufficiently thin diffusive boundary layer. The FireSting optodes were calibrated before the start of the experiment using unfiltered seawater at 36 PSU at the experimental temperatures (regulated using a Thermo NesLab RTE17 Digital One water bath) at 100% and 0% saturation, achieved by bubbling the water with air and nitrogen respectively for >15 minutes. The temperature of the cores was assumed to be equal to the temperature of the surrounding water bath, as measured with an external thermometer connected to the FireSting logger. Oxygen optodes were allowed to measure the change in oxygen concentration in the cores for 8 to 9 hours. After the incubation, the core lids were removed, and the air stone returned to re-oxygenate the overlying water until the next measurement interval.

To assess the rate of C-cycling by bacteria and macrofauna, a stable isotope tracer experiment was conducted after 1 week. Each core was exposed to 12.5 mg of isotopically labelled freeze-dried *P. cornutum* (identical labelling to case study 1) algae, corresponding to 0.44 g C m⁻² or 10% of the annual seafloor flux at the study site. To do this, we first hydrated them in filtered seawater at experimental temperature and then gently injecting them in the core topwater while gently stirring. The algae were allowed to settle for 1.5 hours without the air stone in the core, after which the air stones were replaced, and the cores were allowed to continue incubating for 2 days. Two additional SCOC measurements were undertaken at 10 and 45 hours into the algal incubation. Right before the SCOC measurement, and immediately after removing the core lid for SCOC measurements, a 20 ml water sample was taken for later DI^{13}C analysis. The water was transferred to a 12 ml extainer through a 45 μm cellulose acetate filter and preserved with 10 μl of HgCl solution. Two water samples were collected before the algal introduction to provide background DIC stable isotope information.



Figure 11. Set-up of the multi-stressor incubation experiment during a SCOC measurement interval. Sediment in cores, sealed at the bottom, are placed in buckets of water, and located in cooled incubators. The sealing lid carries the stirrer bar (white) and FireSting oxygen optodes (blue label). After the SCOC interval, the lid including stirrer and optode were removed, and an air stone was replaced to oxygenate the open core. Note that this image was taken shortly after sampling i.e. before the 1-week equilibration period, and the overlying water in some cores were somewhat cloudy.

Sample processing

To obtain SCOC rates, a linear regression was performed on the last 2–3 hours of oxygen optode data from each SCOC measuring interval, when the temperature was stable and change in oxygen concentration was linear. The change in oxygen concentration ($\mu\text{mol O}_2 \text{ L}^{-1} \text{ h}^{-1}$) was converted to seafloor community oxygen consumption rates ($\text{mmol O}_2 \text{ m}^{-2} \text{ d}^{-1}$) using the volume of overlying water and the surface area of the core. SCOC rates are also reported as $\text{mg C m}^{-2} \text{ d}^{-1}$ using a respiratory quotient of 1 (Glud, 2008). SCOC rates were compared to rates reported in the global SCOC database (Stratmann et al., 2019). The difference in SCOC rates between temperature treatments at each time point was tested using the two-sample test. The effect of temperature on the SCOC rate was calculated as a Q_{10} value, which represents the factor by which a certain rate increases for each 10°C degrees temperature rise: $Q_{10} = \left(\frac{R_2}{R_1}\right)^{\frac{10}{T_2 - T_1}}$, where R_1 and R_2 are the rates in the same units at temperature T_1 and T_2 in degrees Celsius.

Total DIC concentration was measured on the DIC samples in an Apollo Sci Tech AS-C5 DIC Analyser, and DIC- $\delta^{13}\text{C}$ on an elemental analyser coupled to an isotope ratio mass spectrometer (EA-IRMS, Flash 1112, DELTA-V, THERMO, see Maier et al. (2020)) at the Royal Netherlands Institute for Sea Research in Yerseke (the Netherlands). DIC production during the SCOC measurement interval resulting from respiration of the enriched algal substrate was determined from excess ^{13}C . This excess was calculated from reported DIC- $\delta^{13}\text{C}$ values: $E = F_{\text{sample}} - F_{\text{background}}$, where $F = \frac{R}{R+1}$ and $R = (1 + \delta^{13}\text{C}/1000) * R_{VPDB}$ ($R_{VPDB} = 0.0112372$). Excess ^{13}C was then converted to DIC production (mg C m^{-2}) using

the labelling of the injected algae (11.8 at%), seawater density of 1035 g/L, and the core surface area. The difference in DIC production before and after the SCOC measurement interval was used to calculate DIC production rates.

At the end of the incubations, the cores were sliced to obtain the 0–2 and 2–5 cm sediment horizons. A quarter of the sediment slice was preserved for Phospho-Lipid derived Fatty Acid (PLFA) analysis and stored at -80°C until processing. Half of the sediment slice was preserved for macrofauna analysis in 4% borax-buffered formaldehyde in a 500 ml HDPE bottle until further analysis. The density of macrofauna and the four replicates provided enough material for analysis of labelled stable isotopes. Reported density and biomass should be considered semi-quantitative, as the volume of material is lower and less well constrained than recommended for a fully quantitative analysis of abundance.

PLFA samples were freeze-dried, homogenised with a pestle and mortar, and processed at the James Hutton Institute in Aberdeen where bacterial fatty-acid markers were isolated. Bacterial biomass was determined using the biomarker C15:0i, which is a bacterial PLFA. Bacterial biomass in the 0–2 cm and 2–5 cm sediment horizon was calculated as $B = C_{C15:0i} / (F \times C_{PLFA})$, where B is the bacterial biomass in nmol C g⁻¹ dry sediment, $C_{C15:0i}$ is the concentration of the C15:0i marker in the sample in nmol g⁻¹ dry sediment, F is the average specific fraction of the C15:0i marker in bacterial dominated sediments (7.4%, Ise Bay (n=8), Rajendran et al. (1993)), and C_{PLFA} is the average concentration of PLFA in bacterial biomass (0.056 g C PLFA g⁻¹ C bacterial biomass, Brinch-Iversen and King (1990)). Biomass was then converted to mg C m⁻² using the thickness of the sediment horizon (in cm) and a Dry Bulk Density (DBD) of 2.50 g cm⁻³ and sediment porosity of 0.61 as measured from sediments on the West African slope at 2,375 m (Thiede et al., 1982). Differences in bacterial biomass between sediment layers could not be tested due to small sample size (n=2 and n=3 for the upper and lower sediment layer, respectively).

For bacterial C uptake, the d¹³C values for PLFA biomarker C15:0i in the different sediment horizons were used to calculate the excess ¹³(E) in the experimental sediment samples, as $E = F_{sample} - F_{background}$, where $F = \frac{R}{R+1}$ and $R = (1 + \delta^{13}C/1000) * R_{VPDB}$ ($R_{VPDB} = 0.0112372$). The excess ¹³C in total PLFA concentration of biomarker C15:0i reported in nmol ester g⁻¹ (dry sediment) was converted to overall C uptake by the benthic bacterial community (mmol C m⁻² d⁻¹), using the same F , C_{PLFA} , DBD and sediment porosity as for the bacterial biomass calculation, combined with the ¹³C labelling of the injected algae culture (11.8%), and the total incubation time of 2 days preserved macrofauna samples were washed over a 300 µm mesh sieve with filtered seawater, to remove the formaldehyde. The macrofauna was then preserved in 70% alcohol until taxonomic identification. Macrofaunal organisms were sorted from the sediment under a stereomicroscope, and identified to family taxonomic level for polychaetes, and to order for all other taxa. Polychaetes were also classified into feeding guilds according to Fauchald and Jumars (1979). The Cape Verde bathyal macrofauna community was studied for its taxonomic composition, diversity, abundance, and biomass, and was compared with other communities in the Atlantic Ocean.

3.2 Results

SCOC and DIC

Initial SCOC rates at T_{60-hr} were 23.4±1.5 mmol O₂ m⁻² d⁻¹ and 35.6±3.7 mmol O₂ m⁻² d⁻¹ for the 6.5°C and 8.5°C treatments respectively (Table 15, Figure 12). The difference between temperature treatments was not significant (two-sample t-test, p = 0.18). At T_{85-hr} the SCOC rates dipped, and no significant

difference between temperatures (two-sample t-test, $p = 0.23$) was observed. At $T_{95\text{-hr}}$ and $T_{125\text{-hr}}$, SCOC rates climbed back up and were almost significantly different at $T_{95\text{-hr}}$ (two-sample t-test, $p = 0.054$). At $T_{125\text{-hr}}$, the SCOC rate in the 8.5°C treatment ($28.3 \pm 1.8 \text{ mmol O}_2 \text{ m}^{-2} \text{ d}^{-1}$) was significantly higher (166%) than the 6.5°C treatment cores ($17.0 \pm 0.6 \text{ mmol O}_2 \text{ m}^{-2} \text{ d}^{-1}$) (Table 15, Figure 12).

Table 15. SCOC rates (mean \pm se, $n = 4$, $\text{mmol O}_2 \text{ mm}^{-2} \text{ d}^{-1}$) measured at various points in time after seafloor retrieval (Incubation time) at 6.5°C (current seafloor conditions) and 8.5°C (future temperature increase at the seafloor) during the equilibration period. Values in brackets are mean SCOC rates converted to $\text{mg C m}^{-2} \text{ d}^{-1}$. Significant differences ($p < 0.05$) in bold. The differences in rate between the two temperatures (and how much greater SCOC is for the warm temperature between brackets) is also given. The Q_{10} value was only calculated for the significant differences.

Incubation time (h)	6.5°C	8.5°C	SCOC	Q_{10}
60	23.4 ± 1.5 (281)	35.6 ± 3.7 (428)	12.1 ($\times 1.52$)	-
85	8.5 ± 0.2 (102)	9.7 ± 0.4 (117)	1.23 ($\times 1.14$)	-
95	11.5 ± 0.4 (138)	18.3 ± 1.4 (220)	6.8 ($\times 1.59$)	-
125	17.0 ± 0.6 (204)	28.3 ± 1.8 (340)	11.3 ($\times 1.66$)	12.8

During the incubation with algae at *in situ* temperature (6.5°C), the SCOC rate at 10 hours post injection was $15.3 \pm 0.72 \text{ mmol O}_2 \text{ m}^{-2} \text{ d}^{-1}$, and $10.1 \pm 0.43 \text{ mmol O}_2 \text{ m}^{-2} \text{ d}^{-1}$ at 45 hours, giving a mean SCOC of $12.7 \pm 1.06 \text{ mmol O}_2 \text{ m}^{-2} \text{ d}^{-1}$. At 8.5°C the SCOC rate also slightly decreased over time during the stable isotope tracer experiment, from $28.0 \pm 4.38 \text{ mmol O}_2 \text{ m}^{-2} \text{ d}^{-1}$ at T10 to $21.1 \pm 4.5 \text{ mmol O}_2 \text{ m}^{-2} \text{ d}^{-1}$ at T45 post injection. The SCOC rate during the stable isotope tracer experiment was almost significantly different between temperatures (Welch t-test, $p = 0.06$ at T10 and Welch t-test, $p = 0.09$ at T45).

The DIC production rate as a result of the injected algae at 6.5°C was $39.8 \pm 4.20 \text{ mg C m}^{-2} \text{ d}^{-1}$ at 10 hours post injection, and almost 8 times lower at 45 hours into the incubation ($5.16 \pm 1.20 \text{ mg C m}^{-2} \text{ d}^{-1}$). At 8.5°C , the DIC production rate was $42.5 \text{ mg C m}^{-2} \text{ d}^{-1}$ at 10 hours post injection and 6 times lower at 45 hours post injection ($6.89 \pm 0.31 \text{ mg C m}^{-2} \text{ d}^{-1}$). The difference between DIC production rates was not significant between temperature treatments 10 hours post injection (t-test, $p = 0.76$), but it was significantly different between temperatures 45 hours post injection (t-test, $p = 0.04$).

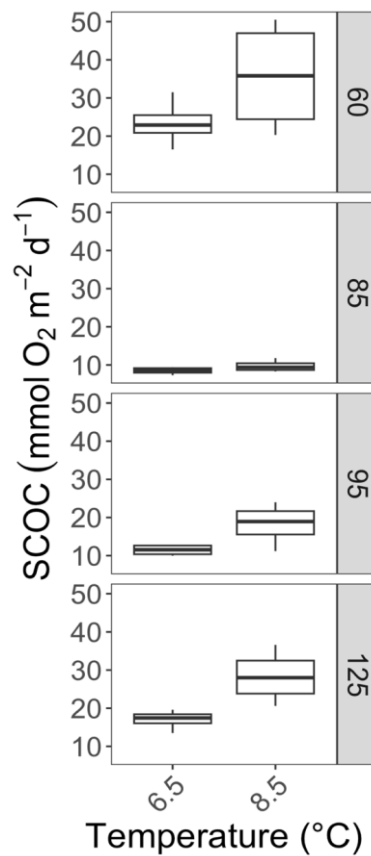


Figure 12. SCOC rates ($\text{mmol O}_2 \text{ m}^{-2} \text{ d}^{-1}$) at 60, 85, 95, and 125 hours into the equilibration period (i.e., before the algae injection) for the 6.5°C and 8.5°C temperature treatments ($n=4$ per treatment).

Bacterial standing stock and C cycling

Bacterial biomass in the unincubated cores was $35.2 \pm 11.1 \text{ mg C m}^{-2}$ ($2.93 \pm 0.93 \text{ mmol C m}^{-2}$) in the upper 2 cm of sediment, and $37.1 \pm 21.7 \text{ mg C m}^{-2}$ ($3.09 \pm 1.81 \text{ mmol C m}^{-2}$) for the lower 2 to 5 cm sediment horizon (Figure 13). Overall, the mean bacterial biomass in the 0-5 sediment layer of these cores was $60.6 \pm 12.8 \text{ mg C m}^{-2}$ ($5.04 \pm 1.06 \text{ mmol C m}^{-2}$). Bacterial biomass (0–5 cm) in the incubated cores at the end of the 48-hour experiment was $66.4 \pm 9.4 \text{ mg C m}^{-2}$ ($5.53 \pm 0.78 \text{ mmol C m}^{-2}$) for the 6.5°C treatment, which is similar to the unincubated cores (Figure 13). Bacterial standing stock was $136.5 \pm 16.9 \text{ mg C m}^{-2}$ ($11.4 \pm 1.4 \text{ mmol C m}^{-2}$) for the 8.5°C treatment (Figure 8), which was significantly greater (t-test, $p=0.01$) than the incubated cores (Figure 13).

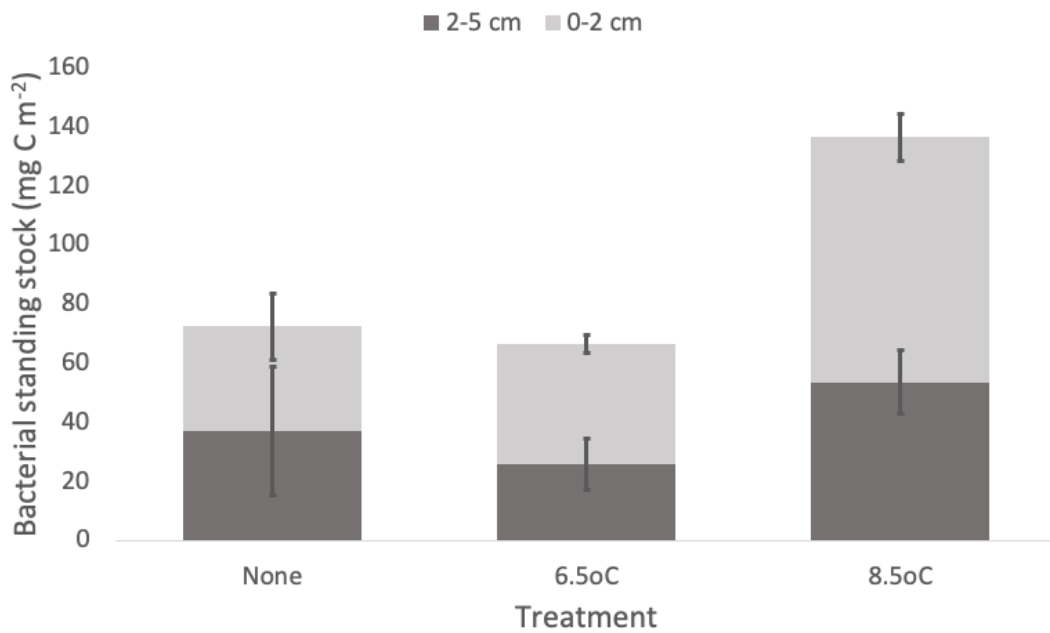


Figure 13. Bacterial standing stock (mg C m^{-2}) in the unincubated cores (Treatment = None, $n=3$) and in the incubated cores at either 6.5°C or 8.5°C after a 48-hour stable isotope tracer experiment with injected algae ($n=4$). Error bars represent 1 standard error.

Bacterial uptake of phytodetritus-derived C at 6.5°C was $0.265 \pm 0.138 \text{ mg C m}^{-2} \text{ d}^{-1}$ ($0.022 \pm 0.011 \text{ mmol C m}^{-2} \text{ d}^{-1}$), with only 1.1% occurring in the 2-5 cm sediment layer. (Figure 14). At 8.5°C bacterial uptake was $0.077 \pm 0.010 \text{ mg C m}^{-2} \text{ d}^{-1}$ ($0.006 \pm 8.6 \times 10^{-4} \text{ mmol C m}^{-2} \text{ d}^{-1}$), with 12% occurring in the 2-5 cm sediment layer (Figure 14). The difference between treatments was non-significant (Welch t-test, $p = 0.27$). The biomass-specific C uptake was an order of magnitude greater in the 6.5°C treatment ($0.00506 \pm 0.00152 \text{ d}^{-1}$) compared to the 8.5°C treatment ($0.00058 \pm 0.00008 \text{ d}^{-1}$), but the difference was not significant (Wilcoxon Mann-Whitney-U test, $p = 0.34$).

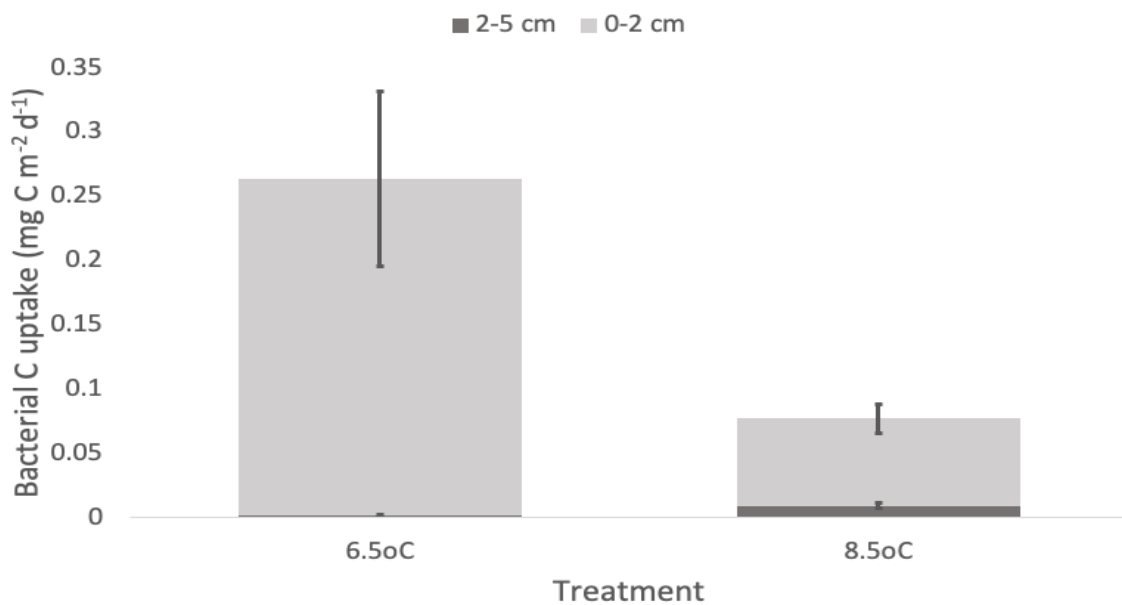


Figure 14. Mean bacterial phytodetritus-derived C uptake ($\text{mg C m}^{-2} \text{ d}^{-1}$) at 6.5°C and 8.5°C after a 48-hour stable isotope tracer experiment with injected algae ($n=4$). Error bars represent 1 standard error.

Macrofaunal diversity and biomass

The mean macrofaunal density in the sediments was $5,384 \pm 2,523$ ind. m^{-2} (SD, $n=7$). The polychaetes were the dominant taxa representing 51% of the total abundance, followed by macrofaunal-sized nematodes (34%), while crustaceans and ribbon worms were less abundant contributing 9% and 5%, respectively (Figure 15a). A total of 13 families of Polychaeta were identified from the cores, where the surface and subsurface deposit feeders (Capitellidae: 52%, Maldanidae: 20%, and Oweniidae: 7%) dominating (Figure 15b). Three orders of crustaceans were found. The Tanaidacea was dominant and represented 72% of the Crustacea abundance, followed by Isopoda (21%) (Figure 15c).

Mean macrofaunal biomass was 427 ± 223 mg DM m^{-2} ($n=7$). The Polychaeta contributed 81% to overall biomass, while macrofaunal sized nematodes and crustaceans contributed 9% and 7% respectively (Figure 15a). However, within the polychaetes, the biomass of the family Amphinomidae was more than half of the total polychaete biomass (62%), followed by Maldanidae (15%) and Spionidae (10%) (Figure 15b). The Tanaidacea contributed most to the crustacean biomass (51%), followed by isopods and ostracods in similar proportions (Figure 15c). The nemertean worms contributed least to biomass (Figure 15a).

3.3 Discussion

Sediments sampled for *ex situ* experiments are always exposed to a certain level of disturbance compared to *in situ* experiments, but they are technically less difficult to execute and allow us to control multiple environmental variables as required for this multi-stressor experiment. Evidence of some initial stress on the sediment community was visible as elevated and variable SCOC rates at the start of the equilibration period but settled soon after that (Figure 12). However, decompression and temperature artefacts should be minimal for sediments sampled above a 1,000 m (Glud, 2008; Sweetman et al., 2009), and the 1-week equilibrium period before starting the stable isotope tracer experiment is sufficient and even longer compared to previous similar studies (e.g. Sweetman et al., 2009).

Table 16. Comparison of SCOC rates at various slopes in the Atlantic at similar depth (700–1,000 m) extracted from the global SCOC database (Stratmann et al., 2019). References: (1) this study; (2) Duineveld et al. (1997); (3) Main et al. (2015); (4) Makela et al. (2018); (5) Jahnke and Jahnke (2000); (6) Glud et al. (1994).

SCOC rate ($mmol O_2 m^{-2} d^{-1}$)	Region	Depth (m)	Temperature (°C)	Reference
17.0	Cabo Vere	874 - 876	6.5	1
1.2 - 2.8	Celtic continental margin	700 – 1.000 (<i>in situ</i> and <i>ex situ</i>)		2
1.5	Goban Spur	995 (<i>ex situ</i>)	9.2	3
4.0	Lancaster Sound	794 (<i>ex situ</i>)		4
3.1 – 13.5	Mid-Atlantic continental slope	731 – 855 (<i>in situ</i>)		5
5.6	S Atlantic Ocean	992 (<i>ex situ</i>)		6

The SCOC rate measured at *in situ* temperature after T_{125-hr} was 17.0 $mmol O_2 m^{-2} d^{-1}$ or 204 $mg C m^{-2} d^{-1}$. Compared to other Atlantic studies that have incubated sediment *in-* or *ex situ* from a similar depth range (700–1,000 m, Table 16), our SCOC value was 1.3 to 14 times greater. Sauter et al. (2001) also

assessed benthic respiration using *ex situ* core micro-profiling from a similar depth (777 m) to our study in the more eutrophic North Atlantic (East Greenland Continental Margin) and found SCOC rates were two orders of magnitude lower ($0.39\text{--}0.5\text{ mmol O}_2\text{ m}^{-2}\text{ d}^{-1}$) than our study, though the Sauter et al study was undertaken at 2°C . While these results imply that increasing temperatures from climate change may elevate seafloor respiration rates, Main et al. (2015) incubated sediments from the Goban Spur *ex situ* at 9.2°C and documented rates of $1.5\text{ mmol O}_2\text{ m}^{-2}\text{ d}^{-1}$.

Our bathyal SCOC rate at Cabo Verde aligns closely with the SCOC rate measured at the nearby but much shallower eutrophic Mauritanian continental shelf (18.6 ± 7.5 [SD] range $6.9\text{--}33.8\text{ mmol O}_2\text{ m}^{-2}\text{ d}^{-1}$) (Duineveld et al., 1993). A study looking at the deeper continental slopes off Africa in the South Atlantic also found a somewhat similar, though slightly lower SCOC rate of $12.9\text{ mmol O}_2\text{ m}^{-2}\text{ d}^{-1}$ at 1,747 m near the Cunene River, which was found to correlate to higher macrofaunal dry mass and the large abundance of benthic foraminifera (Glud et al., 1994). The higher SCOC rates documented during the iMirabilis2 cruise compared to the other studies mentioned previously could be related to a high influx of organic matter to the seafloor at our site since the study site was located just below the OMZ. Lower organic matter remineralisation in the OMZ possibly allows greater POC input to the seafloor in Cabo Verde and higher seafloor respiration rates relative to other areas not exposed to such extreme gradients in oxygen, such as the northern N. Atlantic. The lower borders of OMZs are known to have dense aggregations of high trophic level consumers due to the abundance of food and physiological release from hypoxia (Levin and Dayton, 2009).

Between 10- and 45-hours post algae injection in the stable isotope tracer experiment, the C degradation rate decreased, as indicated by both the SCOC rate and DIC production rate. The DIC production rate had a more dramatic decrease (8- and 6- fold for the 6.5°C and 8.5°C respectively) compared to the decline in SCOC, suggesting a strong initial processing of the injected organic matter.

The bacterial uptake of phytodetritus-derived C ($0.265\text{ mg C m}^{-2}\text{ d}^{-1}$) was of similar magnitude as the bacterial uptake measured in a ^{13}C algal-tracer experiment on the eutrophic NE Atlantic slope at 2,170 m that was measured *ex situ* at 4°C ($0.60\text{ mg C m}^{-2}\text{ d}^{-1}$), and lower than the bacterial C uptake at two other slope systems (Northern Aegean Sea at 698 m and Eastern Mediterranean Sea at 1,552 m) measured *ex situ* at 14°C (4.08 and $1.8\text{ mg C m}^{-2}\text{ d}^{-1}$) respectively (Moodley et al., 2005).

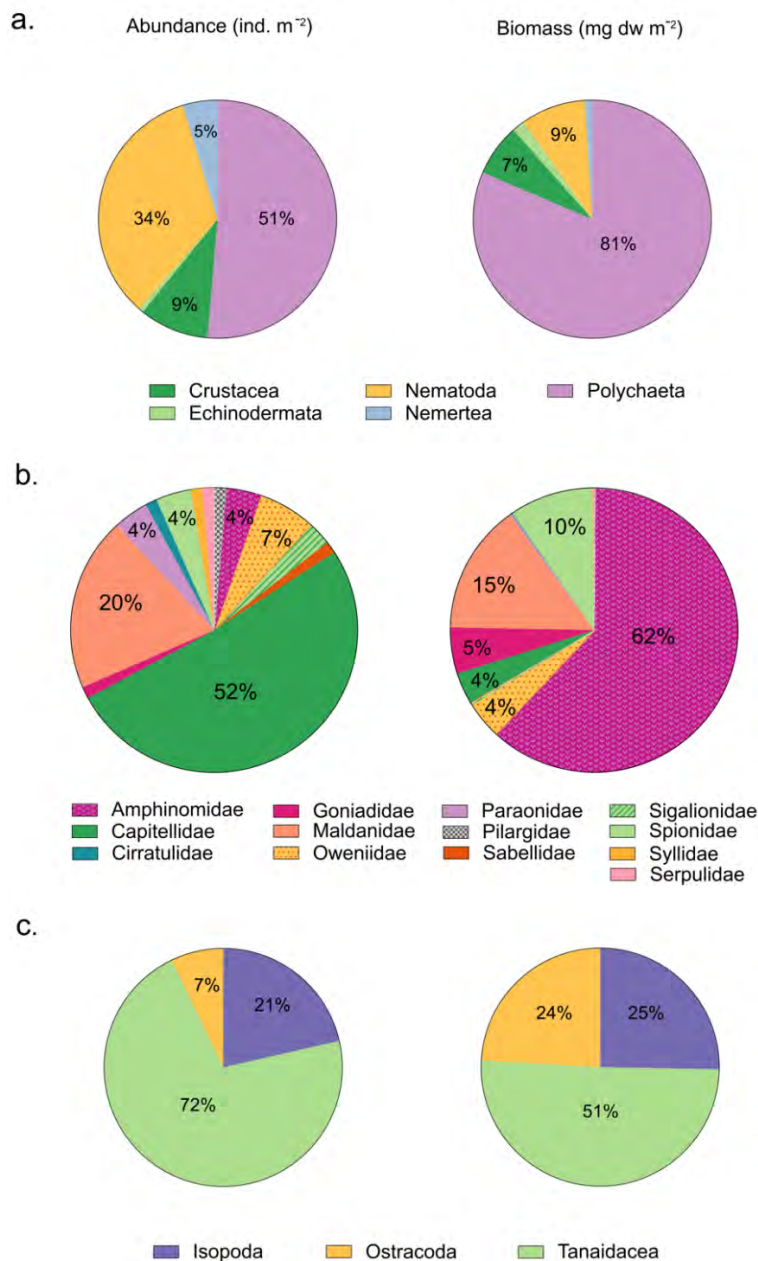


Figure 15. Relative abundance (individuals m⁻²) and biomass (mg DM m⁻²) for Cabo Verde bathyal soft sediments for a) major macrofaunal taxa; b) polychaete families; c) crustaceans orders. Data are from 7 MUC corers.

At 125 hours, the SCOC rate was 28.3 ± 1.8 mmol O₂ m⁻² d⁻¹ at 8.5°C, which is higher than any recorded SCOC rate for the continental slope in the global SCOC database (Stratmann et al., 2019). This exceptionally high SCOC may be the result of a naturally high SCOC rate due to the OMZ boundary and the region’s high productivity as discussed earlier, combined with artificially elevated temperatures increasing basal metabolic rates. Additionally, the elevated SCOC may also be caused by an acute heat stress response to the +2°C temperature increase, which is a large sudden increase for deep water with generally stable temperatures. For comparison, a >2°C temperature anomaly was the definition of a marine heatwave at the western Australia coast (Ainsworth et al., 2020). Future research into the physiological response of deep-sea organisms, e.g., by checking for heat shock proteins, during stressor experiments may elucidate more detailed individual responses (Tomanek, 2014). The SCOC rate was

about 1.7-fold greater with a 2°C increase in temperature (from 6.5 to 8.5°C), which resulted in a Q_{10} value of 12.8. To put this into perspective, the experimental Q_{10} value based on respiration of the California horn shark (*Heterodontus francisci*) was about 2 (Luongo and Lowe, 2018), and also for shallow North Sea sediments (37 m) the experimental Q_{10} based on background respiration was about 2 (Moodley et al., 2005). When those same North Sea sediments were incubated with a pulse of fresh phytodetritus, the respiration based Q_{10} increased to 5. A spatial comparison between two slopes (NE Atlantic 42.6°N 10.0°W and Eastern Mediterranean 35.7°N 26.6°E) at similar depths (2,170 vs. 1,552 m) but differing temperatures (4°C vs 14°C), shows a Q_{10} of 9.2 when comparing *ex situ* respiration rates upon a phytodetritus pulse (Moodley et al., 2005). This Q_{10} of 9.2 for slope sediments is similarly high to our Q_{10} estimate of 12.8, indicating processes in these deep bathyal sediments are very temperature sensitive.

Macrofauna diversity and abundance

This study comprises new data about bathyal ecosystem functioning in the Atlantic Ocean with focus on the macrofaunal abundance and biomass of the CVB. Sampling methods and methods for estimating biomass are inconsistent between studies, with wet mass data prevailing in most studies (Levin and Gooday, 2003), so care has to be taken when comparing our results with previous studies conducted in other Atlantic bathyal basins. Therefore, to avoid disparities, our comparisons were made with studies that used a similar methodology to collect and process the samples, such as the same sampling depth range and mesh size (300 µm) to retain macrofauna (Gage et al., 2002).

Upper bathyal macrofaunal assemblages in Cabo Verde were dominated by annelids and macrofaunal size nematodes, being consistent with other bathyal studies in the Atlantic where polychaetes are very abundant (Flach and Heip, 1996; Hartman, 1965; Rowe et al., 1982), representing up to 60% of the macrofaunal communities in continental slopes (Sanders et al., 1965). Crustaceans are the second most abundant taxon generally reported at similar depths (approx. 1,000 m) on the mid-Atlantic slope (Bernardino et al., 2016; Flach and Heip, 1996), however, in our study they were represented by a lower percentage (8%) after nematodes. Molluscs had been reported in a low proportion for Atlantic middle slopes, being more abundant up 400 m depth (Bernardino et al., 2016), but in our study they were absent.

The macrofaunal density reported in this study (5,384±2,523 [SD] ind. m⁻².) for 900 m depth in the Cabo Verde basin exceeds the average density reported off N. Morocco, Northeast tropical Atlantic (1,132 ind. m⁻² (Pfannkuche et al., 1983)), and off Bermuda (2,979 ind. m⁻² (Sanders et al., 1965)). However, compared with other Northwest Atlantic areas such as Cape Hateras, Long Bay Cape Lookout, and Cape Fear (55,500 ind. m⁻², 21,400 ind. m⁻², 9,439 ind. m⁻², respectively (Schaff et al., 1992)), the macrofaunal density reported here was up to 11 times lower.

Suspension feeders have been reported with high densities previously in the upper slope (1,000-1,500 m (Flach et al., 1998)), while the abundance of deposit feeders is generally related to depth, increasing with deeper waters. In our study, the surface and subsurface deposit feeders exhibited the highest abundance with Capitellidae and Maldanidae. These polychaetes families are known to be present at great abundances in sediments with high organic matter content (Fauchald and Jumars, 1979), because they can rapidly subduct newly deposited carbon in the sediment column to depths of 10 cm or more (Levin et al., 1998). This composition of the macrofauna differs from the study by Sanders et al. (1965) in the North Atlantic, in which they reported a greater richness with 50 families of polychaetes, of which Polynoidae, Syllidae, Nereididae and Serpulidae were the best represented (Hartman, 1965).

At the Eastern Brazilian continental margin (Southwest Atlantic), macrofaunal taxonomic diversity and assemblage composition changed significantly across depth zones, with the highest taxonomic diversity at mid-slope depths (around 1,000 m), which can be related to upwelling events (Bernardino et al., 2016). On the other side of the Atlantic, the oxygen depletion in bottom waters off the coast of North-West Africa is linked to upwelling caused by the Canary Current, where the large flow of organic matter to the seafloor has a significant impact on the structure and function of the benthic communities (Levin and Gooday, 2003). This may explain the total macrofaunal abundance and biomass at the Cape Verde bathyal slope, since were consistent with previous values reported for areas with higher organic matter input (3,984 to 5,428 ind. m⁻², 251 to 405 mg C m⁻²; Galéron et al., 2000) in the Tropical Northeast Atlantic.

Conclusion

The upper bathyal slope of Cabo Verde (875 m) exhibits SCOC rates at the very high end of slope systems (200–2,000 m), with rates similar to the highly productive and relatively nearby Mauritanian continental shelf, well-known for its high productivity and valuable fisheries (Ramos et al., 2017). Additionally, SCOC rates are somewhat similar, though still higher, to another continental slope system further south in the East Atlantic, which is dominated by Foraminifera. The lower-than-expected density and biomass of macrofauna may suggest the Cabo Verde bathyal slope is Foraminifera dominated, unfortunately they were omitted in this study. Dominance of Foraminifera over macrofauna is observed in low oxygen conditions (Woulds et al., 2009). Even though the sediments were sampled below the OMZ and CTD oxygen levels indicate well-oxygenated waters (>100 μmol O₂ kg⁻¹; Engel et al. (2017)), perhaps the depth of the OMZ is seasonal and occasionally reaches our sampling depth. The Cabo Verde basin is known for its complex oceanography with high primary production but low oxygen concentrations (Pelegrí et al., 2017). The relatively high abundance of deposit feeding macrofauna does support a higher input of POM.

The community of the Cabo Verde upper bathyal slope appears to be sensitive to temperature changes. The temperature of the bathyal Atlantic is modelled to increase with 4.4°C by 2100, which could triple SCOC and hence C degradation rates and reduce deep C burial rates (Smith et al., 2008). As slope systems are such an important system for C burial, this could have important consequences for climate change by providing a positive feedback loop.

4. Case study 3 – How do shifts in upper-ocean ecosystems directly impact abyssal scavenger communities? – insights from baited camera lander deployments in the Cabo Verde Abyssal Basin (tropical East Atlantic).

4.1 Materials & Methods

Baited Camera Lander deployments

A total of eight deployments of an autonomous baited camera lander were conducted at the Cabo Verde Abyssal Basin (CVAB, tropical East Atlantic, 14.7°N 25.2°W, ~4,200 m) using either Atlantic mackerel, *Scomber scombrus* (n=4) or Patagonian squid *Doryteuthis gahi* (n=4) bait (Table 17). The deployments took place during the iMirabilis2 campaign in August 2021 from the research vessel Sarmiento de Gamboa (Orejas et al., 2022).

The baited camera lander designed by A.K. Sweetman and built by KC Denmark A/S (Figure 16) was equipped with a deep-sea time lapse camera system which consisted of a NIKON D7200 camera housed in a titanium pressure housing with dome port (settings: 1/25 sec exposure, equivalent focal length of 160 cm [5.2 ft], f-stop 16.0, ISO 200), two flash strobes, and a titanium housing with computer and battery. Pictures were taken every 2.5 mins. A bait plate (12 x 45 cm) was obliquely connected to the lander by a bar (6 x 91 cm) at an angle of 40 degrees, allowing it to rest just on top of the seafloor. The camera was pointed at the bait plate, resulting in an oblique view of the plate and surrounding sediment at an angle of 40 degrees. An ADCP (Aquadopp 6,000 m, Nortek) was mounted on top of the lander frame to measure near bottom currents (~2 mab) every 5 sec.

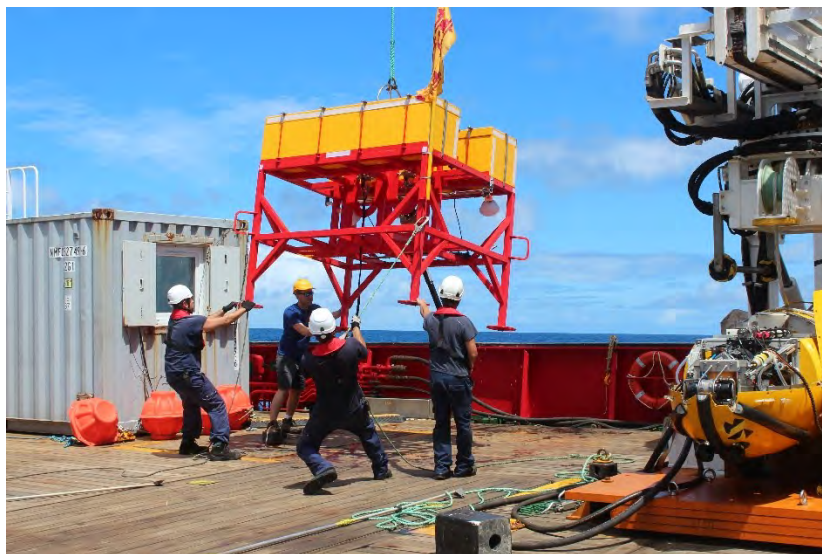


Figure 16. Baited Camera Lander recovery after a deployment to the Cabo Verde Abyssal Basin at ~4,200 m (picture by Beatriz Vinha, iMirabilis2).

Prior to each lander deployment, the bait was defrosted and weighed using a roll-calibrated scale and standardised to approx. 3 kg (range 3.1–3.5 kg, Table 17). The bait was then attached to the bait plate (fish with tie rips through the eye sockets and around the tail fins, squid with a rope) always while wearing nitrile gloves to avoid contaminating the bait (e.g., with sunscreen oils) that would influence the bait odour.

Table 17. Deployments of the Baited Camera Lander and the Baited Trap Lander. Latitude and longitude (Lat, Lon) are given in decimal degrees (DD), Depth in meters. Pictures (n) show the number of pictures taken at the seafloor.

Station ID	Lat, Lon (DD); Depth (m)	Bait	Bait in (kg)	Pictures (n)
<i>Baited Camera Lander</i>				
AKS296-CL1	14.7263, -25.1993; 4,163	<i>Scomber scombrus</i>	3.252	565
AKS298-CL2	14.7278, -25.1901; 4,170	<i>Doryteuthis gahi</i>	3.194	584
AKS299-CL3	14.7193, -25.2093; 4,170	<i>Scomber scombrus</i>	3.434	562
AKS301-CL4	14.7068, -25.1699; 4,187	<i>Doryteuthis gahi</i>	3.120	749
AKS303-CL5	14.7292, -25.1817; 4,225	<i>Scomber scombrus</i>	3.467	673
AKS305-CL6	14.7443, -25.1432; 4,192	<i>Doryteuthis gahi</i>	3.220	580
AKS308-CL7	14.6760, -25.1540; 4,341	<i>Doryteuthis gahi</i>	3.360	756
AKS311-CL8	14.6968, -25.1212; 4,255	<i>Scomber scombrus</i>	3.360	603
<i>Baited Trap Lander</i>				
AKS297	14.7108, -25.2061; 4,175	<i>Scomber scombrus</i>	-	-
AKS304	14.6922, -25.1792; 4,247	<i>Scomber scombrus</i>	-	-
AKS307	14.6986, -25.1091; 4,188	<i>Scomber scombrus</i>	-	-

The lander used 250 kg of ballast to allow it to sink upright to the seafloor. During each deployment the baited camera lander was left at the seafloor for approx. 24 hours. A hydrophone acoustic signal from the vessel to the landers' releases at the end of each deployment released the weights, allowing the lander to ascent to the surface due to the buoyancy of the syntactic foam mounted on the frame. Once onboard, the camera images and ocean current data were downloaded, and any remaining bait was removed to be weighed for scavenging rate estimates.

Collection of reference specimens

Complementary to the camera system, reference specimens of the organisms observed on camera were collected using a baited trap. The trap consisted of a lightweight glass fibre frame with plastic mesh walls, with one-way entrances, fishhooks, and amphipod traps to entrap larger fauna and amphipods (Figure 17). The trap was deployed three times in the same region and to the same depth as the camera lander (Table 17). Only the fish bait *S. scombrus* was used, by mounting it on fishhooks both inside and outside of the mesh, directly on the inside mesh of the lander, and inside amphipod traps. The trap autonomously sank using a 120 kg weight stack attached to an acoustic release and was held in place on the seafloor for about 48 hours before recovery. Glass flotation spheres on a mooring line provided positive buoyancy for ascent and subsequent retrieval onto the vessel deck.



Figure 17. Baited Trap Lander used to collect reference specimens.

On deck, specimens were directly transferred onto ice and placed in a refrigerated space for storage while specimens were processed individually. Fish were weighed in a bag using a luggage scale, and pre-anal fin length was measured. Muscle tissue was cut right below the dorsal fin and stored in sterile sample bags at -80°C for later stable isotope analysis. Amphipods were individually stored in sterile 2 ml Eppendorf tubes at -80°C . A WP2 plankton net ($200\ \mu\text{m}$) was hauled up vertically from 2,146 m depth at $40\ \text{m}\ \text{min}^{-1}$ at a nearby pelagic site (14.8°N , 24.5°E) to collect pelagic zooplankton. Organisms were frozen whole at -80°C for later stable isotope analysis to compare with abyssal scavenger data to infer information about the trophic ecology at the seafloor.

Photograph annotation

Back in the laboratory, the brightness (+0.20) and contrast (-20) of the photographs were adjusted using the 'Photos' application from Apple (V5.0). For each deployment, it was noted if the bait was fully consumed while at the seafloor, and if so, at what point the bait had disappeared to establish the removal time. Removal time was set at the full length of the duration at the seafloor if flesh was still visible when the lander was released from the seafloor. Scavenging rates were calculated as wet mass consumption ($\text{kg}\ \text{d}^{-1}$) based on the change in bait weight and removal time, and as energy consumption ($\text{kJ}\ \text{d}^{-1}$) using the energy content of both bait types ($2.95\ \text{kJ}\ \text{fresh}\ \text{g}^{-1}$ for *D. gahi* (Ferreyra, 1953) and $8.2\ \text{kJ}\ \text{fresh}\ \text{g}^{-1}$ for *S. scombrus* (Sweetman et al., 2014)).

Photo annotations were performed in Biigle 2.0 (Langenkämper et al., 2017) on every second photograph (i.e., taken every 5 minutes), both in overview mode (to annotate all larger organisms) and with 1.37x zoom (to annotate smaller organisms). Organisms were annotated with a rectangular shape and grouped by morphospecies identified to the lowest taxonomic level or grouped under 'No ID' under the lowest taxonomic level of confidence if no morphospecies could be assigned. Non-scavenging (i.e., sessile, and planktonic) organisms, objects on the seafloor, and fish parasites were annotated as well, but not included in the statistical analyses. Annotations were evaluated using the LARGO function in Biigle to check for annotation consistency within and between deployments.

Biigle annotation files were downloaded as CSV formatted files for further processing in R (R

Development Core Team, 2021). For each image the 1) number of individuals per morphospecies, 2) number of all fish and the number of all Crustacea (including unassigned morphospecies), and 3) total number of individuals were counted (omitting individuals unassigned to morphospecies). For each deployment, the 1) time of first arrival for each morphospecies (T_{arr}), 2) maximum number of individuals per morphospecies in one image ($maxN$), and 3) the time of $maxN$ (T_{maxN}) for each morphospecies was calculated. If the $maxN$ abundance was observed in multiple images during a deployment, the earliest occurrence was taken.

Reference specimen processing

In an onshore laboratory, frozen amphipods from the trap were identified to the lowest taxonomic level using a binocular microscope, photographed with a ruler, and tissue collected into pre-weighed tin capsules: pleopod(s) for large amphipods, half the body for medium-sized amphipods, and the full specimens for small amphipods. The length of amphipods was measured from the tip of the rostrum to the end of the telson following the dorsal line, using the multi-line tool in ImageJ (V1.51) (Schneider et al., 2012). For fish, a small amount of muscle tissue was put directly into pre-weighed tin capsules. The capsules were weighed before and after drying at 45°C for at least 2 days. Tissue from the specimens captured in the pelagic net were placed on clean pre-weighed aluminium foil and dried at 45°C until a stable weight was achieved: tissue between eye and dorsal fin or the anterior half for small specimens of pelagic fish, half the specimen for jellies, pleopods for shrimp, and a zooplankton mix. The dry tissue was homogenized with pestle and mortar and transferred into pre-weighed tin caps.

At a stable dry mass, the capsules were crimped closed and analysed for C content, N content, ^{13}C , and ^{15}N at James Hutton Institute in Aberdeen using isotope ratio mass spectrometry. We mathematically corrected the $\delta^{13}\text{C}$ values of organisms with a high lipid content ($\text{C}:\text{N} > 3.5$) as the depletion of lipids in ^{13}C relative to proteins and carbohydrates can skew $\delta^{13}\text{C}$ values, as follows: $\delta^{13}\text{C}_{corrected} = \delta^{13}\text{C}_{untreated} - 3.32 + 0.99 \times \text{C}:\text{N}$, where $\delta^{13}\text{C}_{untreated}$ are the raw reported $\delta^{13}\text{C}$ values and $\text{C}:\text{N}$ is the ratio in the measured tissue (Post et al., 2007).

Trophic levels can be determined by comparing the $\delta^{15}\text{N}$ value of tissue against the $\delta^{15}\text{N}$ of the assumed base of the food-web. The net-caught zooplankton were assumed to be the primary consumers with a trophic level of 2 (i.e., feeding on the primary producers phytoplankton at trophic level 1). Estimates of the trophic level of the reference specimens caught by baited trap were calculated as $TL = TL_{base} + (\delta^{15}\text{N} - \delta^{15}\text{N}_{base})/TEF$, where $TL_{base} = 2$ as the trophic level of zooplankton with a $\delta^{15}\text{N}_{base}$ of 8.6 ± 0.04 (n=2), the Trophic Enrichment Factor TEF of ^{15}N was 2.6‰ based on controlled feeding experiments of aquatic invertebrates (Brauns et al., 2018), and $\delta^{15}\text{N}$ is the stable isotope signature of nitrogen for the net- and trap-caught specimens. The trophic positions of the captured pelagic and demersal specimens (and used bait) were visualised in an isospace biplot of $\delta^{13}\text{C}$ and $\delta^{15}\text{N}$ with convex hulls delineating the pelagic and demersal community.

Data analysis and statistics

All data processing was conducted in R (R Development Core Team, 2021), and means in this section are reported with standard errors (mean \pm s.e.) unless stated otherwise. Significant differences in mean values were tested ($\alpha = 0.05$) using parametric two-sample t-tests or ANOVA for comparing more than two populations, or their non-parametric analogues for heteroscedastic data. If relevant, deployments were cropped at the time of the shortest deployment to allow comparison between deployments.

The density of *Coryphaenoides* sp. and *Barathrites iris* fish in the region N (ind km⁻²) was estimated using the ‘Time of first arrival’ model (Priede and Merrett, 1996), that uses water current velocity V_w (m s⁻¹), fish swimming velocity V_f (m s⁻¹), and the time of first arrival T_{arr} (secs), assuming a uniform distribution of fish:

$$N = \frac{0.3849 \times \left(\frac{1}{V_f} + \frac{1}{V_w}\right)^2}{T_{arr}^2} \times 10^6$$

The fish swimming velocity V_f used in the model for *Coryphaenoides* spp. was 0.077 m s⁻¹ based on *in situ* observed departure speeds (C. Wylie in Henriques et al., 2002), and 0.15347 m s⁻¹ based on Code-Activated Transponders (CATs) ingested by *C. armatus* on the Cape Verde Abyssal Basin (Henriques, 2004). For *B. iris*, a swimming velocity V_f of 0.2135 m s⁻¹ based on CATs at the CVAB (Henriques, 2004) was used in the model. The water current velocity V_w was the mean bottom current speed for the first hour (when both *Coryphaenoides* spp. and *B. iris* appeared at the camera) of the deployments as measured by the ADCP.

A community matrix based on *maxN* for the mobile morphospecies observed at the fish and squid bait (i.e., untransformed count data) was constructed for use with the R-package *vegan* (v. 2.6-4, Oksanen et al., 2022). *Coryphaenoides* spp. was treated as a single species complex in all diversity analysis, but it was checked if the main findings would change if they would be treated as three separate morphospecies which was hypothesised based on the colour and morphology of the rat tails. The species accumulation curve (*specaccum* function, method ‘random’) was checked for its asymptote, to establish if the community had been entirely censused. Species rarefaction curves (*rarecurve* function), rarefaction species richness for smallest sample size (*rarefy* function, n=42), and diversity indices were compared between bait types, using the unbiased Simpson diversity index (*simpson.unb* function for discrete data, less sensitive to sample size, eq. 5 in Hurlbert, 1971) and the Shannon diversity index (*diversity* function, $H = -\sum_i p_i \cdot \ln(p_i)$ where p_i is the proportional abundance of morphospecies i).

The community matrix was subsequently used to conduct 1) nMDS ordination with Bray-Curtis distances (*metaMDS* function, (Minchin, 1987)), 2) ANOSIM analysis with Bray-Curtis distances (*ANOSIM* function, with R-statistic $R = (r_B - r_W)/(N(N - 1)/4)$ where r_B and r_W are the difference of mean ranks between groups and within groups respectively; and 3) SIMPER analysis (*simper* function, (Clarke, 1993)).

Scavenger dynamics was studied by plotting the count of total scavengers, total fish, total Crustacea, and each morphospecies per photograph over time. A Zero-Inflated Negative Binomial Regression Model (to account for the many zero counts and overdispersion) was used to test for a relationship between fish and crustacea abundance at the bait over all deployments.

4.2 Results

Scavenging rates

After deployments with fish bait, tissue and bones always remained on the bait plate. In contrast, no Patagonian squid bait *D. gahi* was left on the bait plate upon lander recovery, and the camera images revealed complete removal of all squid within five hours of the lander reaching the seafloor. The average removal time of squid bait (3.4±0.6 hours) was significantly shorter than the removal time (24.7±0.9 hours) for fish bait (Student’s T-test, p<0.001, df=6, **Figure 18**). Correspondingly, the consumption rate of squid bait was significantly higher (25.4±4.6 WM kg d⁻¹) compared to the

consumption rate (2.8 ± 0.2 WM kg d^{-1}) of fish bait (Welch T-test, $p=0.02$, $df=3.01$) (Figure 18). Even though the energy content of *S. scombrus* was almost three times the energy content of *D. gahi*, the mean estimated energy consumption rate of squid bait ($74,948 \pm 13,518$ kJ d^{-1}) was three times higher than the energy consumption rate of fish bait ($23,126 \pm 1,578$ kJ d^{-1}) (Welch T-test, $p=0.03$, $df=3.08$, Figure 18).

Diversity and abundance

In total, 35 mobile morphospecies were recognised (Table 18) from a total 38,185 annotations and 5,097 seafloor images taken over 8 camera lander deployments, and mostly include various fish and crustaceans, and occasional ophiuroids, gastropods, and swimming polychaetes. The asymptotic species accumulation curve (Figure 19) indicates the community has been adequately sampled to compare biodiversity between treatments.

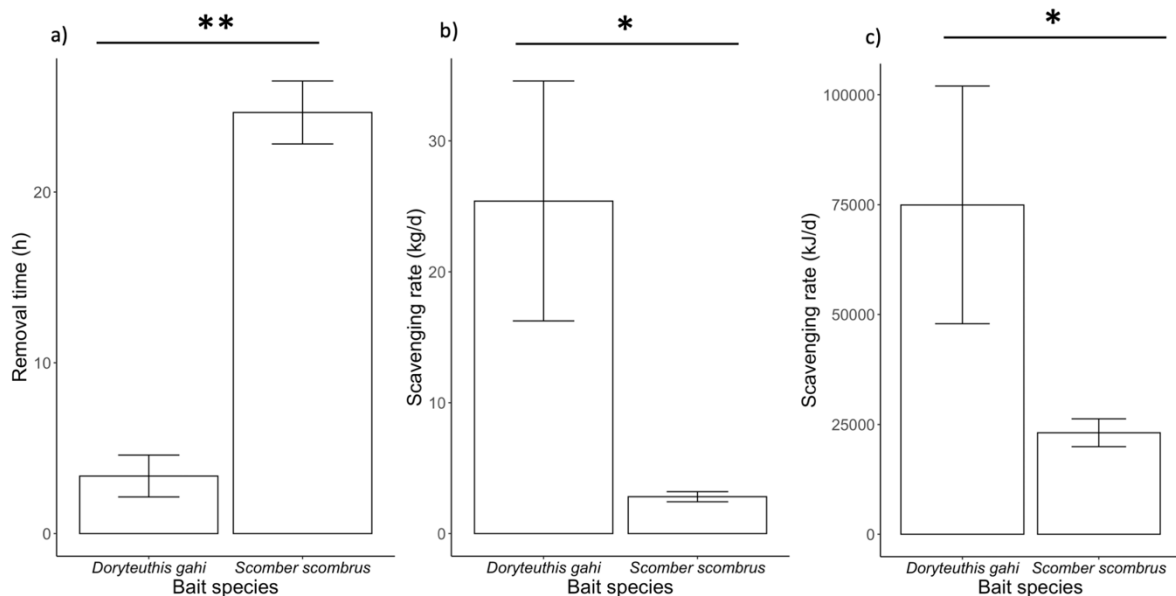


Figure 18. Scavenging rates on squid (*Doryteuthis gahi*) and fish (*Scomber scombrus*) bait, reported as a) removal time (h), b) wet consumption rate (kg WM d^{-1}), and c) energy consumption rate (kJ d^{-1}). ** highly significant ($p < 0.01$), * significant ($p < 0.05$).

The average Simpson's diversity index was 0.89 ± 0.03 and 0.93 ± 0.01 for the fish and squid bait deployments, respectively. The average Shannon's diversity index was 2.68 ± 0.15 and 2.84 ± 0.07 for the fish and squid bait deployments, respectively. The diversity indices of scavengers were not significantly different between bait types (Wilcoxon ranked sum test $p = 0.11$ and 2-sample t-test $p = 0.34$ for Simpson's and Shannon's diversity index, respectively). However, rarefaction curves show that species richness at the squid bait appears to be consistently equal or greater than at the fish bait (Figure 20). This is confirmed by the expected species richness for a sample size of 42 (i.e., smallest overall sample size), which was significantly greater at the squid bait (Student's t-test, $p = 0.04$).

Table 18. A summary of the Baited Camera Lander experiment at the Cabo Verde Abyssal Basin at 4,200 m. Per bait type the mean \pm SE 1) time of first arrival (hours), 2) maximum number of individuals in one image (maxN), and 3) time of maxN (hours) for each morphospecies (Biigle ID in brackets). If the morphospecies is not observed at all for a certain bait type, it's noted as NA. Significant differences, i.e. $p < 0.05$, are in bold.

Morphospecies	Time of first arrival (h)		MaxN		Time of MaxN (h)	
	<i>S. scombrus</i>	<i>D. gahi</i>	<i>S. scombrus</i>	<i>D. gahi</i>	<i>S. scombrus</i>	<i>D. gahi</i>
All morphospecies	0.4 \pm 0.1	0.2 \pm 0.04	53.2 \pm 13.0	17.8 \pm 2.0	18.9\pm1.4	7.6\pm1.7^t
All fish combined	0.4 \pm 0.1	0.2 \pm 0.04	15.5\pm1.6	5.5\pm0.9^t	12.8\pm3.0	1.3\pm0.3^w
Fish						
<i>Coryphaenoides</i> spp. complex	0.4 \pm 0.1	0.2 \pm 0.04	7.8\pm1.0	4\pm0.7^t	9.9\pm1.5	1.0\pm0.2^w
<i>Coryphaenoides</i> msp. 1 (COR_01)	0.9 \pm 0.3	1.3 \pm 0.6	5\pm0.4	1.3\pm0.3^{wm}	10.4 \pm 4.1	1.3 \pm 0.6
<i>Coryphaenoides</i> msp. 2 (COR_02)	0.4 \pm 0.1	0.3 \pm 0.1	7.8\pm1.0	4\pm0.7^t	9.9\pm1.5	1.0\pm0.2^w
<i>Coryphaenoides</i> msp. 3 (COR_03)	NA	0.9 \pm 0.3	NA	1 \pm 0	NA	0.9 \pm 0.3
<i>Barathrites iris</i> (OPH_01)	1.4 \pm 0.2	2.9 \pm 1.0	7.5\pm0.6	1.3\pm0.3^{wm}	12.8\pm3.0	3.1\pm0.9^t
<i>Bassozetus robustus</i> (OPH_02)	3.6	2.3	1	1	3.6	2.3
<i>Histiobranchus bathybius</i> (SYN_01)	4.5	2.6	1	1	4.5	2.6
Decapoda						
<i>Hymenopenaeus laevis</i> (PEN_01)	0.7\pm0.1	1.7\pm0.3^t	18.5 \pm 2.8	12.3 \pm 1.5	18.6\pm1.4	13.8\pm0.8^t
Aristeidae shrimp (PEN_02)	18.2 \pm 3.6	6.7 \pm 0.5	1 \pm 0	1 \pm 0	18.2 \pm 3.6	6.7 \pm 0.5
<i>Cerataspis</i> cf. <i>monstrosus</i> (PEN_03)	8.3 \pm 7.7	4.4 \pm 3.1	1 \pm 0	1 \pm 0	8.3 \pm 7.7	4.4 \pm 3.1
Amphipoda						
cf. <i>Eurythenes</i> sp. (AMP_01)	4.5 \pm 1.4	4.7 \pm 2.1	2.8 \pm 0.5	1.5 \pm 0.5	12.7 \pm 2.3	5.3 \pm 1.5
Amphipoda msp. 1 (AMP_04)	3.4 \pm 2.0	2.8 \pm 1.3	3 \pm 2	1 \pm 0	5.8 \pm 0.4	2.8 \pm 1.3
Amphipoda msp. 2 (AMP_02)	0.8 \pm 0.2	1.1 \pm 0.1	25.5 \pm 12.7	3.3 \pm 0.8	16.6\pm3.4	2.8\pm1.0^t
Amphipoda msp. 3 (AMP_03)	2.6 \pm 0.2	7.4 \pm 4.9	3.5 \pm 0.5	2 \pm 0.4	10.7 \pm 3.3	8.4 \pm 4.6
Mysidae						
Mysidae msp. 1 (MYS_01)	4.2 \pm 1.5	3.8 \pm 0.5	2 \pm 0.4	1.8 \pm 0.3	11.3 \pm 2.0	7.1 \pm 2.1
Mysidae msp. 2 (MYS_02)	2.8 \pm 1.0	1.3 \pm 0.6	6.5 \pm 1.9	4 \pm 0.7	18.9 \pm 3.1	7.2 \pm 2.0
Mysidae msp. 3 (MYS_03)	8.3 \pm 3.1	3.9 \pm 1.0	1.8 \pm 0.5	1.5 \pm 0.5	13.1 \pm 4.1	5.6 \pm 0.7
Mysidae msp. 4 (MYS_04)	6.0 \pm 2.4	1.8 \pm 0.4	4.8 \pm 1.4	3.5 \pm 0.9	15.6 \pm 1.0	9.9 \pm 3.3
Mysidae msp. 5 (MYS_05)	12.0 \pm 3.6	8.8 \pm 2.0	1.3 \pm 0.3	1.8 \pm 0.5	16.3 \pm 3.8	14.9 \pm 2.2
Mysidae msp. 6 (MYS_06)	4.3 \pm 2.6	3.9 \pm 0.7	6.3 \pm 1.7	3.3 \pm 0.6	19.3 \pm 1.5	13.2 \pm 2.4
Mysidae msp. 7 (MYS_07)	9.5 \pm 1.8	5.3 \pm 2.2	3.3 \pm 1.3	1.3 \pm 0.3	17.4\pm1.3	5.4\pm2.2^t
Mysidae msp. 8 (MYS_08)	9.3 \pm 3.1	2.9 \pm 0.8	7.5 \pm 2.6	4 \pm 1.1	18.9\pm2.3	7.8\pm1.1^t
Isopoda						

Morphospecies	Time of first arrival (h)		MaxN		Time of MaxN (h)	
	<i>S. scombrus</i>	<i>D. gahi</i>	<i>S. scombrus</i>	<i>D. gahi</i>	<i>S. scombrus</i>	<i>D. gahi</i>
Munnopsidae (ART_01)	NA	14.4±3.6	NA	1±0	NA	14.4±3.6
Isopoda msp. 1 (ART_02)	13.0±5.2	2.3	1±0	1	13.0±5.2	2.3
Isopoda msp. 2 (ART_03)	5.3±2.2	1.9±0.4	4.5±1.8	4.3±0.9	12.2±3.8	16.1±3.1
Isopoda msp. 3 (ART_04)	5.8±2.3	2.4	1.3±0.3	1	5.8±2.3	2.4
Isopoda msp. 4 (ART_05)	7.2±3.0	4.0±1.3	1.5±0.3	1±0	8.3±2.4	4.0±1.3
Copepoda						
Copepoda msp. 1 (COP_01)	2.4±0.7	0.8±0.3	2.3±0.3	1.3±0.3	4.2±0.6	1.1±0.3^t
Copepoda msp. 2 (COP_02)	8.8±3.2	2.8±0.9	1±0	1±0	8.8±3.2	2.8±0.9
Echinodermata						
Ophiuroidea msp. 1 (ECH_01)	5.4±1.9	3.9±1.6	1.8±0.3	1.5±0.5	11.1±3.5	4.0±1.5
Mollusca						
<i>Mohnia</i> cf. <i>abyssorum</i> (MOL_01)	12.8	16.5±0.6	1	1±0	12.8	16.5±0.6
Gastropoda msp. 1 (MOL_02)	5.8±5.6	14.0	1±0	1	5.8±5.6	14.0
Polychaeta						
Polychaeta msp. 1 (POL_01)	12.1±3.6	9.1±3.8	1±0	1±0	12.1±3.6	9.1±3.8
Polychaeta msp. 2 (POL_02)	8.5±1.8	13.6±1.7	1±0	1±0	8.5±1.8	13.6±1.7
Polychaeta msp. 3 (POL_03)	2.7	11.0±4.4	1	1±0	2.7	11.0±4.4
Polychaeta msp. 4 (POL_04)	14.4±0.9	NA	1±0	NA	14.4±0.9	NA

^t two-sample t-test, ^w two-sample Welch-test, ^{wm} Wilcoxon Mann-Whitney U test.

The nMDS (stress = 0.09, [Figure 21](#)) and related ANOSIM analysis (R-statistic = 0.6, permutation significance = 0.03) showed divergence between the community composition at the different bait types, which became stronger (ANOSIM R-statistic = 0.7) when the *Coryphaenoides* spp. complex was treated as three separate morphospecies. The SIMPER analysis showed a 41.5% difference in overall composition between bait types, with *Coryphaenoides* spp. significantly ($p = 0.001$) contributing 5.3% to the different community compositions ([Table 19](#)). Scavenging rates did not solely explain this observed distinction in community composition between bait types, as the tested correlations between the nMDS x-axis site scores against scavenging rates (in kg, kg d^{-1} , kJ, and kJ d^{-1}) through linear regression were all non-significant.

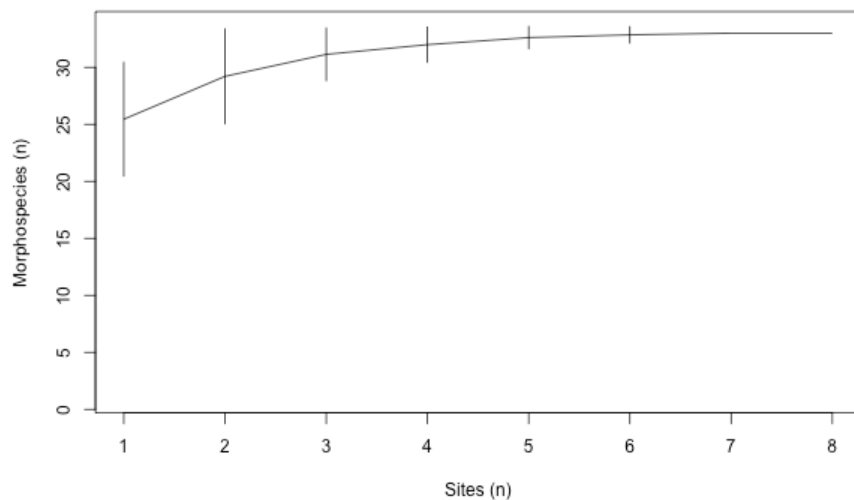


Figure 19. Species accumulation curve for all eight deployments.

The most abundant fish at the bait was the rattail *Coryphaenoides* spp., followed by the cusk eel *Barathrites iris*. Other observed fish were the cusk eel *Bassozetus robustus* and cut-throat eel *Histiobranchus bathybius*. Both these latter taxa were observed at both the fish and squid bait however, they were rare and not captured by the baited trap for tissue samples. The estimated abundance of *Coryphaenoides* spp. was 473 ± 121 individuals km^{-2} based on the *in-situ* departure speed, or 281 ± 73 individuals km^{-2} when based on the CAT-derived swimming speed ([Table 20](#)). Over all deployments and using both swimming speeds the density estimates range from 21 to 900 individuals km^{-2} . The density of *B. iris* is estimated at 6 ± 2 individuals km^{-2} (range 1–18 individuals km^{-2} , [Table 20](#)). The mean bottom current speed in the first hour of each deployment, as used in the ‘Time of first arrival’ model to estimate local densities for both *Coryphaenoides* spp. and *B. iris*, ranged from 62 to 79 mm s^{-1} ([Table 20](#)). Over the 24-hour deployments, the hourly mean bottom current speed ranged from 53 to 88 mm s^{-1} with an hourly mean current direction ranging from 115.6° (E/SE) to 249.3° (W/SW).

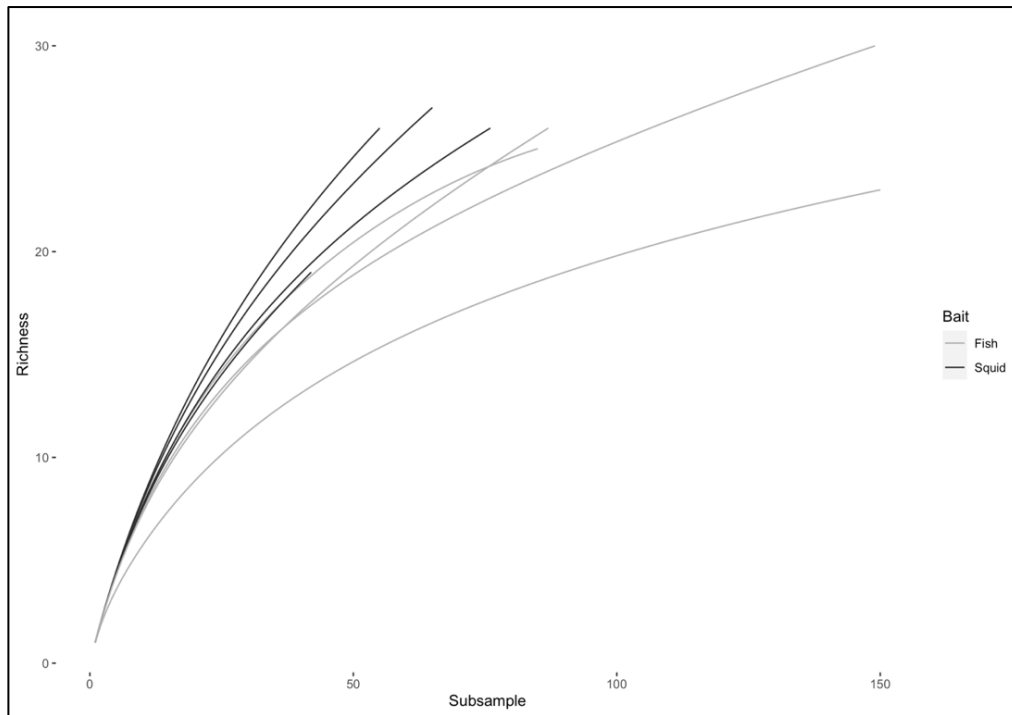


Figure 20. Rarefaction curves for the different camera lander deployments.

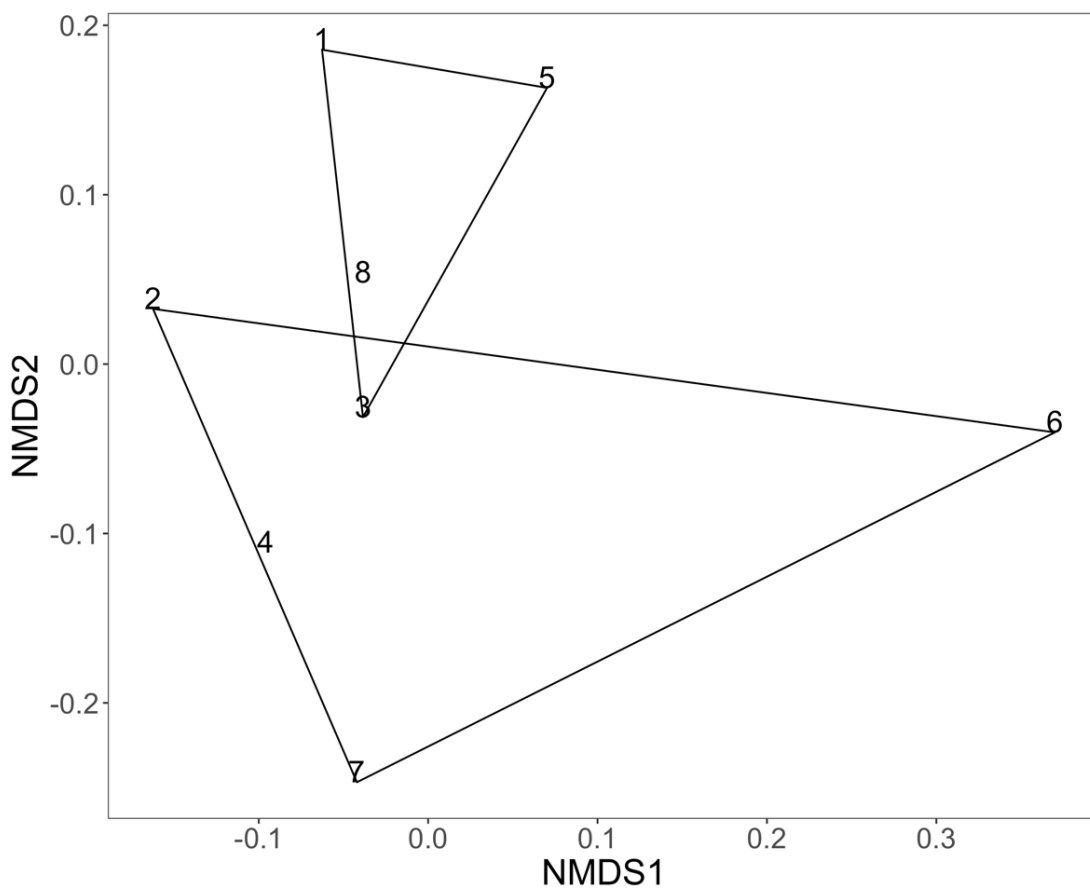


Figure 21. nMDS plot of the community diversity matrix based on maxN data. Solid lines delineate the convex hull per bait type, where fish bait (*Scomber scombrus*) was used at site 1, 3, 5, and 8, and squid bait (*Doryteuthis gahi*) was used at site 2, 4, 6, and 7.

The most abundant decapod observed at both bait types was *Hymenopenaeus laevis* (De Almeida Alves-Júnior et al., 2017), that mostly stayed near the seafloor and was rarely observed swimming. Other decapods regularly visiting the bait were the large *Cerataspis* cf. *monstrosus*, and an unidentified Aristeidae shrimp. Many mysid and amphipod individuals were observed in the baited camera images: amphipods were mostly present right on top of the bait and best visible when disturbed by passing fish, whereas mysids were mostly observed on the surrounding seafloor, occasionally swimming. The mysids and amphipods could not be identified from the photographs beyond their distinction into morphospecies. We delineated eight morphospecies of mysids, and four morphospecies of amphipods including cf. *Eurythenes* spp., even though we know from the trap lander that at least six different amphipod species were present. Finally, a variety of other arthropods was observed, including Munnopsidae, four other morphospecies of isopods, and two copepod morphospecies.

Other observed mobile organisms were gastropods, ophiuroids, and marine swimming polychaetes. The *Mohnia abyssorum* (Bouchet and Warén, 1985) and other smaller gastropods likely from the Buccinidae family seemed to deliberately make their way towards the bait whereas ophiuroids were seen crossing the site regularly, but without clear taxis towards the bait. The ophiuroids could not be identified from the photographs but were seen to bury themselves into the sediment. The marine polychaetes potentially belong to the Acrocirridae family (Simon-Lledó, pers. comm.). Sessile organisms observed on the seafloor around the bait were seapens, sponges, and large xenophyophores. A *Crossota* spp. jellyfish and *Peniagone* spp. holothurian were observed floating by the camera once. Finally, macro-algal material could be seen on the seafloor potentially indicating a food source for the benthos at our abyssal site.

Table 19. Results of SIMPER analysis on both the full diversity matrix ('Original analysis') and a matrix treating the *Coryphaenoides* morphospecies as a single complex ('*Coryphaenoides* complex'), limited to the morphospecies cumulatively contributing the first 70% of differences between bait types and/or with a significant permutation test (significant values in bold).

Morphospecies	Original analysis		<i>Coryphaenoides</i> complex	
	Contribution (%)	Permutation p-value	Contribution (%)	Permutation p-value
Fish				
<i>Coryphaenoides</i> complex	-	-	5.3	0.001
<i>Coryphaenoides</i> msp. 1	4.8	0.001	-	-
<i>Coryphaenoides</i> msp. 2	5.0	0.001	-	-
<i>Barathrites iris</i>	8.2	0.001	8.7	0.001
Arthropoda				
<i>Hymenopenaeus laevis</i>	8.2	0.195	8.7	0.189
Amphipoda msp. 2	25.8	0.001	27.2	0.001
Amphipoda msp. 3	2.1	0.050	2.2	0.051
Mysidae msp. 2	4.5	0.274	4.8	0.242
Mysidae msp. 6	4.3	0.153	4.6	0.173
Mysidae msp. 8	5.3	0.390	5.6	0.372
Isopoda msp. 2	4.1	0.430	4.3	0.453
Other				
Polychaeta msp. 4	0.7	0.001	0.7	0.001

Table 20. *Coryphaenoides* spp. and *Barathrites iris* density estimates N (ind km^{-2}) based on the ‘Time of first arrival’ model from Priede and Merrett (1996), using the bottom water current speed in the first hour of lander deployment (V_w , in m s^{-1}) as measured with the in-situ lander ADCP. To estimate *Coryphaenoides* spp. density N_1 a fish swimming velocity based on observed in situ departure speed was used ($V_{fa} = 0.077 \text{ m s}^{-1}$, C. Wylie in Henriques et al. (2002)). A fish swimming velocity based on Code-Activated Transponders employed at the Cape Verde Abyssal Basin was used to estimate *Coryphaenoides* spp. density N_2 ($V_{fb} = 0.15347 \text{ m s}^{-1}$) and *B. iris* density N ($V_f = 0.2135 \text{ m s}^{-1}$) (Henriques, 2004).

Dep #	V_w	Cor. msp 1		Cor. msp 2		Cor. msp 3		Cor. complex		<i>B. iris</i>
		N_1	N_2	N_1	N_2	N_1	N_2	N_1	N_2	N
<i>S. scombrus</i>										
CL1	0.064	386	230	386	230	-	-	386	230	4
CL3	0.063	35	21	882	529	-	-	882	529	18
CL5	0.064	8	5	35	21	-	-	35	21	6
CL8	0.065	28	17	215	128	-	-	215	128	4
Mean		114±91	68±54	379±182	227±109	-	-	380±182	227±109	8±3
<i>D. gahi</i>										
CL2	0.068	13	8	826	486	-	-	826	486	10
CL4	0.062	900	543	73	44	56	34	900	543	1
CL6	0.062	74	45	226	136	-	-	226	136	1
CL7	0.079	2	1	314	176	14	8	314	176	3
Mean		247±218	149±132	360±163	211±96	35±21	21±13	567±173	335±105	4±2
Mean overall		181±112	109±68	370±113	219±67	35±21	21±13	473±121	281±73	6±2

Succession dynamics

The first scavengers at the two baits were always *Coryphaenoides* spp., which had short arrival times of 8.1 ± 0.6 min and 21.9 ± 9.6 min at the squid and fish bait respectively (Table 18) though this was not significantly different (Wilcoxon Mann-Whitney U test, $p = 0.12$). The cusk eel *B. iris* arrived earlier at the fish bait (1.4 ± 0.1 h) compared to the squid bait (2.9 ± 0.1 h) (Table 18), but again this difference was not significant (Welch t-test, $p = 0.23$). Like *Coryphaenoides* spp., the rarer fish *B. robustus* and *H. bathybius* arrived earlier at the squid bait, but significant differences could not be ascertained as they were both observed only once per bait treatment (Table 18).

The highest total number of fish observed was 20 individuals in one frame, at 7.17 hours (deployment AKS311 - fish bait). The highest total number of fish at the squid bait was 7, at 1.83 hours (deployment AKS308). Overall, fish numbers peaked at 12.8 ± 3.0 hr with an average $maxN$ of 15.5 ± 1.6 on the fish bait, and at 1.3 ± 0.3 hr with an average $maxN$ of 5.5 ± 0.9 on squid bait (Table 18). Both the $maxN$ and time of $maxN$ of all scavenging fishes was significantly different between bait types (t-test, $p = 0.001$ and Welch’s t-test, $p = 0.03$, respectively).

Non-fish morphospecies that arrived faster at the fish bait were *H. laevis*, Amphipoda msp. 3, and the two gastropod morphospecies. Significantly earlier arrival times (t-test, $p = 0.01$) were detected for *H. laevis* at the fish (0.7 ± 0.1 h) compared to the squid (1.7 ± 0.3 h). Morphospecies that arrived faster at the squid bait included the two Aristeidae morphospecies, all mysids, all isopods, all copepods, and the ophiuroids, but none of these arrival times were significantly different (Table 18). The arrival times for the amphipods were similar between the two bait types (except for msp. 3), and there was no clear pattern in arrival times for the polychaetes. In total, 22 of the 35 morphospecies (63%) arrived earlier

at the squid bait and 10 arrived later (29%) at the squid bait.

Despite the faster arrival times for the majority of morphospecies at the squid bait, the *maxN* and time of *maxN* was greater at the fish bait for almost all morphospecies (Table 18). In total, 20 of the 35 morphospecies (57%) had a greater *maxN* at the fish bait, 1 had a smaller (3%) *maxN* (Mysidae msp. 5), and the remaining 14 morphospecies (40%) had a *maxN* of 1. The difference in *maxN* between bait types was significant for all fish morphospecies (Table 18). For 27 morphospecies (77%) the *maxN* was later at the fish bait, and 5 morphospecies (14%) had an earlier time of *maxN*. The time of *maxN* for both *Coryphaenoides* spp. and *B. iris* occurred roughly 9 hours later in the fish deployments compared to the squid deployments (Table 18). Also, the *maxN* for *H. laevis*, Amphipoda msp. 2, Mysid msp. 7 and msp. 8, and Copepoda msp. 1 all occurred significantly later at the fish bait compared to squid (Table 18).

Overall, the highest total number of scavengers observed at the fish bait was 86 at 19.0 hours into deployment AKS303, while for the squid bait it was four times lower (i.e., 21 scavengers at 12.4, 12.8 and 12.8 hours into deployment AKS301). On average, over all deployments, the highest total *maxN* was 53.2 ± 13.0 (at 18.9 ± 1.4 hr) on the fish and 17.8 ± 2.0 (at 7.6 ± 1.7) on squid bait (Table 18, Figure 22). The higher total *maxN* at the fish bait was almost significant (Welch t-test, $p = 0.07$), while the earlier time of *maxN* at the squid bait was highly significant (t-test, $p = 0.002$).

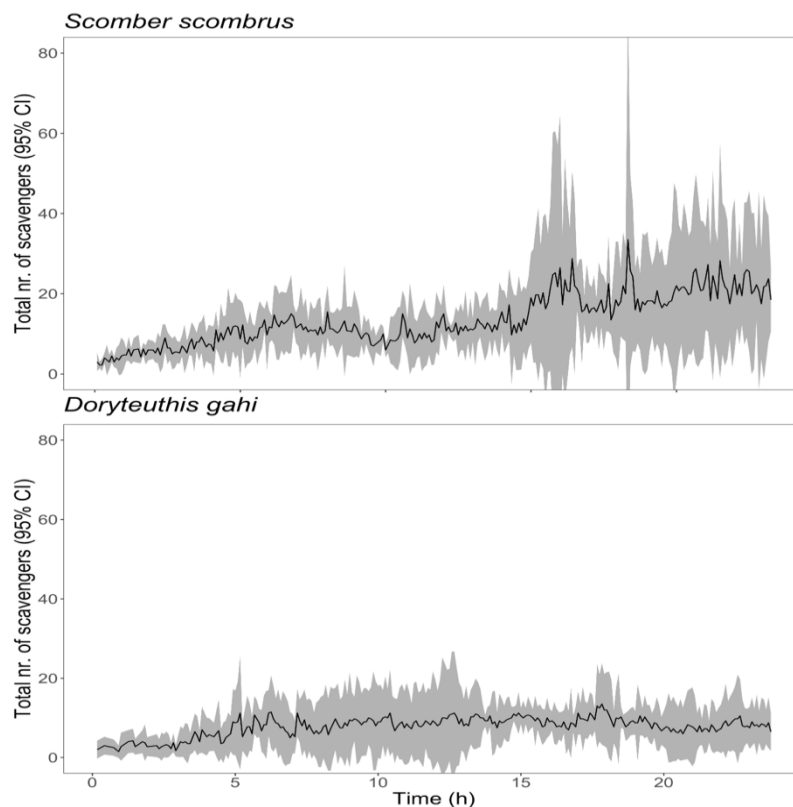


Figure 22. Mean total number of scavengers over time for fish (*Scomber scombrus*, top) and squid (*Doryteuthis gahi*, bottom) bait with 95% CI.

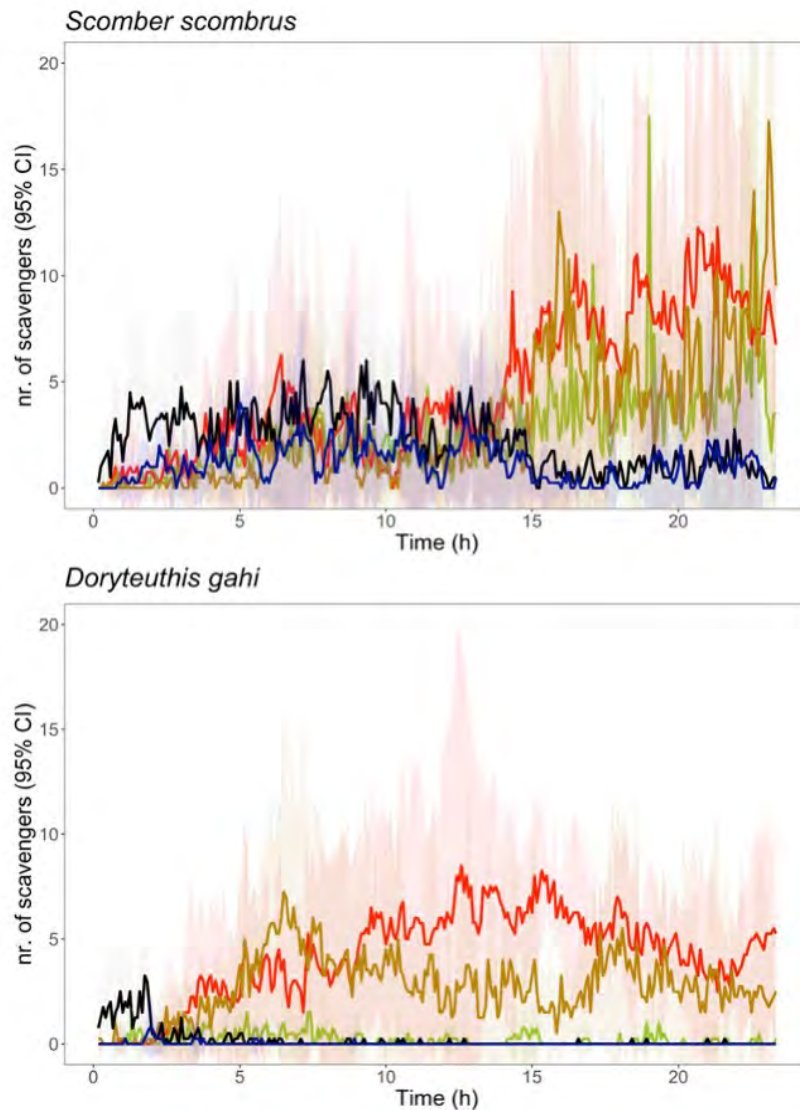


Figure 23. Mean number of *Coryphaenoides* spp. complex (black), *Barathrites iris* (blue), *Hymenopenaeus laevis* (red), all Mysidae morphospecies (yellow), and amphipods msp. 2 (green) over time with 95% CI.

For both bait types, the total number of scavengers at the bait increased over time (Figure 22). At the fish bait, a mean of 5.3 individuals was observed in the first three hours which increased to 22.5 individuals in last three hours of the deployment (Pearson's $R = 0.86$, $p < 0.001$, slope $+0.8 \text{ ind. frame}^{-1} \text{ h}^{-1}$). Although the increase in the number of scavengers at the squid bait was also significant (Pearson's $R = 0.45$, $p < 0.001$, slope $+0.2 \text{ ind. frame}^{-1} \text{ h}^{-1}$), it increased from a mean of 2.8 individuals in the first three hours to only 7.7 individuals in the last three hours.

The dynamics of *Coryphaenoides* spp., *B. iris*, *H. laevis*, all mysids, and Amphipoda msp. 2 for all deployments (Figure 23) showed an increase in crustaceans when fish departed, and the difference in *H. laevis* vs. Amphipoda msp. 2 dominance between bait type as indicated by the SIMPER analysis. Fish and crustacean abundance were indeed significantly inversely correlated (Zero-Inflated Negative Binomial regression, $p \ll 0.001$, Figure 24), suggesting avoidance behaviour by the crustaceans. Plotting fish and crustacean abundance against the hourly current direction showed a link to the local diurnal tides (Figure 25).

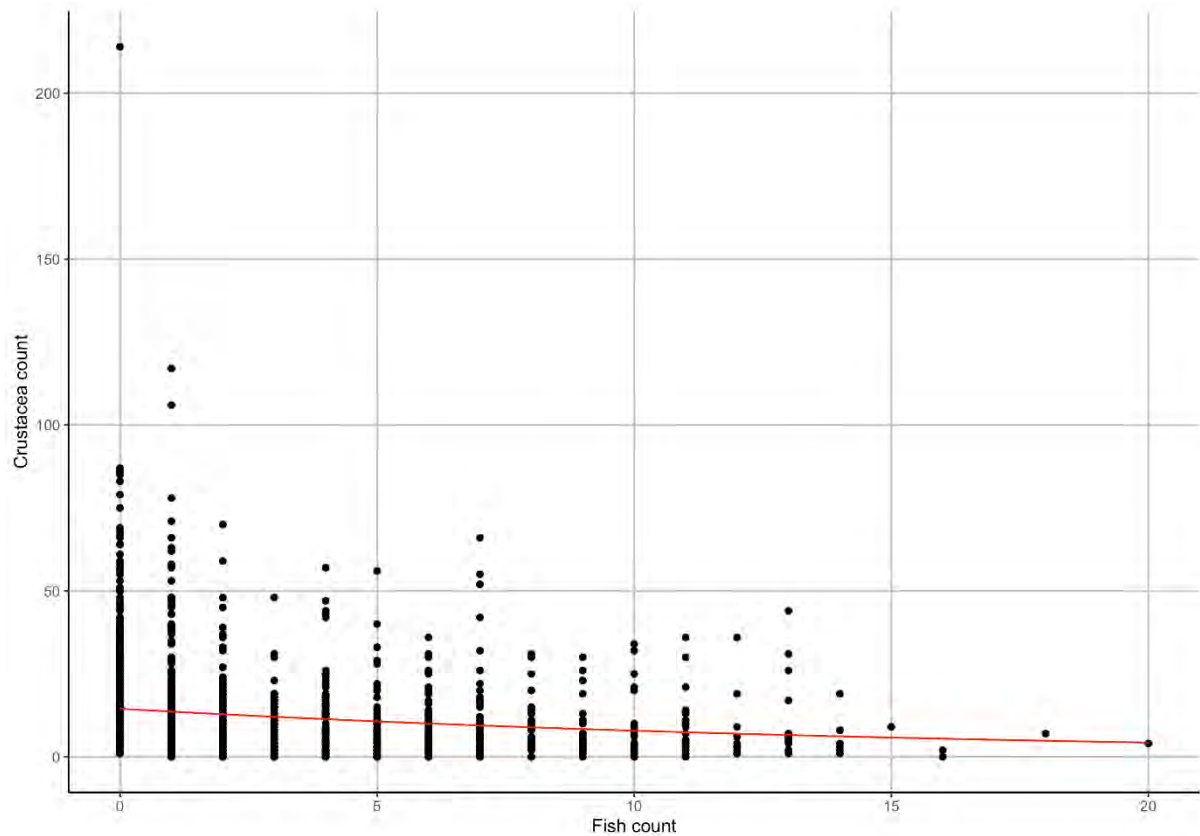


Figure 24. Fitted Zero-Inflated Negative Binomial regression model for total Crustacea versus total fish counts over all eight deployments, $y = e^{2.67 - 0.061 \times x}$, indicating the slope is highly significantly different from 0 ($p \ll 0.001$).

Reference specimens

Coryphaenoides spp. from the baited trap had an average minimum wet mass of 2.12 ± 0.15 kg ($n = 21$) and an average pre-anal fin length of 26.5 ± 0.57 cm ($n = 17$). *B. iris* were pink-white to mottled brown in colour, and had an average minimum wet mass of 3.64 ± 0.49 kg ($n = 6$) and an average pre-anal fin length of 31.8 ± 1.4 cm ($n = 6$). Identification of a random subset of amphipods captured by the baited trap showed the presence of multiple amphipod species, including *Abyssorchomene chevreuxi*, *Abyssorchomene distinctus*, *Abyssorchomene patriciaea*, *Paralicella tenuipes*, *Paralicella caperesca*, and *Eurythenes* sp. No mysids were captured in the baited trap. A large number of empty amphipod exoskeletons was found in the amphipod traps, potentially indicating moulding while feeding; a phenomenon also briefly mentioned in Havermans and Smetacek (2018).

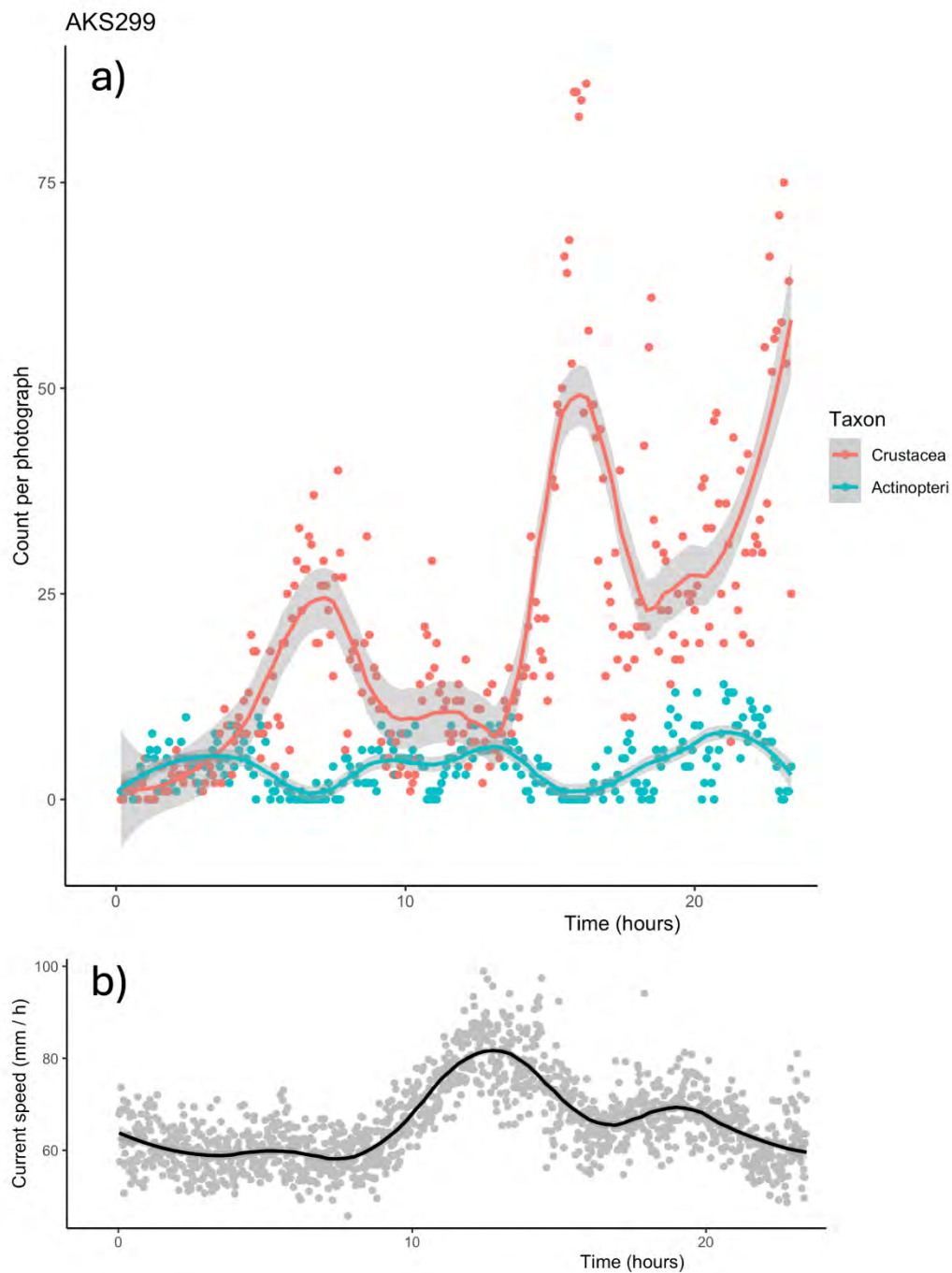


Figure 25. Total fish (blue) and total crustacean (red) abundances during deployment AKS299 using fish *S. scombrus* bait. Lines are smoothed with a Local Polynomial Regression Fitting using an α of 0.3 to show how peaks and troughs of Crustacea and Actinopteri appear opposite. The black line indicates the current direction in degrees, the grey horizontal line is at 180° i.e. below the grey line are eastward currents, the grey line itself is a southward current, and above the grey line are westward currents.

The tissue composition (dry to wet mass ratio, C content and N content as wt% DM, and C: N ratio) and calculated trophic levels of trap-caught specimens can be seen in [Table 21](#). The amphipod *P. caperesca*

had an unusually high average C: N ratio of 15.6 ± 6.8 ($n = 3$). The isospace biplot showed a clear distinction between pelagic and demersal organisms' niches (Figure 26). The pelagic gelatinous fauna had a slightly lower trophic level (1.9) compared to the non-gelatinous zooplankton (assumed base at $TL = 2$), indicating feeding on lower trophic levels such as phytoplankton. The pelagic fish and pelagic shrimp had trophic levels of 2.1 and 2.8 respectively, indicating a higher position in the pelagic trophic web. The trophic level of demersal scavenger amphipods *P. caperesca* ($TL = 2.5$), *A. patriciaea* ($TL = 2.6$), and *A. chevreuxi* ($TL = 2.7$) were similar to the pelagic fish and shrimp (Table 21). The specimens of these three amphipods species were relatively small (ranging from 10.6 ± 1.7 mm to 19.8 ± 5.4 mm) but had a large variation in both their $\delta^{13}C$ and $\delta^{15}N$ values (Figure 26) suggesting a wide variety of food sources in their diet. The considerably bigger amphipod *Eurythenes* sp. (60.4 ± 10.6 mm) was at trophic level 3.4. Other higher trophic level demersal scavengers included the fish *Coryphaenoides* spp. ($TL = 4.0$) and *B. iris* ($TL = 4.0$), and amphipods *A. distinctus* ($TL = 4.2$) and *P. tenuipes* ($TL = 4.1$). *A. distinctus* was only somewhat larger (24.9 ± 4.0 mm) than the other two species in the *Abyssochormene* genus (10.6 ± 1.7 mm and 19.8 ± 5.4 mm) which were living at a lower trophic level. Also, *P. tenuipes* had a similar size (12.1 ± 1.8 mm) to the amphipods living at the lower trophic levels. The similar size range of amphipods with large differences in their trophic niches suggests these differences are based on their diet preference, and not only their size. Ontogenetic diet shifts were only detected for *A. chevreuxi* and *A. distinctus* indicating a similar diet over all sizes tested.

4.3 Discussion

Upper ocean ecosystems are already experiencing changes due to human impact like climate change and fisheries, and these changes will likely proliferate into the future (Edwards and Richardson, 2004; Purcell, 2011). Shifts in pelagic community composition are taking place, with a noticeable shift from fish to squid and jelly-dominated communities (Doubleday et al., 2016). The quantity and quality of abyssal food-falls are directly dependent on these changing pelagic communities. Abyssal food falls are increasingly being recognised as an important food source for abyssal communities and they shape community dynamics and evolution of abyssal scavengers (Hoving et al., 2023). Additionally, the processing of food-falls by scavengers alters the food characteristics, potentially making it suitable for consumption for other benthic organisms and allows distribution of food over wider areas. However, to date, it is unknown how changes in food-fall composition may impact abyssal scavengers and thus these ecosystem functions. This study assessed the response of abyssal scavengers to shifts in food fall composition by deploying a baited camera lander in the Cabo Verde Abyssal Basin baited with either Atlantic mackerel (*S. scombrus*) or squid (*D. gahi*). Both species are found in the Atlantic, although *D. gahi* is mostly known from the South Atlantic. Even though pelagic fish and squid are abundant in the studied region, we suspect regular food falls of these kinds due to the nearby coastal zone and squid beaks being found in the stomachs of many of the scavengers collected at the seafloor. We found a shift from fish to squid bait significantly altered the community composition of bait-attending scavengers and resulted in significantly greater scavenger rates (both wet consumption and energy-corrected rates).

Bait-specific diversity and dynamics

At the beginning of both fish- and squid-baited deployments, when bait was still plentiful, no difference was observed in scavengers arriving at the bait. There was a trend towards faster arrival times for scavengers at the squid bait (63% of morphospecies), but these differences in time of first arrival were not significant. Potentially, the scavenging community around Cabo Verde could be more sensitive to

detecting squid food falls, as squid is known to be abundant around the Cabo Verde archipelago (Merten et al., 2021), even though the oily fish bait contains more lipids and fatty acids responsible for stronger odour plumes (see references in Scheer et al. (2022)).

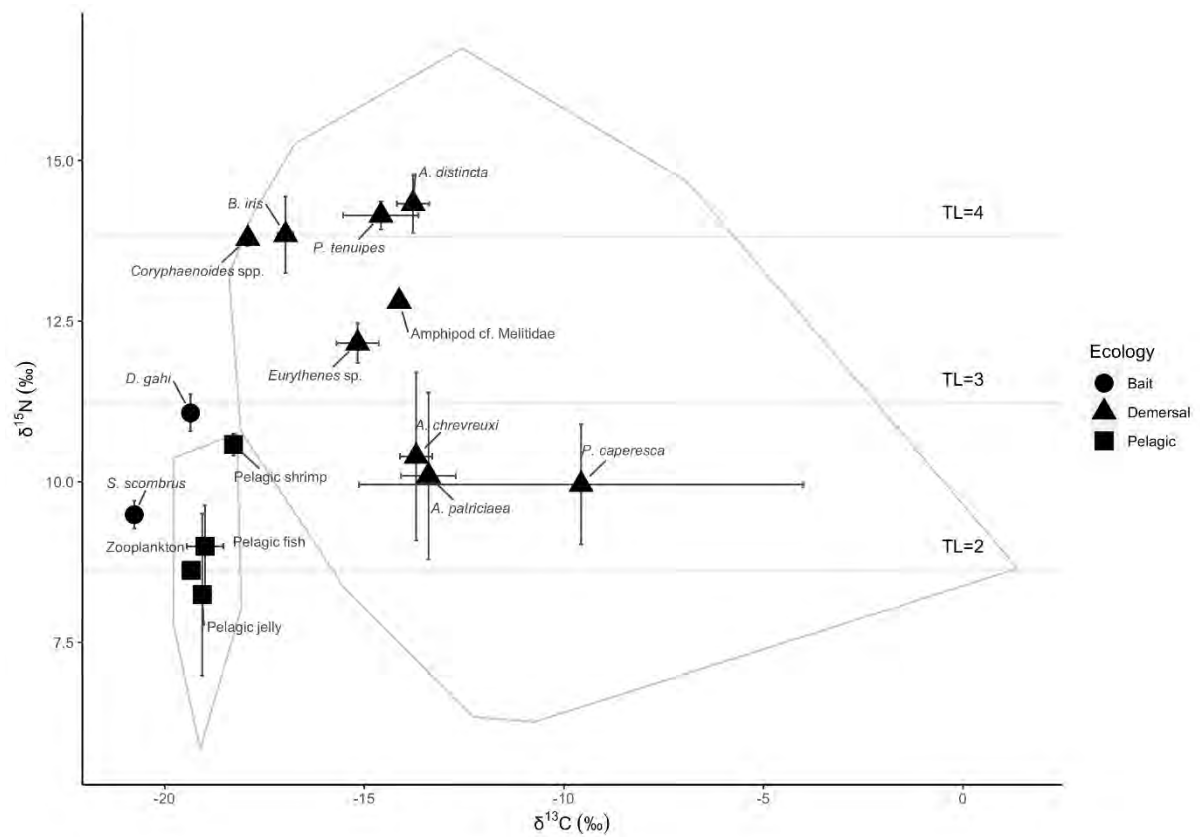


Figure 26. Isospace biplot based on $\delta^{13}\text{C}$ (‰) and $\delta^{15}\text{N}$ (‰) of pelagic and demersal reference specimens. The convex hulls delineate the pelagic and demersal communities. For comparison, the used bait species *S. scombrus* and *D. gahi* are also included. Error bars show standard errors.

Table 21. Tissue composition, size and trophic level of reference specimens: dry mass to wet mass ratio, C content (wt% of DM), N content (wt% of DM), $\delta^{13}\text{C}$ (‰) corrected following Post et al. (2007), $\delta^{15}\text{N}$ (‰), size (mm; pre-anal fin length for fish, dorsal line from tip rostrum to tip telson for amphipods), and the trophic level (TL) based on their mean $\delta^{15}\text{N}$ referenced against the local zooplankton with an assumed TL = 2. The ‘pelagic jelly’ sample is a mix of a salp, siphonophore, and medusa jelly.

Taxon	DM/WM	C content (wt%)	N content (wt%)	C: N	$\delta^{13}\text{C}_{\text{corrected}}$ (‰)	$\delta^{15}\text{N}$ (‰)	Size (mm)	TL
Scavenging fish								
<i>Coryphaenoides</i> spp. (n=10)	0.216±0.008	40.9±1.4	13.0±0.5	3.1±0.01	-17.9±0.1	13.8±0.1	261±7.2 ^c	4.0
<i>Barathrites iris</i> (n=7)	0.103±0.016	35.9±3.0	11.0±1.0	3.3±0.07	-17.0±0.2	13.8±0.6	318±14.0 ^c	4.0
Scavenging amphipods								
<i>Abyssorchomene chevreuxi</i> (n=7)	0.267±0.048	27.0±1.1	4.5±0.3	6.1±0.4	-13.7±0.4	10.4±1.3	19.8±5.4	2.7
<i>Abyssorchomene distinctus</i> (n=10)	0.193±0.031	25.2±1.8	4.3±0.5	6.1±0.3	-13.8±0.4	14.3±0.5	24.9±4.0	4.2
<i>Abyssorchomene patriciaea</i> (n=6)	0.320±0.104	25.8±1.4	4.3±0.3	6.2±0.5	-13.4±0.7	10.1±1.3	10.6±1.7	2.6
Amphipod cf. Melitidae (n=1)	0.128	20.6	4.2	5.0	-14.1	12.8	40.2	3.6
<i>Eurythenes</i> sp. (n=9)	0.186±0.021	29.8±2.7	4.4±0.2	6.8±0.5	-15.2±0.5	12.2±0.3	60.4±10.6	3.4
<i>Paralicella caperesca</i> (n=3)	0.218±0.050	38.9±6.3	3.5±1.2	15.6±6.8	-9.57±5.6	10.0±0.9	16.3±3.7	2.5
<i>Paralicella tenuipes</i> (n=10)	0.344±0.049	42.5±2.2	4.6±0.3	9.8±1.0	-14.6±0.9	14.1±0.2	12.1±1.8	4.1
Pelagic specimens								
Zooplankton mix (n=2)	NA ^a	29.0±4.9	5.8±1.2	5.0±0.2	-19.3±0.1	8.6±0.04	NA	2.0 ^b
Pelagic jelly (n = 3)	0.05±0.001	13.6±2.2	3.6±0.5	3.7±0.2	-19.1±0.2	8.2±1.3	NA	1.9
Pelagic fish (n=4)	0.179±0.036	39.4±2.8	11.8±1.7	3.5±0.3	-19.0±0.5	9.0±0.6	NA	2.1
Pelagic shrimp (n=2)	0.168±0.082	32.6±5.6	8.0±1.9	4.2±0.3	-18.3±0.1	10.6±0.2	NA	2.8
Bait								
<i>Scomber scombrus</i> (n=5)	0.282±0.014	46.3±0.4	13.9±0.1	3.3±0.06	-20.8±0.2	9.49±0.2	NA	NA
<i>Doryteuthis gahi</i> (n=5)	0.253±0.007	43.0±0.3	12.2±0.4	3.6±0.2	-19.4±0.1	11.1±0.3	NA	NA

^a Not obtained as the zooplankton mix contained too much water for a reliable wet mass of just the organisms.

^b Zooplankton assumed as base of the food-web as primary consumers i.e. TL = 2.

^c The reported sizes of *Coryphaenoides* spp. and *B. iris* in this table only concern specimens also studied for tissue composition and stable isotopes, hence will differ from the size values reported in the text which concern all captured organisms.

The squid was very rapidly consumed at a rate ten-fold (wet consumption) or three-fold (energy-corrected rates) greater than the fish bait. The rapid removal of squid may be caused by their smaller size and softer tissue, as more effort may be needed to pierce and consume the more rigid fish skin and tissue fused to bones. Difficulty piercing fish tissue was observed for tuna bait in Harbour et al. (2020). The squid consumption rate of 25.4 kg WM d⁻¹ is a magnitude greater than observed at the Fram Strait (1.3 kg WM d⁻¹, Rohlfer et al., 2022) and in the southern Norwegian Sea (0.7 kg WM d⁻¹, Scheer et al., 2022). Also, the fish consumption rate of 2.8 kg WM d⁻¹ was greater than in previous studies using the same fish species, but the difference is less severe (1.4 kg WM d⁻¹, Sweetman et al., 2014; 0.8 WM d⁻¹, Scheer et al., 2022). Additionally, Scheer et al. (2022) did not observe significant differences in scavenging rates between fish (*S. scrombrus*) and squid (*Illex coindetii*). These different results might be attributed to geographic area as Cabo Verde is a tropical region and a known cephalopod diversity hotspot (Visser et al., 2021), or to depth and related community composition. The fast rate of squid removal indicates that natural squid food falls will be consumed very fast that it is difficult for scientists to observe them *in situ*, as also concluded for jellyfish falls (Sweetman and Chapman, 2015) and a natural fish food fall (Soltwedel et al., 2003). Hence, the importance of squid and other small-sized and soft carrion as a food source for abyssal benthic communities might be currently underestimated (0.2–0.4% of POC flux, Drazen, 2002).

The rapid squid removal caused significant differences in scavenging dynamics, with scavenging fish departing earlier during squid deployments with only a few individuals occasionally attending the camera lander later into the deployment. Whereas at the fish bait scavenging fish keep lingering, and in some deployments, we even observed multiple peaks of fish arrival. These peaks of fish arrival depart from the classic arrival-departure behaviour of scavenging fish (Bailey and Priede, 2002), and were linked to tidal changes in bottom currents, indicating prolonged ability of odour plume detection by surrounding fish communities. After the early departure of scavenging fish at the squid bait a rapid increase in crustaceans was observed, with a peak in maximum abundance significantly earlier compared to the fish bait. Even though the development of the crustacean community occurs earlier during squid bait deployments, their *maxN* is still significantly lower compared to at the fish bait. This indicates that the fast removal of squid bait may cause a faster loss of odour plume detection by crustaceans.

Not only the dynamics, but also the community composition developing was significantly different between bait types. There was a 42% difference in community composition of bait attending morphospecies, mainly caused by *Coryphaenoides* spp., *Barathrites iris*, *Hymenopeneus laevis*, and Amphipoda msp. 2. In contrast, no difference in scavenger composition was found between fish and squid in the southern Norwegian Sea (Scheer et al., 2022), nor between fish and jellyfish (Sweetman et al., 2014), which were studies using relatively similar methodologies. However, the scavenger aggregation was different between two different jellyfish types (Sweetman et al., 2014) and between squid and jellyfish in the Arctic (Rohlfer et al., 2022). Again, these differences may have to do with the different geographic area (i.e., not in the tropics) and depth (i.e., shallower waters) of previous studies, but to our knowledge no such comparative studies between bait types have been conducted at tropical abyssal areas before to compare our results to.

A shift to faster-consumed food falls like squid may favour faster swimming individuals, with slower species arriving later missing the opportunity to feed from the already consumed bait. The *maxN* of *B. iris* was almost six-fold lower at the squid bait, whereas the *maxN* of *Coryphaenoides* spp. was only two-fold lower at the squid bait compared to the fish bait, indicating the response to changing food falls may be less severe for *Coryphaenoides* spp. Although it may be expected the muscular *Coryphaenoides* spp. is a faster swimmer than the more 'jelly-like' *B. iris*, the swimming speeds estimated from transponders indicate the

opposite (Henriques, 2004). However, to our knowledge these are the only two individuals of *B. iris* ever for which swimming speed has been measured, and swimming speed for both species is also variable with time and distance from the bait. *H. laevis* was the dominant morphospecies during the squid bait deployment, with a relative *maxN* of 70%. In contrast, at the fish bait Amphipoda msp. 2 had the highest relative *maxN* at 50%. This difference in dominance may be linked to chemoreception abilities, as it is known that decapods and amphipods have different threshold concentrations to induce feeding behaviour, with faster animals generally having lower detection thresholds (Derby et al., 2016; Havermans and Smetacek, 2018). The bigger, and potentially faster *H. laevis* may be able to better detect the less prominent squid odour plume. The fish tissue and stronger fish odour plume are likely present for longer, which may allow the formation of dense aggregations of amphipods like Amphipoda msp. 2 on the fish bait through social feeding cues. The faster consumption of squid (and other similarly small and soft food-falls) may thus negatively impact amphipods and other scavengers with a higher detection threshold and/or using social chemical cues.

Even though the fast squid removal seems to drive the discussed differences in scavenging dynamics, the scavenging rates alone could not explain the observed divergence in community composition i.e., there were non-significant correlations between the nMDS scores and the various measures of scavenging rates. Additionally, the difference in community composition between baits may also be caused by interactions between scavengers. We showed that the peaks of fish abundance were strongly correlated to dips in crustacean abundance, highlighting the interactions between bait-attending scavengers. Some bait-attending fish are necrophagivores i.e., not feeding directly on the bait but instead preying on crustaceans attracted to the bait (Drazen and Sutton, 2017). This corresponds to the observed behaviour of known necrophagivore, *Bassozetus robustus*, which was never seen eating the bait directly. Therefore, the observed changes in the crustacean community, like the loss of dominance of Amphipoda msp. 2 and a lower crustacean abundance at the squid bait, will consequently negatively impact necrophagivores.

Observed biodiversity was not significantly different between bait types, however, rarefaction indicated a greater expected species richness at the squid bait. This indicates that extrapolation of the initial dynamics and succession of morphospecies at the squid bait would result in overall greater biodiversity, but the fast removal of squid bait and resulting changes in dynamics do not allow this full diversity to develop at the squid bait. At large carcasses, like whale falls, residence time of tissue and bones is long enough for succession to progress beyond the scavenging stage and allow chemoautotrophic systems to develop (Higgs et al., 2014; C. R. Smith et al., 2015). At a single natural fish food fall, amphipods were observed directly on and near the carcass, with necrophagous zoarcid fish presumably preying on the amphipods arriving with the currents, and some ophiuroids feeding at the carcass (Soltwedel et al., 2003).

Trophic position

Stable isotope analysis on trap-caught specimens showed that the isospaces of pelagic and demersal species were distinct, and that the scavengers occupied three different trophic levels (Figure 26). The overlap in $\delta^{13}\text{C}$ values within amphipod groups, but their separation across multiple trophic levels suggests similar basal C-sources, with potential competition for food sources within the amphipod groups in TL2 i.e., *A. chevreuxi*, *A. patriciaea*, and *P. caperesca* and in TL4 i.e., *P. tenuipes* and *A. distinctus*. At the Porcupine Abyssal Plain (PAP) the trophic niche of *A. chevreuxi* (Iken et al., 2001) was much closer to the trophic niche of *A. distinctus* in this study. While little is known about diet of specific *Abyssoorchomene* species in general, they seem to have a varied diet and iteroparous reproduction (multiple reproductive cycles within its lifetime), and therefore may be able to take advantage of greater or varied food availability

from increased organic matter flux to the seafloor (Horton et al., 2020). *A. distinctus* and *A. chevreuxi* were the only two species for which ontogenetic shifts in their diet could be detected based on their $\delta^{15}\text{N}$ values.

The congener amphipods *P. tenuipes* and *P. caperesca* had strikingly different trophic niches (Figure 26). *P. tenuipes* had a high trophic position and a narrow trophic niche, suggesting it is an obligate necrophage. In contrast, *P. caperesca* has a lower trophic position and a wide trophic niche. At the Porcupine Abyssal Plain, *P. tenuipes* was also found to have a higher trophic level than *P. caperesca* ($\delta^{15}\text{N}$ of 15.61‰ and 13.60‰ respectively, Iken et al., 2001), but the absolute difference was smaller compared to the CVAB ($\delta^{15}\text{N}$ of 14.1‰ and 10.0‰ respectively, Table 21). The isotope signatures of *P. caperesca* may be caused by a number of factors, including a lower sample size ($n = 3$ vs. $n = 10$ for *P. tenuipes*), the combination of a high C: N ratio and chitinous tissue potentially skewing results (Tokuda et al., 2020), and/ or a potentially cryptic species complex (Jazdzewska et al., 2021). However, if stable isotope signature reflects true trophic position, it suggests that *P. caperesca* may display alternative feeding modes in addition to obligate necrophagy, such as the consumption of phytodetritus or macroalgal material. Alternative feeding modes are common in other deep scavenging amphipods (Blankenship and Levin, 2007), and in combination with its semelparous reproductive cycle (reproducing once in its lifetime) it would allow quick response to changes in nutrient input (Duffy et al., 2016). Consumption by *P. caperesca* of the large macroalgal mats observed at our study site, which are not known to occur at PAP, could potentially explain the increased difference in $\delta^{15}\text{N}$ between the congeners compared to PAP. A more focused study on diet preferences of *Paralicella* spp., potentially combining stable isotopes with fatty acid analysis (Kelly and Scheibling, 2012; Shi et al., 2020), could help to better understand their varying trophic niches and the potential role of phytodetritus and macrophyte material.

The contrasting trophic niches of *P. tenuipes* and *P. caperesca* may explain the decadal variation in their abundance correlated to the Atlantic Multi-decadal Oscillation index (AMO) (Horton et al., 2020). *P. caperesca* was found to be a key species characterising the AMO warm phase when the organic matter supply would be high. The potential alternative feeding modes of *P. caperesca* would allow them to benefit more from the greater influx of phytodetrital material than *P. tenuipes*. During the AMO cool phase, when organic matter supply is low, *P. tenuipes* becomes the most dominant out of the two as it is not as dependent on the direct influx of phytodetrital material as an obligate necrophage.

The fish *Coryphaenoides* spp. and *B. iris*, which are known to scavenge carrion, had similar trophic niches indicating potential competition. They had a high trophic level (TL = 4.0 for both), but not the highest which was 4.2 for *A. distinctus*. Iken et al. (2001) found that mobile scavengers from the Porcupine Abyssal Plain had a lower trophic position than top benthic predators, indicating they were indeed feeding on pelagic food falls and bypassing the benthic food web where prey would have relatively high $\delta^{15}\text{N}$ values because of the recycling of sedimentary organic matter. *Coryphaenoides* spp. and *B. iris* are known to be facultative scavengers, where carrion makes up a large part of its diet (carrion supplies 69% to the diet of *C. armatus* in the Pacific), but carrion is not the exclusive source of food (Drazen and Sutton, 2017) and predation on benthic fauna has been well documented e.g., Drazen et al. (2008). No ontogenetic diet shift was detected in *Coryphaenoides* spp. However, it is known *C. armatus* does have ontogenetic diet shifts feeding more on benthic invertebrates as juveniles before switching to pelagic prey as adults (Drazen and Sutton, 2017). Stomach content analysis has also shown it to be a very generalist feeder with stomach contents including benthic invertebrates, pelagic prey like fish and squid, and even terrestrial and neritic derived material like insects, vegetable, bird remains, and phytodetritus (Haedrich and Henderson, 1974; Jeffreys et al., 2011). It is possible that the lack of an ontogenetic relationship was due to the limited sampled size range (average

pre-anal fin length of 26.5 ± 0.57 cm, $n = 17$) and the lack of juveniles.

Possible future changes in Cabo Verde abyssal scavengers

Higher seawater temperatures, greater productivity, and C export through the biological C pump, but also expanding Oxygen Minimum Zones (OMZs) are expected in upwelling regions, like the Cabo Verde basin, under climate change (Sweetman et al., 2017). These changes will occur alongside shifts in upper ocean pelagic communities, and thus also impact demersal scavenging communities. As squid can cope better with low oxygen conditions (Doubleday et al., 2016) they are expected to proliferate even more in the upwelling regions of the Cabo Verde basin. The results of this study suggest this will favour faster swimming organisms with lower chemoreception thresholds, causing a change in community composition with potentially cascading effects through the abyssal food web.

Even though it is unclear how food fall distribution is exactly linked to productivity (see references in Janßen et al. (2000)), an increase in food falls in upwelling regions may be expected with increased productivity under climate change. The quality of the material reaching the seafloor will depend on the degradation rate, which is influenced by both temperature – higher temperatures will increase degradation – and oxygen concentration – lower concentrations will slow down degradation (Campanyà-Llovet et al., 2017). However, these changes may be negligible due to the fast-sinking rate of mid-sized carrion like small fish and squid (Lebrato et al., 2011, 2013). Variations in the quality and quantity of food due to climate cycles influences amphipod abundance and diversity (Horton et al., 2020). An increase in productivity and food availability will benefit some amphipods, like *Abyssochomene* spp. and *P. caperesca* which can benefit from greater food availability and variability, thus altering the scavenging community composition. These variations in the amphipod community on decadal time scales may already be visible in the Cabo Verde region, as some amphipods known to the area in 1980 (*Alicella gigantea*, *Cyclocaris* sp., *Hirondellea* sp., and *A. gerulicorbis*; (Thurston, 1990) were not sampled by us. Additionally, we sampled *A. patriciaea* which was not found at all previously.

As fish arrival time – a proxy of fish abundance – is known to be correlated to productivity in the area (Priede et al., 1991), a future increase in productivity will likely result in even greater scavenger fish abundances and shorter arrival times. Our estimated local *Coryphaenoides* spp. density of 473 fish km⁻² was more than twice the density of 185 fish km⁻² estimated for the eastern Cabo Verde abyssal basin (4,000 m, 15°N 20.5°W, 500 km eastwards, Henriques et al. (2002) and also more than twice the density that would be expected solely based on depth (205 fish km⁻², Linley et al., 2018). Our mean fish arrival time over all deployments of 15 minutes was very short; for comparison, it took 49 minutes for fish to arrive at the eastern CVAB site (Henriques et al., 2002) and 138 minutes at the oligotrophic Madeira Abyssal Plain (Priede et al., 1991). The diversity was similar between our study site and the more eastern study site, with *Coryphaenoides* spp., *Barathrites iris*, and *Histiobranchus bathybius* being abundant demersal fauna. Our additional observation of *Bassozetus robustus* provides an addition to the known abyssal scavenging fish in this region. The invertebrate fauna observed in our study was also similar to those observed at the eastern site, including the presence of Aristeidae shrimp *Cerataspis monstrosus*, amphipods and ophiuroids, and floating holothurians.

The observed fish arrival times and estimated densities support the idea that the complex current systems around the Cabo Verde basin support high productivity (Peña-Izquierdo et al., 2012; Pelegrí et al., 2017) and hence densities of demersal scavengers. If material exported from coastal Western Africa brought westwards by the North Equatorial Current and Guinea Dome currents (Peña-Izquierdo et al., 2012) would be the only food source, greater scavenger activity and abundance would be expected in the eastern site

closer to the continent (Henriques et al., 2002), which is not the case. Therefore, the proximity of our study site to the Cabo Verde archipelago and the local productivity, like large squid blooms, might be a more important driver of the local scavenging community than exported material.

Barathrites iris is known to be rare, and its abundance is thought to vary with the overlying trophic regime, with typically greater abundances in oligotrophic areas (Janßen et al., 2000). The estimated abundance of *B. iris* at our study site is indeed low at 6 ± 2 fish km^{-2} which is one to two orders of magnitude lower than the estimated *Coryphaenoides* spp. density. It is hypothesised *B. iris* is not captured on camera in eutrophic regions as much, because they are less dependent on food falls hence not as attracted by bait odour, actively avoiding aggressive amphipods like *Eurythenes* spp., or being dominated by macrourids (Janßen et al., 2000). Contrary to the idea that *B. iris* would be rare in productive areas, at our relatively productive study site the *maxN* abundance of *B. iris* was quite high (*maxN* = 9, AKS299-CL3) similarly to the *maxN* of 11 at the least productive abyssal station in the Arabian Sea (Janßen et al., 2000), and greater than the eastern Cabo Verde abyssal site (*maxN* = 1-2, (Henriques et al., 2002), other Arabian Sea stations (*maxN* = 2 to 5), and the abyssal Sargasso Sea (*maxN* = 2 to 4, Fleury and Drazen, 2013). Although differences in camera angles between studies may explain some of the variation, the observed *B. iris* in this study were mainly attending the bait actively ingesting food i.e., not observed in the periphery of images. Additionally, they were ingesting bait alongside *Coryphaenoides* spp., with similar *maxN* values, and not displaying any avoidance behaviour. It is unclear if the abundance of *B. iris* at the bait was impacted by the abundance of aggressive amphipods like *Eurythenes* sp. but would be deemed unlikely as amphipods were plentiful in both the camera images and amphipod traps. Potentially, the relatively high bait attendance of *B. iris* may suggest larger dependence on carrion in this region. A change in local productivity under climate change may thus influence *B. iris* through trophic interactions, but it's still unclear how exactly. Facultative scavengers like *B. iris* and *Coryphaenoides* spp. may experience limited impact from changing food falls, as they can alternate their feeding strategy.

It is clear that food-fall composition will have a direct effect on demersal scavengers, altering their scavenging activity and community composition. Future research could focus on changes with other known food-fall types, like gelatinous zooplankton, organic waste etc (Henschke et al., 2013; Lebrato et al., 2019; Robison et al., 2005; Yamamoto et al., 2009). Additionally, a better understanding of the function of scavengers in the abyssal food web will help predict how changes in the scavenging community may cascade through the wider deep-sea benthic ecosystem.

5. Case study 4 - Trophic niches of the cold-water corals *Desmophyllum pertusum* (*Lophelia pertusa*) and *Madrepora oculata* in the Lampaul Canyon (Bay of Biscay)

5.1 Material & Methods

Sampling

All samples were taken in the Lampaul Canyon (Figure 27) during the ChEReef 2021 cruise (05/08 – 05/09/2021) onboard RV *Thalassa*. The full cruise report, operation report, sampling metadata and sensor data are available directly from the French Oceanographic Fleet’s website (Menot and Tourolle, 2021).

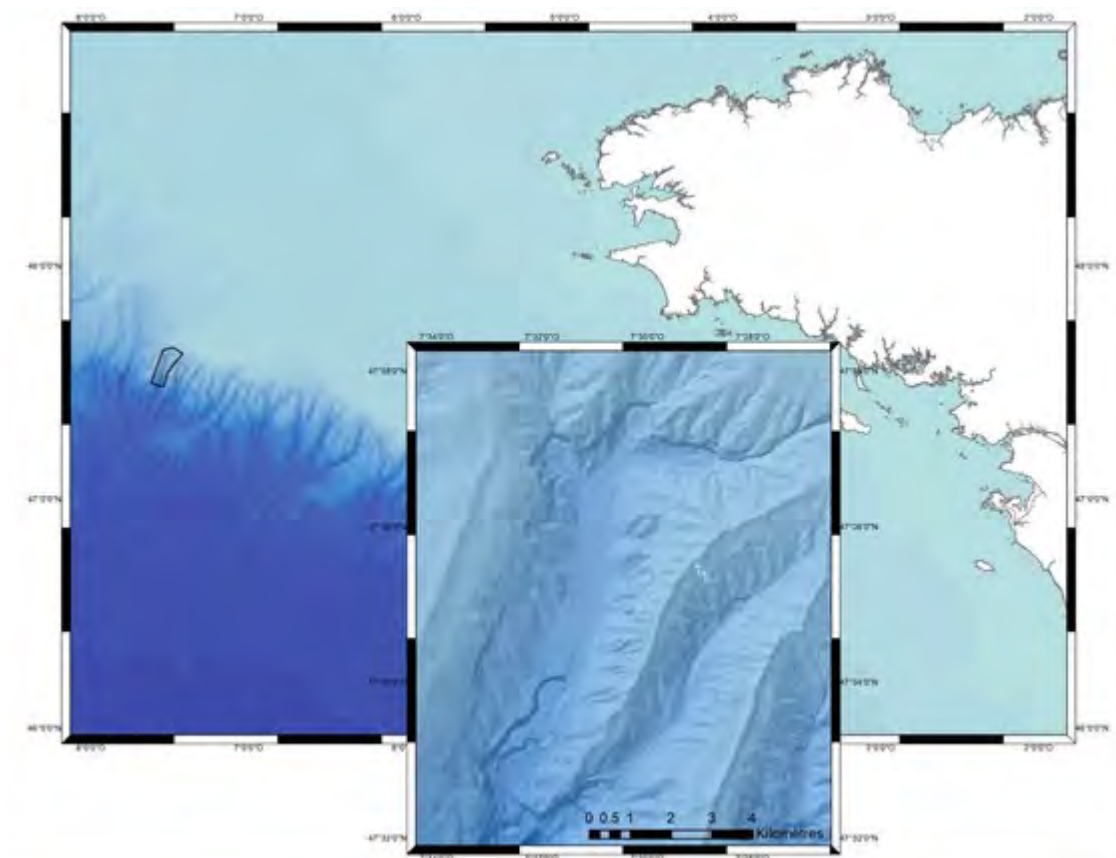


Figure 27. Map of the Lampaul canyon (A) in the northern Bay of Biscay (B).

Coral and associated fauna were sampled using the Hybrid Remotely Operated Vehicles (HROV) Ariane during dives 202, 203, 214 and 218. General dive structures are pictured in Figure 28 below, and full dive logs can be found elsewhere (Menot and Tourolle, 2021). Using the HROV’s arm, 7 colonies of *Desmophyllum pertusum* (*Lophelia pertusa*) and 11 colonies of *Madrepora oculata* were collected during those dives, at depths ranging from 790 to 885 m. They were subsequently placed in boxes and brought back to the surface. On board, coral nubbins (6–12 polyps for *D. pertusum*, 9–13 polyps for *M. oculata*) were separated. Fauna associated with the corals was also retrieved either from the colonies directly or from the sampling boxes. It included several taxa of cnidarians, such as black corals (Antipatharia), anemones (Actiniaria) or Hydrozoa; two morphologically distinguishable bivalve taxa, gastropods, several taxa of Polychaete worms, squat lobsters (Decapoda: Galatzoidea), echinoderms such as brittle stars (Ophiuroidea), feather stars (Crinoidea), and sea urchins (Echinoidea), and sea squirts (Urochordata:

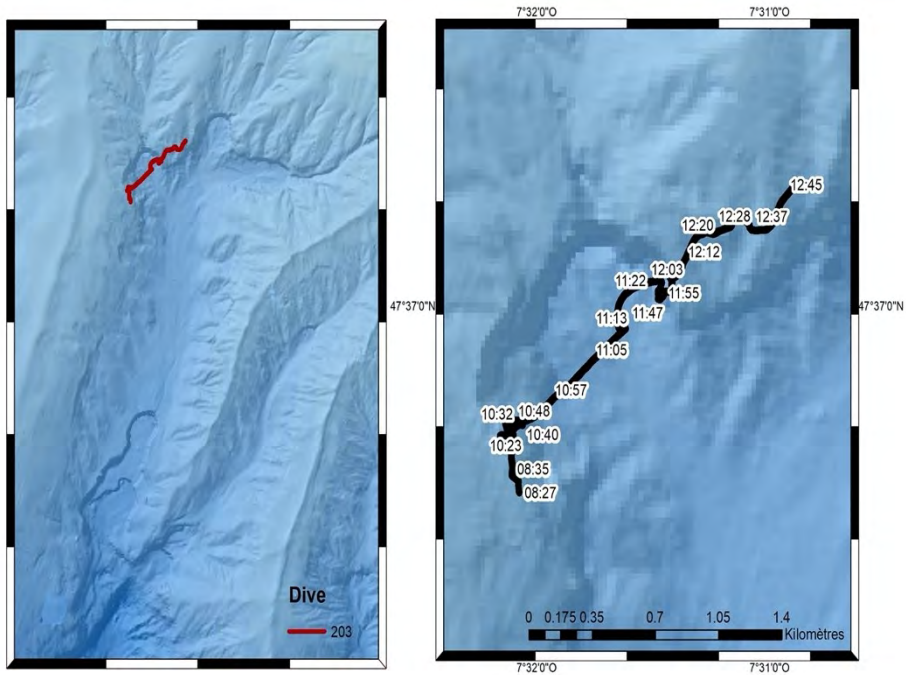
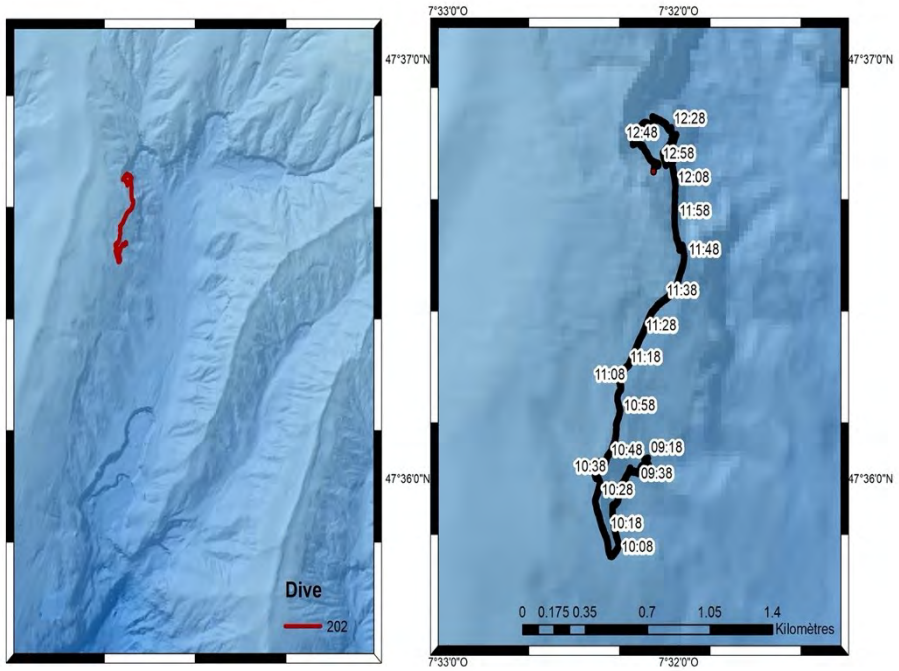
Ascidiaeae). All associated fauna was identified as precisely as possible on board during the cruise.

Moreover, to characterise suspended particulate organic matter (SPOM) present in the water column (*i.e.*, the putative basal food-source for the studied food webs), water samples were taken using Niskin bottles during 8 CTD casts and at 4 different depths (just below the surface, at 20 m below the surface, at 900 m [depths at which CWC density is typically the highest in Lampaul Canyon] and at 20 m above the seafloor). SPOM was directly separated from these water samples by filtration on pre-combusted Whatman GF/F filters. All samples (animals and filters for SPOM) were then frozen at -80°C until the end of the cruise and their transport to Ifremer facilities in Plouzané.

Sample conditioning

Once in the lab, coral nubbins were cold crushed using a Retsch MM301 mixer mill whose sample compartments were immersed in liquid nitrogen prior to operation. Aliquots of sample powder were then freeze-dried for stable isotope analysis, and the rest was placed back at -80°C. Associated fauna samples were conditioned according to sample size. Small animals were freeze-dried whole. Larger animals were thawed and dissected to extract soft, non-metabolically active tissue such as muscle or body wall (Mateo et al., 2008). All samples were then freeze-dried and ground to a fine powder using mortar and pestle. Filters were freeze-dried, then SPOM deposited upon them during filtration was retrieved by delicately scraping it with a scalpel blade.

Inorganic carbon present in samples can be a source of bias in carbon stable isotope analysis (Mateo et al., 2008). Calcified samples (corals and some of the associated fauna) were therefore acidified to remove carbonates prior to analysis. Adequate amounts of sample were placed in silver capsules and acidified by direct addition of 250 µl of 10% HCl (Jaschinski et al., 2008). HCl was added in small, sequential steps (10 µl by 10 µl) to avoid excessive reaction which can lead to sample loss. The efficiency of the acidification procedure was ascertained by running 'Champagne tests' (Jaschinski et al., 2008). They indicated that the procedure successfully removed all carbonates from samples. Since acidification can alter N (Mateo et al., 2008) and S (Connolly and Schlacher, 2013) isotopic ratios, acidified samples were analysed twice: once for C isotopic ratios, using decarbonated material, and once for N and S isotopic ratios using unacidified material.



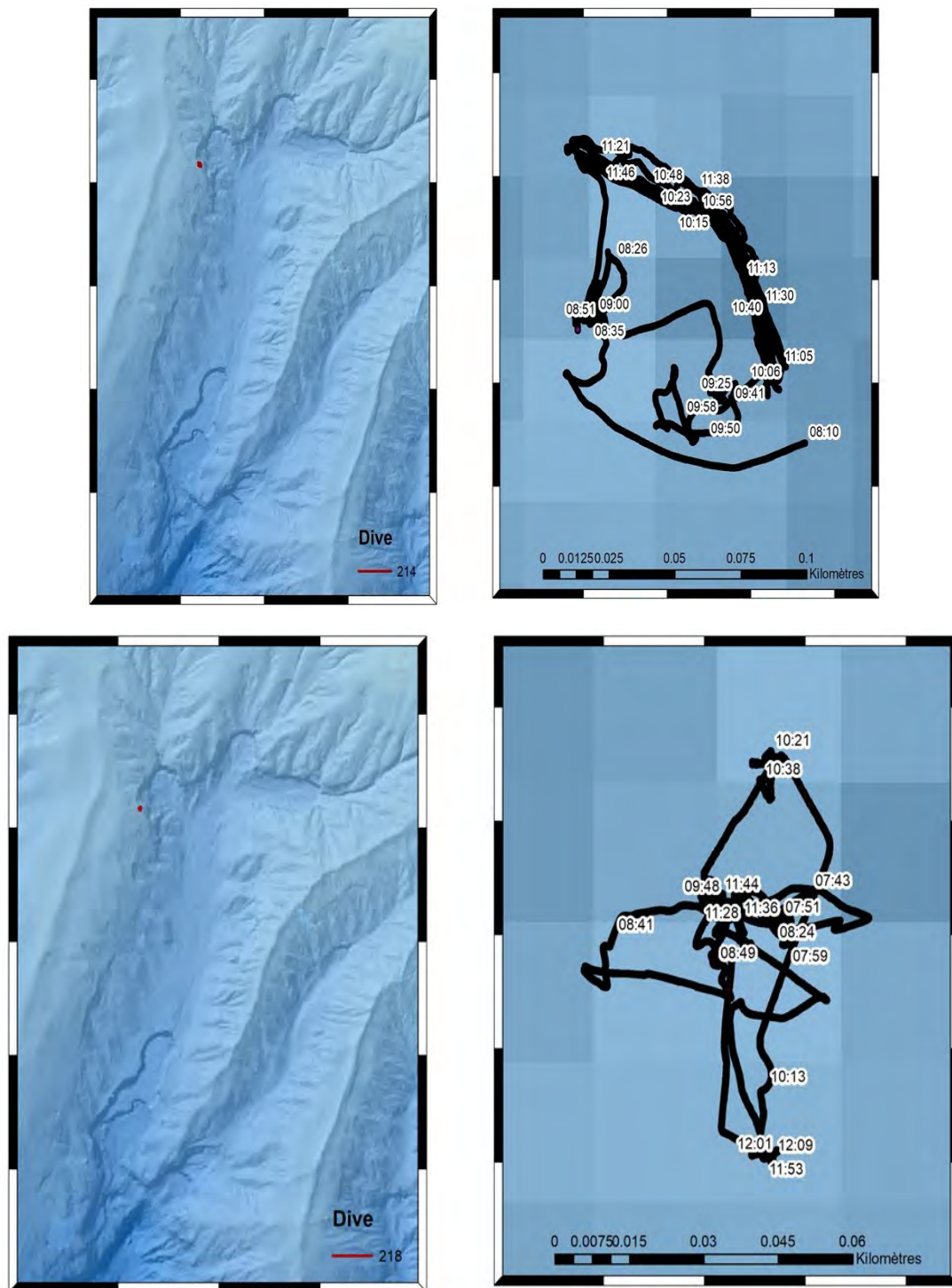


Figure 28. Map of the sampling dives during the ChEReef 2021 cruise.

Stable isotope analyses

Stable isotope ratios measurements were performed via continuous flow – elemental analysis – isotope ratio mass spectrometry (CF-EA-IRMS) at University of Liège (Belgium), using a vario MICRO cube C-N-S elemental analyser (Elementar Analysensysteme GMBH, Hanau, Germany) coupled to an IsoPrime100 isotope ratio mass spectrometer (Isoprime, Cheadle, United Kingdom). Isotopic ratios were expressed using the widespread δ notation (Coplen, 2011), in ‰ and relative to the international references Vienna Pee Dee Belemnite (for carbon), Atmospheric Air (for nitrogen) and Vienna Canyon Diablo Troilite (for

sulphur). IAEA (International Atomic Energy Agency, Vienna, Austria) certified reference materials sucrose (IAEA-C-6; $\delta^{13}\text{C} = -10.8 \pm 0.5\text{‰}$; mean \pm SD), ammonium sulphate (IAEA-N-2; $\delta^{15}\text{N} = 20.3 \pm 0.2\text{‰}$; mean \pm SD) and silver sulphide (IAEA-S-2; $\delta^{34}\text{S} = 22.6 \pm 0.1\text{‰}$; mean \pm SD) were used as primary analytical standards. Sulfanilic acid (Sigma-Aldrich; $\delta^{13}\text{C} = -25.6 \pm 0.4\text{‰}$; $\delta^{15}\text{N} = -0.13 \pm 0.4\text{‰}$; $\delta^{34}\text{S} = 5.9 \pm 0.5\text{‰}$; mean \pm SD) was used as secondary analytical standard. Standard deviations on multi-batch replicate measurements of secondary and internal lab standards (amphipod crustacean muscle) analysed interspersed with samples (one replicate of each standard every 15 analyses) were 0.2‰ for both $\delta^{13}\text{C}$ and $\delta^{15}\text{N}$ and 0.4‰ for $\delta^{34}\text{S}$.

Data analysis

All graphs were made and analyses were conducted using the R v. 4.3.1 statistical computing environment (R Core Team, 2023). Stable isotope data were examined using ‘classical’ isotopic biplots. In addition, where replication permitted (i.e. for taxa with $n \geq 6$), ecological niches were explored using the SIBER (Stable Isotope Bayesian Ellipses in R) package, v. 2.1.7 (Jackson et al., 2011). SIBER involves the use of 2D ellipses or multivariate ellipsoids to define isotopic niches, i.e., the space occupied by an animal population in a bi- or multivariate isotopic space. Since variation in the isotopic composition of animals (i.e., position of points in the isotopic space) is driven by both consumed prey items and habitat use, this isotopic niche can be used as a proxy of the realised ecological niche (Flaherty and Ben-David, 2010; Jackson et al., 2011). However, when dealing with low-mobility or fixed organisms such as most of those analysed here, diet-related processes arguably drive most of the isotopic composition, and isotopic niches could be seen as trophic niche proxies. Size and position of ellipses carry complementary information about animal ecology. A larger ellipse suggests that an animal population commonly uses a wider diversity of trophic resources. Overlap between ellipses associated with different populations suggests that these groups partly exploit the same food. Here, we used standard ellipses (bivariate equivalent of standard deviations). These standard ellipses contain only the ‘typical’ members of a population (but may not encompass outlier individuals in isotopic space). For this reason, they have been termed ‘core isotopic niches’, as it can be used as a proxy of the trophic resources most commonly used by populations (Layman and Allgeier, 2012).

5.2 Results

SPOM had the most negative $\delta^{13}\text{C}$ -value ($\delta^{13}\text{C} = -23.7 \pm 1.4\text{‰}$; mean \pm SD), and the Polynoidae had the least negative $\delta^{13}\text{C}$ -value ($\delta^{13}\text{C} = -16.9 \pm 1.3\text{‰}$; mean \pm SD) (Figure 29). CWC species had $\delta^{13}\text{C}$ -values that were very similar to one another (*D. pertusum*: $\delta^{13}\text{C} = -21.8 \pm 0.9\text{‰}$; *M. oculata*: $\delta^{13}\text{C} = -21.7 \pm 0.7\text{‰}$; mean \pm SD) and were the most negative of all analysed fauna (Figure 29). Coral $\delta^{13}\text{C}$ -values were very similar to Ophiuroidea ($\delta^{13}\text{C} = -21.8 \pm 2.8\text{‰}$; mean \pm SD) and, to a lesser extent, Crinoidea ($\delta^{13}\text{C} = -21.0 \pm 0.2\text{‰}$; mean \pm SD), Galathea ($\delta^{13}\text{C} = -21.0 \pm 1.6\text{‰}$; mean \pm SD) and Actiniaria ($\delta^{13}\text{C} = -20.8 \pm 0.5\text{‰}$; mean \pm SD). SPOM had the lowest $\delta^{15}\text{N}$ -value ($\delta^{15}\text{N} = 6.6 \pm 2.2\text{‰}$; mean \pm SD, Figure 29). The highest $\delta^{15}\text{N}$ -value was for gastropods (mean $\delta^{15}\text{N} = 12.7\text{‰}$). CWC species had $\delta^{15}\text{N}$ -values very similar to one another (*D. pertusum*: $\delta^{15}\text{N} = 11.2 \pm 0.9\text{‰}$; *M. oculata*: $\delta^{15}\text{N} = 11.7 \pm 1.7\text{‰}$; mean \pm SD) and were among the highest measured here (Figure 29). These values were comparable with the values for bivalves ($\delta^{15}\text{N} = 10.7 \pm 0.6\text{‰}$ for one taxon and $\delta^{15}\text{N} = 11.3 \pm 1.0\text{‰}$ for the other; mean \pm SD), the Polynoidae ($\delta^{15}\text{N} = 11.7 \pm 1.7\text{‰}$; mean \pm SD), in *Eunice norvegica* ($\delta^{15}\text{N} = 10.8 \pm 1.0\text{‰}$; mean \pm SD), echinoderms (mean $\delta^{15}\text{N} = 11.0\text{‰}$) and ascidians ($\delta^{15}\text{N} = 10.5 \pm 1.1\text{‰}$; mean \pm SD) (Figure 29).

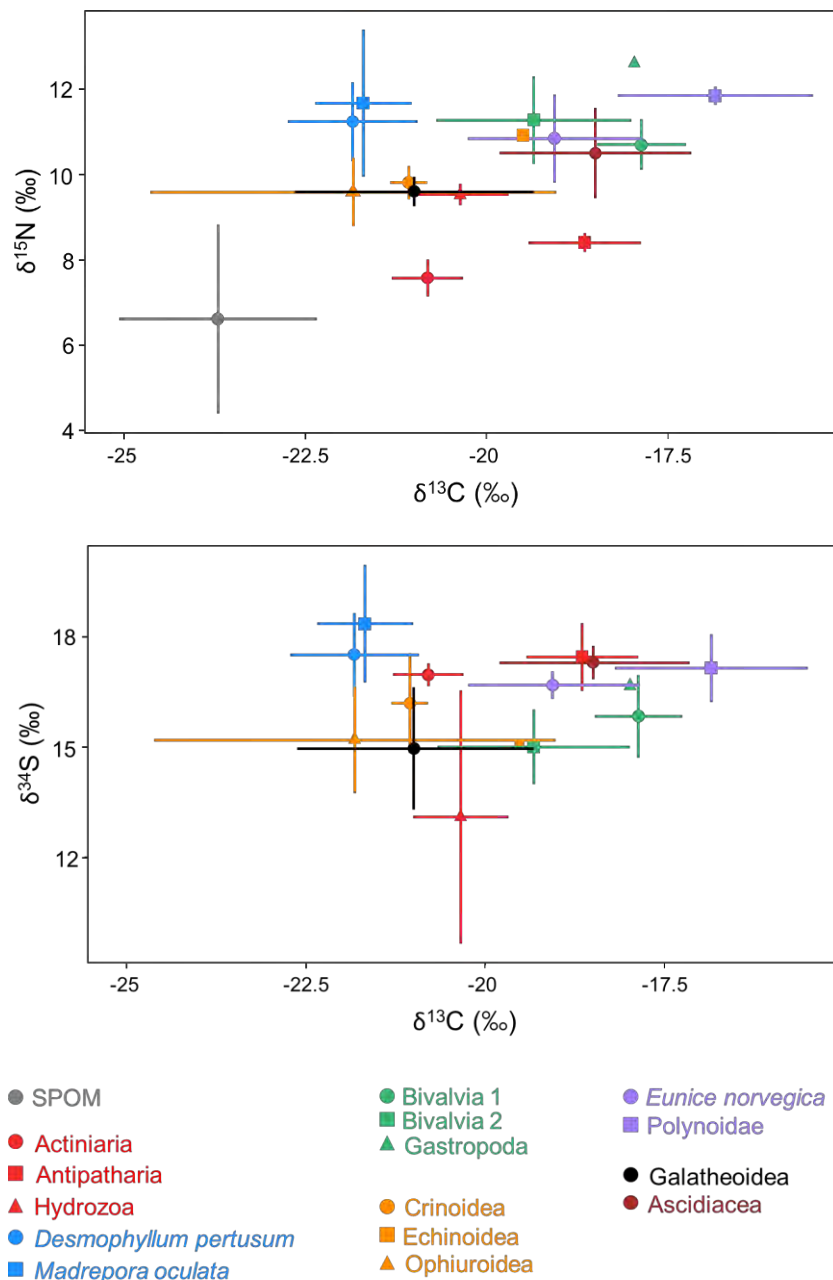


Figure 29. Isotopic compositions of CWCs and associated fauna in the Lampaul Canyon. Top: carbon and nitrogen isotopic ratios. Bottom: carbon and sulphur stable isotope ratios. Points are means; error bars are standard deviations. Grey points indicate suspended particulate organic matter, other colours pertain to larger taxonomic groups (blue: CWCs, red: other cnidaria, green: Mollusca, Purple: Polychaeta, black: Crustacea, orange: Echinodermata, brown: Urochordata).

Due to technical limitations, $\delta^{34}\text{S}$ could not be measured in all samples, and no values were available for SPOM. Most of the sampled fauna were scattered over a continuum roughly ranging from 15.0 to 18.4 ‰, with the notable exception being the Hydrozoa, whose $\delta^{34}\text{S}$ was highly variable and markedly lower than any other taxon ($\delta^{34}\text{S} = 13.1 \pm 3.4$ ‰; mean \pm SD). Inside the aforementioned continuum, taxa were distributed in 3 groups despite high overlap (Figure 29): one with lower $\delta^{34}\text{S}$ values (brittle stars, squat lobsters, sea urchins, one of the bivalve taxa), one with intermediate $\delta^{34}\text{S}$ values (the other bivalve taxon, feather stars) and one with higher $\delta^{34}\text{S}$ values (both CWC species and the rest of the fauna). CWC had the highest $\delta^{34}\text{S}$ measured here (*D. pertusum*: $\delta^{34}\text{S} = 17.5 \pm 1.1$ ‰; *M. oculata*: $\delta^{34}\text{S} = 18.4 \pm 1.6$ ‰; means \pm SD).

Both C vs. N and C vs. S (Figure 30) isotopic niches suggest that CWC species occupied an isotopic space distinct from any other taxon. *D. pertusum* showed weak niche overlap with Crinoidea in the C vs. S space (Figure 30). In the C vs. N space (Figure 30), it was *M. oculata* that showed weak niche overlap with another taxon, in this case Ophiuroidea. However, when considering 3D ellipsoids (data not shown), it was possible to see that this apparent overlap was due to projection biases, and that the 3D isotopic niches of both CWC corals were completely distinct from those of any of the other biomass-dominant taxa. There was however a considerable niche overlap between the two CWC species in both C vs. N (relative overlap: 48% of the cumulative ellipse area occupied by the two species) and C vs. S (relative overlap: 33% of the cumulative ellipse area occupied by the two species) isotopic spaces. Overlap between 3D ellipsoids was 17% of the cumulative ellipsoid volume (data not shown). While this value can seem low, it actually represented 57% of *D. pertusum*'s 3D niche volume. Finally, the standard ellipse area (SEA_C) was higher for *Madrepora oculata* than for *Desmophyllum pertusum* (*Lophelia pertusa*) in both C vs. N (3.7 ‰² vs. 2.8 ‰², respectively) and C vs. S isotopic spaces (3.5 ‰² vs. 2.5 ‰², respectively), suggesting that *M. oculata*'s isotopic niche is wider than the one of *D. pertusum*.

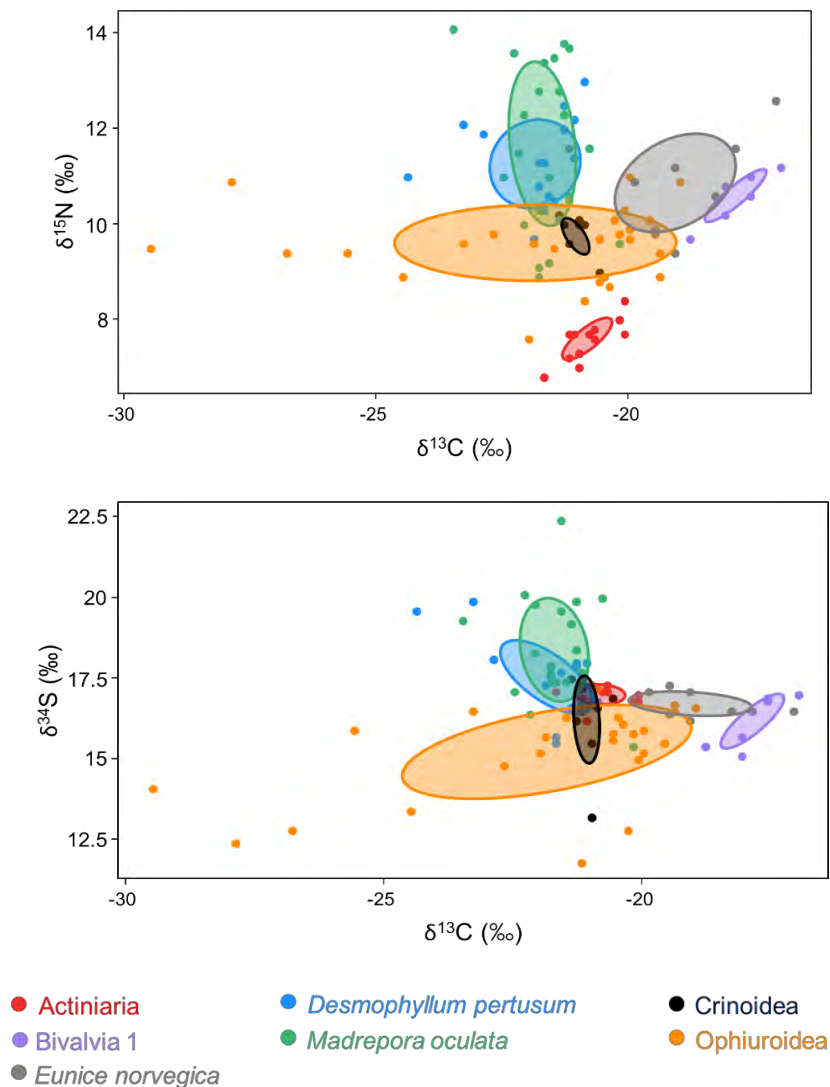


Figure 30. Isotopic niches of CWCs and associated fauna in the Lampaul Canyon. Top: carbon and nitrogen ellipses. Bottom: carbon and sulphur ellipses. Points are individual measurements. Colours pertain to different taxa.

5.3 Discussion

The isotopic ratios of the sampled fauna covered a wide range of values for each element, suggesting that considerable trophic diversity exists within the biological assemblage from the Lampaul Canyon. Some taxa, including CWCs, had very negative $\delta^{13}\text{C}$, indicating they likely rely on SPOM either directly or indirectly and could therefore be negatively impacted by declining overlying productivity resulting from climate change. Others had markedly less negative $\delta^{13}\text{C}$, suggesting they are unlikely to feed solely on fresh SPOM and/ or plankton. These animals could derive part of their nutrition from detrital organic matter reworked by microbes, as seen in other ecosystems (Michel et al., 2016; Mincks et al., 2008). Accordingly, deep *Desmophyllum pertusum* (*Lophelia pertusa*) reefs from Belgica mounds (Porcupine Basin, NE Atlantic) have been shown to host food webs depending mostly on exported phytodetritus (van Oevelen et al., 2018a).

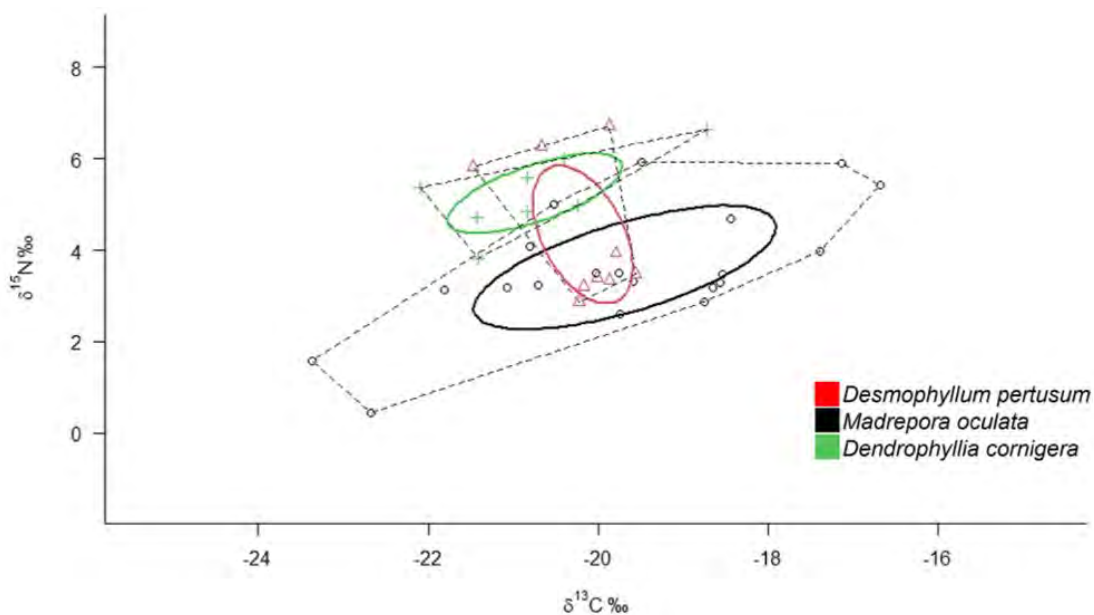


Figure 31. $\delta^{13}\text{C}$ - $\delta^{15}\text{N}$ scatterplot with standard ellipses corrected for small sample size population (SEAC) overlaid for the three CWC species from the central oligotrophic Mediterranean Sea. Image from Da Ros et al. (2022).

Among the wide spectrum of microbial metabolisms that can fuel ecosystems, sulphide oxidation is relatively common in marine sediments, notably in hypoxic layers. This chemosynthetic production mechanism results in very low or even negative $\delta^{34}\text{S}$ values (Vetter and Fry, 1998). Here, the only animals that had $\delta^{34}\text{S}$ values compatible with partial (although putatively moderate) reliance on sulphide oxidation were Actiniaria. The rest of the sampled fauna, particularly CWCs, had much higher $\delta^{34}\text{S}$ signatures.

CWCs also had high $\delta^{15}\text{N}$ as also found along the Angolan Slope (Vinha et al., 2023) and these were comparable or higher to *Eunice norvegica* (generally considered as an omnivore / predator / scavenger species), or similar to Polynoidae, a polychaete family whose representatives are most commonly predators. This suggests that corals in the Lampaul Canyon feed at a relatively high trophic level. Taken together, isotopic ratios of C, N and S suggest that in the Lampaul Canyon, both *D. pertusum* and *M. oculata* could selectively feed on zooplankton. CWCs of the same species from the more oligotrophic Mediterranean Sea had much lower $\delta^{15}\text{N}$ -values (approaching zero) indicative of feeding at much lower trophic positions (e.g., on microbes) (Figure 23) (Da Ros et al., 2022). Thus, it is possible that declining

productivity may force CWCs to revert to feeding at a much lower trophic position which could have significant effects on CWCs if trophic niches become overcrowded. The effects on *D. pertusum* could be more dramatic given its smaller isotope niche compared to *M. oculata* in the Lampaul Canyon.

Interestingly, *D. pertusum* has been shown to feed on zooplankton in shallower and locations close to OMZs (e.g., Angola slope, Vinha et al. (2023)), while its reliance on this resource has been described as lower in deeper locations (van Oevelen et al., 2018a). The comparatively high contribution of zooplankton to CWC diet in the deep Lampaul Canyon might be linked with local oceanographic (e.g., existence of one or several mechanisms explaining strong coupling between production in the euphotic zone and consumption several hundreds of meters below) or biological (e.g., phenology of zooplankton blooms) processes. While zooplankton constitutes a high-energy resource for CWCs, allowing them to efficiently synthesise lipid reserves, its availability can also be limiting, leading corals to shift towards less profitable but more easily available resources (Maier et al., 2019a).

Here, stable isotope markers suggested that in the Lampaul Canyon, CWC have distinct ecological habits (*i.e.*, isotopic niche overlap low to non-existent) when compared with dominant associated fauna, including other suspension feeders such as Ophiuroidea, Crinoidea or bivalves (Figure 21 and 22). This once again contrasts with the situation in the deep CWC reefs of the Belgica mounds (that develop at depths comparable to those were sampling took place here), where both *D. pertusum* and *M. oculata* seemed to feed on resources similar to associated organisms (e.g., other CWCs such as *Cirripathes* sp.) as described in van Oevelen et al. (2018a). On the other hand, in the shallower (around 300 m) reefs of Traena (Norwegian continental shelf), *D. pertusum* occupied an isotopic niche distinct from any other consumer (see Figure 2 in van Oevelen et al. (2018a)). In the Lampaul Canyon, the two CWC species however seemed to share a considerable portion of their niche space and may therefore partly rely on the same resources. Fine-scale niche segregation between the two taxa as seen in *D. pertusum* and other taxa on the Traena reefs (van Oevelen et al., 2018a) could exist but was not detected by the trophic markers used here due to their lack of resolution. Nevertheless, if food availability turns out to be limiting for CWC under present or future environmental conditions, competition between *D. pertusum* and *M. oculata* could occur in the Lampaul Canyon. On that aspect, it is worth noting that *M. oculata*'s isotopic niche was wider than *D. pertusum*'s, (Figure 30) suggesting that in the studied system, the former species exhibits a greater trophic diversity than the latter.

6. Case Study 5 – Comparisons of the live and dead coral framework from multiple Atlantic sites

6.1 Materials & Methods

Evaluation of live: dead coral framework and carbon turnover

Live and dead framework evaluations are critical when understanding the function of CWC reefs for multiple reasons. Two recent studies (Vad et al. (2017) and De Clippele et al. (2021) have developed techniques that are potentially scalable and integrative into machine learning analysis, and are therefore of keen interest here.. Support of associated biodiversity will vary depending on the proportion between live and dead framework, with dead framework supporting different biodiversity than living framework, with the most biologically diverse part of a CWC reef typically being the transition area from live to dead framework (Henry and Roberts 2007; Henry and Roberts 2017). This dead framework also physically supports the live coral, which is often situated on top of the framework structure in relatively strong water currents (highlighting the importance of the structural integrity of supporting framework) (Hennige et al.,

2021). Both the live and dead fractions of the coral framework will also contribute to overall carbon turnover of reef structures, due to the respiration and growth of live CWC, and respiration of associated biodiversity within the dead framework (De Clippele et al., 2021). Additionally, the framework of coral will act to baffle water flow and lead to accumulation of fine sediments, which also contribute significantly to C and N cycling of these ecosystems (de Froe et al., 2019, De Clippele et al., 2021).

A major difference in the two approaches taken to quantify coral framework is illustrated in [Figure 32](#). There are clear advantages to using each method depending upon the end variable desired. Quantification by Vad et al. (2017) follows the growth of coral colonies and gives an accurate representation of the proportion of live and dead coral material, whereas De Clippele et al. (2021) measures the surface area of the whole image, allowing determination of the entire live and dead proportion within the video frame or image. This then allows calculation of biomass to be estimated by using a conversion factor of the mean mass of the reef taken by suction, grab or box-core samples. The linear nature of the Vad et al. (2017) method allows for an estimate of colony age based on estimated growth rates. When we consider the impact of climate change upon the live and dead framework of these reefs, the amount of dead material is a critical factor to consider, as that is at most risk from coralporosis (Hennige et al., 2020). Methods by Vad et al. (2017) would allow for potentially more direct assessment of reef crumbling due to structural instability caused by loss of dead skeletal framework. The methods of De Clippele et al. (2021) assess how much dead material there is within a given area, and therefore what the impacts of framework loss may be upon the biodiversity provision and CN turnover of a reef area. Ultimately, the framework forming ability of these corals are complex, and as framework ratios change, so too will local hydrodynamics, having a direct impact upon local food provision and the survivability of living coral framework due to food provision (Hennige et al., 2021).

For this case study, methods by De Clippele et al. (2021) will be used to allow estimation of biomass and carbon turnover. To allow comparison between already published values of the proportion of live and dead coral from Atlantic reefs with those analysed here, a comparison of both methodologies is run on one dataset. Due to the whole image approach by De Clippele et al. (2021), and without individual coral colony tracking (and hence no accounting for 3-D compression of the images onto a planar surface), results can potentially increase the proportion of live coral as seen in [Figure 32](#), where the proportion of living coral: whole colony is 0.14 (Vad et al., 2017) and 0.44 (De Clippele et al., 2021).

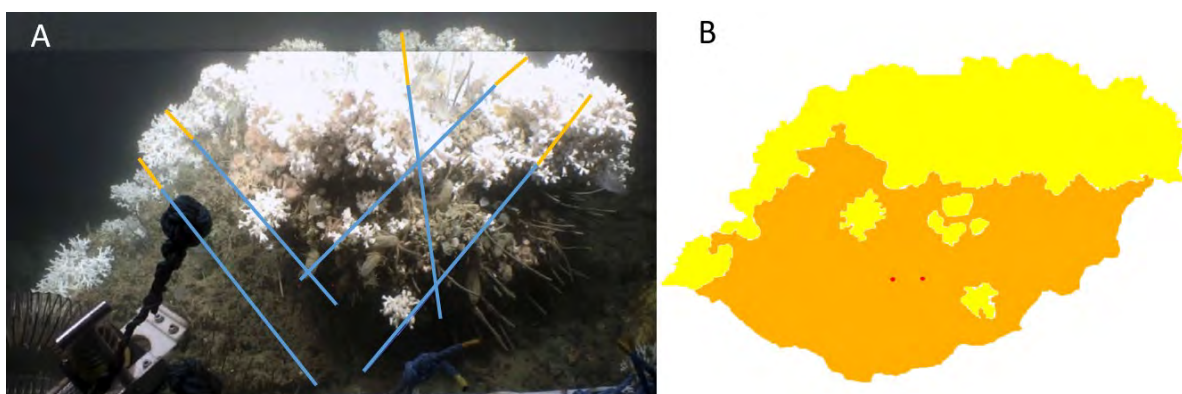


Figure 32. The difference in methods shown for Colony 1. (A). Image adapted from Vad et al. (2017) who calculated the living layer: whole colony ratio as 0.14, with overlay bars from blue to orange, denoting dead and living layers within the same plane; (B). Image segmentation output from Photoshop using the method by van der Kaaden and De Clippele's (2021) which calculated the living layer: whole colony ratio as 0.44.

Comparison of techniques – Images from the supplemental information in Vad et al. (2017) were downloaded for analysis using the methods set out in De Clippele et al. (2021). The images were taken of *Desmophyllum pertusum* (*Lophelia pertusa*) colonies at the Mingulay Reef Complex (depths ranging from 127–179 meters) and Pisces, Rockall Bank (depths ranging from 260–262 meters) (Roberts et al., 2013). Of the 18 colonies analysed in Vad et al., (2017), 16 were suitable for this comparison. The two colony images that were not analysed either did not have visible lasers for scaling or cropped out some of the colony.

All images were imported into Photoshop 23.1.0 for manual annotation. In each image, the laser scales, dead coral and live coral sections were colour coded in one layer following the method by van der Kaaden and De Clippele (2021). All images were exported as tiff files before being analysed in Rstudio (version 2022.02.03+492) (Rstudio Team, 2019) running R version 4.2.0. (R Core Team, 2022) using the codes created by van der Kaaden and De Clippele (2021). Code output calculated the area of the entire image and the percentage of live and dead coral. From these values, the area of the coral colony, live colony, and dead framework as well as the ratio of living layer: whole colony (LL: WC) were calculated. A Shapiro-Wilk test was done to confirm normality before performing a paired t-test in Rstudio to compare results from the two methods (linear measures in Vad et al. (2017) with whole colony measures in De Clippele et al. (2021)). Both site datasets were normally distributed with p-values > 0.05. The paired-t test showed that the two methods produced significantly different results (p-value = 0.00003). With the exceptions of Colonies 7, 9, and 17, the LL: WC ratios found by Vad et al. (2017) were significantly lower than the ratio derived from the De Clippele et al. (2021) methods used in this study (Table 22, Figure 33).

Table 22. Results from comparing living layer: whole colony ratio using van der Kaaden and De Clippele’s (2021) method on the images from Vad et al. (2017).

Location	Colony Number	Vad et al., 2017	This study using De Clippele et al. (2021) approaches
Mingulay Reef Complex	1	0.14	0.44
Mingulay Reef Complex	3	0.22	0.73
Mingulay Reef Complex	4	0.20	0.37
Mingulay Reef Complex	5	0.27	0.67
Mingulay Reef Complex	6	0.12	0.21
Mingulay Reef Complex	7	0.22	0.23
Mingulay Reef Complex	8	0.17	0.49
Mingulay Reef Complex	9	0.11	0.11
Mingulay Reef Complex	10	0.16	0.37
Mingulay Reef Complex	11	0.19	0.39
Mingulay Reef Complex	13	0.10	0.34
Mingulay Reef Complex	14	0.22	0.50
Pisces	15	0.13	0.43
Pisces	16	0.18	0.35
Pisces	17	0.17	0.15
Pisces	18	0.18	0.59

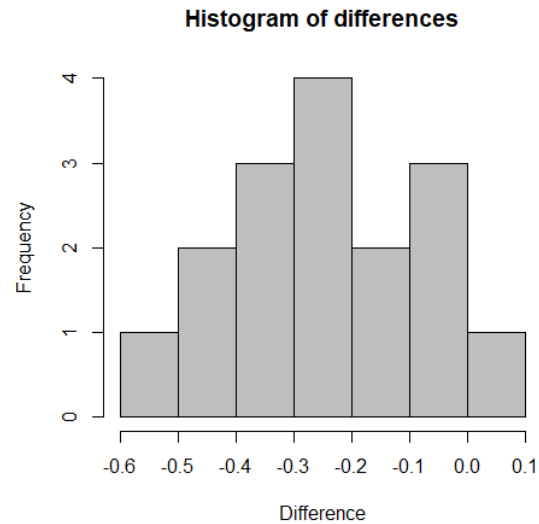


Figure 33. Histogram of differences between LL: WC for the method used in Vad et al. (2017) and the whole colony approach in De Clippele et al. (2021) applied to the same images. Difference values relate to the difference in ratio values, with most images having a higher ratio of live: whole colony values between 0.2 to 0.3 using methods by De Clippele et al. (2021). Of note is the range of differences.

The significant differences in the LL: WC ratio between methods were expected as the two methods measured separate parameters. Vad et al. (2017) measured colony size and live: dead proportion with a linear technique while De Clippele et al. (2021) measured surface area in m^2 over the whole colony. The method in Vad et al., (2017) (which was also utilised in Orejas et al. (2021)) requires manual tracking of a colony growth and accounts for the 3-D nature of the colonies as attention was paid to projection/ planar alignment to calculate the LL: WC ratio. Projections were not considered in the method of De Clippele et al. (2021). This difference was evident in [Figure 32](#), where image A only designates live corals in the same plane as the living layer. When creating the image segmentation seen in B ([Figure 32](#)), all live coral, regardless of the plane was grouped into the living layer. In the three instances where the two methods produced the same or roughly the same result, the colony image was situated in one plane ([Figure 34](#)).

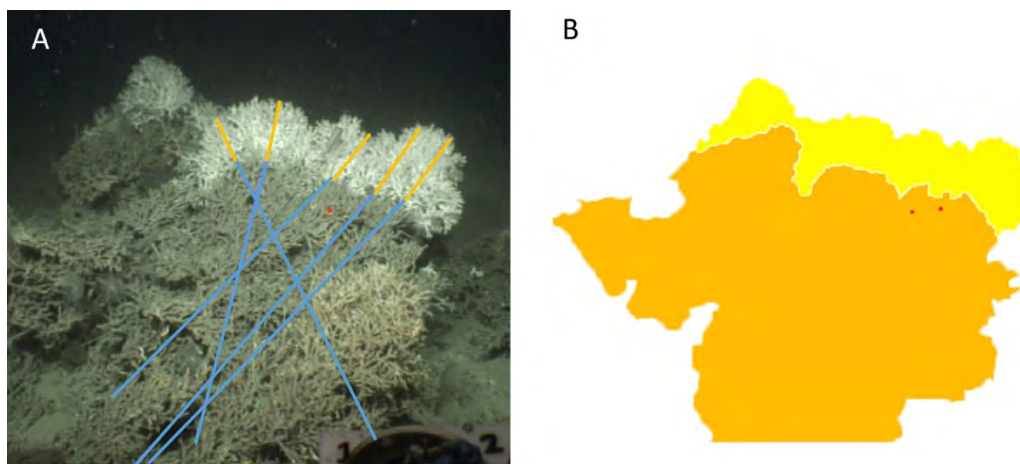


Figure 34. The difference in methods shown for Colony 17. A. Image adapted from Vad et al. (2017) who calculated the living layer: whole colony ratio as 0.17. B. Image segmentation output from Photoshop using the method by van der Kaaden and De Clippele (2021) which calculated the living layer: whole colony ratio as 0.15.

Skeletal density

Coral growth occurs at the individual colony-scale but collectively the growth of coral assemblages has a major control on the ecological productivity and geomorphology of entire CWC communities. To manage these ecosystems effectively, we need to better understand the mechanisms that regulate their growth dynamics, such as coral life history traits including skeletal density. Coral skeletal density is an important growth characteristic that determines the strength of the corals and its ability to sustain physical pressure, and ultimately, how they will break as the framework increases in size (explored in more detail in models below). Bulk density is defined by the pattern in which the material is laid down (micro-density) and by the volume of the voids enclosed in the skeleton (porosity) (Bucher et al., 1998). Micro-density refers to the specific gravity of the material of which the skeleton is formed. As porosity decreases, bulk density will approach micro-density, and neither can exceed the density of pure aragonite (2.94 g cm^{-3} ; Bucher et al., 1998) due to the presence of an intra-crystalline organic matrix which is absent in abiotic carbonates (Cuif et al., 1999). Therefore, micro-density values are constrained by the structure of the aragonitic crystals and the relative proportion of inter-crystalline organic matter, while bulk density and porosity reflect the growth patterns of corals, which are often related to environmental variables.

Studying coral skeletal density is particularly important because of predicted reductions in skeletal density as a consequence of ocean acidification, resulting in cold-water corals more susceptible to chemical dissolution and erosion by bioeroders (Büsher et al., 2019, 2022; Hennige et al., 2020). The rate at which structural collapse will occur, and the impact on local hydrodynamic loading to potential death of live coral due to a change in their position is directly related to the structural integrity and density of coral skeletons. Here, we present the first comparison of skeletal density (bulk density, micro-density and porosity), in five cold-water scleractinian coral species, *Desmophyllum pertusum* (*Lophelia pertusa*), *Madrepora oculata*, *Dendrophyllia cornigera*, *Desmophyllum dianthus* and *Caryophyllia* sp. (Figure 35). The aim was to compare skeletal density among different CWCs species and among three geographic regions, the NE Atlantic continental margin of Norway, Ireland and Scotland, in the central NE Atlantic region of the Azores and in the NW Mediterranean. An additional objective was to investigate the relationship between coral skeletal density and the physical-chemical parameters in each region to enhance our understanding on the baseline conditions in each region and better predict changes in future ocean conditions.

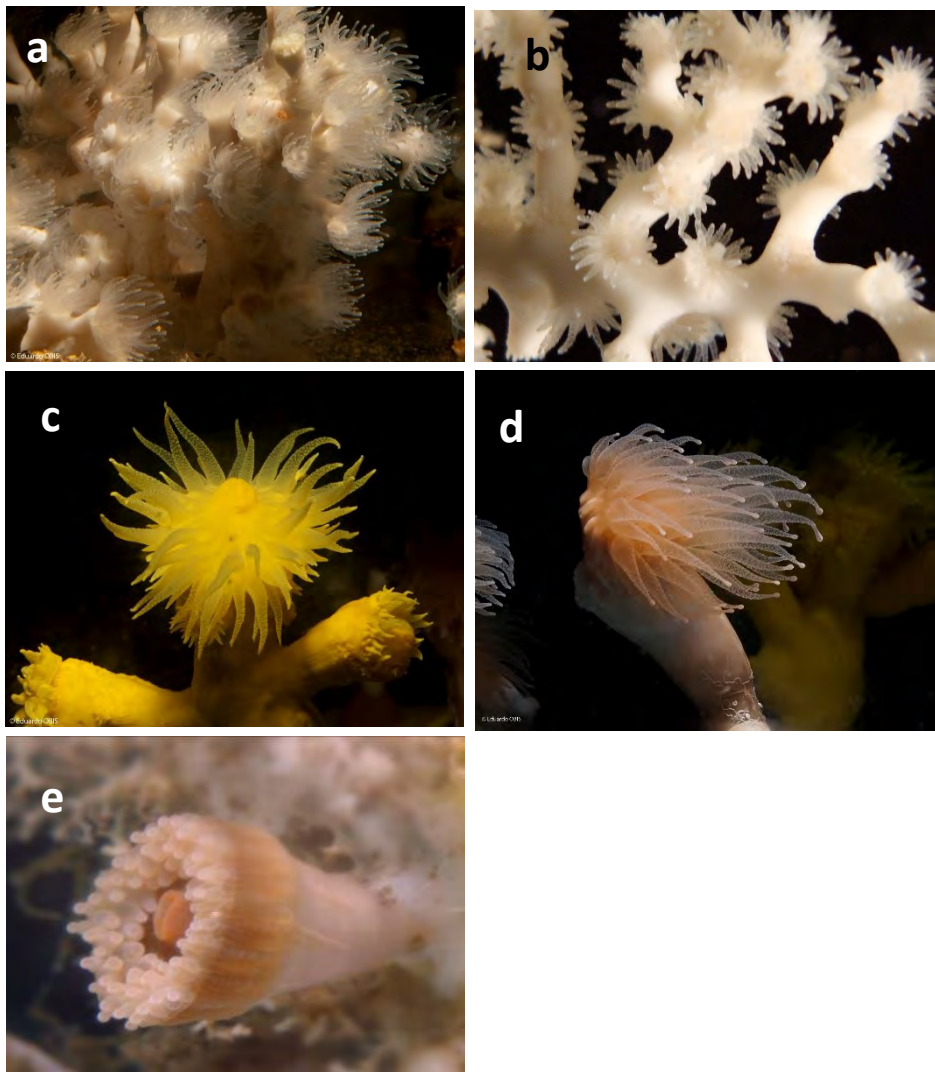


Figure 35. Scleractinian cold-water corals examined in the study: (a) *Desmophyllum pertusum* (*Lophelia pertusa*); (b) *Madrepora oculata*; (c) *Dendrophyllia cornigera*; (d) *Desmophyllum dianthus*; (e) *Caryophyllia* sp. Photo credit: a, c, d © Eduardo Obis, b © Andrea Gori, CSIC aquaria facilities; e c © Rodrigo Sá da Bandeira, DeepSeaLab facilities, IMAR-UAz.

Cold-water corals were collected in three different geographic regions: the NE Atlantic continental margin of Norway, Ireland and Scotland, UK, Central NE Atlantic region of the Azores, and in the NW Mediterranean Sea (for comparative purposes) (Figure 36, Table 23): *NE Atlantic continental shelf of Norway* – colonies of *D. pertusum* (*L. pertusa*) were collected from an inshore Norwegian cold-water coral habitat in the outer Trondheim-Fjord near the island Nord-Leksa (Leska and Acesta Reefs) and an offshore reef, Sula Reef, using the manned submersible JAGO (GEOMAR 2017) during RV *POSEIDON* cruise POS455 in June/July 2013 (Form et al., 2014; Busher et al., 2019). *NE Atlantic continental margins of Ireland and Scotland, UK* – Colonies of *D. pertusum* were collected from the Mingulay Reef Complex, Logachev and Pisces mounds (Rockall Bank) during the ‘Changing Oceans’ campaign on board RSS James Cook during May 18th to June 15th 2012 financed by the UK Ocean Acidification Research Programme’s Benthic Consortium project (awards NE/H01747X/1 and NE/H017305/1) funded by NERC (Roberts et al., 2013). *Central NE Atlantic, Azores region* – Colonies of *M. oculata*, *D. pertusum*, *D. cornigera*, *D. dianthus* and *Caryophyllia* sp. were obtained from bycatch material from longline fishing cruises with RV *Arquipélago* (ARQDAÇO campaigns) and from the local longline fleet, and from observer onboard programme financed

by the EU CoralFISH project (EC/FP7:ENV/2007/1/213144). Samples of *M. oculata* and *D. pertusum* from the Menez Gwen seamount (Mid-Atlantic Ridge, MAR) were obtained during the scientific cruise MenezMar cruise (M82/3 cruise) on board R/V Meteor during September 2010 (Dubilier, 2010). The material was deposited in the biological reference collection of the University of the Azores (COLETA). NW Mediterranean Sea – Colonies of *M. oculata*, *D. pertusum*, *D. cornigera* and *D. dianthus* colonies were collected in the Cap de Creus canyon (NW Mediterranean Sea) during the cruises ‘Deep Coral I_Coral4’ and ‘HERMES IV_Coral8’ in July 2006 and September 2007 on board RV Garcia del Cid (Gilli, 2006; Orejas, 2007), financed by EU projects HERMES (Goce-CT-2005-511234-I), HERMIONE (Grant Agreement Number 226354).

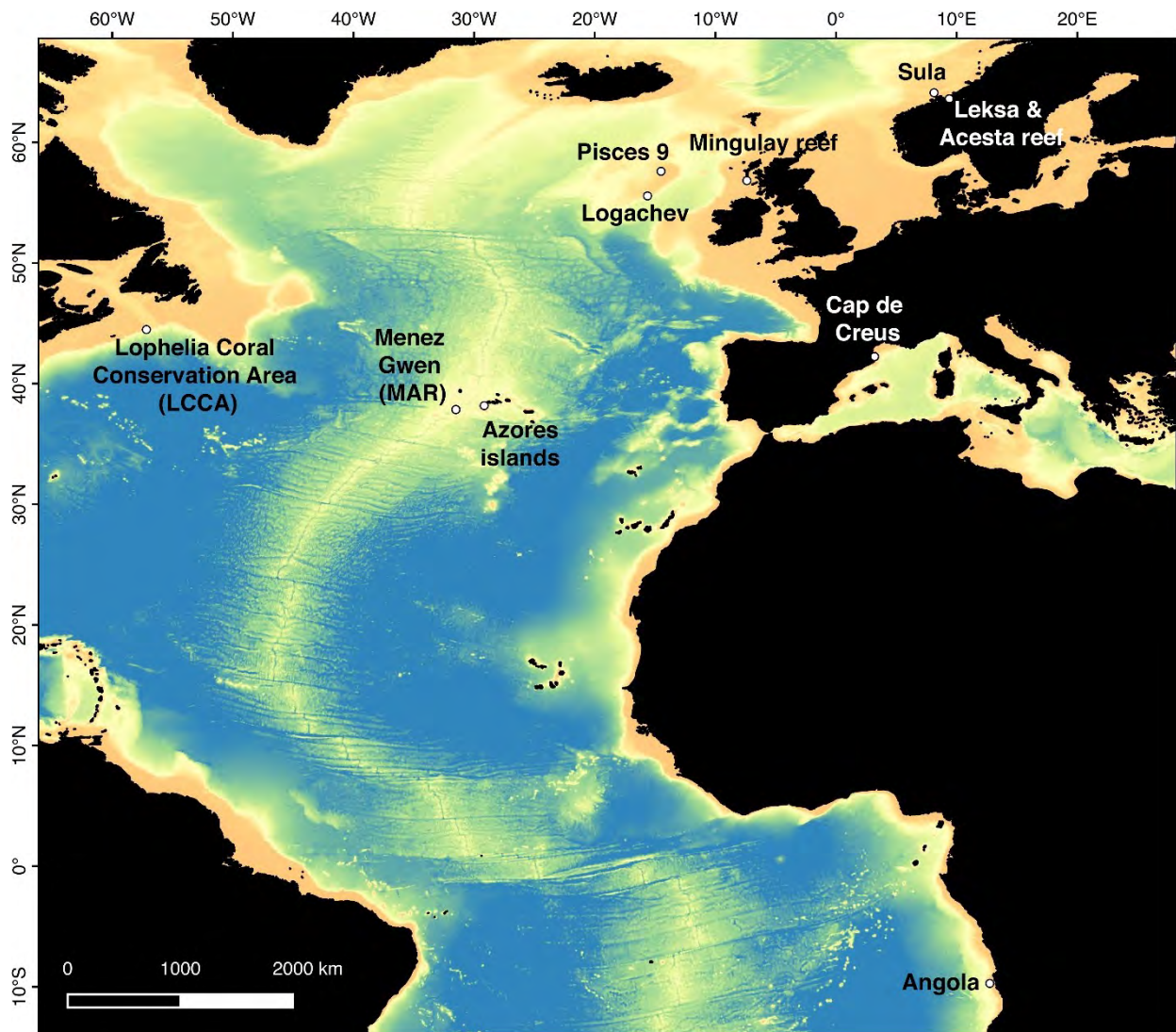


Figure 36. Map showing the collection sites of corals used in the study.

Table 23. Collection sites and depths of the cold-water coral species used in the study.

Species	Site	Latitude, Longitude	Depth (m)
NE Atlantic continental shelf of Norway			
<i>Desmophyllum pertusum</i>	Leksa reef	63.608 N; 9.379 E	152-159
<i>(Lophelia pertusa)</i>	Acesta reef	63.607 N; 9.382 E	216

Species	Site	Latitude, Longitude	Depth (m)
	Sula Reef	64.110 N; 8.118 E	300
NE Atlantic continental margins of Ireland and Scotland, UK			
<i>Desmophyllum pertusum</i> (<i>Lophelia pertusa</i>)	Mingulay Reef	56.822 N; 7.395 W	133
	Logachev site 1	55.554 N; 15.634 W	660
	Logachev site 2	55.494 N; 15.827 W	844
	Pisces 9	57.594 N; 14.512 W	217
Central NE Atlantic, Azores region			
<i>Desmophyllum pertusum</i> (<i>Lophelia pertusa</i>)	São Jorge Island slope	38.670 N; 28.270 W	1,071
	Menez Gwen seamount (MAR)	37.844 N; 31.520 W	898
<i>Madrepora oculata</i>	São Jorge Island slope	38.670 N; 28.270 W	1,071
	Menez Gwen seamount (MAR)	37.844 N; 31.521 W	898
<i>Dendrophyllia cornigera</i>	Baixa de São Mateus	38.339 N; 28.592 W	446
<i>Desmophyllum dianthus</i>	Condor Seamount	38.170 N; 29.170 W	625
<i>Caryophyllia cyathus</i>	Condor Seamount	38.514 N; 29.002 W	456
NW Mediterranean Sea			
<i>Desmophyllum pertusum</i> (<i>Lophelia pertusa</i>)	Cap de Creus canyon	42.232N, 3.190 E	300
<i>Madrepora oculata</i>			250
<i>Dendrophyllia cornigera</i>			250
<i>Desmophyllum dianthus</i>			300

Environmental seawater properties (Table 24) for the Norwegian shelf sites were collected during in July/August 2014, with RV *POSEIDON* (POS473) as reported in Büsher et al. (2019). Data for Mingulay Reef Complex, Logachev and Pisces mounds (Rockall Bank) was collected during the 'Changing Oceans' campaign on board RSS *James Cook* during May 18th to June 15th, 2012. Data for Cap de Creus Canyon were collected during the FishJelly campaign during July 2011. Data on temperature, salinity and pH in the Azores was obtained from different cruises in the region (MenezMar, CoralFish, MIDAS, BlueAzores2018). Measurements of total alkalinity followed standard procedures described in Dickson et al. (2007). The carbonate system was computed from the measured temperatures, salinities, phosphates, pH, TA and DIC concentrations using the CO2SYS program with the dissociation constants for carbonic acid of Mehrbach et al. (1973) after the refit of Dickson and Millero (1987).

Table 24. Physical-chemical parameters at the study sites. Data on Norwegian reefs from Büsher et al. (2019).

Site	Depth (m)	Salinity (ppt)	Temperature (°C)	TA ($\mu\text{mol kg}^{-1}$)	DIC ($\mu\text{mol kg}^{-1}$)	pH (total scale)
NE Atlantic continental shelf of Norway						
Leksa reef	190	35.1	7.7	2,306.7	2,157.0	7.994
Acesta reef	219	35.4	7.7	2,310.0	2,136.3	8.052
Sula reef	304	35.5	7.5	2,312.9	2,142.6	8.043

(Continuation)

Site	Depth (m)	Salinity (ppt)	Temperature (°C)	TA ($\mu\text{mol kg}^{-1}$)	DIC ($\mu\text{mol kg}^{-1}$)	pH (total scale)
	ρCO_2 (μatm)	$\Omega_{\text{Aragonite}}$				
Leksa reef	453.5	1.7				
Acesta reef	390.7	1.9				
Sula reef	399.8	1.9				
NE Atlantic continental margins of Ireland and Scotland, UK						
Mingulay Reef	133	35.27	9.30	2,295.1	2,101.1	8.08
Logachev site 1	660	35.38	9.54	2,309.9	2,148.9	7.97
Logachev site 2	844	35.22	7.16	2,321.7	2,159.2	8.00
Pisces 9	217	35.35	9.21	2,328.4	2,148.5	8.03
(Continuation)						
	ρCO_2 (μatm)	$\Omega_{\text{Aragonite}}$				
Mingulay Reef	362.3	2.09				
Logachev site 1	452.5	1.60				
Logachev site 2	405.4	1.53				
Pisces 9	404.0	1.91				
Central NE Atlantic, Azores region						
São Jorge Island slope	1,071	35.33	7.53	2,337.8	2,176.7	7.98
Menez Gwen seamount (MAR)	898	35.42	9.26	2,334.6	2,169.3	7.97
Baixa de São Mateus	446	35.66	12.46	2,344.8	2,132.1	8.04
Condor Seamount	456	35.66	12.49	2,345.1	2,132.0	8.04
Açor Seamount	625	35.49	10.93	2,333.7	2,153.1	7.99
(Continuation)						
	ρCO_2 (μatm)	$\Omega_{\text{Aragonite}}$				
São Jorge Island slope	420.6	1.47				
Menez Gwen hydrothermal vent field	442.5	1.56				
Baixa de São Mateus	391.9	2.15				
Condor Seamount	391.5	2.16				
Açor Seamount	435.2	1.80				

Site	Depth (m)	Salinity (ppt)	Temperature (°C)	TA ($\mu\text{mol kg}^{-1}$)	DIC ($\mu\text{mol kg}^{-1}$)	pH (total scale)
NW Mediterranean						
Cap de Creus canyon	250	38.49	13.30	2,578.7	2,311.5	8.08
	300	38.43	13.25	2,570.3	2,313.4	8.04
(Continuation)						
	$p\text{CO}_2$ (μatm)	$\Omega_{\text{Aragonite}}$				
Cap de Creus canyon	406.5	2.72				
	397.5	2.70				

Determination of skeletal density parameters - Measurements of skeletal micro-density followed the protocol described in Bucher (1998). Coral tissue was totally removed by immersing the samples in a sodium hypochlorite solution for 3 days, and then rinsing them in distilled water for another 3 days, with daily water changes. Corals were dried for 3–4 days at 50 °C. Specimens presenting signs of bioerosion were excluded from the analysis. To obtain the skeletal parameters, the weight of coral samples was measured using digital balance with underfloor weighing capability (Mettler-Toledo MS204S; accuracy of the balance: ~ 0.1 mg). For dry weight, coral fragments were placed on top of weighing pan. For buoyant weight measurements, the standard pan was replaced by a suspended weighing cradle attached to an underwater weighing pan submerged in 15-L aquaria filled with distilled water at 19 °C. A cover isolated the device from air flow within the laboratory. Each measurement was replicated three times for each specimen. Values were used to generate an estimate of mean volume for each specimen.

To ensure thorough cleaning, coral fragments were soaked in acetone, and placed in a vacuum oven to reduce pressure by 250mmHg until no visible gas escapes from skeletons (approximately 1 minute). This ensured maximum penetration of the acetone to displace air and dissolve residual waxes. The samples were allowed to stand in the acetone for 2 days with a further pressure reduction each day. Acetone was rinsed from the corals by adding fresh water in a continuous, gentle flow for 3 min allowing the excess to overflow. Coral samples were allowed to stand in the water overnight and were rinsed a second time before being returned to the vacuum oven and subjected to negative pressure of 500 mm Hg for 30 minutes. The vacuum oven was allowed to return to ambient pressure and left to stand for 3 days before saturated buoyant weights of cleaned material (BW_{sat}) were recorded. The coral fragments were oven-dried at 50°C to constant weight (DW_{clean}) and skeletal micro-density was calculated for each fragment following the equation below, where δm is density of the fluid medium (in this case, distilled water: 0.998 g cm⁻³ at 19 °C and 1 atm).

$$\text{Micro-density} = \text{DW}_{\text{clean}} \div \text{V}_{\text{matrix}}$$

$$\text{V}_{\text{matrix}} = (\text{DW}_{\text{clean}} - \text{BW}_{\text{sat}}) \times \delta m$$

For bulk density measurements, a thin coat of paraffin wax was applied to each clean sample (see above) by quickly dipping it into a pot of molten at 105–110°C. Then, the dry (DW_{wax}) and buoyant (BW_{wax}) weight of waxed coral skeletons were measured. The bulk weight and porosity were calculated following the equations:

$$\text{Bulk-density} = \text{DW}_{\text{clean}} \div \text{V}_{\text{enclosed}}$$

$$\text{V}_{\text{enclosed}} = (\text{DW}_{\text{wax}} - \text{BW}_{\text{wax}}) \times \delta m$$

$$\text{Porosity} = 100 \times (V_{\text{enclosed}} - V_{\text{matrix}}) \div V_{\text{enclosed}}$$

Multivariate analysis was performed using the statistical package PRIMER-E v.6 with the permutational multivariate analysis of variance (PERMANOVA) + add on (Anderson et al., 2008). A two-way analysis of variance (ANOVA) was used to test for differences in skeletal micro-density and bulk density among coral species and geographical regions. Differences in coral skeleton porosity percentage data were logit-transformed to linearise the data. The analyses used a resemblance matrix based on Euclidean distance and PERMANOVA was run using 9,999 permutations with partial sum of squares and unrestricted permutation of raw data to produce p-values. Significant main PERMANOVA tests were followed by pairwise PERMANOVA tests. Permutational P-values (PPERM) were interpreted when the number of unique permutations >100; alternatively, Monte Carlo P-values (PMC) were considered (Anderson and Robinson, 2003). Pearson's correlation coefficients were used to determine the relationship between the different skeletal density parameters and physical-chemical variables.

Modelling growth and death of coral reef framework

Water velocity dictates the delivery speed of zooplankton prey to coral, and there is an optimum velocity that is required for successful prey capture. Too fast and the tentacles of the coral retract, and a slow velocity allows the prey to evade capture (Orejas et al., 2016). As a coral colony grows, it alters the local hydrodynamics around its structure, directly impacting the live:dead ratio of its own colony. Larger colonies will impact (likely reducing incoming velocity) coral polyps 'lower down' the colony, to a point where low velocity equates to insufficient food capture rates. This is why coral colonies typically comprise of live coral around the top of the framework, with dead coral framework underneath as its own successful growth and ecosystem engineering has left conditions for the older parts sub optimal for survival. As colonies continue to grow, they will often fuse together with neighbouring colonies, further enhancing the complexity and density of the framework overall. This further modifies local hydrodynamics and illustrates the constant competition for coral to grow into optimum current velocities (Hennige et al., 2021) and why there typically a significant proportion of dead coral framework in many observed CWC reefs. This supports observations by Vad et al. (2017), where the proportion of living coral decreased as colonies increased in size and growth of the colony decreases.

Following methods from Hennige et al. (2021) and Georgoulas et al. (2023), a fully Lagrangian numerical Smooth Particle Hydrodynamics (SPH) approach was developed to model and capture the dynamic and complex hydrodynamic fluid–solid interactions of coral growth. In brief, the SPH method operates using integral interpolation theory to discretise a set of partial differential equations into meshless points that are subsequently solved iteratively using an appropriate time integration scheme. A newly settled single hemispherical coral is situated at the centre of the seabed, where the coral's growth is predicted using a set of simple rules; the coral colony will grow towards surrounding regions where the hydrodynamic flow conditions are favourable within the optimum reported range. As the coral grows it alters the hydrodynamics around it, modifying the dynamic flow environment for itself. Optimum current flow conditions around the corals are the metric used to determine coral growth, and it is assumed that when that condition is met that corals are able to capture and ingest prey, providing them with energy for growth. Likewise, when flow conditions are undesirable, a death rule is implemented to ascertain when the above rules no longer apply, and a living coral particle will 'die'. This 'death rule' can be modified to allow corals to survive for a variable amount of simulated growth time in suboptimal flow conditions, and by doing so, simulate the use of its energetic reserves by the corals. No arbitrary branching rules were applied in the model, and any branching observed is a result of the dynamic interaction of the flow and

the set of prescribed rules as outlined above.

The preliminary SPH model developed by Hennige et al. (2021) was advanced here to include energetic reserves within the living coral (i.e., how long can the coral survive in sub optimum hydrodynamic conditions), and to include finite food reserves. The latter is particularly important when considering how these ecosystems will fare in the future, as food supplies will change (Sweetman et al., 2017). The growth model here investigated how energetic reserves can affect coral growth and mortality. The simulation parameters (Table 25) are based on a mono-directional flow from left to right and a simplified growth principle; the coral colony would only grow in optimal conditions and towards regions with average flow velocities between 2 and 6 cm/s (Georgoulas et al., 2023). It investigated and showcased how the Goldilocks Principle can be applied to cold-water coral growth and how coral energetic reserves can affect their growth and longevity.

Table 25. Coral growth simulation parameters for Smooth Particle Hydrodynamic models to simulate coral growth and death (Georgoulas et al., 2023).

Simulation	A	B	C
Top layer velocity (m/s)	0.5		
Optimal layer velocity (cm/s)	2–6		
Initial Energetic Reserves, ER (units of energy)	∞	1.1	3.1
Ratio of live to total coral particles, (at step 120)	100	0	10.7

6.2 Results

Live and dead CWC framework at different Atlantic sites

Using methods from De Clippele et al. (2021) on published images, surface area of live and dead coral framework at 3 Atlantic sites were compared (*Desmophyllum pertusum* (*Lophelia pertusa*) and *M. oculata*) in the Canadian *Lophelia* Coral Conservation Area, Angola, and Pisces (UK) (Table 26). Live CWC framework per m² of reef analysed was in the same order of magnitude for all sites. There was a larger contrast amongst dead coral framework, with the Canadian *Lophelia* Coral Conservation Area having very low quantities of dead framework compared to Angola or UK CWC areas. In many images analysed from the Canadian *Lophelia* Coral Conservation Area, dead coral framework was entirely absent. Average values (\pm SE) of coral per m² were 0.06 \pm 0.02 and 0.01 \pm 0.01 for live and dead respectively. Pisces average values of live and dead coral per m² were 0.05 \pm 0.01 and 0.10 \pm 0.02 respectively. Combined, *M. oculata* had a larger colony density including live and dead coral material (*L. pertusa*) than Pisces or Canada (Orejas et al., 2021) of 0.54 \pm 0.37 compared to 0.15 (Pisces) and 0.05 (Canada). The large difference between Canada and Angola is the lack of dead framework in Canada, and the significant dead framework of *M. oculata* in Angola (Orejas et al., 2021).

Table 26. Locations of the three study sites for surface area of live and dead coral framework in the Atlantic

Site	Latitude	Longitude	Reference
<i>Lophelia</i> Coral Conservation Area (LCCA), Canada	44.47353	-57.176393	Korabik et al. (2022)
Angola	-9.724813	12.741125	Orejas et al. (2021)
Pisces	57.5947	-14.5125	Roberts et al. (2013)

Carbon turnover

Using methods outlined in De Clippele et al. (2021) and the values above, carbon turnover $\text{m}^{-2} \text{yr}^{-1} \text{g}^{-1}$ of coral (live and dead) was calculated and compared to existing values (Table 27, Figure 37). For *D. pertusum*, calculation of values including average polyp numbers m^{-2} , respiration rates of live and dead coral, and biomass conversions were all taken from values in De Clippele et al. (2021). For *M. oculata* reef framework, equations were modified to include the average polyp count per m^2 (using images from Orejas et al. (2021), an average count of 5,520 compared to a count of 3,100 m^2 in *D. pertusum* framework in De Clippele et al., 2021 due to the smaller nature of *M. oculata* polyps), polyp weight values (Maier et al., 2013) and respiration values of *M. oculata* from Naumann et al. (2014). An additional correction of ‘hidden’ polyps within reef framework was also applied (to account for the higher factor of visible polyps in *M. oculata* framework, correction factor of 5,520/3,100 polyps = 1.78). New values here were within the same range as those previously published by De Clippele et al. (2021), with the more notable differences again being observed in dead coral framework. There was no significant difference between live coral carbon turnover rates between sites, but there was for the dead coral framework, with Angola, Pisces and Canada all significantly differing from each other. Combined carbon turnover values also significantly differed, with Angola being significantly higher than Pisces and Canada. There was no significant difference in combined carbon turnover values between Pisces and Canada (Table 27). Of note is that *M. oculata* specific dead coral framework values were not integrated with the equations of De Clippele et al. (2021), as there are currently no framework scale assessments for dead *M. oculata* respiration rates, so *D. pertusum* equation values were used.

Table 27. The average carbon turnover rates (\pm SE) per g of coral (live, dead and total) per m^2 per year. Values are highlighted of framework forming corals *Desmophyllum pertusum* (*Lophelia pertusa*) (LP) and *Madrepora oculata* (MO) in Angola, Mingulay, Pisces and Canada. Mingulay values (*) were already published in De Clippele et al. (2021) but converted here from T of Carbon into g of Carbon for comparative purposes. Values are also combined to give a total comparative value. Image sample sizes across sites were uneven and ranged from 4–28 available images.

	Carbon turnover Live coral $\text{g C y}^{-1} \text{m}^{-2}$	Carbon turnover Dead coral $\text{g C y}^{-1} \text{m}^{-2}$	Total Carbon turnover $\text{g C y}^{-1} \text{m}^{-2}$
Mingulay (LP)*	18.8	25.9	44.7
Pisces site (LP)	21.1 (1.90)	10.5 (2.25)	31.6
Canada (LP)	21.4 (5.99)	1.11 (0.96)	22.5
Angola (MO)	31.1 (3.91)	21.9 (2.64)	53.0

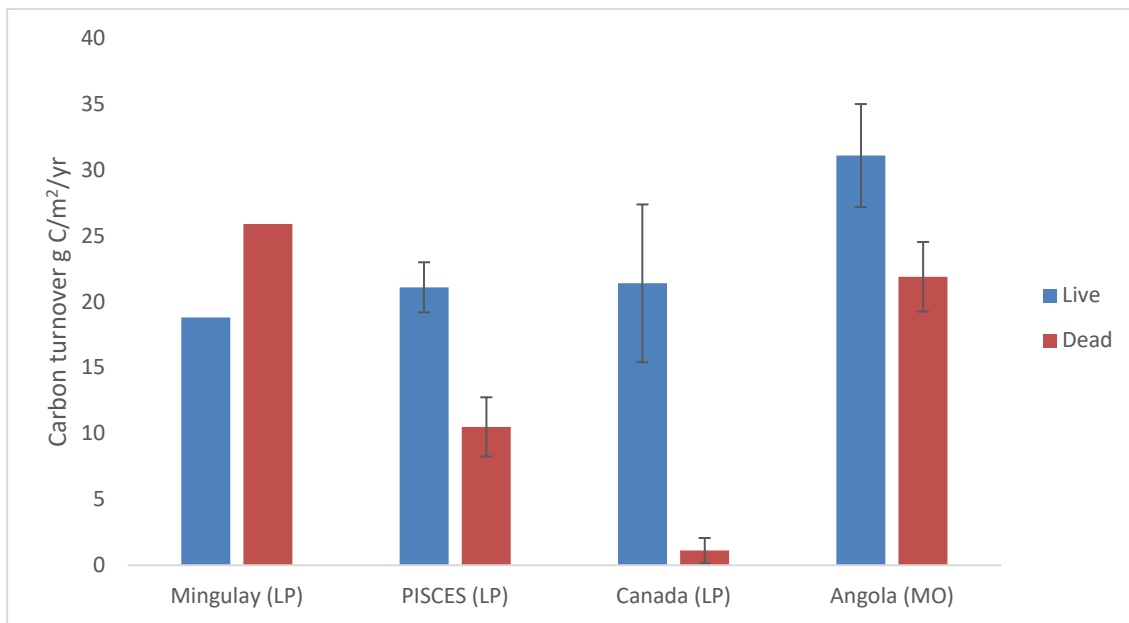


Figure 37. Graphical comparison of average carbon turnover rates (\pm SE) per g of coral (live, dead and total) per m^2 per year. Values are highlighted of framework forming corals *Desmophyllum pertusum* (*Lophelia pertusa*) (LP) and *Madrepora oculata* (MO) in Angola, Mingulay, Pisces and Canada. Mingulay values (*) were already published in De Clippele et al. (2021) but converted here from T of Carbon into g of Carbon for comparative purposes.

Comparison of values

In the previous section, *M. oculata* carbon turnover rates were calculated using respiration values from Naumann et al. (2014). Carbon turnover rates were also calculated using respiration rates from Maier et al. (2013) and using *D. pertusum* (*L. pertusa*) values from De Clippele et al. (2021) (Table 28). This was to ascertain the suitability in using *D. pertusum* (*L. pertusa*) specific values for another major framework forming CWC, and the range in carbon turnover from using key variables from the published literature, and not specifically from the region analysed below. Carbon turnover rates were highest when using *D. pertusum* (*L. pertusa*) specific values (respiration, polyp numbers per unit area and weight of coral polyps) compared to *M. oculata* specific adjustments (Table 28). Values using *M. oculata* specific calculations were of the same magnitude as those using *D. pertusum* (*L. pertusa*) ranges but were 10–20 g of Carbon per year per m^2 lower.

Table 28. Average carbon turnover rates per g of live coral per m^2 per year for *M. oculata* in Angola. Values are compared using *M. oculata* specific polyp numbers, polyp weight and respiration values from two different studies, with equations from *D. pertusum* (*L. pertusa*) (De Clippele et al., 2021).

	Carbon turnover Live coral $g C y^{-1} m^{-2}$
Angola <i>Madrepora oculata</i> (values calculated using <i>Desmophyllum pertusum</i> (<i>Lophelia pertusa</i>) equations from de Clippele et al., 2021)	40.6
Angola <i>Madrepora oculata</i> (respiration values from Naumann et al., 2014)	31.1
Angola <i>Madrepora oculata</i> (respiration values from Maier et al., 2013)	20.4

Variability in live and dead framework proportions

There was significant variability between and within sites with regard to the amount of live and dead coral framework. From the Canadian *Lophelia* Coral Conservation Area, a large proportion of the images that contained *D. pertusum* (*L. pertusa*) only contained low percentages of live coral overall (Table 29). This ranged from <1 % to 29% in one instance, but overall, there was low live coral cover from the images analysed (Average 5.5%, n = 23 images, Median = 1.57). However, within these images, there was only very low occurrences of dead coral framework, with the coral being often entirely alive on exposed substrate. Out of 23 images that contained evidence of *D. pertusum* (*L. pertusa*), there were only 3 occurrences where any dead material was evident, giving a very high overall living coral ratio (Table 29).

Table 29. Results from the Canadian *Lophelia* Coral Conservation Area of living layer: whole colony ratio, and the percentage of live coral overall compared to the whole image area with average, standard error, and median metrics.

Image number	% live coral overall	LL: WC
1	0.81	1.00
2	10.1	1.00
3	1.61	1.00
4	0.68	1.00
5	3.50	1.00
6	0.06	1.00
7	0.53	1.00
8	16.5	1.00
9	5.03	1.00
10	8.84	0.30
11	0.07	1.00
12	0.95	1.00
13	1.20	1.00
14	13.0	0.95
15	5.19	1.00
16	0.20	1.00
17	1.31	1.00
18	6.21	1.00
19	0.23	1.00
20	1.06	1.00
21	29.7	1.00
22	18.2	0.90
23	1.57	1.00
Average	5.51	0.96
SE	1.61	0.031
Median	1.57	1.00

Canada is an extreme example of how the live and dead coral framework proportions may change, and comparing data of live and dead from the NE, NW and SE Atlantic, (Mingulay Reef Complex, PICES, Canada and Angola) using methods described above highlights the range and variability of LL:WC ratios in live coral framework of two major framework forming species, *D. pertusum* (*L. pertusa*) and *M. oculata*. With the exception of data from Canada, all sites had a wide range of LL: WC values, with minimum levels (~0.1)

demonstrating high levels of dead coral framework. Average values of ~ 0.38 were found at the MRC, Pisces and Angola (Table 30). Data from Canada has a low replicate number of available image frames with live coral present, and of those instances, very little dead coral material was evident although this was evident in other images within the region not assessed through the workflow described above. Importantly, all data showcased the significant presence (and variability) of dead coral skeleton.

Table 30. Site comparisons of Living Layer: Whole Colony ratio of framework forming corals including *D. pertusum* (*L. pertusa*) (LP) off Angola, Canada, the Mingulay Reef Complex (MRC) and Pisces, with standard error, median, and min/max values. Published values for the live and dead ratio are included in the table for comparative purposes, although absolute values may differ due to the Vad et al. methodology used (compared in full in earlier section). Angola *M. oculata* values are from Orejas et al. (2021) (*) and show LL:WC values using published average coral live and dead sizes.

Site	LL:WC average	LL:WC median	LL:WC Min	LL:WC Max
MRC (LP)	0.38 (0.05)	0.47	0.11	0.73
Pisces (LP)	0.39 (0.09)	0.39	0.15	0.59
Canada (LP)	0.96 (0.03)	1.00	0.30	1.00
MRC (Vad et al., 2017) (LP)	0.17 (0.02)	0.18	0.11	0.27
Pisces (Vad et al., 2017) (LP)	0.16 (0.01)	0.18	0.13	0.18
Angola (MO)	0.29			

Variations in skeletal density across species and regions

Skeletal density is a measure of a coral's investment in its structure that combined with other growth components (calcification, linear extension) can determine the vulnerability of corals to physical damage and changes in environmental conditions (Lough and Barnes, 2000). Here we provide a baseline characterisation of the skeletal density for five common CWC species in the Atlantic that can be used to detect changes related to future ocean conditions.

Bulk density and porosity in the CWC examined were more variable than micro-density both between species and for the same species within different geographic regions (Table 31 and Figure 38). Bulk density was strongly negatively correlated with porosity for all coral species and geographic regions (Pearson correlation $p < 0.001$), but both of these parameters were independent of micro-density (Pearson correlation $p > 0.05$). The same trend was observed in studies examining skeletal density in tropical (Bucher et al., 1998) and temperate coral species (Caroselli et al., 2011; Goffredo et al., 2015; Özalp et al., 2018), suggesting that variations in bulk density and porosity were not influenced by the micro-density of corals.

The values of skeletal microdensity, bulk density and porosity reported here are within the range of values reported for tropical and temperate coral species (Bucher, 1998; Caroselli et al., 2011, Hughes, 1987, Morgan and Kench, 2012, Ng et al., 2019). Microdensity of the studied corals did not vary significantly for the species *D. dianthus*, *Caryophyllia* sp., *D. pertusum* (*L. pertusa*) and *M. oculata* across the different regions studied ($2.76\text{--}2.81\text{g}\cdot\text{cm}^{-3}$ PERMANOVA $p > 0.05$, Table 3), except for *D. pertusum* (*L. pertusa*) and *M. oculata* collected in the slopes of the island São Jorge in the Azores ($2.32 \pm 0.14\text{g}\cdot\text{cm}^{-3}$ for *D. pertusum* (*L. pertusa*) and $2.57 \pm 0.08\text{g}\cdot\text{cm}^{-3}$ for *M. oculata*, PERMANOVA pair-wise comparison $p < 0.05$). The species *D. cornigera* also presented significantly lower skeletal microdensity when compared with other species but was not different between the Azores and the Mediterranean (2.69 ± 0.12 and 2.63 ± 0.11 respectively, PERMANOVA $p > 0.05$). Differences in skeletal bulk density and porosity within and across geographic region were greater than microdensity differences. Lowest bulk densities and highest porosity were recorded for the solitary corals *D. dianthus* and *Caryophyllia* sp. studied in the Azores (Table 31) likely

related to the morphology of the corals.

Table 31. Skeletal density parameters (micro-density, bulk density and porosity) for the different species studied and for the different study sites within three geographic regions (NE Atlantic, Central NE Atlantic, NW Mediterranean). Values are mean \pm SD, n=3–12.

Species	Site	Micro-density (g.cm ⁻³)	Bulk Density (g.cm ⁻³)	Porosity (%)
NE Atlantic continental shelf of Norway				
<i>Desmophyllum pertusum</i> (<i>Lophelia pertusa</i>)	Leksa reef	2.76 \pm 0.04	1.30 \pm 0.22	52.43 \pm 8.27
	Acesta reef	2.72 \pm 0.09	1.37 \pm 0.14	49.55 \pm 6.42
	Sula reef	2.77 \pm 0.01	1.27 \pm 0.01	54.37 \pm 0.32
NE Atlantic continental margins of Ireland and Scotland, UK				
<i>Desmophyllum pertusum</i> (<i>Lophelia pertusa</i>)	Mingulay Reef	2.76 \pm 0.03	1.43 \pm 0.36	48.1 \pm 13.8
	Logachev site 1	2.78 \pm 0.04	1.27 \pm 0.18	53.4 \pm 7.01
	Logachev site 2	2.77 \pm 0.06	1.88 \pm 0.11	31.6 \pm 3.62
	Pisces 9	2.76 \pm 0.20	1.40 \pm 0.56	49.8 \pm 9.89
Central NE Atlantic (Azores region)				
<i>Desmophyllum pertusum</i> (<i>Lophelia pertusa</i>)	São Jorge Island slope	2.32 \pm 0.14	1.51 \pm 0.09	35.0 \pm 3.30
	Menez Gwen	2.81 \pm 0.04	1.63 \pm 0.36	42.2 \pm 10.1
<i>Madrepora oculata</i>	São Jorge Island slope	2.57 \pm 0.08	1.87 \pm 0.09	21.3 \pm 2.30
	Menez Gwen (MAR)	2.81 \pm 0.01	2.06 \pm 0.23	26.8 \pm 8.10
<i>Dendrophyllia cornigera</i>	Baixo de São Mateus	2.69 \pm 0.12	1.25 \pm 0.36	53.7 \pm 12.80
<i>Desmophyllum dianthus</i>	Açor Seamount	2.77 \pm 0.04	0.98 \pm 0.14	64.9 \pm 5.06
<i>Caryophyllia</i> sp.	Condor Seamount	2.78 \pm 0.03	1.21 \pm 0.21	55.6 \pm 7.56
NW Mediterranean Sea				
<i>Desmophyllum pertusum</i> (<i>Lophelia pertusa</i>)	Cap de Creus canyon	2.77 \pm 0.12	1.29 \pm 0.15	53.3 \pm 6.2
	<i>Madrepora oculata</i>	2.78 \pm 0.03	1.61 \pm 0.13	42.0 \pm 4.5
<i>Dendrophyllia cornigera</i>		2.63 \pm 0.11	1.39 \pm 0.24	45.9 \pm 6.7
<i>Desmophyllum dianthus</i>		2.77 \pm 0.03	1.44 \pm 0.21	47.9 \pm 7.1

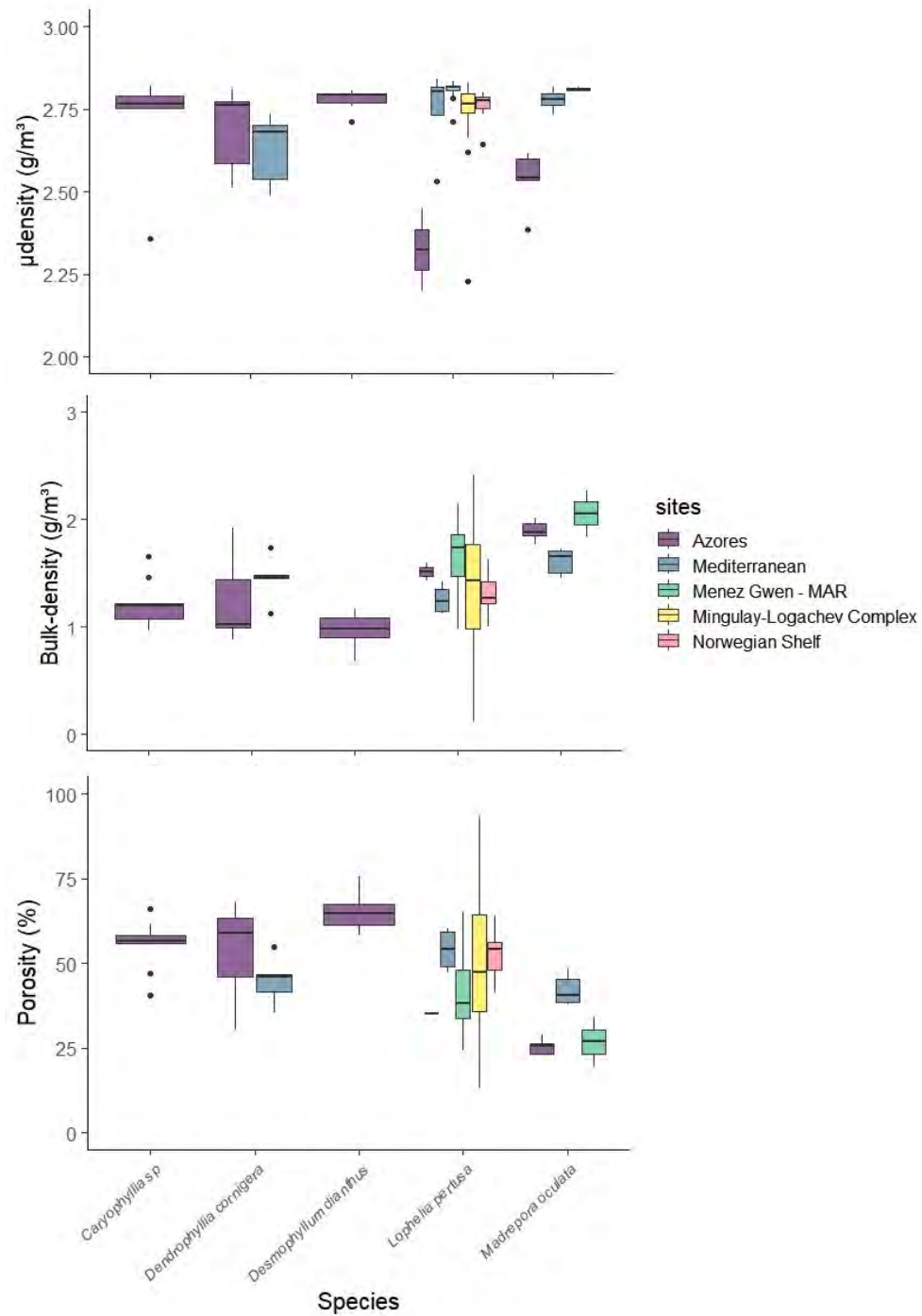


Figure 38. Skeletal density parameters (micro-density, bulk density and porosity) for the different species studies in three geographic regions (NE Atlantic, Central NE Atlantic, NW Mediterranean).

Correlation analysis between *D. pertusum* (*L. pertusa*) average skeletal bulk density, porosity and physical chemical variables across different geographic regions (Table 24) revealed that skeletal porosity tended to be lower at higher depths (Pearson, $r=-0.77$, $p=0.01$), whereas bulk density tended to increase with depth (Pearson $r=0.63$, $p=0.06$). The inverse pattern between bulk density and porosity is not surprising as they are strongly negatively correlated. No other physical-chemical variables tested showed a significant correlation with bulk density or porosity. Factors such as water motion and food availability not examined here could contribute to the observed pattern and this should be further examined.

Modelling growth of live and dead CWC

The growth model investigated how energetic reserves can affect coral growth and mortality. Initially the model was used to simulate coral growth with no energetic growth constraints or death (Figure 39). As the image progresses from left to right, you can observe live red coral ‘particles’ growing from 20, to 60 to 120 steps of the dynamic growth model. The final structure is a branching coral from a single base, with all coral particles alive. This is contrary to what is observed *in situ*, where 100% live coral is not observed.

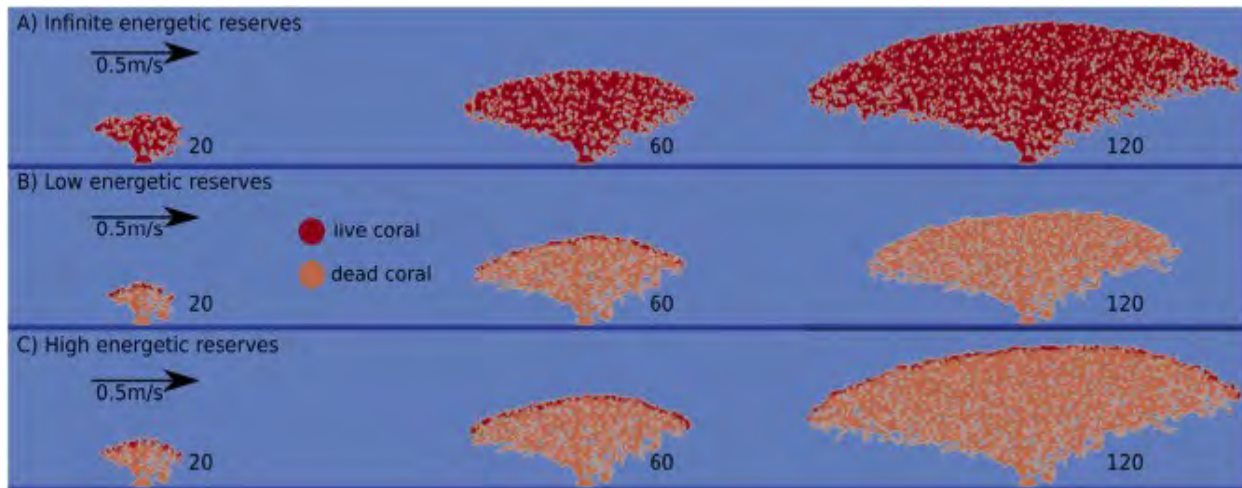


Figure 39. Coral Growth using the Goldilocks Principle (that coral will grow where conditions are ‘just right’) in simulations with A) infinite initial energetic reserves, B) low initial energetic reserves and C) high initial energetic reserves. Growth is shown between the 20th, 60th and 120th growth steps. Flow is in one direction and is from left to right at 0.5 m/s.

Previous studies have shown that *D. pertusum* (*L. pertusa*) reefs can survive in sub-optimal conditions for a period of months by using their energetic reserves to cover their energetic demands (Georgoulas et al., 2023). Simulation ‘B’ above introduced a ‘death’ rule that was based on each coral particle's available energetic reserves (see methods). The amount of the initial energetic reserves for a coral particle indicated how many consecutive growth steps this particle could survive in sub-optimal conditions. If during a growth step the coral particle was in sub-optimal regions and had no available energetic reserves left, then the death rule was applied, and the particle was considered ‘dead’. It could no longer branch out and grow but it would be part of the coral's skeleton for the remaining simulated time. When the coral particles were initialised to have near-zero or very low energetic reserves then eventually the entire coral framework died when it was exposed to consecutive non-optimal flow conditions (i.e. it did not have the energetic reserves to survive periods of no food intake due to sub optimum water flow conditions). In the simulations with higher initial energetic reserves (C) the resulting coral framework consisted of dead coral skeleton on the inside with branches of live coral on the outer edges, similar to what can be observed in *in situ* reefs (Figure 39).

The above model showcases how live framework can transition to dead framework if exposed to sub optimal flow conditions as it grows. In doing so, it accounts for energetic reserves of the live coral, but not whether it can replenish the reserves as they do *in situ*. By modifying the SPH to allow each coral particle to replenish its energetic reserve we can investigate the longevity of coral under different situations.

Table 32. Dynamic energetic reserves in 2D SPH simulations. The presented properties of the coral colonies are taken from the 100th growth-steps of the simulations.

Ability to replenish energetic	Ratio of live to total coral	Relative average energetic
0	9.8±0.11	0.91±0.04
0.1	10.1±0.11	1.22±0.04
0.3	10.6±0.11	1.42±0.07
0.5	11.2±0.11	1.56±0.07
0.7	12.5±0.13	1.78±0.09
0.9	14.1±0.14	1.96±0.09

When coral particles had higher abilities to replenish their energetic reserves the resultant coral colonies had higher average energetic reserves. It is also notable that being able to stay alive for longer resulted to colonies that had higher number of live coral particles compared to the total amount of coral particles in the domain. This ratio was dropping as the simulations progressed and was higher for simulations that allowed the colonies to replenish their energetic reserves faster (Table 32).

A limitation of the previous SPH model was that it disregarded the effects of gravity in coral growth. This is particularly important in the context of this case study, where the proportion of live and dead corals are considered *in situ*. In real world reef situations, once a coral reaches a certain size then it will be unable to sustain its form and will break. This is why the skeletal density variability explored above is so important. The breaking process is well documented in many ecosystems and is particularly evident in the Pisces coral systems where it would be impossible for a single point to support all this newly created mass of coral structure above it, and the colonies would start to break-down according to the mechanism suggested by Wilson (1979). In order to mimic this mechanism and visualise more realistic coral colonies an intermediate 'gravity' step has been included in the following model. Here, the coral colony would initially grow similarly to the previous model until it reached the 60th growth step. At that moment a break-down mechanism was initiated to simulate the effects of gravity to the coral colony. After the simulation of this intermediate gravity-step reached steady state, the additional gravitational acceleration was again set to zero, the particles of the top boundary were re-initialised with the input velocity (0.5 m/s) and the growth model started once again to simulate coral growth based on the newly imposed boundary conditions (Figure 40).

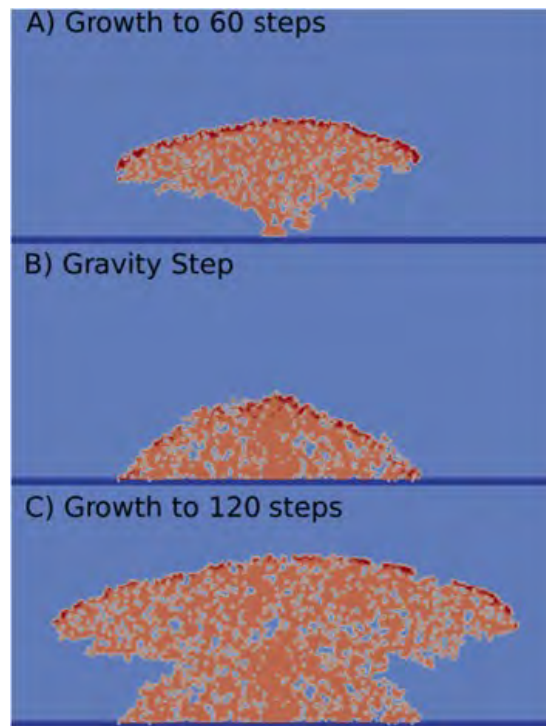


Figure 40. Including the effects of gravity in coral growth. Initially a coral colony grew from a single point for 60 growth steps (A). At this point a break-down mechanism was initiated and the resultant colony is shown to include **gravitational effects** (B). Finally, growth in the domain has been re-initiated and coral growth at 120 growth steps is shown (C).

Figure 41 shows the velocity vector shortly after the gravity step of the growth model (70th growth step). The velocity magnitude of the water in the domain is zero at the bottom boundary where the no-slip condition is enforced, and it increases with the height of the domain until it reaches its maximum value (0.5 m/s) at the top boundary (omitted in the figures). A region of recirculating flow is created downstream of the colony that helps elevate low velocity regions. Its position and size depend on the incident velocity and the shape of the dynamically growing coral colony. The below coral colony is now starting to look more like colonies *in situ*, where live coral can often be found on top of a dense aggregation of dead coral framework.

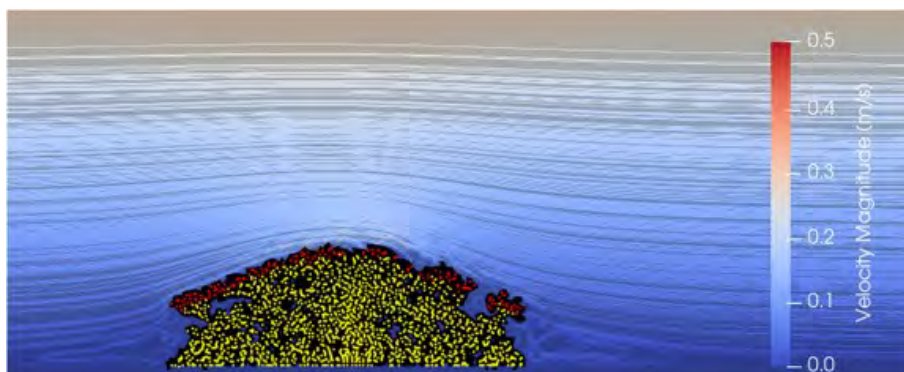


Figure 41. Velocity profile with streamlines around the coral colony at the 70th growth step. Red particles show live coral particles while yellow particles denote dead coral framework. For interpretation of the references to colour in this figure legend, please refer to Georgoulas et al. (2023).

6.3 Discussion

It is clear that there is variability between and within sites in terms of coral cover and the proportion of live and dead coral, which feeds directly into their carbon cycling and ecosystem function. It is important to note that the variability highlighted also reflects the way in which data is gathered. An ROV focussed on finding and imaging live coral areas will likely return images with a higher proportion of coral cover than a transect over a reef area due to bare patches being imaged. It is equally important to recognise that data here represents a snapshot of each region and does not reflect the coral cover over each region. However, it is still critical to have this data for comparisons, to understand a current baseline of each region, and to consider what impact future environmental change may have.

The coral growth models highlight how local hydrodynamics will impact coral growth and death. While we cannot quantify this in each image, the modelling allows us to understand why there is significant variability even within one site. To counter this, future work can build on the baseline created here to add in more images and sites to reduce intra-site variability error.

The amount of dead and live coral framework was quantified for two major coral species; *D. pertusum* (*L. pertusa*) and *M. oculata*. Both species provide similar functions but differ with regard to some species-specific growth rates and forms. Image data here, mostly gathered from ROV surveys where images would have been taken in dense coral locations, highlighted the variability in live and dead coral coverage per m². Most striking was the lack of dead material in the Canada *Lophelia* conservation area. The other sites have values in a similar range with respect to carbon turnover of live coral, but there was a difference with regard to the ratio of live and dead contribution to carbon turnover. For the Mingulay Reef Complex, dead material contributed a higher average of carbon turnover than live coral. This was in contrast to Angola (*M. oculata*), Canada and Pisces, where there was less contribution to carbon turnover from dead coral framework. For Canada, this is a clear reflection of the lack of dead coral material, and the high values at the MRC reflect the large amount of dead coral framework contributing to the overall carbon turnover. Carbon turnover analysed here was on a scale of per m² which allows for comparisons between sites at a baseline level.

However, this scale does not inform on ecosystem carbon turnover value, as that requires knowledge of the extent of the reef area. This can be done through *in situ* observations or through predictive mapping as in De Clippele et al. (2021).

Importantly, *M. oculata* carbon turnover values were similar to those of *D. pertusum* (*L. pertusa*) when the calculations were modified to account for the higher density of *M. oculata* polyps per m² (they are smaller than those of *D. pertusum* (*L. pertusa*)), the smaller weight per polyp, and the respiration rates specific to *M. oculata*. With the exception of Canada which had an abnormally small amount of dead coral framework, region values for Carbon Turnover ranged from 31–53 g C m² yr⁻¹. Including Canada this range was 22–53 g C m² yr⁻¹ when using average values from each region. The variability within these values is driven by the quantity of dead material but also respiration values. This is particularly clear when assessing *M. oculata* carbon turnover values calculated with differing respiration rates and also with *D. pertusum* (*L. pertusa*) specific values. However, the values for all calculations were still within the range of the cross-site comparisons above although it is worth noting the values using *D. pertusum* (*L. pertusa*) values were double that of using *M. oculata* specific variables. This highlights that to get accurate representations of carbon turnover per site, species specific details are needed. More experimentally derived respiration rates from target species from different regions would also help refine calculations, as would more dead material respiration rates, requiring specialised equipment such as eddy covariance landers (Rovelli et al.

2015; de Froe et al. 2019).

Live and dead framework knowledge (Living: Whole Colony ratios) varied considerably, with a large range at many sites. This again reflects the heterogeneous conditions within regions and sites, and the amount of dead material will directly be driven by local hydrodynamics and food supply (Maier et al., 2023; Vinha et al., 2023). Aside from the Canadian dataset, which is dominated by live coral, a clear trend is that over 50% of the framework at all sites is dominated by dead coral framework. This is reflective of the role it plays in overall carbon turnover as well, as it is worth considering how the two different coral species, *D. pertusum* (*L. pertusa*) and *M. oculata* may differ with regard to their baffling capacity for fine sediment, which will also significantly contribute to carbon turnover (de Froe et al., 2019).

When considering the live and dead framework within coral growth models, the variability observed in different *in situ* locales reflects both broad and small-scale effectors. On the broad scale, food supply (in terms of quantity) will be critically important in determining the amount of living material (Georgoulas et al., 2023). Environmentally, regional currents will dictate the food supply to the corals. Food supplies will determine primarily whether a coral will live or die, but also the energetic reserves and growth potential of live coral (along with other environmental conditions that are optimal for growth). This in turn will dictate how the coral will grow, and how this will influence local hydrodynamics and reduce food supply to 'older' coral polyps lower down, leading to an increase in dead coral framework. This is seen directly in SPH assessments here, and how limited food supplies will lead to higher proportions of dead material. This is a particular challenge when considering the future of these ecosystems, as they are entirely reliant upon food supply rates. When conducting future climate scenario experiments of framework forming CWC, a common theme has also been that they can survive future conditions (to a point with plenty of caveats on unknown energetic allocations) if food supply is adequate. The live:dead ratio of framework will thus also be affected by the reliability and quality of future food supplies, which is expected to change (Sweetman et al., 2017). Addressing this challenge will require experimental work to quantify energetic allocation under different scenarios, observational efforts of reefs with differing food supplies, and *in silico* studies where results from the above can be validated and tested in theoretical models, similar to Georgoulas et al. (2023).

Regarding current observations of live: dead coral variability, the biological condition of the coral will also play an important role here with regard to the energetic reserves it contains, and how much live coral occurs within the framework. It is known from experimental studies that energetic reserves can be depleted over time to assist corals in surviving environmental stressors (Buscher et al., 2017). Cold-water corals are characterised by various processes that require high energetic inputs; calcification, tissue and mucus production, reproduction, and maintenance (Hennige et al., 2014). Energetic demands in different sites and for different species could vary, with more energetic reserves used to maintain stable calcification rates and keeping coral 'alive'. The SPH model presented here examined how the rate that CWC can replenish energy during growth steps with optimal flow conditions can affect coral longevity. The results suggest that when the coral particles were allowed to replenish more energy in optimal time-steps, colonies had a higher ratio of live coral particles to total coral particles in the domain. As expected, this also meant that in higher energetic reserve value simulations the average energetic reserves at later stages of simulations were higher and these colonies could therefore survive longer in sub-optimal conditions. This does not quantify the variability observed in live: dead ratios observed above but gives an indication on why there is such variability, as it will depend on local conditions, which will vary in each and every image. The long-term prosperity and longevity of CWC colonies will also depend on their ability to store a portion of the energy they create by capturing prey. This could make a significant difference in periods

that they are exposed to continuous sub-optimal flow conditions or in situations where their energetic demands increase due to changes in environmental variables. This is particularly important when we look forward into how these reefs and their functioning may change in the future, as food supply will change in addition to growth rates of coral (environmentally driven).

Vad et al. (2017) showed that the ratio of living coral to the whole colony size was between 0.10 and 0.27. It was also shown that this ratio is negatively correlated to the whole colony size. [Table 33](#) below shows the ratio of live coral particles to the total coral particles in the domain in simulations with various energetic reserve configurations. In the modelled coral colonies, the ratio varied between 0.098 and 0.17 between the 50th and the 100th growth step showing the same negative correlation with the colony size as well - the ratio drops in value as the simulations progress while the total coral particle number can only increase.

Table 33. Ratio of live to total coral particles in the domain at the 50th and 100th growth steps based on the simulated ability of the colonies to replenish their energetic reserves.

Ability to replenish energetic reserves	Ratio of live to total coral particles (%)	
	At 50 growth steps	At 100 growth steps
0	15.1±0.14	9.8±0.11
0.1	15.7±0.14	10.1±0.11
0.3	15.9±0.14	10.6±0.11
0.5	16.2±0.15	11.2±0.11
0.7	16.5±0.16	12.5±0.13
0.9	16.9±0.16	14.1±0.14

At later stages of the simulations the ratio of live coral particles to the whole coral particles is lower than observed *in situ*. The domain size was chosen initially to be large enough that it would not affect the growth of the coral colonies, but also not too large that it would make the simulations very computationally expensive. As the coral colonies grow and occupy larger parts of the finite numerical domain, it is possible that at later stages the dimensions of the domain start to affect growth. The ratio of live coral to total coral particles can be used then as a method to end the simulations when it starts to drop too far below the expected values.

While data here highlights the variability in the ratio of live to dead coral, it is biased through only occurring in data frames where live coral is present. This means that for analysis in terms of future ecosystem degradation through ocean acidification led coralporosis, it can underestimate the occurrence of dead coral material in regions as a whole. Going forward, it is clear that across Atlantic locations that the occurrence of dead coral skeleton is significant. The variability means that for modelling work, local assessments should be used where possible, but broad scale variables available from the literature will give you values within the range showcased here.

The question of how the ratio of live:dead coral skeletal material varies between and within sites/ species becomes particularly pertinent when considering future impacts of climate change ([Figure 42](#)). With the major environmental stressors including ocean acidification, deoxygenation and temperature increases, major changes are expected with regard to the ways in which live corals will grow, and how dead corals will erode.

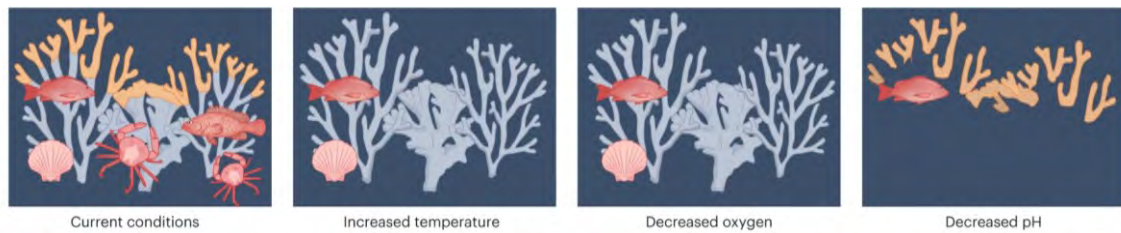


Figure 42. Adapted from Barnhill et al. (2022). Examples illustration how the ratio of live:dead coral reef framework by be impacted by environmental conditions.

Each stressor may singly have a different impact upon this reef accretion (or erosion) process, with deoxygenation and temperature changes impacting the live coral directly and indirectly, through an environmental envelope beyond which survival is not possible, but also in growth rates. Ocean acidification will act primarily upon the exposed dead coral framework, although it may impact the energetic requirements of the living coral as well, which regulates pH internally to allow it to grow (Hennige et al., 2015; McCulloch et al., 2012). In key framework forming reefs living in extreme environmental conditions (e.g. reefs off California which are in aragonite undersaturated water analogous to future ocean acidification conditions that most deep-sea reefs will experience (Guinotte et al., 2006; Hennige et al., 2020), reefs grow with a lack of dead coral framework. It is unknown whether those reefs transition from those with mixed live and dead framework to those primarily with live framework, or whether coral started growing there in already aragonite undersaturated waters. Regardless, this underlines the process that live coral growth and dead coral erosion reaches an imbalance in future ocean acidification scenarios, with dead framework erosion negating net coral reef growth.

When we look at the skeletal density of skeletons, which will directly contribute to the *rate* at which the above process of a mixed live and dead reef transitioning to a primarily live reef can happen, there is significant variability and evidence above highlights several interesting avenues to explore that may drive this. Variations in microdensity related to different proportion of organic matter in the skeleton have been reported as inter-species differences (Cuif et al., 1999) and related to the changes in intra-crystalline OM content with age (Caroselli et al., 2011; Goffredo et al 2015). The consistently lower microdensity of *D. cornigera* in both the Azores and the Mediterranean suggests and species-specific characteristics related to the irregularly porous thecal wall of dendrophyllids, with the pores and tissue lining the pores being continuous from the outside to the inside of the corallum (Cairns et al., 2002), conferring *D. cornigera*'s light and brittle skeletons. Micro-density is the specific gravity of the material of which the skeleton is made constrained by the structure of the aragonitic crystals and the relative proportion of inter-crystalline organic matter (Cuif et al., 1999). The reasons for the lower micro-density in *D. pertusum* (*L. pertusa*) and *M. oculata* collected in the island slopes are unclear. A potential explanation could be related to changes in the crystal arrangement of skeletons and shells in response to elevated nutrient concentrations (Belda et al., 1993; Kinsey and Davies, 1979; Risk and Sammarco, 1991; Simkiss, 1964). Although we did not collect data on nutrient concentrations at the site of collection, video observations revealed the presence of plant leaves (F. Tempera, pers. observ.), which very likely reflects the high land-based input of organic matter and nutrients from the São Jorge island to deep-sea areas. Depths of 500 m are attained within only 200 m from the coast of the island, which makes deep-sea areas particularly susceptible to land-based inputs.

Variations in bulk density and porosity between the species examined here likely reflect their different morphology (e.g. calicular diameter). Studies in tropical corals have found large differences in bulk density/porosity among growth forms (Hughes, 1987; Morgan and Kench et al., 2012; Ng et al., 2019) that although not directly comparable with CWCs, support the contention that the growth form can be an

important factor influencing bulk density/porosity. Apart from growth morphology, environmental factors such as depth, water motion and temperature have been shown to be important factors influencing skeletal bulk densities for both tropical (e.g. Morgan and Kench et al., 2012; Ng et al., 2019) and temperate CWC (Caroselli et al., 2011, 2015; Goffredo et al., 2015; Özalp et al., 2018). Lower skeletal density has also been associated with a reduction in Ω_{arag} in tropical corals (Helmle et al., 2011; Mollica et al., 2018). In our study we could only detect a significant pattern in increasing bulk density and decreasing porosity with depth, but not with other variables associated with depth (e.g. temperature, carbonate chemistry), which could be a result of the low number of samples and sampling sites. In addition, patterns in skeletal density could be influenced by other factors not included in our study such as water motion and food availability, and this should be further examined. Studies on bulk density and porosity on tropical coral species have found that linear extension decrease whilst skeletal density increases with water depth (Lough and Barnes, 2000; Scoffin et al., 1992). The reasoning behind the inverse pattern is that lower extension rates allow more time for skeletal thickening (assuming no significant change in tissue thickness) (Lough and Barnes, 2000), possibly favouring the mechanical resistance of the skeleton in depth (Goffredo et al., 2015; Özalp et al 2018).

Future studies where skeletal density, linear extension and calcification are measured simultaneously for the same coral specimens will help clarify the relationship between these growth characteristics and their controlling factors. Amongst the different macronutrients, phosphate has been found to be particularly detrimental to coral density because phosphate ions are capable of replacing carbonate ions in the crystal lattice, distorting the orderly array of ions on the crystal surface (Simkiss, 1964). As a result of this distortion, coral skeletal integrity may be compromised due to the production of a porous and structurally weaker calcium carbonate/calcium phosphate skeleton (Simkiss, 1964). The incorporation of phosphate ions in cold-water coral skeletons has been confirmed by Montagna et al. (2006) who found a strong correlation between phosphate within the coral skeleton of *D. dianthus* and the water column, and this warrants further investigation.

Looking forward, understanding drivers of live and dead fractions with the understanding of how local conditions and structural stability can impact this proportion through SPH modelling with skeletal density modified per species will allow us to better predict future impacts of environmental change to the structure and functioning of these reefs. To do this, *in silico* reefs (Figure 43) (Wolfram et al., 2022) can be created to apply dissolution rates/ coralporosis projections to dead coral skeletons, while different growth rates can be applied to live coral. This will give a timescale of when larger habitats will start to undergo net losses or changes. This is a step beyond experimental and observational evidence, but a requirement is the live:dead ratio of reefs, biomass mapping, and the specific climate projections for that region, all of which is now becoming understood.

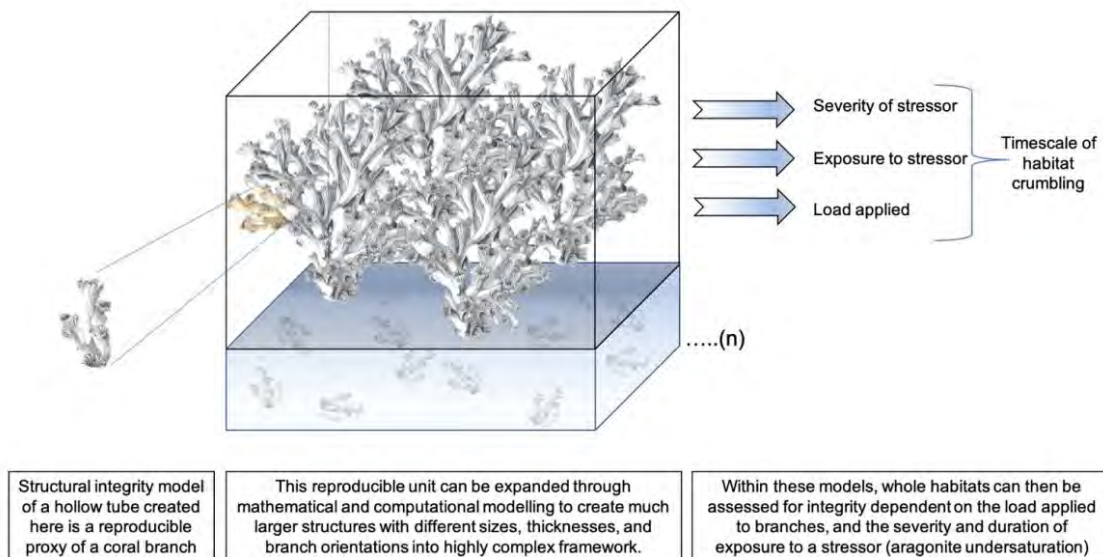


Figure 43. Scaling up from branch to habitat. Schematic of how the structural integrity model of a theoretical coral is reproducible and can be expanded through mathematical and computational modelling to create much larger, complex framework. The structural integrity of the framework can then be assessed by integrating information of the exposure to, and severity of the stressor to quantify timescales of habitat crumbling. The shaded area with coral fragments below the coral framework represents coral rubble infilled with sediment, and (...)(n) indicates how the framework can be extended to much larger sizes in a reproducible way. The starting ratio of live:dead coral would dictate whether this framework is susceptible to ocean acidification/ the proportion that is. Image adapted from Hennige et al. (2020).

As we look across the Atlantic, the NE and NW Atlantic are relatively eutrophic environments and characterised by high pH and O₂ conditions (Figure 44). In contrast, the deep layers of the S Atlantic are lower in O₂ concentration and seawater pH (Figure 44) and are characterised by less food availability. We know that food availability is crucial for these CWC reefs and drives their distribution (Maier et al. (2023) and references therein), so reefs where there is less food availability could potentially be vulnerable to live coral death and an increase in the proportion of dead coral material.

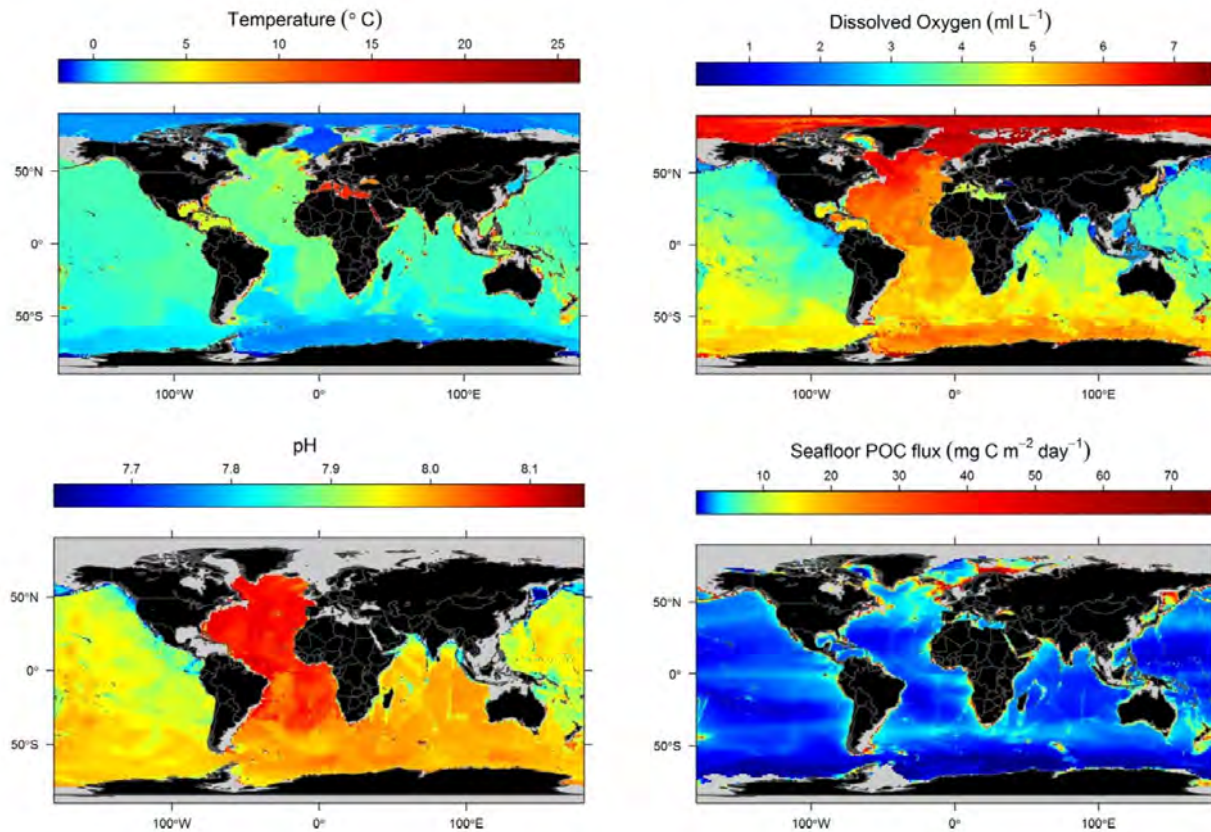


Figure 44. Present-day environmental conditions at the deep seafloor. Temperature ($^{\circ}\text{C}$), dissolved oxygen (mL L^{-1}), pH, and seafloor POC flux ($\text{mg C m}^{-2} \text{d}^{-1}$) conditions at the deep ($> 200 \text{ m}$) seafloor. Figure from Sweetman et al. (2017).

However, carbon turnover results above highlight that across sites, there was no significant difference in the carbon turnover ($\text{m}^{-2} \text{yr}^{-1}$) of the live coral fraction based upon amounts per unit area analysed. The difference between sites was driven primarily by the contribution of the dead coral fraction, which is over 50% in all sites examined here and accounts for the majority of reef framework in most cases. While the oxygen and nitrogen flux are primarily driven by the live coral (de Froe et al., 2023), the carbon cycling of *dead* coral material in addition to live coral is a critical driver of their carbon cycling overall and their reef function. This underlines the point that when we consider the ecosystem function of these reefs, further efforts need to be done to understand the functioning of dead material in addition to live. An interesting avenue for future research as well will be to determine the baffling differences and sediment accumulation rates of different coral species, as the sediment accumulation within dead framework will additionally feed into the overall functioning and CN cycling of these ecosystems. It is now well understood how complex the drivers are of CWC reef function (Maier et al., 2023), but through multiple avenues of research at multiple levels (e.g., crystal to reef – skeletal densities leading to growth rate variability and structural stability, biomass of different reef systems, CN cycling of live and dead reef framework, and modelling of coral growth and death depending upon energetic reserves), we can better understand these ecosystems in the present and future to sustain these diversity-productivity hotspots.

7. Key conclusions from the different case studies

The initial objective of the present Deliverable was to compare deep-ocean ecosystem dynamics from a number of habitats with the Atlantic Ocean Basin that varied in environmental conditions to be able to try and assess the response of deep Atlantic ecosystems to anthropogenic climate change using a space-for-time approach. The Covid-19 pandemic as well as alterations to ship schedules caused by cancellations and sudden, unexpected ship repairs prevented us from visiting many of the study sites we initially intended to visit, which put significant constraints on what was achieved in Deliverable 4.2. Nevertheless, we were able to undertake a number of studies in the Atlantic Basin and compare our results to similar studies conducted in other areas of the Atlantic and elsewhere to derive a number of conclusions about how climate change may impact the deep Atlantic.

The comparison of the datasets collected from the soft-sediment abyssal experiments conducted around Cabo Verde during iAtlantic and in the Porcupine Abyssal Plain in 2000 (Case study 1) showed that the abyssal CVAB is functioning as a mesotrophic abyssal habitat rather than an oligotrophic ecosystem. While we found lower bacterial biomass at the CVAB compared to the PAP, we documented greater bacterial C processing rates at CVAB. This indicates that the short-term bacterial processing efficiency (i.e., unit biomass⁻¹) is greater on the CVAB compared to the PAP and suggests that declining productivity caused by climate change could lead to a reduction in bacterial biomass as noted in numerous studies, but an increase in bacterial C-processing efficiency. Greater meiofauna C-processing efficiency was also found for the CVAB when compared to the PAP. Consistent with the *in situ* benthic ecosystem function results, our LIM model analysis (Case study 1) also showed greater C-cycling efficiency at the CVAB compared to the more eutrophic PAP. For example, the ecosystem size expressed as the Total System Throughflow (TST) of C at the CVAB was 69% of the ecosystem size at the PAP. Therefore, we can conclude that as food supply to the seafloor decreases with climate change, differences in food-web organisation and flows will possibly force abyssal ecosystems to use the available C more efficiently and have a relatively large TST compared to the total C influx.

The greater importance of microbes in more oligotrophic settings was not only observed by comparing the abyssal experimental data from CVAB and PAP but was also suggested when comparing isotope data of CWC reefs from Lampaul Canyon in the eutrophic NE Atlantic (Case study 4) to the same species of CWCs from more oligotrophic environments. In Lampaul Canyon, we detected both *D. pertusum* (*L. pertusa*) and *M. oculata* were largely feeding on zooplankton as also found by Carlier et al. (2009), yet the same species in the warmer, central oligotrophic Mediterranean Sea had much lower $\delta^{15}\text{N}$ -values indicative of feeding at much lower trophic positions, possibly on microorganisms. Moreover, we found that the two CWC species from Lampaul Canyon shared a considerable portion of their dietary niche space and could be relying on the same resources in this eutrophic region. Thus, if food availability becomes limiting in future due to climate change it is plausible that competition for food by *D. pertusum* and *M. oculata* increases and these faunas rely more on microbes as part of their diet.

Additional experiments conducted during the iMirabilis2 expedition quantified the ecosystem functioning of bathyal slope environments using an *ex-situ* approach (Case Study 2). We found higher SCOC rates compared to the other studies in the Atlantic, which could be related to a high influx of organic matter to the seafloor at our site due to the intense upwelling and OMZ that has developed east of the Cabo Verde archipelago. The lower organic matter remineralisation in the OMZ possibly allowed for greater POC input to the bathyal seafloor in Cabo Verde and higher seafloor respiration rates relative to other areas not exposed to such extreme gradients in oxygen, such as the more northerly N. Atlantic.

Our experiments to study how changes in upper pelagic ecosystems (e.g., shifts from fish to squid) may impact the demersal and benthic scavengers of the Atlantic (Case study 3) showed a clear difference in the community composition of scavengers, and feeding activity at the squid and fish baits. We found that the squid was very rapidly consumed compared to the fish bait. The rapid removal of squid was likely related to the smaller size and softer tissue compared to the oil mackerel since more energy would be expelled piercing and consuming the more rigid fish skin and tissue fused to the fish bones. Compared to other sites, we found that the squid and fish consumption rates were greater than at shallower depths from the more eutrophic Arctic Ocean, and the southern Norwegian Sea, which could indicate that declining productivity may lead to more intense scavenging activity at the seafloor. This would then likely benefit faster swimming fauna, which was also the most likely reason for the different community composition being detected between the fish and squid baits. Ultimately, these experiments showed how changes to upper ocean ecosystems may cause effects thousands of meters below the ocean surface and the close connection between food input and deep-sea ecosystem processes.

Finally, we evaluated the live and dead portions of CWC reefs from 4 sites in the Atlantic, which included areas beneath eutrophic waters and bathed in high O₂ and pH settings (e.g., MRC, PICES, Canada) as well as areas in more oligotrophic settings (Angola) naturally exposed to lower O₂ and pH conditions to assess how the proportions differed, and their carbon turnover m⁻². Our findings showed a dominance of dead coral material at the majority of sites, and the total carbon turnover m⁻² was highest in the Angola site compared to NE and NW Atlantic sites. These results were complemented by analysis of skeletal densities (underlying structural integrity of coral framework) demonstrated that skeletal density varies among different species and with depth, with solitary corals (e.g. *D. dianthus* and *Caryophyllia* sp.) having lowest bulk densities and highest porosity and the colonial *D. cornigera* having lowest skeletal microdensity, related with different growth form and skeletal arrangement. We recorded increasing skeletal bulk density and decreasing porosity with depth, while microdensity did not show a significant trend with depth or other depth-related environmental variables. Moreover, we used models of coral growth where we demonstrated how decreasing food supply will lead to a decreased proportion of living coral, which will directly contribute to changes in carbon turnover. Changing O₂, pH conditions and a reduction in food availability may therefore have significant impacts on the growth and death of these hard substrate Vulnerable Marine Ecosystems (VMEs) in the Atlantic, and ultimately on their biodiversity support and function.

8. References

- Aberle, N., & Witte, U. (2003). Deep-sea macrofauna exposed to a simulated sedimentation event in the abyssal NE Atlantic: In situ pulse-chase experiments using ¹³C-labelled phytodetritus. *Marine Ecology Progress Series*, 251, 37–47. <https://doi.org/10.3354/meps251037>
- Ahrens, M. J., Graf, G., & Altenbach, A. V. (1997). Spatial and temporal distribution patterns of benthic foraminifera in the Northeast Water Polynya, Greenland. *Journal of Marine Systems*, 10(1–4), 445–465. [https://doi.org/10.1016/S0924-7963\(96\)00052-8](https://doi.org/10.1016/S0924-7963(96)00052-8)
- Ainsworth, T. D., Hurd, C. L., Gates, R. D., & Boyd, P. W. (2020). How do we overcome abrupt degradation of marine ecosystems and meet the challenge of heat waves and climate extremes? *Global Change Biology*, 26(2), 343–354. <https://doi.org/10.1111/GCB.14901>
- Amano, C., Zhao, Z., Sintès, E., Reinthaler, T., Stefanschitz, J., Kisadur, M., Utsumi, M., & Herndl, G. J. (2022). Limited carbon cycling due to high-pressure effects on the deep-sea microbiome. *Nature Geoscience* 2022 15:12, 15(12), 1041–1047. <https://doi.org/10.1038/s41561-022-01081-3>
- Anderson, M. J., Gorley, R. N., and Clarke, K. R. (2008). PERMANOVA+ for PRIMER: Guide for software and statistical methods (PRIMER-E: Plymouth, UK.).
- Anderson, M. J., and Robinson, J. (2003). Generalized discriminant analysis based on distances. *Aust. N. Z. J. Stat.* 45 (3), 301–318.
- Arrigo, K. R., van Dijken, G., & Pabi, S. (2008). Impact of a shrinking Arctic ice cover on marine primary production. *Geophysical Research Letters*, 35(19). <https://doi.org/10.1029/2008GL035028>
- Auffret, G.-A., Geitsdoerfer, P., Ondreas, H., Mauviel, A., Gaillard, J.-F., Reyss, J.-L., Rabouille, C., Voisset, M., Coutelle, A., Müller, C., KERBRAT, R., & MONTI, S. (1992). Caractérisation sédimentologique et biologique préliminaire des sites du projet EUMELI. *Comptes Rendus de l'Académie Des Sciences. Série 2, Mécanique, Physique, Chimie, Sciences de l'univers, Sciences de La Terre*, 314(2), 187–194.
- Avril, B. (2013). *Dissolved organic carbon measured on water bottle samples during L'Atalante cruise EUMELI3*. PANGAEA. <https://doi.org/10.1594/PANGAEA.804911>
- Bailey, D. M., & Priede, I. G. (2002). Predicting fish behaviour in response to abyssal food falls. *Marine Biology*, 141(5), 831–840. <https://doi.org/10.1007/S00227-002-0891-9>
- Barnes, D.J., Devereux, M.J., (1988). Variations in skeletal architecture associated with density banding in the hard coral *Porites*. *J. Exp. Mar. Biol. Ecol.* 121, 37–54. Barnes, D.J., Lough, J.M., 1993.
- Barnhill, K.A., Roberts, J.M., Myers-Smith, I. et al. (2023). Incorporating dead material in ecosystem assessments and projections. *Nat. Clim. Chang.* 13, 113–115
- Belda CA Cuff C, Yellowlees D (1993) Modification of shell formation in the giant clam *Tridacna gigas* at elevated nutrient levels in sea water. *Mar. Biol.* 117: 251–257
- Bernardino, A. F., Berenguer, V., & Ribeiro-Ferreira, V. P. (2016). Bathymetric and regional changes in benthic macrofaunal assemblages on the deep Eastern Brazilian margin, SW Atlantic. *Deep Sea Research Part I: Oceanographic Research Papers*, 111, 110–120. <https://doi.org/10.1016/J.DSR.2016.02.016>
- Bianchelli, S., Gambi, C., Zeppilli, D., & Danovaro, R. (2010). Metazoan meiofauna in deep-sea canyons and adjacent open slopes: A large-scale comparison with focus on the rare taxa. *Deep-Sea Research I*, 57, 420–433. <https://doi.org/10.1016/j.dsr.2009.12.001>
- Billett, D. S. M., Bett, B. J., Rice, A. L., Thurston, M. H., Galéron, J., Sibuet, M., & Wolff, G. A. (2001). Long-term change in the megabenthos of the Porcupine Abyssal Plain (NE Atlantic). *Progress in Oceanography*, 50(1–4), 325–348. [https://doi.org/10.1016/S0079-6611\(01\)00060-X](https://doi.org/10.1016/S0079-6611(01)00060-X)
- Bittig, H. C., Körtzinger, A., Neill, C., van Ooijen, E., Plant, J. N., Hahn, J., Johnson, K. S., Yang, B., & Emerson, S. R. (2018). Oxygen optode sensors: Principle, characterization, calibration, and application in the ocean. *Frontiers in Marine Science*, 4(JAN), 1–25. <https://doi.org/10.3389/fmars.2017.00429>
- Blankenship, L. E., & Levin, L. A. (2007). Extreme food webs: Foraging strategies and diets of scavenging amphipods from the ocean's deepest 5 kilometers. *Limnology and Oceanography*, 52(4), 1685–1697. <https://doi.org/10.4319/LO.2007.52.4.1685>
- Blazewicz-Paszkowycz, M., & Ligowski, R. (2002). Diatoms as food source indicator for some Antarctic Cumacea and Tanaidacea (Crustacea). *Antarctic Science*, 14(1), 11–15.

- <https://doi.org/10.1017/S0954102002000524>
- Bopp, L., Aumont, O., Cadule, P., Alvain, S., & Gehlen, M. (2005). Response of diatoms distribution to global warming and potential implications: A global model study. *Geophysical Research Letters*, 32(19). <https://doi.org/https://doi.org/10.1029/2005GL023653>
- Bouchet, P., & Warén, A. (1985). *Revision of the northeast Atlantic bathyal and abyssal Neogastropoda excluding Turridae (Mollusca, Gastropoda): Vol. Supplemento 1*. Società italiano di malacologia,. <https://doi.org/10.5962/bhl.title.140763>
- Brauns, M., Boëchat, I. G., de Carvalho, A. P. C., Graeber, D., Gücker, B., Mehner, T., & von Schiller, D. (2018). Consumer-resource stoichiometry as a predictor of trophic discrimination ($\Delta^{13}\text{C}$, $\Delta^{15}\text{N}$) in aquatic invertebrates. *Freshwater Biology*, 63(10), 1240–1249. <https://doi.org/10.1111/FWB.13129>
- Breitbart, D., Levin, L. A., Oschlies, A., Grégoire, M., Chavez, F. P., Conley, D. J., Garçon, V., Gilbert, D., Gutiérrez, D., Isensee, K., Jacinto, G. S., Limburg, K. E., Montes, I., Naqvi, S. W. A., Pitcher, G. C., Rabalais, N. N., Roman, M. R., Rose, K. A., Seibel, B. A., ... Zhang, J. (2018). Declining oxygen in the global ocean and coastal waters. *Science*, 359(6371). https://doi.org/10.1126/SCIENCE.AAM7240/ASSET/5ABDCCC4-FCCB-4103-A62B-F643E8891DDE/ASSETS/GRAPHIC/359_AAM7240_FA.JPEG
- Brinch-Iversen, J., & King, G. M. (1990). Effects of substrate concentration, growth state, and oxygen availability on relationships among bacterial carbon, nitrogen and phospholipid phosphorus content. *FEMS Microbiology Ecology*, 7(4), 345–355. <https://doi.org/10.1111/J.1574-6941.1990.TB01701.X>
- Brunnegård, J., Grandel, S., Ståhl, H., Tengberg, A., & Hall, P. O. J. (2004). Nitrogen cycling in deep-sea sediments of the Porcupine Abyssal Plain, NE Atlantic. *Progress in Oceanography*, 63(4), 159–181. <https://doi.org/10.1016/j.pocean.2004.09.004>
- Buchanan, J. B. (1984). Sediment analysis. In N. A. Holme & A. D. McIntyre (Eds.), *Methods for the study of marine benthos*. (pp. 41–65). Blackwell Scientific Publications.
- Bucher DJ, Harriott VJ, Roberts LG (1998). Skeletal micro-density, porosity and bulk density of acroporid corals. *J. Exp. Mar. Biol. Ecol.* 228: 117–136.
- Burd, A. B., Hansell, D. A., Steinberg, D. K., Anderson, T. R., Arístegui, J., Baltar, F., Beupré, S. R., Buesseler, K. O., DeHairs, F., Jackson, G. A., Kadko, D. C., Koppelman, R., Lampitt, R. S., Nagata, T., Reinthaler, T., Robinson, C., Robison, B. H., Tamburini, C., & Tanaka, T. (2010). Assessing the apparent imbalance between geochemical and biochemical indicators of meso- and bathypelagic biological activity: What the @\$#! is wrong with present calculations of carbon budgets? *Deep-Sea Research Part II: Topical Studies in Oceanography*, 57(16), 1557–1571. <https://doi.org/10.1016/j.dsr2.2010.02.022>
- Büscher, J. V., Form, A. U., & Riebesell, U. (2017). Interactive Effects of Ocean Acidification and Warming on Growth, Fitness and Survival of the Cold-Water Coral *Lophelia pertusa* under Different Food Availabilities. *Frontiers in Marine Science*. 4
- Büscher, J. V., Wisshak, M., Form, A. U., Titschack, J., Nachtigall, K., & Riebesell, U. (2019). In situ growth and bioerosion rates of *Lophelia pertusa* in a Norwegian fjord and open shelf cold-water coral habitat. *PeerJ* 7: e7586.
- Büscher, J. V., Form, A. U., Wisshak, M., Kiko, R., & Riebesell, U. (2022). Cold-water coral ecosystems under future ocean change: Live coral performance vs. framework dissolution and bioerosion. *Limnology and Oceanography*, 67(11), 2497-2515.
- Cairns, S.D. (2002) Dendrophylliina. Dendrophylliidae Gray 1847. Version 28 October 2002. <http://tolweb.org/Dendrophylliidae/19165/2002.10.28> in The Tree of Life Web Project, <http://tolweb.org/>
- Campanyà-Llovet, N., Snelgrove, P. V. R., & Parrish, C. C. (2017). Rethinking the importance of food quality in marine benthic food webs. *Progress in Oceanography*, 156, 240–251. <https://doi.org/10.1016/J.POCEAN.2017.07.006>
- Carlier, A., Le Guilloux, E., Olu, K., Sarrazin, J., Mastrototaro, F., Taviani, M., Clavier, J., 2009. Trophic relationships in a deep Mediterranean cold-water coral bank (Santa Maria di Leuca, Ionian Sea). *Mar. Ecol. Progr. Ser.* 397, 125–137.
- Caroselli E, Nanni V, Levy O, Falini G, Dubinsky Z, Goffredo S (2015) Latitudinal variations in biometry and

- population density of a Mediterranean solitary coral suggest higher tolerance to seawater warming for non-zooxanthellate species. *Limnol Oceanogr* 60:1356-1370
- Caroselli E, Prada F, Pasquini L, Marzano FN, Zaccanti F, Falini G, Goffredo S (2011). Environmental implications of skeletal micro-density and porosity variation in two scleractinian corals. *Zoology*, 114(5): 255-264.
- Catullo, R. A., Llewelyn, J., Phillips, B. L., & Moritz, C. C. (2019). The Potential for Rapid Evolution under Anthropogenic Climate Change. *Current Biology*, 29(19), R996–R1007. <https://doi.org/10.1016/J.CUB.2019.08.028>
- Cecchetto, M. M., Moser, A., Smith, C. R., van Oevelen, D., & Sweetman, A. K. (2023). Abyssal seafloor response to fresh phytodetrital input in three areas of particular environmental interest (APEIs) in the western clarion-clipperton zone (CCZ). *Deep Sea Research Part I: Oceanographic Research Papers*, 195, 103970. <https://doi.org/10.1016/J.DSR.2023.103970>
- Clarke, K. R. (1993). Non-parametric multivariate analyses of changes in community structure. *Australian Journal of Ecology*, 18(1), 117–143. <https://doi.org/10.1111/J.1442-9993.1993.TB00438.X>
- Cosson, N., Sibuet, M., & Galeron, J. (1997). Community structure and spatial heterogeneity of the deep-sea macrofauna at three contrasting stations in the tropical northeast Atlantic. *Deep Sea Research Part I: Oceanographic Research Papers*, 44(2), 247–269. [https://doi.org/10.1016/S0967-0637\(96\)00110-0](https://doi.org/10.1016/S0967-0637(96)00110-0)
- Cuif JP, Dauphin Y, Gautret P (1999) Compositional diversity of soluble mineralizing matrices in some recent coral skeletons compared to fine-scale growth structures of fibres: discussion of consequences for biomineralization and diagenesis. *Int. J. Earth Sci.* 88, 582–592.
- Dadou, I., Lamy, F., Rabouille, C., Ruiz-Pino, D., Andersen, V., Bianchi, M., & Garçon, V. (2001). An integrated biological pump model from the euphotic zone to the sediment: A 1-D application in the Northeast tropical Atlantic. *Deep-Sea Research Part II: Topical Studies in Oceanography*, 48(10), 2345–2381. [https://doi.org/10.1016/S0967-0645\(00\)00177-6](https://doi.org/10.1016/S0967-0645(00)00177-6)
- Danovaro, R., Dell'Anno, A., Corinaldesi, C., Magagnini, M., Noble, R., Tamburini, C., & Weinbauer, M. (2008). Major viral impact on the functioning of benthic deep-sea ecosystems. *Nature*, 454(7208), 1084–1087. <https://doi.org/10.1038/nature07268>
- Danovaro, R., Dell'Anno, A., & Fabiano, M. (2001). Bioavailability of organic matter in the sediments of the Porcupine Abyssal Plain, northeastern Atlantic. *Marine Ecology Progress Series*, 220, 25–32. <https://doi.org/10.3354/meps220025>
- Danovaro, R., Dinet, A., Duineveld, G., & Tselepidis, A. (1999). Benthic response to particulate fluxes in different trophic environments: a comparison between the Gulf of Lions–Catalan Sea (western-Mediterranean) and the Cretan Sea (eastern-Mediterranean). *Progress in Oceanography*, 44(1–3), 287–312. [https://doi.org/10.1016/S0079-6611\(99\)00030-0](https://doi.org/10.1016/S0079-6611(99)00030-0)
- De Almeida Alves-Júnior, F., De Sá Leitão Cmara De Araújo, M., & Souza-Filho, J. F. (2017). New records of deep-sea shrimps of family Solenoceridae Wood-Mason & Alcock, 1891 (Crustacea: Decapoda: Dendrobranchiata) from Southwestern Atlantic. *Zootaxa*, 4254(4), 473–484. <https://doi.org/10.11646/zootaxa.4254.4.4>
- De Clippele, L. H., Rovelli, L., Ramiro-Sánchez, B., Kazanidis, G., Vad, J., Turner, S., Glud, R. N. & Roberts, J. M. (2021a). Mapping cold-water coral biomass: an approach to derive ecosystem functions. *Coral Reefs* 40, 215–231.
- De Clippele, L. H., van der Kaaden, A.-S., Maier, S. R., de Froe, E. & Roberts, J. M. (2021b). Biomass mapping for an improved understanding of the contribution of cold-water coral carbonate mounds to C and N cycling. *Frontiers in Marine Science* 8, 1608.
- De Froe E, Rovelli L, Glud RN, Maier SR, Duineveld G, Mienis F, Lavaley M and van Oevelen D (2019) Benthic Oxygen and Nitrogen Exchange on a Cold-Water Coral Reef in the North-East Atlantic Ocean. *Front. Mar. Sci.* 6:665.
- De Jonge, D. S. W., Stratmann, T., Lins, L., Vanreusel, A., Purser, A., Marcon, Y., Rodrigues, C. F., Esquete, P., Cunha, M. R., Breugel, P. Van, Sweetman, A. K., Soetaert, K., & Oevelen, D. Van. (2020). Abyssal food-web model indicates faunal carbon flow recovery and impaired microbial loop 26 years after a

- sediment disturbance experiment. *Progress in Oceanography*.
<https://doi.org/https://doi.org/10.1016/j.pocean.2020.102446>
- De Jonge, V. N. (1980). Fluctuations in the organic carbon to chlorophyll a ratios for estuarine benthic diatom populations. *Mar. Ecol. Prog. Ser.*, 2, 345–353. <https://doi.org/10.3354/meps002345>
- Derby, C. D., Kozma, M. T., Senatore, A., & Schmidt, M. (2016). Molecular Mechanisms of Reception and Perireception in Crustacean Chemoreception: A Comparative Review. *Chemical Senses*, 41(5), 381–398. <https://doi.org/10.1093/CHEMSE/BJW057>.
- Dickson AG, Sabine CL, Christian JR. 2007 Guide to best practices for ocean CO2 measurements. PICES Special Publication 3.
- Dickson AG, Millero FJ. (1987) A comparison of the equilibrium constants for the dissociation of carbonic acid in seawater media. *Deep Sea Res.* 34, 1733– 1743
- Doubleday, Z. A., Prowse, T. A. A., Arkhipkin, A., Pierce, G. J., Semmens, J., Steer, M., Leporati, S. C., Lourenço, S., Quetglas, A., Sauer, W., & Gillanders, B. M. (2016). Global proliferation of cephalopods. *Current Biology : CB*, 26(10), R406-7. <https://doi.org/10.1016/j.cub.2016.04.002>
- Drazen, J. C. (2002). Energy budgets and feeding rates of *Coryphaenoides acrolepis* and *C. armatus*. *Marine Biology* 2002 140:4, 140(4), 677–686. <https://doi.org/10.1007/S00227-001-0747-8>.
- Drazen, J.C. *et al.* By passing the abyssal benthic food web: Macrourid diet in the eastern North Pacific inferred from stomach content and stable isotopes analyses. *Limnol. Oceanogr.* 53, 2644–2654 (2008).
- Drazen, J. C., & Sutton, T. T. (2017). Dining in the Deep: The Feeding Ecology of Deep-Sea Fishes. *Annual Review of Marine Science*, 9(1), 337–366. <https://doi.org/10.1146/annurev-marine-010816-060543>
- Duffy, G. A., Gutteridge, Z. R. S., Thurston, M. H., & Horton, T. (2016). A comparative analysis of canyon and non-canyon populations of the deep-sea scavenging amphipod *Paralichthys caperesca*. *Journal of the Marine Biological Association of the United Kingdom*, 96(8), 1687–1699. <https://doi.org/10.1017/S0025315415002064>
- Duineveld, G. C. A., de Wilde, P. A. W. J., Berghuis, E. M., & Kok, A. (1993). The benthic infauna and benthic respiration off the Banc d'Arguin (Mauritania, Northwest Africa). *Ecological Studies in the Coastal Waters of Mauritania*, 107–117. https://doi.org/10.1007/978-94-011-1986-3_10
- Duineveld, G. C. A., Lavaleye, M. S. S., Berghuis, E. M., De Wilde, P. A. W. J., Van Der Weele, J., Kok, A., Batten, S. D., & De Leeuw, J. W. (1997). Patterns of benthic fauna and benthic respiration on the celtic continental margin in relation to the distribution of phytodetritus. *Internationale Revue Der Gesamten Hydrobiologie Und Hydrographie*, 82(3), 395–424. <https://doi.org/10.1002/IROH.19970820312>
- Durden, J. M., Ruhl, H. A., Pebody, C., Blackbird, S. J., & van Oevelen, D. (2017). Differences in the carbon flows in the benthic food webs of abyssal hill and plain habitats. *Limnology and Oceanography*, 62(4), 1771–1782. <https://doi.org/10.1002/lno.10532>
- Eardly, D. F., Carton, M. W., Gallagher, J. M., & Patching, J. W. (2001). Bacterial abundance and activity in deep-sea sediments from the eastern North Atlantic. *Progress in Oceanography*, 50(1–4), 245–259. [https://doi.org/10.1016/S0079-6611\(01\)00056-8](https://doi.org/10.1016/S0079-6611(01)00056-8)
- Edwards, M., & Richardson, A. J. (2004). Impact of climate change on marine pelagic phenology and trophic mismatch. *Nature*, 430(7002), 881–884. <https://doi.org/10.1038/nature02808>
- Engel, A., Wagner, H., Le Moigne, F. A. C., & Wilson, S. T. (2017). Particle export fluxes to the oxygen minimum zone of the eastern tropical North Atlantic. *Biogeosciences*, 14, 1825–1838. <https://doi.org/10.5194/bg-14-1825-2017>
- Fabiano, M., Danovaro, R., & Fraschetti, S. (1995). A three-year time series of elemental and biochemical composition of organic matter in subtidal sandy sediments of the Ligurian Sea (northwestern Mediterranean). *Continental Shelf Research*, 15, 1453–1469. [https://doi.org/10.1016/0278-4343\(94\)00088-5](https://doi.org/10.1016/0278-4343(94)00088-5)
- Fauchald, K., & Jumars, P. a. (1979). The diet of worms: a study of polychaete feeding guilds. *Oceanography and Marine Biology. An Annual Review*, 17(May), 193–284. <http://www.umaine.edu/marine/people/sites/pjumars/preprints/diet.pdf>

- Ferreira, R. (1953). Bromatological study of the flesh of *Loligo gahi* (a squid). *An. Fac. Farm. Bioquim., Lima*, 4, 85–89.
- Finn, J. T. (1976). Measures of ecosystem structure and function derived from analysis of flows. *Journal of Theoretical Biology*, 56(2), 363–380. [https://doi.org/10.1016/S0022-5193\(76\)80080-X](https://doi.org/10.1016/S0022-5193(76)80080-X)
- Flach, E., & Heip, C. (1996). Vertical distribution of macrozoobenthos within the sediment on the continental slope of the Goban Spur area (NE Atlantic). *Marine Ecology Progress Series*, 141(1–3), 55–66. <https://doi.org/10.3354/MEPS141055>
- Flach, E., Lavaleye, M., De Stigter, H., & Thomsen, L. (1998). Feeding types of the benthic community and particle transport across the slope of the N.W. European continental margin (Goban Spur). *Progress in Oceanography*, 42(1–4), 209–231. [https://doi.org/10.1016/S0079-6611\(98\)00035-4](https://doi.org/10.1016/S0079-6611(98)00035-4)
- Fleury, A. G., & Drazen, J. C. (2013). Abyssal Scavenging Communities attracted to Sargassum and fish in the Sargasso Sea. *Deep Sea Research Part I: Oceanographic Research Papers*, 72, 141–147. <https://doi.org/10.1016/J.DSR.2012.11.004>
- Form, A. U., Büscher, J., Hissmann, K., Flögel, S., Wisshak, M., Rüggeberg, A., Hennige, S., Bennecke, S., Bannister, R., Schauer, J. & Fenske, M. (2014) RV POSEIDON Cruise Report POS455 LORELEI Lophelia REef Lander Expedition and Investigation, Bremerhaven - (Kristiansund) - Kiel, 24.06. - (12.07.) - 17.07.2013. GEOMAR Helmholtz-Zentrum für Ozeanforschung, Kiel, 29 pp. https://doi.org/10.3289/CR_POS_455.
- Fox, R., Barnes, R. D., Ruppert, E. E. E., Barnes, D., & Ruppert, E. E. E. (2003). *Invertebrate Zoology: A Functional Evolutionary Approach*. (7th ed.). Brooks/Cole Thompson Learning.
- Fukuda, R., Ogawa, H., Nagata, T., & Koike, I. (1998). Direct determination of carbon and nitrogen contents of natural bacterial assemblages in marine environments. *Applied and Environmental Microbiology*, 64, 3352–3358.
- Gage, J. D., Hughes, D. J., & Vecino, J. L. G. (2002). Sieve size influence in estimating biomass, abundance and diversity in samples of deep-sea macrobenthos. *Marine Ecology Progress Series*, 225, 97–107. <https://doi.org/10.3354/meps225097>
- Galéron, J., Sibuet, M., Mahaut, M., & Dinét, A. (2000). Variation in structure and biomass of the benthic communities at three contrasting sites in the tropical Northeast Atlantic. *Marine Ecology Progress Series*, 197, 121–137. <https://doi.org/10.3354/meps197121>
- Galéron, J., Sibuet, M., Vanreusel, A., Mackenzie, K., Gooday, A. J., Dinét, A., & Wolff, G. A. (2001). Temporal patterns among meiofauna and macrofauna taxa related to changes in sediment geochemistry at an abyssal NE Atlantic site. *Progress in Oceanography*, 50, 303–324. [https://doi.org/10.1016/S0079-6611\(01\)00059-3](https://doi.org/10.1016/S0079-6611(01)00059-3)
- Georgoulas, K., Hennige, S.J., Chu Lee, Y. (2023) Smoothed particle hydrodynamics for modelling cold-water coral habitats in changing oceans. *Journal of Sea Research* 192, 102358
- Gilli, J. M., & UTM-CSIC. (2006). Cruise Report: DEEPCORALI-CORAL 4 (Coral Survey in the Cap de Creus canyon, Western Mediterranean), RV García del Cid, 11th -15th - July – 2006.
- Glud, R. N. (2008). Oxygen dynamics of marine sediments. *Marine Biology Research*, 4(4), 243–289. <https://doi.org/10.1080/17451000801888726>
- Glud, R. N., Gundersen, J. K., Jørgensen, B. B., Revsbech, N. P., & Schulz, H. D. (1994). Diffusive and total oxygen uptake of deep-sea sediments in the eastern South Atlantic Ocean: in situ and laboratory measurements. *Deep-Sea Research Part I*, 41(11–12), 1767–1788. [https://doi.org/10.1016/0967-0637\(94\)90072-8](https://doi.org/10.1016/0967-0637(94)90072-8)
- Goffredo S, Mancuso A, Caroselli E, Prada F, Dubinsky Z, Falini G, Levy O, Fantazzini P, Pasquini L (2015) Skeletal mechanical properties of Mediterranean corals along a wide latitudinal gradient. *Coral Reefs* 34:121–132.
- Gooday, A. J. (1996). Epifaunal and shallow infaunal foraminiferal communities at three abyssal NE Atlantic sites subject to differing phytodetritus input regimes. *Deep-Sea Research Part I: Oceanographic Research Papers*, 43(9), 1395–1421. [https://doi.org/10.1016/S0967-0637\(96\)00072-6](https://doi.org/10.1016/S0967-0637(96)00072-6)
- Gooday, A. J., Levin, L. A., Linke, P., & Heeger, T. (1992). The role of benthic foraminifera in deep-sea food webs and carbon cycling. In *Deep-sea food chains and the global carbon cycle* (pp. 63–91).

https://doi.org/10.1007/978-94-011-2452-2_5

- Gooday, A. J., Schoenle, A., Dolan, J. R., & Arndt, H. (2020). Protist diversity and function in the dark ocean – Challenging the paradigms of deep-sea ecology with special emphasis on foraminiferans and naked protists. *European Journal of Protistology*, 75, 125721. <https://doi.org/10.1016/j.ejop.2020.125721>
- Gowing, M. M., & Wishner, K. F. (1986). Trophic relationships of deep-sea calanoid copepods from the benthic boundary layer of the Santa Catalina Basin, California. *Deep-Sea Research*, 33, 939–962.
- Guildford, S. J., & Hecky, R. E. (2000). Total nitrogen, total phosphorus, and nutrient limitation in lakes and oceans: Is there a common relationship? *Limnology and Oceanography*, 45(6), 1213–1223. <https://doi.org/10.4319/lo.2000.45.6.1213>
- Guinotte JM, Orr JC, Cairns S, Freiwald A, Morgan L, George RY. 2006 Will human-induced changes in seawater chemistry alter the distribution of deep-sea scleractinian corals? *Front. Ecol. Environ.* 4, 141–146.
- Haedrich, R. L., & Henderson, N. R. (1974). Pelagic food of *Coryphaenoides armatus*, a deep benthic rattail. *Deep Sea Research and Oceanographic Abstracts*, 21(9), 739–744. [https://doi.org/10.1016/0011-7471\(74\)90080-1](https://doi.org/10.1016/0011-7471(74)90080-1)
- Hall, P. O. J., Brunnegård, J., Hulthe, G., Martin, W. R., Stahl, H., & Tengberg, A. (2007). Dissolved organic matter in abyssal sediments: Core recovery artifacts. *Limnology and Oceanography*, 52(1), 19–31. <https://doi.org/10.4319/lo.2007.52.1.0019>
- Harbour, R. P., Leitner, A. B., Ruehlemann, C., Vink, A., & Sweetman, A. K. (2020). Benthic and Demersal Scavenger Biodiversity in the Eastern End of the Clarion-Clipperton Zone – An Area Marked for Polymetallic Nodule Mining. *Frontiers in Marine Science*, 7. <https://doi.org/10.3389/fmars.2020.00458>
- Hartman, O. (1965). Deep-water benthic polychaetous annelids off New England to Bermuda and other North Atlantic areas. *Occasional Papers of the Allan Hancock Foundation*, 28, 1–384. <http://digitalibrary.usc.edu/cdm/ref/collection/p15799coll82/id/20299>
- Havermans, C., & Smetacek, V. (2018). Bottom-up and top-down triggers of diversification: A new look at the evolutionary ecology of scavenging amphipods in the deep sea. *Progress in Oceanography*, 164(July 2017), 37–51. <https://doi.org/10.1016/j.pocean.2018.04.008>
- Heip, C. H. R., Duineveld, G., Flach, E., Graf, G., Helder, W., Herman, P. M. J., Lavaleye, M., Middelburg, J. J., Pfannkuche, O., Soetaert, K., Soltwedel, T., De Stigter, H., Thomsen, L., Vanaverbeke, J., & De Wilde, P. (2001). The role of the benthic biota in sedimentary metabolism and sediment-water exchange processes in the Goban Spur area (NE Atlantic). *Deep-Sea Research Part II: Topical Studies in Oceanography*, 48(14–15), 3223–3243. [https://doi.org/10.1016/S0967-0645\(01\)00038-8](https://doi.org/10.1016/S0967-0645(01)00038-8)
- Helmle, K. P., Dodge, R. E., Swart, P. K., Gledhill, D. K., & Eakin, C. M. (2011). Growth rates of Florida corals from 1937 to 1996 and their response to climate change. *Nature Communications*, 2(1), 215.
- Hennige, S.J., Morrison, C.L., Form, A.U., Buscher, J., Kamenos, N.A., Roberts, J.M. (2014) Self-recognition in corals facilitates deep-sea habitat engineering. *Nature Scientific Reports* 4: 6782
- Hennige S.J., Wicks L.C., Kamenos N.A., Perna, G., Findlay H.S., Roberts J.M. (2015) Hidden impacts of ocean acidification to live and dead coral framework. *Proceedings of the Royal Society B*. 282: 20150990.
- Hennige, S. J., Wolfram, U., Wickes, L., Murray, F., Roberts, J. M., Kamenos, N. A., Schofield, S., Groetsch, A., Spiesz, E. M., Aubin-tam, M. & Etnoyer, P. J. (2020) Crumbling Reefs and Cold-Water Coral Habitat Loss in a Future Ocean: Evidence of “Coralporosis” as an Indicator of Habitat Integrity. *Frontiers in Marine Science*. 7: 668
- Hennige, S. J., Larsson, A. I., Orejas, C., Gori, A., De Clippele, L. H., Lee, Y. C., Jimeno, G., Georgoulas, K., Kamenos, N. A., & Roberts, J. M. (2021). Using the Goldilocks Principle to model coral ecosystem engineering. *Proceedings of the Royal Society B: Biological Sciences*, 288(1956), 20211260. <https://doi.org/10.3389/fmars.2020.570620>
- Henriques, C. (2004). *In situ lander observations of deep-sea fishes in the eastern Atlantic ocean*.
- Henriques, C., Priede, I. G., & Bagley, P. M. (2002). Baited camera observations of deep-sea demersal fishes of the northeast Atlantic Ocean at 15–28°N off West Africa. *Marine Biology*, 141(2), 307–314.

- <https://doi.org/10.1007/s00227-002-0833-6>
- Henry, L. A., and Roberts, J. M. (2007). Biodiversity and ecological composition of macrobenthos on cold-water coral mounds and adjacent off-mound habitat in the bathyal Porcupine Seabight. NE Atlantic. *Deep. Res. Part I Oceanogr. Res. Pap.* 54, 654–672
- Henry, L. A., & Roberts, J. M. (2017). Global Biodiversity in Cold-Water Coral Reef Ecosystems. In: Rossi, S., Bramanti, L., Gori, A., Orejas, C. (eds) *Marine Animal Forests*. Springer, Cham. https://doi.org/10.1007/978-3-319-21012-4_6
- Henschke, N., Bowden, D., Everett, J., Holmes, S., Kloser, R., Lee, R., & Suthers, I. (2013). Salp-falls in the Tasman Sea: A major food input to deep-sea benthos. *Marine Ecology Progress Series*, 491, 165–175. <https://doi.org/10.3354/meps10450>
- Hessler, R. R., & Jumars, P. A. (1974). Abyssal community analysis from replicate □ cores in the central North Pacific. *Deep Sea Research and Oceanographic Abstracts*, 21(3), 185–209. [https://doi.org/10.1016/0011-7471\(74\)90058-8](https://doi.org/10.1016/0011-7471(74)90058-8)
- Heymans, J. J., Coll, M., Libralato, S., Morissette, L., & Christensen, V. (2014). Global patterns in ecological indicators of marine food webs: A modelling approach. *PLoS ONE*, 9(4). <https://doi.org/10.1371/journal.pone.0095845>
- Higgs, N. D., Gates, A. R., & Jones, D. O. B. (2014). Fish food in the deep sea: Revisiting the role of large food-falls. *PLoS ONE*, 9(5). <https://doi.org/10.1371/journal.pone.0096016>
- Horton, T., Thurston, M. H., Vlierboom, R., Gutteridge, Z., Pebody, C. A., Gates, A. R., & Bett, B. J. (2020). Are abyssal scavenging amphipod assemblages linked to climate cycles? *Progress in Oceanography*, 184, 102318. <https://doi.org/10.1016/j.POCEAN.2020.102318>
- Hoving, H.-J. T., Bush, S. L., Haddock, S. H. D., & Robison, B. H. (2017). Bathyal feasting: Post-spawning squid as a source of carbon for deep-sea benthic communities. *Proceedings of the Royal Society B: Biological Sciences*, 284(20172096). <https://doi.org/10.1098/rspb.2017.2096>
- Hurlbert, S. H. (1971). The Nonconcept of Species Diversity: A Critique and Alternative Parameters. *Ecology*, 52(4), 577–586. <https://doi.org/10.2307/1934145>
- Hughes TP (1987) Skeletal density and growth form of corals. *Mar Ecol Prog Ser* 35, 259–266.
- Ikeda, T., Yamaguchi, A., & Matsuishi, T. (2006). Chemical composition and energy content of deep-sea calanoid copepods in the Western North Pacific Ocean. *Deep-Sea Research Part I: Oceanographic Research Papers*, 53(11), 1791–1809. <https://doi.org/10.1016/j.dsr.2006.08.002>
- Iken, K., Brey, T., Wand, U., Voigt, J., & Junghans, P. (2001). Food web structure of the benthic community at the Porcupine Abyssal Plain (NE Atlantic): A stable isotope analysis. *Progress in Oceanography*, 50(1–4), 383–405. [https://doi.org/10.1016/S0079-6611\(01\)00062-3](https://doi.org/10.1016/S0079-6611(01)00062-3)
- Ingels, J., Amon, D., Bernardino, A. F., Bhadury, P., Bik, H., Clark, M., Dahlgren, T. G., Jones, D. O. B., McClain, C., Nunnally, C. C., Snelgrove, P. V., Tuhumwire, J. T., & Yasuhara, M. (2021). Abyssal Plains. In *The Second Global Integrated Marine Assessment: World Ocean Assessment II* (Vol. 1, pp. 453–476). United Nations.
- https://www.researchgate.net/publication/351037991_Chapter_7M_Abyssal_Plains_in_The_Second_Global_Integrated_Marine_Assessment_World_Ocean_Assessment_II_United_Nations_New_York
- Ingels, J., Vanreusel, A., Pape, E., Pasotti, F., Macheriotou, L., Arbizu, P. M., Sørensen, M. V., Edgcomb, V. P., Sharma, J., Sánchez, N., Homoky, W. B., Woulds, C., Leduc, D., Gooday, A. J., Pawlowski, J., Dolan, J. R., Schratzberger, M., Gollner, S., Schoenle, A., ... Zeppilli, D. (2020). Ecological variables for deep-ocean monitoring must include microbiota and meiofauna for effective conservation. *Nature Ecology and Evolution*, November, 18–23. <https://doi.org/10.1038/s41559-020-01335-6>
- Jahnke, R. A., & Jahnke, D. B. (2000). Rates of C, N, P and Si recycling and denitrification at the US Mid-Atlantic continental slope depocenter. *Deep Sea Research Part I: Oceanographic Research Papers*, 47(8), 1405–1428. [https://doi.org/10.1016/S0967-0637\(99\)00118-1](https://doi.org/10.1016/S0967-0637(99)00118-1)
- Jakobsen, H. H., & Markager, S. (2016). Carbon-to-chlorophyll ratio for phytoplankton in temperate coastal waters: Seasonal patterns and relationship to nutrients. *Limnology and Oceanography*, 61(5), 1853–1868. <https://doi.org/10.1002/lno.10338>

- Janßen, F., Treude, T., & Witte, U. (2000). Scavenger assemblages under differing trophic conditions: a case study in the deep Arabian Sea. *Deep Sea Research Part II: Topical Studies in Oceanography*, 47(14), 2999–3026. [https://doi.org/10.1016/S0967-0645\(00\)00056-4](https://doi.org/10.1016/S0967-0645(00)00056-4)
- Jax, K. (2005). Function and “functioning” in ecology: What does it mean? *Oikos*, 111(3), 641–648. <https://doi.org/10.1111/j.1600-0706.2005.13851.x>
- Jażdżewska, A. M., Horton, T., Hendrycks, E., Mamos, T., Driskell, A. C., Brix, S., & Arbizu, P. M. (2021). Pandora’s Box in the Deep Sea –Intraspecific Diversity Patterns and Distribution of Two Congeneric Scavenging Amphipods. *Frontiers in Marine Science*, 8, 1673. <https://doi.org/10.3389/FMARS.2021.750180/BIBTEX>
- Jeffreys, R. M., Lavaleye, M. S. S., Bergman, M. J. N., Duineveld, G. C. A., & Witbaard, R. (2011). Do abyssal scavengers use phytodetritus as a food resource? Video and biochemical evidence from the Atlantic and Mediterranean. *Deep Sea Research Part I: Oceanographic Research Papers*, 58(4), 415–428. <https://doi.org/10.1016/J.DSR.2011.02.002>
- Jensen, P. (1984). Measuring carbon content in nematodes. *Helgoland Marine Research*, 38, 83–86.
- Jones, D. O. B., Yool, A., Wei, C. L., Henson, S. A., Ruhl, H. A., Watson, R. A., & Gehlen, M. (2014). Global reductions in seafloor biomass in response to climate change. *Global Change Biology*, 20(6), 1861–1872. <https://doi.org/10.1111/gcb.12480>
- Jumars, P. A., Dorgan, K. M., & Lindsay, S. M. (2015). Diet of worms emended: an update of polychaete feeding guilds. *Annual Review of Marine Science*, 7, 497–520.
- Kamenskaya, O. E., Melnik, V. F., & Gooday, A. J. (2013). Giant protists (xenophyophores and komokiaceans) from the Clarion-Clipperton ferromanganese nodule field (Eastern Pacific). *ZHURNAL OBSHCHEI BIOLOGII*, 73(5), 377–388. http://apps.webofknowledge.com.proxy-ub.rug.nl/full_record.do?product=UA&search_mode=GeneralSearch&qid=1&SID=T15EYVKBZuXlHfTAVsm&page=24&doc=233&cacheurlFromRightClick=no
- Kelly, J. R., & Scheibling, R. E. (2012). Fatty acids as dietary tracers in benthic food webs. *Marine Ecology Progress Series*, 446, 1–22. <https://doi.org/10.3354/MEPS09559>
- Khripounoff, A., & others. (1980). *Les peuplements benthiques de la faille Vema: données quantitatives et bilan d’énergie en milieu abyssal*.
- Khripounoff, A., Vangriesheim, A., & Crassous, P. (1998). Vertical and temporal variations of particle fluxes in the deep tropical atlantic. *Deep-Sea Research Part I: Oceanographic Research Papers*, 45(2–3), 193–216. [https://doi.org/10.1016/S0967-0637\(97\)00104-0](https://doi.org/10.1016/S0967-0637(97)00104-0)
- Kinsey DW, Davies PJ (1979) Effects of elevated nitrogen and phosphorus on coral reef growth. *Limnol. Oceanogr.* 24, 935–940.
- Korabik, Michelle; Beazley, Lindsay; Kenchington, Ellen; Lirette, Camille (2022), “Photo Archive of In Situ Benthic Imagery from the *Lophelia* Coral Conservation Area”, Mendeley Data, V3, <https://doi.org/10.17632/dwth772x62.3>
- Kones, J. K., Soetaert, K., van Oevelen, D., & Owino, J. O. (2009). Are network indices robust indicators of food web functioning? A Monte Carlo approach. *Ecological Modelling*, 220(3), 370–382. <https://doi.org/10.1016/j.ecolmodel.2008.10.012>
- Lahajnar, N., Rixen, T., Schäfer, P., & Ittekkot, V. (2005). Dissolved organic carbon (DOC) fluxes of deep-sea sediments from the Arabian Sea and NE Atlantic. *Deep Sea Research Part II: Topical Studies in Oceanography*, 52(14–15), 1947–1964. <https://doi.org/10.1016/J.DSR2.2005.05.006>
- Langenkämper, D., Zuerowietz, M., Schoening, T., & Nattkemper, T. W. (2017). BIIGLE 2.0 - Browsing and Annotating Large Marine Image Collections. *Frontiers in Marine Science*, 4. <https://doi.org/10.3389/fmars.2017.00083>
- Lebrato, M., de Jesus Mendes, P., Steinberg, D. K., Cartes, J. E., Jones, B. M., Birsa, L. M., Benavides, R., & Oschlies, A. (2013). Jelly biomass sinking speed reveals a fast carbon export mechanism. *Limnology and Oceanography*, 58(3), 1113–1122. <https://doi.org/10.4319/LO.2013.58.3.1113>
- Lebrato, M., Pahlow, M., Frost, J. R., Küter, M., de Jesus Mendes, P., Molinero, J. C., & Oschlies, A. (2019). Sinking of Gelatinous Zooplankton Biomass Increases Deep Carbon Transfer Efficiency Globally. *Global Biogeochemical Cycles*, 33(12), 1764–1783. <https://doi.org/10.1029/2019GB006265>

- Lebrato, M., Pahlow, M., Oschlies, A., Pitt, K. A., Jones, D. O. B., Molinero, J. C., & Condon, R. H. (2011). Depth attenuation of organic matter export associated with jelly falls. *Limnology and Oceanography*, 56(5), 1917–1928. <https://doi.org/10.4319/LO.2011.56.5.1917>
- Legeleux, F., Reyss, J. L., & Schmidt, S. (1994). Particle mixing rates in sediments of the northeast tropical Atlantic: Evidence from ²¹⁰Pbxs, ¹³⁷Cs, ²²⁸Thxs and ²³⁴Thxs downcore distributions. *Earth and Planetary Science Letters*, 128(3–4), 545–562. [https://doi.org/10.1016/0012-821X\(94\)90169-4](https://doi.org/10.1016/0012-821X(94)90169-4)
- Leitner, A. B., Neuheimer, A. B., Donlon, E., Smith, C. R., & Drazen, J. C. (2017). Environmental and bathymetric influences on abyssal bait-attending communities of the Clarion Clipperton Zone. *Deep Sea Research Part I: Oceanographic Research Papers*, 125, 65–80. <https://doi.org/10.1016/J.DSR.2017.04.017>
- Levin, L. A., Blair, N., & DeMaster, D. (1998). Rapid subduction of organic matter by maldanid polychaetes on the North Carolina slope. *Oceanographic Literature Review*, 1(45), 74. <https://www.infona.pl//resource/bwmeta1.element.elsevier-950bba77-4ae4-398b-ac69-5110c5d70cd2>
- Levin, L. A., & Dayton, P. K. (2009). Ecological theory and continental margins: where shallow meets deep. *Trends in Ecology and Evolution*, 24(11), 606–617. <https://doi.org/10.1016/j.tree.2009.04.012>
- Levin, L. A., & Gooday, A. J. (2003). The deep Atlantic Ocean. In P. A. Tyler (Ed.), *Ecosystems of the world: Ecosystems of the deep oceans* (Vol. 28, pp. 111–178). Elsevier.
- Li, W. K. W., McLaughlin, F. A., Lovejoy, C., & Carmack, E. C. (2009). Smallest algae thrive as the arctic ocean freshens. *Science*, 326(5952), 539. https://doi.org/10.1126/SCIENCE.1179798/SUPPL_FILE/LI.SOM.PDF
- Linley, T. D., Craig, J., Jamieson, A. J., & Priede, I. G. (2018). *Bathyal and abyssal demersal bait-attending fauna of the Eastern Mediterranean Sea*. 165, 159. <https://doi.org/10.1007/s00227-018-3413-0>
- Lochte, K., & Soltwedel, T. (1999). *Biochemical investigation of sediment core D204-MUC1*. PANGAEA. <https://doi.org/10.1594/PANGAEA.54565>
- Lough, J.M., & Barnes, D.J. (2000) Environmental controls on growth of the massive coral *Porites*. *J. Exp. Mar. Biol. Ecol.* 245: 225–243
- Lucas, C. H., Jones, D. O. B., Hollyhead, C. J., Condon, R. H., Duarte, C. M., Graham, W. M., Robinson, K. L., Pitt, K. A., Schildhauer, M., & Regetz, J. (2014). Gelatinous zooplankton biomass in the global oceans: Geographic variation and environmental drivers. *Global Ecology and Biogeography*, 23(7), 701–714. <https://doi.org/10.1111/geb.12169>
- Luongo, S. M., & Lowe, C. G. (2018). Seasonally acclimated metabolic Q10 of the California horn shark, *Heterodontus francisci*. *Journal of Experimental Marine Biology and Ecology*, 503, 129–135. <https://doi.org/10.1016/J.JEMBE.2018.02.006>
- Maier, S. R., Kutti, T., Bannister, R. J., Fang, J. K. H., van Breugel, P., van Rijswijk, P., & van Oevelen, D. (2020). Recycling pathways in cold-water coral reefs: Use of dissolved organic matter and bacteria by key suspension feeding taxa. *Scientific Reports*, 10(1), 1–14. <https://doi.org/10.1038/s41598-020-66463-2>
- Maier, C., Bils, F., Weinbauer, M. G., Watremez, P., Peck, M. A., and Gattuso, J.-P.: Respiration of Mediterranean cold-water corals is not affected by ocean acidification as projected for the end of the century, *Biogeosciences*, 10, 5671–5680,
- Maier, S.R., Brooke, S., De Clippele, L.H., de Froe, E., van der Kaaden, A.-S., Kutti, T., Mienis, F. and van Oevelen, D. (2023), On the paradox of thriving cold-water coral reefs in the food-limited deep sea. *Biol Rev.* <https://doi.org/10.1111/brv.12976>
- Main, C. E., Ruhl, H. A., Jones, D. O. B., Yool, A., Thornton, B., & Mayor, D. J. (2015). Hydrocarbon contamination affects deep-sea benthic oxygen uptake and microbial community composition. *Deep Sea Research Part I: Oceanographic Research Papers*, 100, 79–87. <https://doi.org/10.1016/J.DSR.2014.12.008>
- Mehrbach C, Culberso CH, Hawley JE, Pytkowic RM. (1973) Measurement of apparent dissociation constants of carbonic acid in seawater at atmospheric pressure. *Limnol. Oceanogr.* 18, 897 – 907
- McClain, C. R., Johnson, N. A., & Rex, M. A. (2004). Morphological disparity as a biodiversity metric in lower

- bathyal and abyssal gastropod assemblages. *Evolution*, 58, 338–348.
- McCulloch, M., Falter, J., Trotter, J. et al. Coral resilience to ocean acidification and global warming through pH up-regulation. *Nature Clim Change* 2, 623–627 (2012). <https://doi.org/10.1038/nclimate1473>
- Menzies, R. J. R. J. (1962). On the food and feeding habits of abyssal organisms as exemplified by the Isopoda. *Int. Rev. Hydrobiol.*, 47, 339–358. <https://doi.org/10.1002/iroh.19620470303>
- Merten, V., Bayer, T., Reusch, T. B. H., Puebla, O., Fuss, J., Stefanschitz, J., Lischka, A., Hauss, H., Neitzel, P., Piatkowski, U., Czudaj, S., Christiansen, B., Denda, A., & Hoving, H. J. T. (2021). An Integrative Assessment Combining Deep-Sea Net Sampling, in situ Observations and Environmental DNA Analysis Identifies Cabo Verde as a Cephalopod Biodiversity Hotspot in the Atlantic Ocean. *Frontiers in Marine Science*, 8, 1770. <https://doi.org/10.3389/FMARS.2021.760108/BIBTEX>
- Minchin, P. R. (1987). An evaluation of the relative robustness of techniques for ecological ordination. *Vegetatio*, 69(1–3), 89–107. <https://doi.org/10.1007/BF00038690/METRICAL>.
- Mollica, N. R., Guo, W., Cohen, A. L., Huang, K. F., Foster, G. L., Donald, H. K., & Solow, A. R. (2018). Ocean acidification affects coral growth by reducing skeletal density. *Proceedings of the National Academy of Sciences*, 115(8), 1754–1759.
- Montagna P, McCulloch M, Taviani M, Mazzoli C, Vendrell B (2006) Phosphorus in cold-water corals as a proxy for seawater nutrient chemistry. *Sci* 312, 1788–1791.
- Moodley, L., Middelburg, J. J., Soetaert, K., Boschker, H. T. S., Herman, P. M. J., & Heip, C. H. R. (2005). Similar rapid response to phytodetritus deposition in shallow and deep-sea sediments. *Journal of Marine Research*, 2.
- Morgan, K. M., & Kench, P. S. (2012). Skeletal extension and calcification of reef-building corals in the central Indian Ocean. *Marine Environmental Research*, 81, 78–82. <https://doi.org/10.1016/j.marenvres.2012.08.001>
- Mortensen, P. B., Hovland, M., Brattegard, T. and Farestveit, R. (1995). Deep water bioherms of the scleractinian coral *Lophelia pertusa* (L.) at 64° N on the Norwegian shelf: Structure and associated megafauna. *Sarsia*, 80, 145–158. <https://doi.org/10.1080/00364827.1995.10413586>
- Murina, G.-V. (1984). Ecology of Sipuncula. *Marine Ecology Progress Series*, 17, 1–7. <https://doi.org/10.3354/meps017001>
- Naumann, M. S., Orejas, C. & Ferrier-Pagès, C. (2014). Species-specific physiological response by the cold-water corals *Lophelia pertusa* and *Madrepora oculata* to variations within their natural temperature range. *Deep-Sea Research Part II: Topical Studies in Oceanography* 99, 36–41
- Ng, C. S. L., Lim, J. X., Sam, S. Q., Kikuzawa, Y. P., Toh, T. C., Wee, T. W., ... & Chou, L. M. (2019). Variability in skeletal bulk densities of common hard corals in Southeast Asia. *Coral Reefs*, 38, 1133–1143.
- Oksanen, J., Blanchet, F. G., Kindt, R., Legendre, P., Minchin, P. R., O'Hara, R. B., Simpson, G. L., Solymos, P., Henry, M., Stevens, H., & Wagner, H. (2022). *vegan: Community Ecology Package* (2.6-4). <https://cran.r-project.org/package=vegan>
- Orejas, C. & UTM-CSIC (2007). Cruise Report: HERMES IV-CORAL 8 (Coral Survey in the Cap de Creus canyon, Western Mediterranean), RV Garcia del Cid, 3rd -16th - September – 2007.
- Orejas, C., Gori, A., Rad-Menéndez, C., Last, K. S., Davies, A. J., Beveridge, C. M., ... & Roberts, J. M. (2016). The effect of flow speed and food size on the capture efficiency and feeding behaviour of the cold-water coral *Lophelia pertusa*. *Journal of Experimental Marine Biology and Ecology*, 481, 34–40. <https://doi.org/10.1016/j.jembe.2016.04.002>
- Orejas, C., Wienberg, C., Titschack, J., Tamborrino, L., Freiwald, A., & Hebbeln, D. (2021). *Madrepora oculata* forms large frameworks in hypoxic waters off Angola (SE Atlantic). *Scientific Reports* 2021 11:1, 11(1), 1–13. <https://doi.org/10.1038/s41598-021-94579-6>
- Orejas, C., Huvenne, V., Sweetman, A. K., Vinha, B., Abella, J. C., Andrade, P., Afonso, A., Antelo, J., Austin-Berry, R., Baltasar, L., Barbosa, N., Barnhill, K. A., Barreiro, A., Bettencourt, R., Blanco, S., Buigues, A., Calado, A., Casal, I., Torre, J. de la, ... Vélez-Belchí, P. (2022). *Expedition report iMirabilis2 survey* (Issue August, p. 342). Zenodo. <https://doi.org/10.5281/zenodo.6352141>
- Özalp, H. B., Caroselli, E., Raimondi, F., & Goffredo, S. (2018). Skeletal growth, morphology and skeletal parameters of a temperate, solitary and zooxanthellate coral along a depth gradient in the

- Dardanelles (Turkey). *Coral Reefs*, 37, 633-646.
- Paterson, G. L. J., Wilson, G. D. F., Cosson, N., & Lamont, P. (1998a). Hessler and Jumars (1974) revisited: abyssal polychaete assemblages from the Atlantic and Pacific. *DEEP-SEA RES PT II*, 45(1-3), 225-251. <https://pure.uhi.ac.uk/en/publications/hessler-and-jumars-1974-revisited-abyssal-polychaete-assemblages->
- Paterson, G. L. J., Wilson, G. D. F., Cosson, N., & Lamont, P. A. (1998b). Hessler and jumars (1974) revisited: Abyssal polychaete assemblages from the Atlantic and Pacific. *Deep-Sea Research Part II: Topical Studies in Oceanography*, 45(1-3), 225-251. [https://doi.org/10.1016/S0967-0645\(97\)00084-2](https://doi.org/10.1016/S0967-0645(97)00084-2)
- Pelegrí, J. L., Peña-Izquierdo, J., Machín, F., Meiners, C., & Presas-Navarro, C. (2017). Oceanography of the Cape Verde Basin and Mauritanian Slope Waters. In A. Ramos, F. Ramil, & J. L. Sanz (Eds.), *Deep-Sea Ecosystems Off Mauritania: Research of Marine Biodiversity and Habitats in the Northwest African Margin* (Issue September, pp. 1-683). Springer Science+Business Media. https://doi.org/10.1007/978-94-024-1023-5_3
- Peña-Izquierdo, J., Pelegrí, J. L., Pastor, M. V., Castellanos, P., Emelianov, M., Gasser, M., Salvador, J., & Vázquez-Domínguez, E. (2012). The continental slope current system between Cape Verde and the Canary Islands. *Scientia Marina*, 76(SUPPL.1), 65-78. <https://doi.org/10.3989/scimar.03607.18C>
- Pfannkuche, O., & Lochte, K. (2001). *Physical oceanography at CTD station M42/2_-2*. PANGAEA. <https://doi.pangaea.de/10.1594/PANGAEA.59792>
- Pfannkuche, O., Theeg, R., & Thiel, H. (1983). *Benthos activity, abundance and biomass under an area of low upwelling off Morocco, Northwest Africa*.
- Pierre, C. (2001). *Part of the global seawater delta oxygen-18 database from reference Pierre 1994*. PANGAEA. <https://doi.pangaea.de/10.1594/PANGAEA.57878>
- PlotDigitizer Online App*. (n.d.). Retrieved May 4, 2023, from <https://plotdigitizer.com/app>
- Post, D. M. (2002). The long and short of food-chain length. *Trends in Ecology and Evolution*, 17(6), 269-277. [https://doi.org/10.1016/S0169-5347\(02\)02455-2](https://doi.org/10.1016/S0169-5347(02)02455-2)
- Post, D. M., Layman, C. A., Arrington, D. A., Takimoto, G., Quattrochi, J., & Montaña, C. G. (2007). Getting to the fat of the matter: Models, methods and assumptions for dealing with lipids in stable isotope analyses. *Oecologia*, 152(1), 179-189. <https://doi.org/10.1007/S00442-006-0630-X/FIGURES/5>
- Priede, I. G., Bagley, P. M., Armstrong, J. D., Smith, K. L., & Merrett, N. R. (1991). Direct measurement of active dispersal of food-falls by deep-sea demersal fishes. *Nature* 1991 351:6328, 351(6328), 647-649. <https://doi.org/10.1038/351647a0>
- Priede, I. G., & Merrett, N. R. (1996). Estimation of abundance of abyssal demersal fishes; a comparison of data from trawls and baited cameras. *Journal of Fish Biology*, 49(SUPPL. A), 207-216. <https://doi.org/10.1111/J.1095-8649.1996.TB06077.X>
- Purcell, J. E. (2011). Jellyfish and Ctenophore Blooms Coincide with Human Proliferations and Environmental Perturbations. <https://doi.org/10.1146/Annurev-Marine-120709-142751>, 4, 209-235. <https://doi.org/10.1146/ANNUREV-MARINE-120709-142751>
- Purser A, Larsson AI, Thomsen L, van Oevelen D (2010) The influence of flow velocity and food concentration on *Lophelia pertusa* (Scleractinia) zooplankton capture rates. *Journal of Experimental Marine Biology and Ecology* 395: 55-62 [doi 10.1016/j.jembe.2010.08.013](https://doi.org/10.1016/j.jembe.2010.08.013)
- R Development Core Team. (2021). *R: A language and environment for statistical computing*. (4.1.0). R Foundation for Statistical Computing. <http://www.r-project.org>
- Rabouille, C., Crassous, P., Kripounoff, A., Gaillard, J. F., Jahnke, R., Pierre, C., & Relexans, J. C. (1993). A model of early diagenesis in the tropical North Atlantic: Processes and mass balances in the sediments of the EUMELI program. *Chemical Geology*, 107(3-4), 463-466. [https://doi.org/10.1016/0009-2541\(93\)90232-8](https://doi.org/10.1016/0009-2541(93)90232-8)
- Rabouille, C., Stahl, H., Bassinot, F., Tengberg, A., Brunnegard, J., Hall, P., Kiriakoulakis, K., Reyss, J. L., Dezileau, L., Crassous, P., Roos, P., & Lampitt, R. S. (2001). Imbalance in the carbonate budget of surficial sediments in the North Atlantic Ocean: Variations over the last millenium? *Progress in Oceanography*, 50(1-4), 201-221. [https://doi.org/10.1016/S0079-6611\(01\)00054-4](https://doi.org/10.1016/S0079-6611(01)00054-4)
- Rajendran, N., Suwa, Y., & Urushigawa, Y. (1993). Distribution of phospholipid ester-linked fatty acid

- biomarkers for bacteria in the sediment of Ise Bay, Japan. *Marine Chemistry*, 42(1), 39–56. [https://doi.org/10.1016/0304-4203\(93\)90248-M](https://doi.org/10.1016/0304-4203(93)90248-M)
- Ramos, A., Sanz, J. L., Pelegrí, J. L., Fernández-Peralta, L., Pascual-Alayón, P. J., Ramil, F., Castillo, S., García-Isarch, E., Rocha, F., Gil, M., & Calero, B. (2017). An Overview on Biodiversity and Ecosystems Off Mauritanian Deep-Waters. *Deep-Sea Ecosystems Off Mauritania: Research of Marine Biodiversity and Habitats in the Northwest African Margin*, 615–660. https://doi.org/10.1007/978-94-024-1023-5_17/FIGURES/19
- Relexans, J. C., Deming, J., Dinet, A., Gaillard, J. F., & Sibuet, M. (1996). Sedimentary organic matter and micro-meiobenthos with relation to trophic conditions in the tropical northeast Atlantic. *Deep-Sea Research Part I: Oceanographic Research Papers*, 43(8), 1343–1368. [https://doi.org/10.1016/0967-0637\(96\)00062-3](https://doi.org/10.1016/0967-0637(96)00062-3)
- Rex, M. A., Etter, R. J., Morris, J. S., Crouse, J., McClain, C. R., Johnson, N. A., Stuart, C. T., Deming, J. W., Thies, R., & Avery, R. (2006). Global bathymetric patterns of standing stock and body size in the deep-sea benthos. *Marine Ecology Progress Series*, 317, 1–8. <https://doi.org/10.3354/meps317001>
- Risk, M. J., & Sammarco, P. W. (1991). Cross-shelf trends in skeletal density of the massive coral *Porites lobata* from the Great Barrier Reef. *Marine Ecology Progress Series*, 195–200. <https://www.jstor.org/stable/44634779>
- Roberts, J. M., Henry, L. A., Long, D., & Hartley, J. P. (2008). Cold-water coral reef frameworks, megafaunal communities and evidence for coral carbonate mounds on the Hatton Bank, north east Atlantic. *Facies*, 54(3), 297–316. <https://doi.org/10.1007/s10347-008-0140-x>
- Roberts, J. M., Wheeler, A., Freiwald, A., and Cairns, S. D. (2009). Cold-water corals: The biology and geology of deep-sea coral habitats. Cambridge: Cambridge University Press.
- Roberts, J. M. & shipboard party (2013) Changing Oceans Expedition 2012. RRS James Cook 073 Cruise Report. Heriot-Watt University. 224 pp. https://www.bodc.ac.uk/resources/inventories/cruise_inventory/reports/jc073.pdf
- Robison, B. H., Reisenbichler, K. R., & Sherlock, R. E. (2005). Giant larvacean houses: Rapid carbon transport to the deep sea floor. *Science*, 308(5728), 1609–1611. <https://doi.org/10.1126/science.1109104>
- Rohal, M., Thistle, D., & Easton, E. E. (2018). Extraction of metazoan meiofauna from muddy deep-sea samples: Operator and taxon effects on efficiency. *Journal of Experimental Marine Biology and Ecology*, 502, 105–110. <https://doi.org/10.1016/j.jembe.2017.01.006>
- Rohlfer, E. K., Scheer, S. L., Bergmann, M., Sweetman, A. K., & Hoving, H. J. T. (2022). Contrasting residence time and scavenging communities of experimental invertebrate food falls in the Arctic deep sea. *Deep Sea Research Part I: Oceanographic Research Papers*, 189, 103832. <https://doi.org/10.1016/J.DSR.2022.103832>
- Rowe, G. T. (1983). Biomass and production of the deep-sea macrobenthos. *Deep-Sea Biology*, 8(November), 97–121.
- Rowe, G. T., Polloni, P. T., & Haedrich, R. L. (1982). The deep-sea macrobenthos on the continental margin of the northwest Atlantic Ocean. *Deep Sea Research Part A. Oceanographic Research Papers*, 29(2), 257–278. [https://doi.org/10.1016/0198-0149\(82\)90113-3](https://doi.org/10.1016/0198-0149(82)90113-3)
- Rowe, G. T., Polloni, P. T., & Horner, S. G. (1974). Benthic biomass estimates from the northwestern atlantic ocean and the northern Gulf of Mexico. *Deep Sea Research and Oceanographic Abstracts*, 21(8), 641–650. [https://doi.org/10.1016/0011-7471\(74\)90048-5](https://doi.org/10.1016/0011-7471(74)90048-5)
- Rstudio Team. (2019). RStudio: Integrated development for R. RStudio, Inc., Boston MA. In RStudio. <https://doi.org/10.1007/978-3-642-20966-6>
- Salonen, K., & Sarvala, J. (1980). The effect of different preservation methods on the carbon content of megacyclops gigas. *Hydrobiologia*, 72(3), 281–285. <https://doi.org/10.1007/BF00005632>
- Sanders, H. L., Hessler, R. R., & Hampson, G. R. (1965). An introduction to the study of deep-sea benthic faunal assemblages along the Gay Head-Bermuda transect. *Deep Sea Research and Oceanographic Abstracts*, 12(6), 845–867. [https://doi.org/10.1016/0011-7471\(65\)90808-9](https://doi.org/10.1016/0011-7471(65)90808-9)
- Scoffin TP, Tudhope AW, Brown BE, Chansang H, Cheeney RF (1992) Patterns and possible environmental controls of skeletogenesis of *Porites lutea*, South Thailand. *Coral Reefs* 11:1–11

- Schaff, T., Levin, L., Blair, N., Demaster, D., Pope, R., & Boehme, S. (1992). Spatial Heterogeneity of benthos on the Carolina continental slope: large (100 km)-scale variation. *Marine Ecology Progress Series*, 88(2–3), 143–160. <https://doi.org/10.3354/MEPS088143>
- Scheer, S., Sweetman, A., Piatkowski, U., Rohlfer, E., & Hoving, H. (2022). Food fall-specific scavenging response to experimental medium-sized carcasses in the deep sea. *Marine Ecology Progress Series*, 685(March), 31–48. <https://doi.org/10.3354/meps13973>
- Scheltema, A. H. (1997). Aplacophoran molluscs: Deep-sea analogs to polychaetes. *Bulletin of Marine Science*, 60(2), 575–583.
- Schneider, C. A., Rasband, W. S., & Eliceiri, K. W. (2012). NIH Image to ImageJ: 25 years of image analysis. *Nature Methods*, 9(7), 671–675. <https://doi.org/10.1038/NMETH.2089>
- Sebastian, S., Raes, M., De Mesel, I., & Vanreusel, A. (2007). Comparison of the nematode fauna from the Weddell Sea Abyssal Plain with two North Atlantic abyssal sites. *Deep-Sea Research Part II: Topical Studies in Oceanography*, 54(16–17), 1727–1736. <https://doi.org/10.1016/j.dsr2.2007.07.004>
- Shi, L., Zhang, X., Xiao, W., Pan, B., Liu, Z., & Xu, Y. (2020). Ontogenetic diet change of hadal amphipods in the New Britain Trench revealed by fatty acid biomarker and stable isotope ratio. *Deep Sea Research Part I: Oceanographic Research Papers*, 160, 103276. <https://doi.org/10.1016/J.DSR.2020.103276>
- Simkiss K (1964) Phosphates as crystal poisons of calcification. *Biol. Rev.* 39, 487–504.
- Sibuet, M., Albert, P., Charmasson, S., Deming, J., Dinet, A., Galeron, J., Guidi-Guilvard, L., Mahaut, M. L., & others. (1993). The benthic ecosystem in the three EUMELI sites in the northeast tropical Atlantic: general perspectives and initial results on biological abundance and activities. *Ann. Inst. Océanogr. Paris*, 69, 21–33.
- Sibuet, M., Lambert, C. E., Chesselet, R., & Laubier, L. (1989). Density of the major size groups of benthic fauna and trophic input in deep basins of the Atlantic Ocean. *Journal of Marine Research*, 47(4), 851–867. <https://doi.org/10.1357/002224089785076064>
- Sibuet, M., Monniot, C., Desbruyeres, D., Dinet, A., Khripounoff, A., Rowe, G., & Segonzac, M. (1984). Peuplements benthiques et caractéristiques trophiques du milieu dans la plaine abyssale de Demerara. *Oceanologica Acta*, 7(3), 345–358. <https://archimer.ifremer.fr/doc/00131/24217/22210.pdf>
- Smith, A. B., & Stockley, B. (2005). The geological history of deep-sea colonization by echinoids: roles of surface productivity and deep-water ventilation. *Proceedings of the Royal Society - Biological Sciences.*, 272, 865–869.
- Smith, C. R., De Leo, F. C., Bernardino, A. F., Sweetman, A. K., & Arbizu, P. M. (2008a). Abyssal food limitation, ecosystem structure and climate change. *Trends in Ecology and Evolution*, 23(9), 518–528. <https://doi.org/10.1016/j.tree.2008.05.002>
- Smith, C. R., De Leo, F. C., Bernardino, A. F., Sweetman, A. K., & Arbizu, P. M. (2008b). Abyssal food limitation, ecosystem structure and climate change. *Trends in Ecology and Evolution*, 23(9), 518–528. <https://doi.org/10.1016/j.tree.2008.05.002>
- Smith, C. R., Glover, A. G., Treude, T., Higgs, N. D., & Amon, D. J. (2015). Whale-Fall Ecosystems: Recent Insights into Ecology, Paleoecology, and Evolution. *Annual Review of Marine Science*, 7(1), 571–596. <https://doi.org/10.1146/annurev-marine-010213-135144>
- Snelgrove, P. V. R., Soetaert, K., Solan, M., Thrush, S., Wei, C. L., Danovaro, R., Fulweiler, R. W., Kitazato, H., Ingole, B., Norkko, A., Parkes, R. J., & Volkenborn, N. (2018). Global Carbon Cycling on a Heterogeneous Seafloor. *Trends in Ecology and Evolution*, 33(2), 96–105. <https://doi.org/10.1016/j.tree.2017.11.004>
- Soetaert, K. (2009). Package NetIndices, network indices and food web descriptors in R. *Ecology*, 1, 1–10.
- Soetaert, K., & Van Oevelen, D. (2010). *Package LIM, implementing linear inverse models in R*. 37.
- Soltwedel, T., Von Juterzenka, K., Premke, K., & Klages, M. (2003). What a lucky shot! Photographic evidence for a medium-sized natural food-fall at the deep seafloor. *Oceanologica Acta*, 26(5–6), 623–628. [https://doi.org/10.1016/S0399-1784\(03\)00060-4](https://doi.org/10.1016/S0399-1784(03)00060-4)
- Ståhl, H., Tengberg, A., Brunnegård, J., & Hall, P. O. J. (2004). Recycling and burial of organic carbon in sediments of the Porcupine Abyssal Plain, NE Atlantic. *Deep-Sea Research Part I: Oceanographic*

- Research Papers*, 51(6), 777–791. <https://doi.org/10.1016/j.dsr.2004.02.007>
- Stratmann, T. (2023). Role of polymetallic-nodule dependent fauna on carbon cycling in the eastern Clarion-Clipperton Fracture Zone (Pacific). *Frontiers in Marine Science*, 10, 787. <https://doi.org/10.3389/FMARS.2023.1151442>
- Stratmann, T., Mevenkamp, L., Sweetman, A. K., Vanreusel, A., & van Oevelen, D. (2018). Has Phytodetritus Processing by an Abyssal Soft-Sediment Community Recovered 26 Years after an Experimental Disturbance? *Frontiers in Marine Science*, 5(February), 1–13. <https://doi.org/10.3389/fmars.2018.00059>
- Stratmann, T., Soetaert, K., Wei, C.-L., Lin, Y.-S., & van Oevelen, D. (2019). The SCOC database – a large, open and global database with sediment community oxygen consumption rates. *Dryad Digital Repository*, 1, <https://doi.org/10.5061/dryad.25nd083>. <https://doi.org/10.1038/s41597-019-0259-3>
- Sweetman, A. K., & Chapman, A. (2015). First assessment of flux rates of jellyfish carcasses (jelly-falls) to the benthos reveals the importance of gelatinous material for biological C-cycling in jellyfish-dominated ecosystems. *Frontiers in Marine Science*, 2, 1–7. <https://doi.org/10.3389/fmars.2015.00047>
- Sweetman, A. K., Smith, C. R., Dale, T., & Jones, D. O. B. (2014). Rapid scavenging of jellyfish carcasses reveals the importance of gelatinous material to deep-sea food webs. *Proceedings of the Royal Society B: Biological Sciences*, 281, 20142210. <https://doi.org/10.1098/rspb.2014.2210>
- Sweetman, A. K., Smith, C. R., Shulse, C. N., Maillot, B., Lindh, M., Church, M. J., Meyer, K. S., Oevelen, D., Stratmann, T., & Gooday, A. J. (2019). Key role of bacteria in the short-term cycling of carbon at the abyssal seafloor in a low particulate organic carbon flux region of the eastern Pacific Ocean. *Limnology and Oceanography*, 64(2), 694–713. <https://doi.org/10.1002/lno.11069>
- Sweetman, A. K., Sommer, S., Pfannkuche, O., & Witte, U. (2009). Retarded response by macrofauna-size foraminifera to phytodetritus in a deep Norwegian fjord. *Journal of Foraminiferal Research*, 39(1), 15–22. <https://doi.org/10.2113/gsfir.39.1.15>
- Sweetman, A. K., Thurber, A. R., Smith, C. R., Levin, L. A., Mora, C., Wei, C.-L., Gooday, A. J., Jones, D. O. B., Rex, M., Yasuhara, M., Ingels, J., Ruhl, H. A., Frieder, C. A., Danovaro, R., Würzberg, L., Baco, A., Grupe, B. M., Pasulka, A., Meyer, K. S., ... Roberts, J. M. (2017). Major impacts of climate change on deep-sea benthic ecosystems. *Elem Sci Anth*, 5(0), 4. <https://doi.org/10.1525/elementa.203>
- Sweetman, A. K., & Witte, U. (2008). Response of an abyssal macrofaunal community to a phytodetrital pulse. *Marine Ecology Progress Series*, 355, 73–84. <https://doi.org/10.3354/MEPS07240>
- Tecchio, S., van Oevelen, D., Soetaert, K., Navarro, J., & Ramírez-Llodra, E. (2013). Trophic Dynamics of Deep-Sea Megabenthos Are Mediated by Surface Productivity. *PLoS ONE*, 8(5). <https://doi.org/10.1371/journal.pone.0063796>
- Thiede, J., Suess, E., & Muller, P. J. (1982). Late Quaternary Fluxes of Major Sediment Components to the Sea Floor at the Northwest African Continental Slope. *Geology of the Northwest African Continental Margin*, 605–631. https://doi.org/10.1007/978-3-642-68409-8_25
- Thiel, M., & Kruse, I. (2001). Status of the Nemertea as predators in marine ecosystems. *Hydrobiologia*, 456(1), 21–32. <https://doi.org/10.1023/A:1013005814145>
- Thurber, A. R., Sweetman, A. K., Narayanaswamy, B. E., Jones, D. O. B., Ingels, J., & Hansman, R. L. (2014). Ecosystem function and services provided by the deep sea. *Biogeosciences*, 11(14), 3941–3963. <https://doi.org/10.5194/bg-11-3941-2014>
- Thurston, M. H. (1990). Abyssal necrophagous amphipods (Crustacea: Amphipoda) in the northeast and tropical Atlantic Ocean. *Progress in Oceanography*, 24(1–4), 257–274. [https://doi.org/10.1016/0079-6611\(90\)90036-2](https://doi.org/10.1016/0079-6611(90)90036-2)
- Tobor-Kapłon, M. A., Holtkamp, R., Scharler, U. M., Doroszuk, A., Kuenen, F. J. A., Bloem, J., & de Ruiter, P. C. (2007). Evaluation of information indices as indicators of environmental stress in terrestrial soils. *Ecological Modelling*, 208(1), 80–90. <https://doi.org/10.1016/J.ECOLMODEL.2007.04.022>
- Tokuda, A. K., Drazen, J. C., Geringer, M. E., Popp, B. N., Grammatopoulou, E., & Mayor, D. J. (2020). Trophic interactions of megafauna in the Mariana and Kermadec trenches inferred from stable isotope analysis. *Deep Sea Research Part I: Oceanographic Research Papers*, 164, 103360.

- <https://doi.org/10.1016/J.DSR.2020.103360>
- Tomanek, L. (2014). Proteomics to study adaptations in marine organisms to environmental stress. *Journal of Proteomics*, 105, 92–106. <https://doi.org/10.1016/J.JPROT.2014.04.009>
- Trott, T. J. (1998). Gustatory responses of priapulid caudatus de lamarck, 1816 (priapulida, priapulidae): Feeding behavior and chemoreception by a living fossil. *Marine and Freshwater Behaviour and Physiology*, 31(4), 251–257. <https://doi.org/10.1080/10236249809387076>
- Trueman, C. N., Johnston, G., O’Hea, B., & MacKenzie, K. M. (2014). Trophic interactions of fish communities at midwater depths enhance long-term carbon storage and benthic production on continental slopes. *Proceedings of the Royal Society B: Biological Sciences*, 281(1787), 20140669–20140669. <https://doi.org/10.1098/rspb.2014.0669>
- Tsounis G, Orejas C, Reynaud S, Gili JM, Allemand D, Ferrier-Pagès C (2010) Prey-capture rates in four Mediterranean cold water corals. *Marine Ecology Progress Series* 398: 149-155 [doi 10.3354/meps08312](https://doi.org/10.3354/meps08312)
- Vad, J., Orejas, C., Moreno-Navas, J., Findlay, H. S., & Roberts, J. M. (2017). Assessing the living and dead proportions of cold-water coral colonies: Implications for deep-water Marine Protected Area monitoring in a changing ocean. *PeerJ*, 2017(10), 1–20. <https://doi.org/10.7717/peerj.3705>
- van der Kaaden, A.-S., & De Clippele, L. (2021). AnnavdKaaden/ImageAnnotation: Image/Video Annotation and Analysis (Version v3). In Zenodo. <https://doi.org/10.5281/ZENODO.5547565>
- van Oevelen, D., van den Meersche, K., Meysman, F. J. R., Soetaert, K., Middelburg, J. J., & Vézina, A. F. (2010). Quantifying food web flows using linear inverse models. *Ecosystems*, 13(1), 32–45. <https://doi.org/10.1007/s10021-009-9297-6>
- van Oevelen, D., Soetaert, K., & Heip, C. (2012). Carbon flows in the benthic food web of the Porcupine Abyssal Plain: The (un)importance of labile detritus in supporting microbial and faunal carbon demands. *Limnology and Oceanography*, 57(2), 645–664. <https://doi.org/10.4319/lo.2012.57.2.0645>
- van Oevelen, D., Duineveld, G. C. A., Lavaleye, M. S. S., Kutti, T. & Soetaert, K (2018). Trophic structure of cold-water coral communi- ties revealed from the analysis of tissue isotopes and fatty acid composition. *Mar. Biol. Res.* **14**, 287–306. <https://doi.org/10.1080/17451000.2017.1398404>.
- Vinha, B., Rossi, S., Gori, A. et al. Trophic ecology of Angolan cold-water coral reefs (SE Atlantic) based on stable isotope analyses. *Sci Rep* 13, 9933 (2023)
- Visser, F., Merten, V. J., Bayer, T., Oudejans, M. G., De Jonge, D. S. W., Puebla, O., Reusch, T. B. H., Fuss, J., & Hoving, H. J. T. (2021). Deep-sea predator niche segregation revealed by combined cetacean biologging and eDNA analysis of cephalopod prey. *Science Advances*, 7(14), 1–12. <https://doi.org/10.1126/sciadv.abf5908>
- Wang, D., Gouhier, T. C., Menge, B. A., & Ganguly, A. R. (2015). Intensification and spatial homogenization of coastal upwelling under climate change. *Nature* 2015 518:7539, 518(7539), 390–394. <https://doi.org/10.1038/nature14235>
- Wieser, W. (1953). Die Beziehung zwischen Mundhoehlgestalt, Emaehrungsweise und Vorkommen bei freilebenden Wieser, W. *Kanwisher, J.(1961). Ecological and Physiologimarininen Nematoden. Arkiv. Zool*, 4, 439484.
- Wilson, J. (1979). ‘Patch’ development of the deep-water coral *Lophelia Pertusa* (L.) on Rockall Bank. *Journal of the Marine Biological Association of the United Kingdom*, 59(1), 165-177.
- Witbaard, R., Duineveld, G. C. A., Van der Weele, J. A., Berghuis, E. M., & Reyss, J. P. (2000). The benthic response to the seasonal deposition of phytopigments at the Porcupine Abyssal Plain in the North East Atlantic. *Journal of Sea Research*, 43(1), 15–31. [https://doi.org/10.1016/S1385-1101\(99\)00040-4](https://doi.org/10.1016/S1385-1101(99)00040-4)
- Witte, U., Wenzhöfer, F., Sommer, S., Boetius, A., Heinz, P., Aberle, N., Sand, M., Cremer, A., Abraham, W. R., Jørgensen, B. B., & Pfannkuche, O. (2003). In situ experimental evidence of the fate of a phytodetritus pulse at the abyssal sea floor. *Nature*, 424(6950), 763–766. <https://doi.org/10.1038/nature01799>
- Wolfram, U., Peña Fernández, M., McPhee, S. et al. Multiscale mechanical consequences of ocean

- acidification for cold-water corals. *Sci Rep* **12**, 8052 (2022).
- Woulds, C., Andersson, J. H., Cowie, G. L., Middelburg, J. J., & Levin, L. A. (2009). The short-term fate of organic carbon in marine sediments: Comparing the Pakistan margin to other regions. *Deep-Sea Research Part II: Topical Studies in Oceanography*, *56*(6–7), 393–402. <https://doi.org/10.1016/j.dsr2.2008.10.008>
- Yamamoto, J., Nobetsu, T., Iwamori, T., & Sakurai, Y. (2009). Observations of food falls off the Shiretoko Peninsula, Japan, using a remotely operated vehicle. *Fisheries Science*, *75*, 513–515. <https://doi.org/10.1007/s12562-008-0055-z>
- Zeng, Q., Huang, D., Lin, R., & Wang, J. (2018). Deep-sea metazoan meiofauna from a polymetallic nodule area in the Central Indian Ocean Basin. *Marine Biodiversity*, *48*, 395–405. <https://doi.org/10.1007/s12526-017-0778-0>

9. Document Information

EU Project N°	818123	Acronym	iAtlantic
Full Title	Integrated Assessment of Atlantic Marine Ecosystems in Space and Time		
Project website	www.iatlantic.eu		

Deliverable	N°	4.2	Title	Baseline ecosystem functioning in selected deep-sea environments.
Work Package	N°	4	Title	Impacts of multiple stressors

Date of delivery	Contractual	Month 52	Actual	Month 57
Dissemination level	PU	PU Public, fully open, e.g. web		
		CO Confidential restricted under conditions set out in Model Grant Agreement		
		CI Classified, information as referred to in Commission Decision 2001/844/EC		

Authors (Partner(s))	Andrew K. Sweetman, Danielle de Jonge, Daniela Gaurisas, Angelo Bernadino, Loïc N. Michel, Corentin Le Goff, Christophe Brandily, Marjolaine Matabos, Eve-Julie Pernet, Julie Tourolle, Lénaïck Menot, Sebastian Hennige, Kelsey Barnhill, Marina Carreiro Silva, Laurence De Clippele, Covadonga Orejas.			
Responsible Author	Name	Andrew Sweetman	Email	Andrew.Sweetman@sams.ac.uk